

Magazine of Civil Engineering

125th

ISSN
2712-8172



121(5), 2023



Magazine of Civil Engineering

ISSN 2712-8172

Online peer-reviewed open-access scientific journal in the field of Civil and Construction Engineering

Founder and Publisher: Peter the Great St. Petersburg Polytechnic University

This journal is registered by the Federal Service for Supervision of Communications, Information Technology, and Mass Media (ROSKOMNADZOR) in 2020. Certificate EI No. FS77-77906 issued February 19, 2020.

Periodicity: 8 issues per year

Publication in the journal is open and free for all authors and readers.

Indexing: Scopus, Web of Science (ESCI, RSCI), DOAJ, Compendex, Google Academia, Index Copernicus, ProQuest, Ulrich's Serials Analysis System, CNKI

Corresponding address: 29 Polytechnicheskaya st., Saint Petersburg, 195251, Russia

Chief science editor: associate member of RAS, D.S. in Engineering, Vitaly V. Sergeev

Deputy chief science editors:

D.S. in Engineering, Galina L. Kozinets

D.S. in Engineering, Sergey V. Korniyenko

Executive editor: Ekaterina A. Linnik

Translator, editor: Darya Yu. Alekseeva

DT publishing specialist:

Anastasiya A. Kononova

Contacts:

E-mail: mce@spbstu.ru

Web: <http://www.engstroy.spbstu.ru>

Date of issue: 14.08.2023

© Peter the Great St. Petersburg Polytechnic University. All rights reserved.

© Coverpicture – Ilya Smagin

Editorial board:

T. Awwad, PhD, professor, Damascus University, Syrian Arab Republic

M.I. Balzannikov, D.Sc., professor, Samara State University of Economics, Russia

A.I. Belostotsky, D.Sc., professor, StaDyO Research & Engineering Centre, Russia

A.I. Borovkov, PhD, professor, Peter the Great St. Petersburg Polytechnic University, Russia

A. Borodinecs, Dr.Sc.Ing., professor, Riga Technical University, Latvia

M. Veljkovic, PhD, professor, Delft University of Technology, The Netherlands

R.D. Garg, PhD, professor, Indian Institute of Technology Roorkee (IIT Roorkee), India

M. Garifullin, PhD, postdoctoral researcher, Tampere University, Finland

T. Gries, Dr.-Ing., professor, RWTH Aachen University, Germany

T.A. Datsyuk, D.Sc., professor, Saint-Petersburg State University of Architecture and Civil Engineering, Russia

V.V. Elistratov, D.Sc., professor, Peter the Great St. Petersburg Polytechnic University, Russia

T. Kärki, Dr.-Ing., professor, Lappeenranta University of Technology, Russia

G.L. Kozinets, D.Sc., professor, Peter the Great St. Petersburg Polytechnic University, Russia

D.V. Kozlov, D.Sc., professor, National Research Moscow State Civil Engineering University, Russia

S.V. Korniyenko, D.Sc., professor, Volgograd State Technical University, Russia

Yu.G. Lazarev, D.Sc., professor, Peter the Great St. Petersburg Polytechnic University, Russia

M.M. Muhammadiev, D.Sc., professor, Tashkent State Technical University, Republic of Uzbekistan

H. Pasternak, Dr.-Ing.habil., professor, Brandenburgische Technische Universität, Germany

F. Rögner, Dr.-Ing., professor, Technology Arts Science TH Köln, Germany

V.V. Sergeev, D.Sc., professor, Peter the Great St. Petersburg Polytechnic University, Russia

T.Z. Sultanov, D.Sc., professor, Tashkent Institute of Irrigation and Agricultural Mechanization Engineers, Republic of Uzbekistan

M.G. Tyagunov, D.Sc., professor, National Research University "Moscow Power Engineering Institute", Russia

M.P. Fedorov, D.Sc., professor, Peter the Great St. Petersburg Polytechnic University, Russia

D. Heck, Dr.-Ing., professor, Graz University of Technology, Austria

A.G. Shashkin, D.Sc., "PI Georekonstruktsiya", LLC, Russia

V.B. Shtilman, D.Sc., JSC "B.E. Vedeneev VNIIG", Russia

Contents

Korniyenko, S.V., Dubov, I.A., Nazarov, K.R. Field study of thermal comfort in dwelling during the winter, mid-season and summer	12101
Minaev, O.P. Soil friction on a retaining wall under seismic load	12102
Erofeev, V.I., Monich, D.V., Grebnev, P.A., Pavlov, I.S. Calculation method for sound insulation of lightweight enclosures at low frequencies	12103
Vakalova, T., Sergeev N., D. Tolegenov, D. Tolegenova. High-strength building ceramics based on fly ash – red mud mixtures	12104
Tyukalov, Yu.Ya. Triangular prism finite element based on piecewise constant stress approximations	12105
Sharafutdinov, R.F. Clay soil stiffness under consolidated isotropic drained triaxial tests	12106
Akhazhanov, S.B., Vatin, N.I., Akhmediyev, S., Akhazhanov, T., Khabidolda, O., Nurgoziyeva, A. Beam on a two-parameter elastic foundation: Simplified finite element model	12107
Lesovik, V.S., Popov, D.Y., Fediuk, R.S., Sabri, M.M., Vavrenyuk, S.V., Liseitsev, Yu.L. Shrinkage of ultra-high performance concrete with superabsorbent polymers	12108
Rodin, A.I., Ermakov, A.A., Kyashkin, V.M., Rodina, N.G., Erofeev, V.T. Processes of foaming and formation of the structure of porous glass ceramics from siliceous rocks	12109
Shakhov, S.A. Structural and phase features of ceramics from loam and incinerated sewage sludge ash	12110



Research article

UDC 628.87

DOI: 10.34910/MCE.121.1



Field study of thermal comfort in dwelling during the winter, mid-season and summer

S.V. Korniyenko  , I.A. Dubov, K.R. Nazarov

Volgograd State Technical University, Volgograd, Russian Federation

✉ svkorn2009@yandex.ru

Keywords: adaptive thermal comfort models, dwelling, climate zone, neutral cold environment, comfort temperature, free-running thermal environments, energy efficiency

Abstract. This research focused on adaptive thermal comfort in dwelling in the cold winter and hot summer climate zone of Russia. A field study was conducted throughout the three seasons (winter, mid-season and summer) beginning in September 2019 and ending in June 2020 in Volgograd (48°43.164'N, 44°30.108'E), Russia. The survey included simultaneous measurements of outdoor and indoor environmental parameters and an assessment of the participants' sensations using questionnaires. The living room and bedroom of an apartment building for a family with a child were chosen as the research environment for indoor physical parameters and for administering the questionnaires. Only free-running thermal environments were considered in this research. The sensation ratings were analyzed, and thermal comfort temperature was calculated using regression methods. Results showed that in winter there were deviations in the thermal sensation, satisfaction, expectation of residents, and that they preferred a neutral cold environment. There were differences between the mid-season results and those of winter and summer. The thermal comfort assessment in premises under continental climate conditions should be based on thermal adaptation models. We calculated that the acceptable temperature range for residents in winter was 17.5–22.5 °C, 20–25 °C (with acceptable deviation of 2.5 °C) in mid-season and 22.5–27.5 °C in summer. The actual indoor relative humidity was almost within the applicable ranges (30–60 %) as well. The ASHRAE55-2013 and EN15251-2007 adaptive thermal comfort models are suitable for premises in mid-season and summer. The predictions of both mid-season and summer models were reliable. The main solutions to improve the indoor temperature conditions include heat flux control in heaters within the apartment in accordance with the adaptation thermal comfort model, as well as control of natural ventilation in winter. In this case it is predicted, that the reduction of total heating load is 24.2 %. Indoor thermal neutral temperature at the small energy demand in premises can be obtained by implementing the smart home concept. These results can be used to assess indoor thermal comfort in dwelling and help create friendly and energy efficiency building environments in Russia.

Citation: Korniyenko, S.V., Dubov, I.A., Nazarov, K.R. Field study of thermal comfort in dwelling during the winter, mid-season and summer. Magazine of Civil Engineering. 2023. 121(5). Article no. 12101. DOI: 10.34910/MCE.121.1

1. Introduction

Indoor thermal environments significantly influence human health and comfort, since most of the time people are indoors [1]. Thermal comfort and adaptation are considered important issues in the interior design of buildings [2]. Also, energy consumption is required to ensure comfortable indoor conditions [3–5]. Therefore, the main task of designers is to obtain the comfortable conditions in the premises using minimum energy consumption [6, 7].

The first human comfort model was developed by Fanger in 1967. Fanger used the seven-point form of a thermal sensation scale along with numerous experiments involving human subjects in various environments [8, 9]. He related the subject's response to various variables which influence the condition of thermal comfort. This mathematical model is probably the most well-known and is the easiest to use because it has been put in both chart and graph form.

Bogoslovsky developed the original theory of thermal comfort in the premises and proposed two conditions of comfort, as shown in paper [10].

Later, the Pierce Model was developed at the John B. Pierce Foundation [11]. This model considers the human body as two isothermal, concentric compartments, one representing the internal section or core and the other representing the skin. This allows the passive heat conduction from the core compartment to the skin to be taken into account.

The LSTM model is quite similar to that of the Pierce Foundation. The main difference between the two models is that the LSTM model predicts thermal sensation differently for warm and cold environment [12].

Tabunshchikov developed the theory of buildings as single energy systems [13]. Currently, some adaptive thermal comfort models have been included in ASHRAE 55-2013 and EN 15251-2007 standards.

The paper [14] provides a comparison of the country's requirements for building energy efficiency and how the application of different standards in combination with ventilation alternatives in each analyzed city affects annual energy consumption in the Saint Petersburg region. IDA Indoor Climate and Energy (ICE) 4.7 dynamic simulation software was used to evaluate normative requirement effect on building energy consumption in different areas of the Baltic Sea region.

The research method [15] is based on a review of technical parameters; in well ventilated buildings all CO₂ sensors showed similar results and the difference between sensors located in different zones was minimal.

The paper [16] analyses typology of Latvian fire stations and their energy consumption. Standardized IFC model was developed to evaluate effect of implementation of energy efficiency measures in a selected building.

The focus of the paper [17] is to develop a verified simulation model for a cooling panel with integrated phase-change materials (PCMs).

The PMV measurements in a temporary shelter showed that the thermal comfort is very low as the PMV values were outside the range of -1 to $+1$ for 57 % of the time [18].

Many researches have been exploring ways to predict the thermal sensation of people in their environment based on the personal, environmental and physiological variables that influence thermal comfort [19–22]. From the research done, some mathematical models that simulate occupants thermal response to their environment have been developed.

Adaptive comfort theory considers that the optimal indoor operative temperature for occupants who can interact with the building and its devices relates primarily to the outdoor environmental conditions, and the application conditions differ among building types and outdoor temperatures [23]. For buildings located in a tropical climate, several field studies have estimated the thermal comfort and adaptability using adaptation theory. The studies usually report the thermal adaptability, adaptive thermal comfort model, and deviations between proposed models with reference cases [24]. In recent years, researchers have conducted extensive field studies in different climatic regions (mainly in cold and warm environments), but most of them focused on residential [25, 26], office [27], educational buildings [28], churches [29, 30], long-distance trains [31], etc.

It is important to note that the actual data illustrating occupants' adaptability to thermal environment in the premises during the winter (heating), mid-season and summer are not detailed in the scientific literature.

The research objectives were as follows:

1. To investigate the thermal environment and comfort of premises based on the field tests.
2. To determine the neutral, comfort, and acceptable temperature ranges of premises in different seasons, using different adaptive comfort models.
3. To conduct a comparative analysis of this models.

2. Methods

The field study included simultaneous instrumentation measurements of indoor environment parameters (air temperature, relative humidity), including analyses of outdoor environment parameters, and the assessment of the thermal comfort conditions in the rooms of the apartment building (Fig. 1).

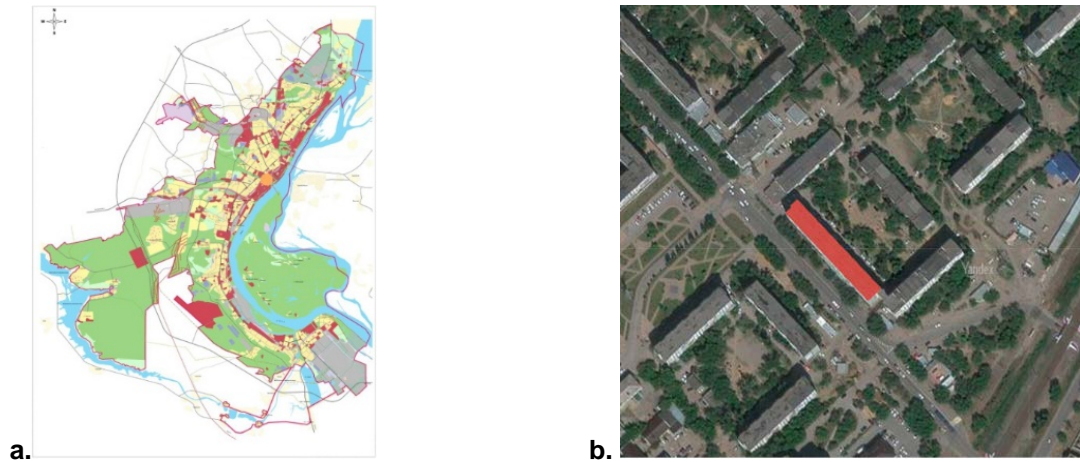


Figure 1. Location of the study object: master plan (a) and Google photography (b) (Volgograd, Russia).

The field study began in September 2019 and ended in June 2020. Data were collected in winter, summer, and mid-season (spring and autumn). Winter (heating) included a season with average daily outdoor air temperatures less or equal to 8 °C, summer was June through August, mid-season was autumn (from September to the start of the heating season) and spring (from the completion of the heating season to May).

2.1. Climatic conditions

Volgograd (48°43.164'N, 44°30.108'E) experiences a continental climate. Volgograd is in the cold winter and hot summer zone of the Russian building-climate zone. It is one of the hottest summer cities in Russia. The average air temperature in February ranges from -21.9 to 1.3 °C; in July it ranges from 19.8 to 28.9 °C. The average annual temperature is 8.8 °C. The amount of precipitation is 267 mm. The total average annual cloudiness is 6.1 points. The average annual wind speed is 5.0 m/s. The average annual relative humidity is 70 %. The average temperature of the heating season is -2.2 °C; its duration is 177 days.

The outdoor meteorological data were collected from the Russian Meteorological Data Center, including the hourly values of outdoor air temperature. These data were used in the adaptive comfort models.

2.2. Surveyed building

The living room (1) and bedroom (2) (Fig. 2, a) of an apartment building for a family with a child were chosen as the research environment for indoor physical parameters and for administering the questionnaires.

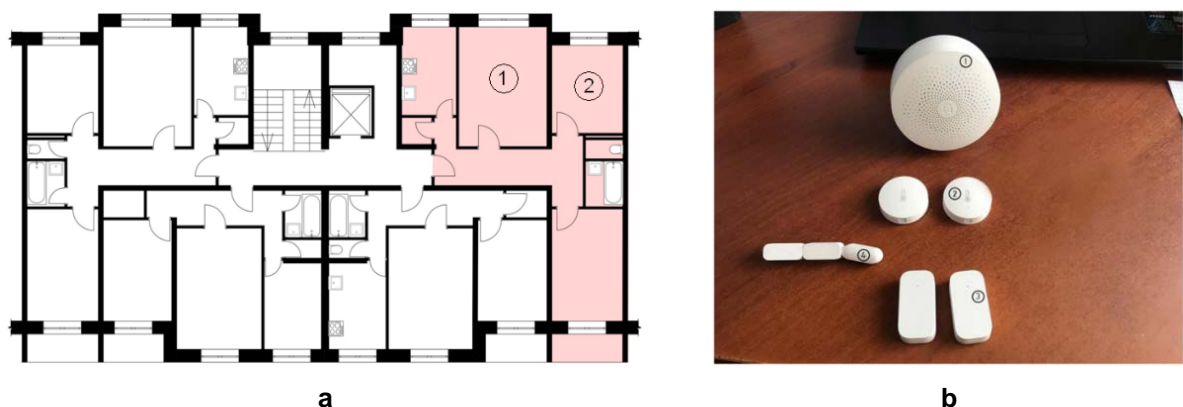


Figure 2. Plan of the block-section (a) and instrumentation (b) (1 – head unit, 2 – air temperature sensors, 3 – relative humidity sensors, 4 – window/door opening sensors).

An assessment of the field conditions revealed that the rooms had air conditioners (AC), but most residents did not use them. Therefore, only free-running thermal environments were considered in this research. The main characteristics of the subject of inquiry are given in Table 1.

Table 1. Characteristics of the subject of inquiry.

Name	Characteristic	Name	Characteristic
Type	Apartment building	R-value	1.21 m ² K·W ⁻¹ (wall) 0.56 m ² K·W ⁻¹ (window)
Configuration	Rectangular	Internal heat gains	80 W (person) 20 W (electric devices)
Number of block sections	4	Air exchange rate in winter	1.6·h ⁻¹ (window is open) 1.1·h ⁻¹ (window is closed)
Number of storeys	9	Natural ventilation	Yes
Basement	Yes	Smart sensors	Yes
Attic	Yes	District heating	Yes

Note: The walls are made of prefabricated reinforced concrete panels (PRCP), windows are made of single-chamber double-glazed units, the average air flow rate in winter as well as the heat gain are given according to expert assessment.

Instruments listed in Table 2 were utilized to measure indoor air temperature, relative humidity (RH), and windows opening monitoring (see Fig. 2, b).

Table 2. Instrumentation measurement range and accuracy.

Parameter	Instrumentation	Accuracy	Accuracy requirements in GOST 30494–2011 (National Standard)
Air temperature	AT sensor	±0.3 °C, range: -20...60 °C	Minimum: ±0.5 °C, ideal: ±0.1 °C
Relative humidity	RH sensor	±3.0 % RH, range: 0...99 %	±5.0 % RH
Air exchange	Window/door opening (WDO) sensor	Qualities analysis only	No requirements

Note: The data specified in the table are given in: <https://osensorax.ru/klimat/datchik-temperatury-i-vlazhnosti-xiaomi>.

The evaluation process of the indoor thermal environment was based on the ASHRAE 55-2013 and EN 15251-2007 standards. The main radiant temperature (MRT) was determined according to the method specified in Interstate Standard GOST 30494–2011, using the surface temperature of building components. In this case, the standard MRT can be calculated approximately using the equation summed over all zone surfaces [9]. Then the operative temperature was derived from the air temperature and mean radiant temperature. The obtained values of operative temperature were used in evaluation of thermal comfort in rooms.

2.3. Determining the indoor thermal comfort zone in the living room

At present, the main standards for determining the indoor thermal comfort zone of a free-running environment when using the thermal adaptation model are the ASHRAE 55-2013 and European Standard (EN 15251-2007). The estimate of indoor thermal comfort zone in the room using these standards is below.

The model of ASHRAE 55-2013 defines two comfort zones: 80 % acceptability, and 90 % acceptability. If the prevailing mean outdoor temperature is not within the specified domain of 10.0 °C to 33.5 °C, the model is not applicable.

The model of EN 15251-2007 also accounts for people's clothing adaptation in naturally conditioned spaces by relating the acceptable range of indoor temperatures to the outdoor climate, so it is not necessary to estimate the clothing values for the space. No humidity or air-speed limits are required when this option is used. The model defines three comfort zones: category I (90% acceptability), category II (80 % acceptability), category III (65 % acceptability). If the prevailing mean outdoor temperature is not within the specified domain of 10.0 °C to 30.0 °C, the model is not applicable.

The comfort zone boundaries in this model can be calculated by following formulas (see Table 3).

Table 3. Indoor temperature conditions for the thermal adaptation models according to Standard ASHRAE 55-2013 and Standard EN 15251-2007.

ASHRAE 55-2013		EN 15251-2007	
Category	Formula	Category	Formula
Comfort temperature	$T_{ot} = 0.31T_o + 17.8$	Comfort temperature	$T_{ot} = 0.33T_o + 18.8$
90% acceptability limit	$T_{ot} = 0.31T_o + 17.8 \pm 2.5$	I – 90 % acceptability limit	$T_{ot} = 0.33T_o + 18.8 \pm 2.0$
80% acceptability limit	$T_{ot} = 0.31T_o + 17.8 \pm 3.5$	II – 80 % acceptability limit	$T_{ot} = 0.33T_o + 18.8 \pm 3.0$
		III – 65 % acceptability limit	$T_{ot} = 0.33T_o + 18.8 \pm 4.0$

Note: T_{ot} is the operative temperature (°C), calculated as the average of the indoor air dry-bulb temperature and the mean radiant temperature of zone inside surface; T_o is the prevailing mean outdoor air dry-bulb temperature (°C).

The explanations of categories for European Standard EN 15251-2007 are listed in Table 4.

Table 4. Categories for European Standard EN 15251-2007.

Category	Explanation
I	High level of expectation recommended for spaces occupied by very sensitive and fragile persons with special requirements like handicapped, sick, very young children and elderly persons
II	Normal level of expectation, should be used for new buildings and renovations
III	An acceptable, moderate level of expectation, may be used for existing buildings
(IV)	Values outside the criteria for the above categories. This category should only be accepted for a limited part of the year

In Russia basic requirements for the thermal protection of enclosing structures and optimal/permissible air parameters of living rooms are defined by Interstate Standard (GOST 30494-2011) "Residential and public buildings: Microclimate parameters for indoor enclosures" (Table 5).

Table 5. Optimal and acceptable air parameters of living room according to Interstate Standard (GOST 30494-2011).

Time of the year	Air parameters (optimal/acceptable)			
	Temperature T_i , °C	Operative temperature T_{ot} , °C	RH, %	Speed v_i , m·s ⁻¹
Cold period	20–22	19–20	30–45	0.15
	18–24	17–23	60	0.2
Non-cold period	22–25	22–24	30–60	0.2
	20–28	18–27	65	0.3

In addition to the above, a questionnaire was offered to the residents. The questionnaire was compiled through an interview. The questionnaire included the following options: thermal sensation (range from cold to hot), preference (should be cooler or warmer), and acceptability (acceptable or unacceptable).

2.4. Heating consumption

Simple models can be used to determine the heat flow rate for a room during the heating period, as shown in Fig. 3a. By reducing the circuit to the simplest possible dynamic process, 1R1C model is built (Fig. 3b).

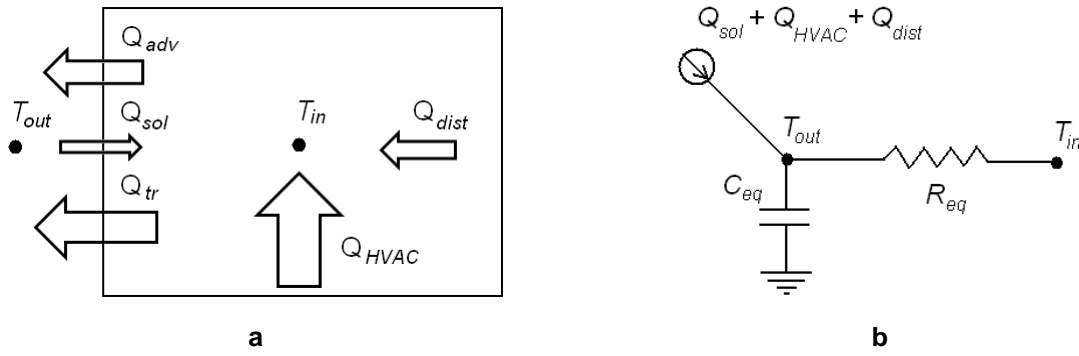


Figure 3. Thermal system for the room (a) and 1R1C electrical circuit (b) with two nodes of air temperatures (indoor T_{in} and outdoor T_{out}).

The model uses the available input and output data [32]. The equivalent thermal resistance R_{eq} of building components (wall and window) can be calculated like the electrical circuit taking into account the transmission (Q_{tr}) and advection (Q_{adv}) heat loss (through infiltration and ventilation). Similarly, the global equivalent thermal capacitance C_{eq} represents the building components of the total equivalent thermal mass, demonstrated the dynamic ability of the system to accumulate heat (Q_{st}). It is important to note that this thermal capacitance is not the air capacitance, but it reflects the behavior of the building, including building components and air. Other heat sources such as solar heat gains through window (Q_{sol}), heating load (Q_{HVAC}), and internal heat gains from electric devices (Q_{dist}) can be accounted for in the model.

The state equation based on energy conservation is as follows:

$$(Q_{tr} + Q_{adv}) + Q_{HVAC} + Q_{dist} + Q_{sol} - Q_{st} = 0. \quad (1)$$

Taking a global equivalent thermal resistance between indoor and outdoor air, and a global capacitance which stores and releases the heat from/to the air and the building components, Eq. (1) can be transformed to the following:

$$R_{eq}^{-1}(T_{in} - T_{out}) + Q_{HVAC} + Q_{dist} + Q_{sol} - C_{eq} \frac{\partial T_{in}}{\partial t} = 0. \quad (2)$$

In Eq. (2), we use the symbol (t) to indicate time.

It is expected that indoor air temperature varies slightly with time, so the thermal model (2) can be simplified $\left(Q_{st} = C_{eq} \frac{\partial T_{in}}{\partial t} = 0 \right)$.

The windows for all surveyed rooms occupied by the participants are oriented to north-eastern (see Fig. 1), which practically prevents the direct sunlight from entering the surveyed rooms during the heating season.

3. Results and Discussion

According to the results of the questionnaire, all residents noted a warm sensation in the heating season. At the same time, residents noted low air humidity. The main preference of residents was decrease in air temperature. Some residents noted unacceptable conditions. To improve temperature and humidity conditions, residents used frequent ventilation and humidification of air in rooms and other adaptation solutions.

3.1. Thermal and humidity parameters

The field test data in the representative room (living room) are presented in Fig. 4. The hourly indoor air temperature and relative humidity were obtained from the actual values. The hourly outdoor air temperature is calculated from a full annual weather file that must be specified for the simulation.

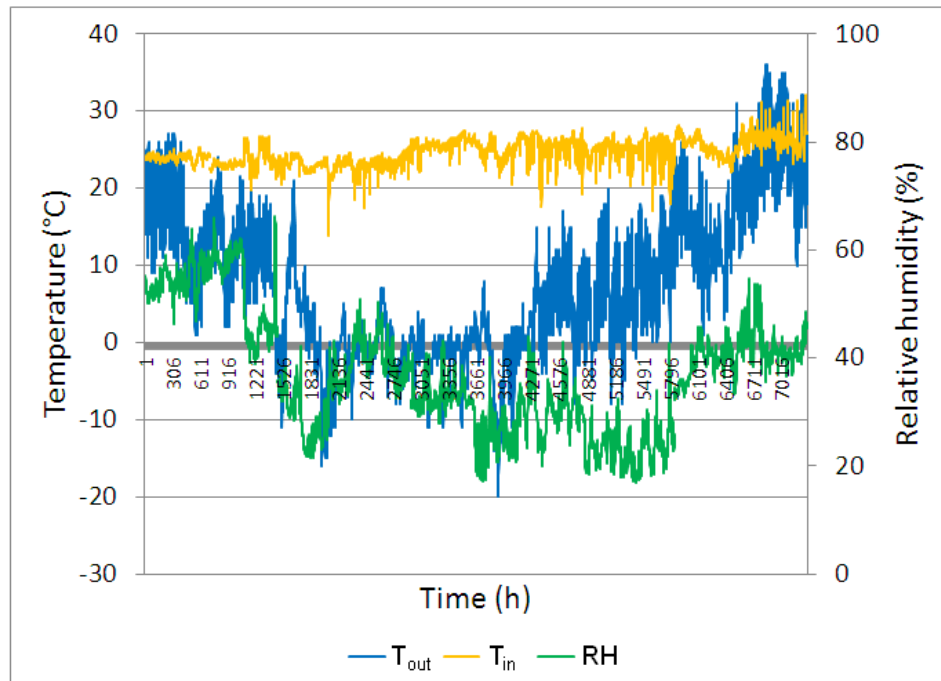


Figure 4. Outdoor, indoor air temperatures (left scale) and relative humidity (right scale) for the observed period (hourly values) in representative room.

The window opening status during the winter is 15.6 % (open) and 84.4 % (closed). Uniform ventilation of the room degrades its temperature and humidity parameters. The field test results are correlated with the questionnaire data. The peaks of temperature and relative air humidity (see Fig. 4) corresponded to the instances when the windows were open.

Overviews of the indoor and outdoor thermal environment parameters are given in Table 6. These thermal environment parameters clearly vary by season. The fluctuation of indoor air temperatures in all seasons of the year is relatively small. The fluctuation of outdoor air temperatures in winter is at the maximum. The fluctuation of indoor relative humidity in winter is the largest. The observed phenomenon is due to the residents periodically opening the windows.

Table 6. Indoor and outdoor average thermal physical parameters.

Season	Statistical information	Outdoor air temperature (°C)	Indoor air temperature (°C)	Relative humidity (%)
Winter	Minimum	-20.0	13.8	16.9
	Maximum	21.0	27.7	66.1
	Mean	1.3	24.5	30.7
	Standard deviation	13.7	1.9	17.6
Summer	Minimum	10.0	22.9	35.6
	Maximum	36.0	32.0	54.8
	Mean	24.0	26.5	42.7
	Standard deviation	11.7	2.4	5.5
Mid-season	Minimum	0.0	17.9	18.8
	Maximum	31.0	28.4	66.0
	Mean	13.7	24.4	46.7
	Standard deviation	5.5	1.6	10.2

In Table 6, the standard deviations of the observed characteristics were calculated by formula (3):

$$SD = \sqrt{\frac{1}{n} \sum_{i=1}^n (x_i - \bar{x})^2}, \quad (3)$$

where n is the sample size, x_i is i -th fetch item, \bar{x} is the arithmetic mean sample.

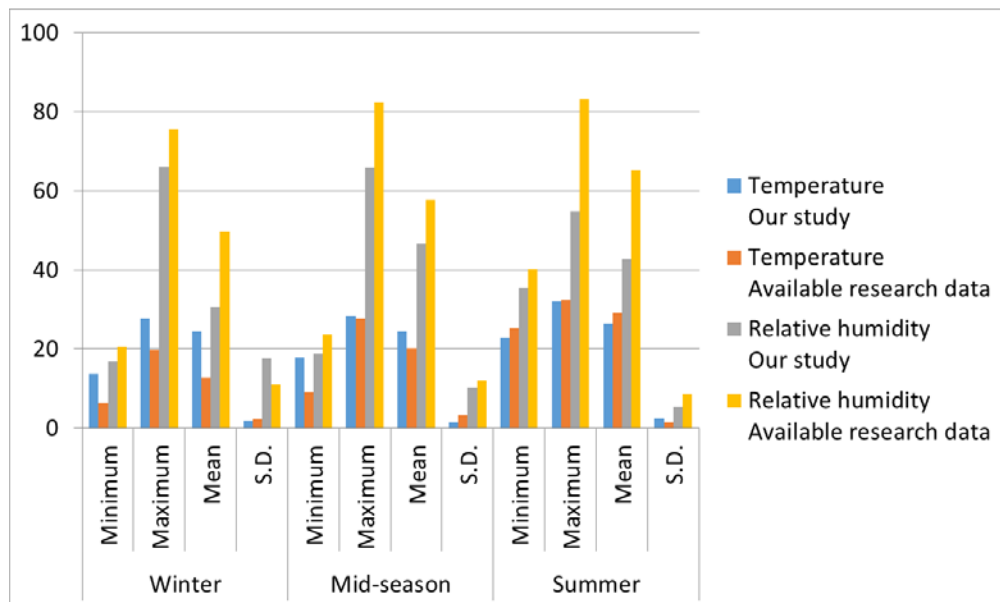


Figure 5. Comparison of the obtained field test data with the available research data [25].

Comparison of the obtained field test data with the available research data [25] demonstrated that our data agrees well with those of other researchers in the mid-season (Fig. 5). However, our investigations showed that in winter and summer, there were deviations due to the features of the environment and buildings.

3.2. Indoor thermal and humidity conditions and heating load analysis

The indoor thermal conditions analyses when using ASHRAE 55-2013 and EN 15251-2007 standards are derived in Fig. 6 (actual results indicated as points). In order to increase accuracy, the analysis of the results was performed using the average daily values of meteorological parameters.

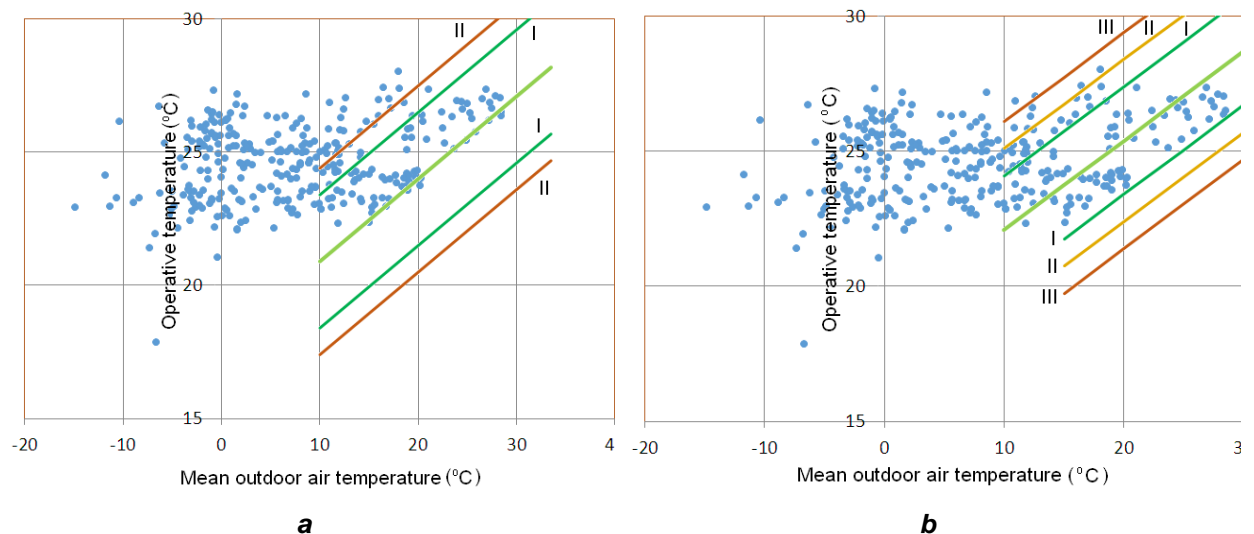


Figure 6. Thermal conditions analysis in representative room according to thermal adaptation models in ASHRAE 55-2013 (a) and EN 15251-2007 (b) standards.

As can be seen from these figures, the suitable outdoor temperature conditions for the thermal adaptation model ranged within 10–33.5 °C in ASHRAE 55-2013 and 10–30.0 °C in EN 15251-2007. In our study, the mean outdoor air temperature was within –15.2–8.0 °C in winter, 22.3–28.7 °C in summer, and 8.1–22.2 °C in mid-season. Therefore, in winter, 98.5 % of data points exceed the applicable range of the model for ASHRAE 55-2013, while 97.6 % exceed the applicable range of the model for EN 15251-2007. In the summer and mid-season, the actual indoor operative temperatures were almost within the applicable ranges for these models.

The actual indoor relative humidity was almost within the applicable ranges as well (Fig. 7).

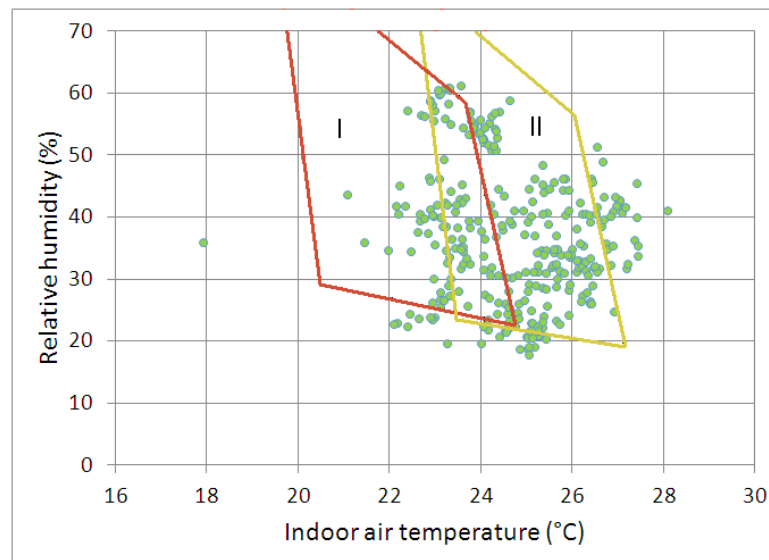


Figure 7. Humidity conditions analysis in representative room according to thermal adaptation model in ASHRAE 55 (I – winter, II – summer).

The indoor thermal and humidity conditions analysis when using International Standard (GOST 30494-2011) is demonstrated in Fig. 8 (actual results indicated as points, available ranges indicated as red lines).

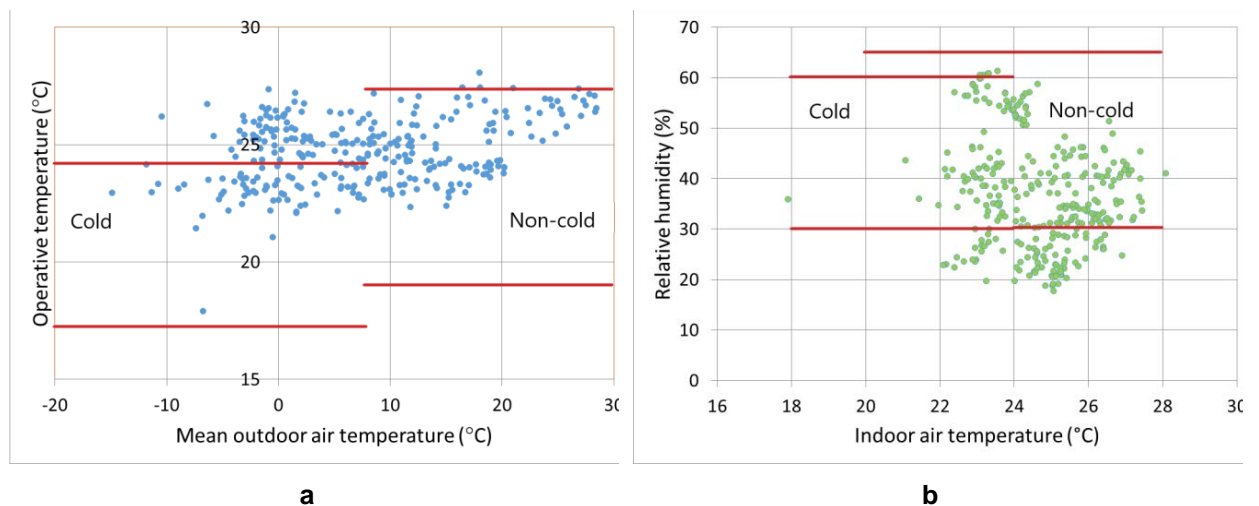


Figure 8. Thermal (a) and humidity (b) conditions analysis in representative room according to the National Standard model (GOST 30494-2011).

As can be seen from these figures, in winter, most data points correspond to the applicable range of the model for Interstate Standard GOST 30494-2011. In the summer, the actual indoor operative temperatures were also almost within the applicable ranges of this model (Fig. 8, a).

The actual indoor relative humidity also was almost within the applicable ranges of the model for Interstate Standard GOST 30494-2011 (Fig. 8, b).

The heating load analyses for 3D model of the representative room when using hourly values of meteorological parameters are derived in Fig. 9.

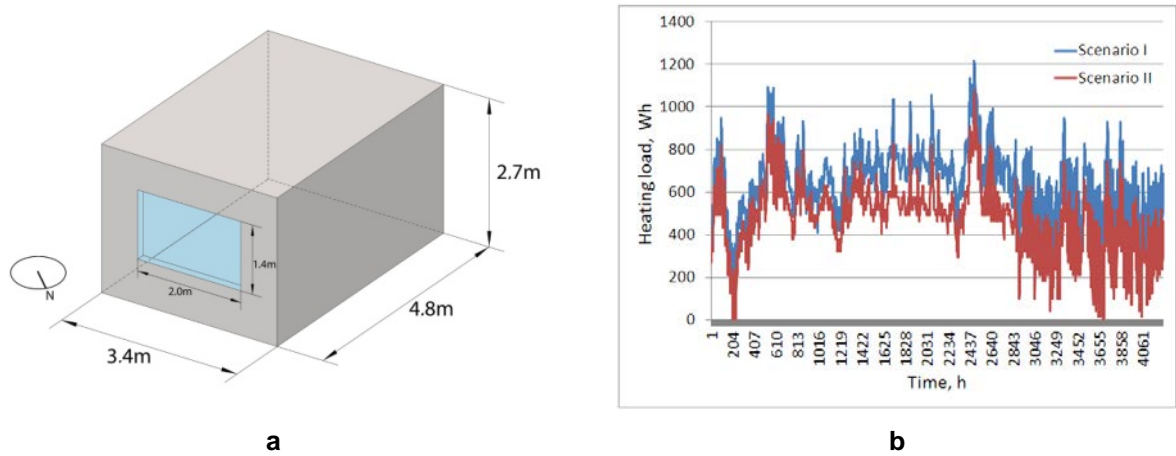


Figure 9. 3D model of the representative room (a) and its heating load (b).

The heating loads were obtained based on actual (1) and modified (2) calculation scenarios. The first calculation scenario used the actual thermal and humidity parameters listed in Table 1 (at the actual air temperature range and average air exchange rate in the room in winter of 1.2 h^{-1}). The second calculation scenario used optimal thermal and humidity parameters in this room (at the air temperature of $20 \text{ }^\circ\text{C}$ and average air exchange rate in the room in winter of 1.1 h^{-1}).

Analysis of the calculation results shows that according to the first scenario, the largest heating load is 1.22 kWh; the smallest heating load is 0.05 kWh. In the second scenario, the largest heating load is 1.08 kWh; the smallest heating load is -0.068 kWh . The total heating load in the first scenario is 2704 kWh, in the second scenario – 2049 kWh. Consequently, the reduction of total heating load is 24.2 %.

Thus, the actual temperatures were significantly different from the indoor temperature conditions for the thermal adaptation models according to ASHRAE 55-2013 and EN 15251-2007 Standards in winter (room overheating effect), as plotted in Fig. 6. The results indicate that it is necessary to improve the indoor temperature conditions using the adaptive comfort models. The main solutions are the heat flux control in heaters within the apartment in accordance with the thermal adaptation model of thermal comfort, as well as improvement of indoor environment quality with controlled natural ventilation in winter. Indoor thermal neutral temperature at the small energy demand in premises can be obtained using the smart home concept [33]. The choice of the best scenario is based on the use of a self-learning computer program in interactive user mode (Fig. 10).

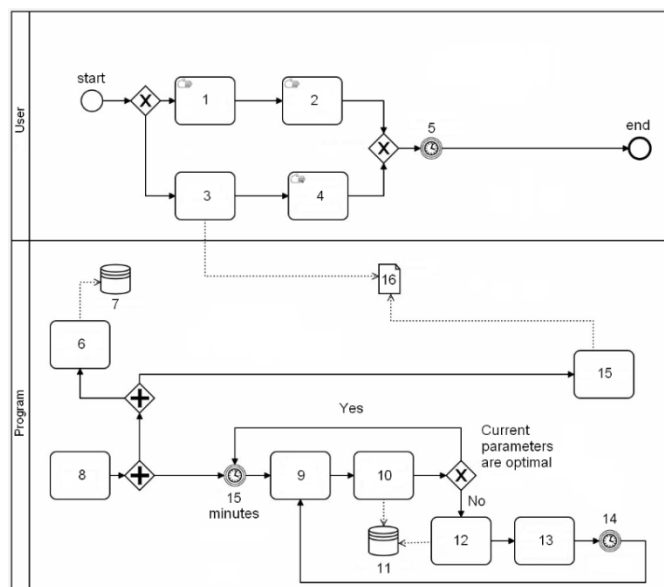


Figure 10. Schematic block diagram for indoor environment optimization: 1 – indoor environment assessment; 2 – turning on the equipment, opening the window; 3 – indoor environment control; 4 – turning on the equipment through the application; 5 – time of equipment operation/ventilation; 6 – sending readings to the server; 7 – Xiaomi server; 8 – sensor readings received; 9 – sensor activation, parameter measurement; 10 – comparison with optimal scenario; 11 – HUB built-in memory; 12 – selecting the optimal scenario; 13 – turn on the equipment according to the scenario; 14 – equipment operation time; 15 – display; 16 – sensor readings.

4. Conclusions

Objective physical measurements of the indoor thermal environments in premises and subjective assessments of the thermal sensation and adaptive thermal comfort of participants in winter, mid-season and summer under continental climate conditions (on the example of Volgograd, Russia) were conducted. The conclusions drawn from our detailed analyses and discussions are as follows:

1. Our investigations showed that in winter there were deviations in the thermal sensation, satisfaction, expectation of residents, and that they preferred a neutral cold environment. There were differences between the mid-season results and those of winter and summer.

2. The thermal comfort assessment in premises under continental climate conditions should be based on thermal adaptation models. We calculated that the acceptable temperature range for residents in winter was 17.5–22.5 °C, 20–25 °C (with acceptable deviation of ± 2.5 °C) in mid-season and 22.5–27.5 °C in summer. The actual indoor relative humidity was almost within the applicable ranges (30–60 %) as well.

3. The ASHRAE55-2013 and EN15251-2007 adaptive thermal comfort models are suitable for premises in mid-season and summer. The predictions of both mid-season and summer models were reliable.

4. The main solutions to improve the indoor temperature conditions include heat flux control in heaters within the apartment in accordance with the thermal adaptation model of thermal comfort, as well as control of natural ventilation in winter. In this case it is predicted, that the reduction of total heating load is 24.2 %. Indoor thermal neutral temperature at the small energy demand in premises can be obtained by implementing the smart home concept.

5. These results can be used to assess indoor thermal comfort in dwelling and help create friendly and energy efficiency building environments in Russia.

References

1. Wang, D., Chen, G., Song, C., Liu, Y., He, W., Zeng, T., Liu, J. Experimental study on coupling effect of indoor air temperature and radiant temperature on human thermal comfort in non-uniform thermal environment. *Building and Environment*. 2019. 165 (August). Pp. 1–13. DOI: 10.1016/j.buildenv.2019.106387
2. Wargocki, P., Bakó-Biró, Z., Clausen, G., Fanger, P.O. Air quality in a simulated office environment as a result of reducing pollution sources and increasing ventilation. *Energy and Buildings*. 2002. 34 (8). Pp. 775–783. DOI: 10.1016/S0378-7788(02)00096-8
3. Ji, R., Zhang, Z., He, Y., Liu, J., Qu, S. Simulating the effects of anchors on the thermal performance of building insulation systems. *Energy and Buildings*. 2017. 140. Pp. 501–507. DOI: 10.1016/j.enbuild.2016.12.036
4. Vatin, N., Korniyenko, S.V. Energy performance of buildings made of textile-reinforced concrete (TRC) sandwich panels. *Magazine of Civil Engineering*. 2022. 113(5). DOI: 10.34910/MCE.113.3
5. Korniyenko, S.V. *Magazine of Civil Engineering* The influence of the sky radiative temperature on the building energy performance. 2022. 114 (11412). DOI: 10.34910/MCE.114.12
6. Braulio-Gonzalo, M., Bovea, M.D., Jorge-Ortiz, A., Juan, P. Contribution of households' occupant profile in predictions of energy consumption in residential buildings: A statistical approach from Mediterranean survey data. *Energy and Buildings*. 2021. 241. DOI: 10.1016/j.enbuild.2021.110939
7. Vatin, N., Korniyenko, S.V., Gorshkov, A.S., Pestryakov, I.I., Olshevskiy, V. Actual thermophysical characteristics of autoclaved aerated concrete. *Magazine of Civil Engineering*. 2020. 96(4). Pp. 129–137. DOI: 10.18720/MCE.96.11
8. Ole Fanger, P., Toftum, J. Extension of the PMV model to non-air-conditioned buildings in warm climates. *Energy and Buildings*. 2002. 34(6). Pp. 533–536. DOI: 10.1016/S0378-7788(02)00003-8
9. d'Ambrosio Alfano, F.R., Olesen, B.W., Palella, B.I. Povl Ole Fanger's impact ten years later. *Energy and Buildings*. 2017. 152. Pp. 243–249. DOI: 10.1016/j.enbuild.2017.07.052
10. Naumov, A.L., Tabunshchikov, I.A., Kapko, D.V., Brodach, M.M. Air jet protection to prevent window surface condensation from air moisture. *Energy and Buildings*. 2015. 86. Pp. 314–317. DOI: 10.1016/j.enbuild.2014.10.037
11. Hellwig, R.T., Teli, D., Schweiker, M., Choi, J.H., Lee, M.C.J., Mora, R., Rawal, R., Wang, Z., Al-Atrash, F. A framework for adopting adaptive thermal comfort principles in design and operation of buildings. *Energy and Buildings*. 2019. 205. DOI: 10.1016/j.enbuild.2019.109476
12. Kim, J.T., Lim, J.H., Cho, S.H., Yun, G.Y. Development of the adaptive PMV model for improving prediction performances. *Energy and Buildings*. 2015. 98. Pp. 100–105. DOI: 10.1016/j.enbuild.2014.08.051
13. Fedoseev, A.V., Salnikov, M.V., Sukhinin, G.I. Simulation of heat and moisture transfer in a porous material. *Journal of Physics: Conference Series*. 2019. 1268(1). Pp. 803–807. DOI: 10.1088/1742-6596/1268/1/012069
14. Baranova, D., Sovetnikov, D., Borodinecs, A. The extensive analysis of building energy performance across the Baltic Sea region. *Science and Technology for the Built Environment*. 2018. 24(9). Pp. 982–993. DOI: 10.1080/23744731.2018.1465753
15. Borodinecs, A., Palcikovskis, A., Jacnevs, V. Indoor Air CO₂ Sensors and Possible Uncertainties of Measurements: A Review and an Example of Practical Measurements. *Energies*. 2022. 15(19). DOI: 10.3390/en15196961
16. Borodinecs, A., Prozuments, A., Zajacs, A., Zemitis, J. Retrofitting of fire stations in cold climate regions. *Magazine of Civil Engineering*. 2019. 90(6). Pp. 85–92. DOI: 10.18720/MCE.90.8
17. Millers, R., Korjakins, A., Lešinskis, A., Borodinecs, A. Cooling panel with integrated PCM layer: A verified simulation study. *Energies*. 2020. 13(21). DOI: 10.3390/en13215715
18. Zemitis, J., Borodinecs, A., Bogdanovics, R., Geikins, A. A case study of thermal comfort in a temporary shelter. *Journal of Sustainable Architecture and Civil Engineering*. 2021. 29(2). Pp. 139–149. DOI: 10.5755/j01.sace.29.2.29240

19. Schellen, L., Van Marken Lichtenbelt, W., Loomans, M., Frijns, A., Toftum, J., De Wit, M. Thermal comfort, physiological responses and performance of elderly during exposure to a moderate temperature drift. 9th International Conference and Exhibition – Healthy Buildings 2009, HB 2009. 2009. (2005). Pp. 2007–2010.
20. Liu, J., Wang, J. Thermal comfort and thermal adaptive behaviours in office buildings: A case study in Chongqing, China. IOP Conference Series: Earth and Environmental Science. 2019. 371 (2). Pp. 153–170. DOI: 10.1088/1755-1315/371/2/022002
21. Naumov, A.L., Tabunshchikov, I.A., Kapko, D.V., Brodach, M.M. Research of the microclimate formed by the local DCV. Energy and Buildings. 2015. 90. Pp. 1–5. DOI: 10.1016/j.enbuild.2015.01.006
22. Fux, S.F., Ashouri, A., Benz, M.J., Guzzella, L. EKF based self-adaptive thermal model for a passive house. Energy and Buildings. 2014. 68 (PART C). Pp. 811–817. DOI: 10.1016/j.enbuild.2012.06.016
23. Damiani, S.A., Zaki, S.A., Rijal, H.B., Wonorahardjo, S. Field study on adaptive thermal comfort in office buildings in Malaysia, Indonesia, Singapore, and Japan during hot and humid season. Building and Environment. 2016. 109. Pp. 208–223. DOI: 10.1016/j.buildenv.2016.09.024
24. Wang, L., Kubichek, R., Zhou, X. Adaptive learning based data-driven models for predicting hourly building energy use. Energy and Buildings. 2018. 159. Pp. 454–461. DOI: 10.1016/j.enbuild.2017.10.054
25. Jiao, Y., Yu, H., Yu, Y., Wang, Z., Wei, Q. Adaptive thermal comfort models for homes for older people in Shanghai, China. Energy and Buildings. 2020. 215. DOI: 10.1016/j.enbuild.2020.109918
26. Williamson, T., Daniel, L. A new adaptive thermal comfort model for homes in temperate climates of Australia. Energy and Buildings. 2020. 210. DOI: 10.1016/j.enbuild.2019.109728
27. Sourbron, M., Helsen, L. Evaluation of adaptive thermal comfort models in moderate climates and their impact on energy use in office buildings. Energy and Buildings. 2011. 43(2–3). Pp. 423–432. DOI: 10.1016/j.enbuild.2010.10.005
28. Heracleous, C., Michael, A. Thermal comfort models and perception of users in free-running school buildings of East-Mediterranean region. Energy and Buildings. 2020. 215. DOI: 10.1016/j.enbuild.2020.109912
29. Vella, R.C., Martinez, F.J.R., Yousif, C., Gatt, D. A study of thermal comfort in naturally ventilated churches in a Mediterranean climate. Energy and Buildings. 2020. 213. DOI: 10.1016/j.enbuild.2020.109843
30. Sovetnikov, D., Baranova, D., Borodinecs, A., Korniyenko, S. Technical problems in churches in different climatic conditions. Construction of Unique Buildings and Structures. 2018. 64 (1). Pp. 20–35. DOI: 10.18720/CUBS.64.2
31. Maier, J., Zierke, O., Hoermann, H.-J., Goerke, P. Effects of personal control for thermal comfort in long-distance trains. Energy and Buildings. 2021. 247. Pp. 111125. DOI: 10.1016/j.enbuild.2021.111125
32. Rasooli, A., Itard, L. Automated in-situ determination of buildings' global thermo-physical characteristics and air change rates through inverse modelling of smart meter and air temperature data. Energy and Buildings. 2020. 229. DOI: 10.1016/j.enbuild.2020.110484
33. Korniyenko, S.V. Renovation of Residential Buildings of the First Mass Series. IOP Conference Series: Materials Science and Engineering. 2018. 463 (2). DOI: 10.1088/1757-899X/463/2/022060

Information about authors:

Sergey Korniyenko, Doctor of Technical Science

ORCID: <https://orcid.org/0000-0002-5156-7352>

E-mail: svkorn2009@yandex.ru

Igor Dubov,

E-mail: dubov_i_architect@mail.ru

Konstantin Nazarov,

E-mail: nazkostja@gmail.com

Received 30.07.2021. Approved after reviewing 26.05.2023. Accepted 31.05.2023.



Research article

UDC 626/627:699.841:624.1

DOI: 10.34910/MCE.121.2



Soil friction on a retaining wall under seismic load

O.P. Minaev^{1,2} 

¹ Military Academy of Logistics named after General of the Army A.V. Hrulev, St. Petersburg, Russian Federation

² Admiral Makarov State University of Maritime and Inland Shipping, St. Petersburg, Russia Federation

✉ minaev.op@bk.ru

Keywords: retaining wall, active pressure, soil friction, dynamic load, foundation, bearing capacity, stability, wave action, seismic intensity

Abstract. The paper is the first to establish that the classical quasi-static analytical calculation of the retaining wall for seismic load indirectly reflects the wave nature of the impact of the sandy backfill soil on the rear surface of a retaining wall. The evidence provided includes the comparative results of the designed gravity retaining wall made from reinforced concrete and having a front cantilever that consider and disregard soil friction under the calculated operational static and seismic loads. The calculations were carried out for given dimensions of the retaining wall and characteristics of sandy backfill soils on weak clay foundation soils. It is emphasized that the calculation results are quite consistent with the research data on the behavior of sandy soils in the plate base under dynamic wave loads. These results were used to obtain the dependence necessary for determining the angle of soil friction against the rear surface of the wall under seismic load of varying intensities. It seems quite convincing that the calculation of the retaining stack for a seismic load of 9 points can be carried out without taking into account soil friction, since in this case, under seismic action, soil slippage along the rear surface of the retaining wall is possible. With a seismic load of 7 and 8 (or less) points, the angle of friction of the soil against the rear surface of the retaining wall should be determined from the obtained dependence to determine the angle of friction of the soil under a seismic load of varying intensity given in this article.

Citation: Minaev, O.P. Soil friction on a retaining wall under seismic load. Magazine of Civil Engineering. 2023. 121(5). Article no. 12102. DOI: 10.34910/MCE.121.2

1. Introduction

The basic principles for calculating and designing the natural base and pile foundation of a gravity retaining wall for static (erection and operating) loads [1–8], as well as for dynamic one, in particular seismic load, have to be elaborated further and studied comprehensively considering the results of the calculation [1]. Modern geotechnical solutions that take into consideration static [9–12] and dynamic [13–19] loads are discussed in a number of works by Russian and foreign scientists.

Papers [20, 21] present the calculation results of different types of gravity retaining walls given a wide range of soil conditions in the foundation and sandy backfill soils for seismic load. However, these calculations do not consider the soil friction against the rear surface of the retaining wall.

It is known [1, 2] that the soil friction on the rear surface of the retaining wall significantly affects the results of the design carrying capacity and stability under static load of the retaining wall.

Usually (for example, [2]) calculations conventionally assume that the angle at which soil frictions against the retaining wall is equal to the angle φ of internal friction of the backfill soil or to its half $\varphi/2$.

Given the wave character of the dynamic effect on the retaining wall, it seems that such a convention in determining the angle of internal friction of soil against the retaining wall is not likely to be applicable to calculate seismic loads. The reason for that is described below.

Headed by Prof. P.L. Ivanov the soil mechanics laboratory of the Department of Underground Structures, Foundations and Bases, Peter the Great St. Petersburg Polytechnic University was responsible for numerous studies of the effect produced by dynamic wave load on the friction of sandy soil on the surface of a vibrating plate installed on its surface. In the experiments with a vibrating plate for in-plane shear, in addition to the static stresses from the weight of the plate and the vibrator, the mechanical vibrator added dynamic stresses from the rotation of the vibrator cams that acted according to harmonic law. The vertical mechanical vibrator varied the stresses raging within the values of $\pm\Delta\sigma$. The dynamic pressure amplitude was controlled by changing the eccentricity of the vibrator cams while the frequency was adjusted by their rotation speed. The shear resistance considered according to the Coulomb dependence in the form of $\tau = (\sigma - \Delta\sigma)tg\varphi$ indicates a periodic shear of the plate on the sand surface.

As a result of the tests it has been found that within the range of vibration acceleration up to 1.0 g the angle of internal soil friction does not change while the decreasing shear resistance should be taken into account through changing normal stresses at the plate bottom. Thus, in case of vibration and seismic effects the shear stability of structures has to be tested given the dynamic component of stresses at a constant value of the angle of internal soil friction, imposed on the static tests.

This work is aimed at identifying the calculation and design specifics of the natural base and pile foundation of a gravity reinforced concrete corner retaining wall with a front cantilever given seismic load. It also identifies the specific feature of the calculation and design of the natural base and pile foundation of a retaining wall considering the soil friction against the rear surface on the seismic load based on the results of the calculations obtained. In addition, we interpreted these results on the basis of the known research data on the behavioral patterns of sandy soils under dynamic loads and determined the dependence for calculating the angle of soil friction against the wall under seismic loads of various intensities.

In addition, we interpreted these results on the basis of known data from studies of the behavior of sandy soils under dynamic loads and obtained the dependence for calculating the angle of friction of the soil against the wall under seismic loads of various intensities.

2. Methods

2.1. Theoretical dependencies

When calculating static load, width b of the base of a reinforced concrete retaining wall with a front cantilever is usually determined using the formula of A.Z. Zarkhi, which has the following form

$$b = 2.2 \sqrt{\frac{E_a y_a}{(h_w + h_{cant})(0.75\gamma_m - \gamma_w) + h_0\gamma_0}}, \quad (1)$$

where E_a is the active lateral pressure force on the retaining wall, kN; y_a is the height of the applied active lateral pressure force relative to the bottom of the wall, m; h_w is the depth of water next to the embankment, m; h_{cant} is the depth of the front wall cantilever, m; h_0 is the elevation of the wall above the water level, m; γ_m is the specific weight of the wall material, kN/m³; γ_w is the specific weight of water, γ_0 is the elevation coefficient h_0 of the wall above the water level, which is assumed to be 1 kN/m³. In formulas (1) that are used for determining width b of the wall bottom at seismic load, values E_a and y_a have to be substituted for values E_a^s and y_a^s , respectively.

When designing hydraulic structures to be erected in seismic areas, it is necessary to consider separately the seismic pressure of soil and water (in case soil is under water) on the wall during seismic impacts.

In the general case, as backfill soil is above the water level and under it, it is proposed to use the dependence for determining the ordinate e_a^s of lateral pressure of soil and water

$$e_a^s = \left(q + \gamma_w h_w + \sum \gamma_i^s y_i \right) \lambda_a^s, \quad (2)$$

where y_i^s is the resulting force of specific weight γ_i of soil and volumetric seismic force (per unit volume); h_w is the depth of water from the water table (WT) of backfill to the wall bottom; y_i is the thickness of the i -th layer of backfill soil; λ_a^s is the coefficient of active pressure (outward pressure) under seismic impact.

The value e_a^s is the ordinate of the seismic pressure diagram of soil and free water on the wall surface. The values include both soil pressure e_a^s in usual static conditions, and additional seismic pressure of soil and water on it.

The coefficient of active lateral pressure λ_a^s given angle ω of soil friction against the retaining wall under seismic impact is determined according to the dependence

$$\lambda_a^s = \frac{\cos^2(\varphi - \varepsilon)}{(1 + \sqrt{z})^2 \cos \varepsilon}, \quad (3)$$

where

$$z = \frac{\sin(\varphi - \varepsilon) \sin(\varphi + \omega)}{\cos(\omega + \varepsilon)}. \quad (4)$$

According to the existing norms for calculating a retaining wall for seismic load [22], the most hazardous is the horizontal direction of the seismic pressure of soil. In this case

$$\gamma^s = \frac{\gamma_i}{\cos \varepsilon}, \quad (5)$$

where $\varepsilon = \arctg AK_1$ is the angle of deviation from the vertical of the specific gravity equilibrium γ_i of soil and seismic force $y_i^s AK_1$, A is the coefficient whose values should be taken as equal to 0.1; 0.2; 0.4 respectively for the calculated seismic intensity of 7, 8 and 9 points, K_1 is the coefficient considering the admissible damage to buildings and structures, taken for hydraulic structures as equal to 0.25.

In the case the lateral active pressure of water-saturated soil on the retaining wall under seismic effects is determined, the weight of suspended soil y_{sb} should be introduced into the formulas, just as in case of operational load, while seismic force $y_{satur} AK_1$ should be determined according to the density of saturated soil y_{satur} . In this case, the deviation angle of the resultant is determined by the following formula

$$\varepsilon_{satur} = \arctg \frac{y_{satur}}{y_{sb}} AK_1. \quad (6)$$

The value of the force E_a^s of the active lateral pressure on the retaining wall under seismic load is determined as the area of the active lateral pressure diagram e_a^s , and the height of application from the soil foundation is proportional to the areas of the diagram e_a^s in separate sections along the height of the retaining wall.

With a static load in formula (2), instead of the coefficient λ_a^s , the coefficient λ_a of the active lateral pressure under a static load is taken, the values of which are determined by the formula

$$\lambda_a = \left(\frac{\cos \varphi}{1 + \sin \varphi} \right)^2 = \operatorname{tg} \left(45^\circ - \frac{\varphi}{2} \right), \quad (7)$$

where φ is calculated angle of internal friction of the backfill soil.

In this case, the force E_a of active lateral pressure under static load and the height y_a of its application relative to the ground base are calculated similarly.

Checking the stability of the retaining wall for sliding under flat shear in the plane of the sole under the action of a seismic load is performed by the formula

$$K^{plan} = \frac{N_{oper}tg\varphi + bc}{E_a^s} \geq 1.15, \quad (8)$$

where K^{plan} is the stability factor for flat shear; φ and c are respectively, the calculated angle of internal friction and adhesion of the base soil.

Checking the stability of the wall for deep shear is carried out according to the method when the slip line limiting the area of the limit state of the base soil is taken in the form of two straight segments connected to each other by a curvilinear insert described by the equation of a logarithmic spiral. The actual eccentrically loaded foundation is replaced by an equivalent centrally loaded one with a reduced width b_{red} equal to $b_{red} = b - 2e^s$, where e^s is the eccentricity of the application of the vertical force N_{oper} from the weight of the backfill wall and soil in the operational case under seismic load.

As a result, a graph of the bearing capacity of the base $\tau_{ult} = f(\sigma)$ is constructed, where τ_{ult} is the limiting shear resistance of soils. According to the voltage $\sigma_{oper} = N_{oper}/b_{red}$ in the operational case under seismic load, the corresponding limiting shear stress τ_{oper}^{ult} is determined. The safety factor for deep shear K^{deep} is finally calculated from the ratio

$$K^{deep} = \tau_{oper}^{ult} b_{red} / E_a^s \geq 1.15. \quad (9)$$

2.2. Initial parameters and loads

The calculations were carried out for a reinforced concrete retaining wall with a front cantilever. The total height of the retaining wall was 7.4 m, the water depth h_e next to the embankment was 6.1 m and the height of wall elevation h_0 above water level was 1.3 m. Average sand with specific weight $\gamma = 18.4 \text{ kN/m}^3$ and humidity $W = 14 \%$ was taken as backfill soil. The foundation of the retaining wall is composed of water saturated clayey soils (highly plastic clay-bearing soils) having specific weight $\gamma = 20.0 \text{ kN/m}^3$ and humidity $W = 24 \%$. The humidity of clayey soils at liquid limit $W_L = 0.30$ and at plastic limit $W_p = 0.16$. The design angle φ of internal friction of sandy soils was 32° , and that of clayey soils was 17° with cohesion $c = 16.67 \text{ kPa}$. Elastic modulus E of sandy soils was 31 MPa and that of clayey soils was 17 MPa.

The value of the useful load q on the surface of the base (on the cordon) was 29 kPa.

Initially, the values of active lateral pressure under operational and seismic load of 7, 8 and 9 points were estimated without considering soil friction and at the angle of soil friction against the rear surface of the retaining wall being equal to the angle of internal friction of backfill soil or to its half $\varphi/2$.

For all of these cases, the width of bottom of the retaining wall was calculated.

Further comparative calculations on the bearing capacity and stability of the retaining wall were made for a maximum seismic load of 9 points without considering soil friction and at the angle of soil friction against the rear surface of the retaining wall being equal to angle φ of internal friction of backfill soil or to its half $\varphi/2$.

The results of these calculations were used for analyzing the behavior of soils under dynamic wave loads.

The calculations consider an alternative variant of the pile foundation in the base of the retaining wall. The diameter of the piles was taken as $d = 30 \text{ cm}$ depth of immersion, equal to the width of the retaining wall b .

The required number of piles is determined by a separate calculation for vertical and horizontal loads. At the first stage of the calculation, the highest of the values obtained is taken for vertical and inclined piles with the angle of installation of the piles $\alpha = 0.6\delta$, where $\delta = \arctg(E_a/N_{oper})$ or $\delta^s = \arctg(E_a^s/N_{oper}^s)$ is the slope angle of the resultant force to the vertical for the operational (seismic) case, but no more than 19° , which corresponds to the pile slope 3:1 (given the capabilities of pile-driving equipment). The final version of the pile foundation is set by the smallest number of piles in all design cases – vertical piles or inclined piles (with the installation angle δ for an operational or seismic case).

In all cases the number of piles is maximum under the horizontal seismic load. When the piles are positioned in the plan, the distance between the axes of the piles should be at least $3D$ in order to maximize the bearing capacity of each pile in the cluster.

The piles must be equally loaded, for which the contact diagram σ under the bottom of the retaining wall is divided into equal areas and the axes of the longitudinal rows of piles are positioned against the centers of gravity of each of its parts.

2.3. Methodology for calculating bearing capacity and stability

In compliance with the existing norms and rules, the calculation of the retaining wall in terms of bearing capacity and stability of the bases and foundations is carried out according to group I of limit states for the main and special combination of maximum loads.

The possibility of erecting a wall on soils of a natural foundation was studied given the design pressure on the foundation. According to the existing standards, this calculation is made for two design cases when the values of maximum stresses σ_{max} under the bottom of the retaining wall do not exceed the limit design pressure R^p on foundation soils, as well as the average values of stresses $0.5(\sigma_{max} + \sigma_{min})$ of value $1.2 R^p$.

In addition, a computer-aided diagram of ϕ_c -isolines with highlighted plastic deformation zones was drawn on a personal computer using the OSNOVA-2 program developed by Prof. V.M. Kirillov. It revealed their significant distribution in the base of the retaining wall.

The presence of plastic deformation zones in the base of the retaining wall made it necessary to replace the weak foundation soils with a backfill sand cushion. In this case, the compaction of sandy backfill soils and the cushion at the base of the retaining wall must be carried out using the well-known vibrodynamic methods so that the specified soil characteristics are achieved [23, 24].

The width of the sand cushion is set equal to 0.7 of its maximum spreading depth at the right edge of the wall and its half at the left edge of the wall. In addition, the sand cushion should be re-compacted to the appropriate angle of internal soil friction in order to limit the spreading of plastic deformation zones to a depth not exceeding $0.25 b$ of the retaining wall width, according to the existing standards.

In case the retaining wall does not meet the shear stability condition, measures must be taken to increase the bearing capacity of the foundation. Then the retaining wall stability is calculated for the case of a sand cushion rather than weak clay soils in the foundation of the retaining wall. If a sand cushion is built in the foundation, the in-plane shear of the retaining wall may occur along a weak layer of foundation soil, and the surcharge weight G_{surch} from the sand cushion must be added to the value N_{oper} of the weight of the wall and backfill soil.

In the shear analysis of the sand cushion construction, the ultimate resistance R_{ult}^* of the foundation soils must be determined given the surcharge $q_{cant}^{found} + q_{surch}^{found}$ of the foundation uplift zones caused by the weight of the foundation soil at the depth of the retaining wall bottom and the thickness of the sand cushion. The shear resistance limit τ_{ult}^{surch} is determined by the graph $\tau_{ult} = f(\sigma)$ taking into account the increasing stresses under the bottom of the retaining wall $\sigma_{oper}^{surch} = N_{oper} + G_{surch}/b_{red}$ due to the surcharge imposed by the sand cushion layer.

The calculations have been carried out in accordance with the regulatory documents.

In general, the calculations have shown fairly similar results with and without considering the soil friction on the rear surface of the retaining wall. The results of these calculations are described in more detail below.

3. Results and Discussion

3.1. Active lateral pressure calculated for different seismic intensities

The coefficients of active lateral pressure λ_a^s calculated by formulas (3) – (6) for seismic intensity of 7, 8 and 9 points are presented in Table 1.

Table 1. The coefficients of active lateral pressure for seismic intensity of 7, 8 and 9 points.

Item No.	Angle of soil friction against the wall, ω	Operational load, λ_a	The coefficient of active lateral pressure of soil on the wall					
			Seismic intensity					
			above water area,			under water area,		
			7 points	8 points	9 points	7 points	8 points	9 points
				λ_{a1}^s		λ_{a2}^s		
1	2	3	4	5	6	7	8	9
1	0	0.307	0.321	0.336	0.365	0.336	0.365	0.431
2	$\varphi/2$	0.278	0.293	0.308	0.340	0.308	0.340	0.412
3	φ	0.277	0.293	0.311	0.347	0.311	0.347	0.434

The data in the table imply that the value of active lateral pressure coefficient λ_a under operational load is $\lambda_a = 0.307$ without considering the soil friction against the wall and reduces considerably down to $\lambda_a = 0.278(0.277)$ at the angle of soil friction against the wall $\varphi/2(\varphi)$.

Under seismic load of 7, 8 and 9 points in comparison with operational load, the active lateral pressure coefficient $\lambda_a = 0.307$ grows above water up to $\lambda_{a1}^s = 0.321$, $\lambda_{a1}^s = 0.336$ and $\lambda_{a1}^s = 0.365$, and under water up to $\lambda_{a1}^s = 0.336$, $\lambda_{a1}^s = 0.365$ and $\lambda_{a1}^s = 0.431$ without considering the soil friction against the wall. Under seismic load of 7 and 8 points in case the soil friction against the wall is considered, the same as under operational load, the active lateral pressure coefficient λ_{a1}^s above water reduces from $\lambda_{a1}^s = 0.321$ and $\lambda_{a1}^s = 0.336$ without considering the soil friction against the wall down to $\lambda_{a1}^s = 0.293(0.293)$ and $\lambda_{a1}^s = 0.308(0.311)$ at the angle of soil friction against the wall $\varphi/2$ and φ , while under water from $\lambda_{a1}^s = 0.336$ and $\lambda_{a1}^s = 0.365$ without considering the soil friction against the wall down to $\lambda_{a1}^s = 0.308(0.311)$ and $\lambda_{a1}^s = 0.340(0.347)$ at the angle of soil friction against the wall $\varphi/2$ and φ .

Under seismic load of 9 points, the active lateral pressure coefficient λ_{a1}^s above water reduces from $\lambda_{a1}^s = 0.365$ without considering the soil friction against the wall down to $\lambda_{a1}^s = 0.340$ and $\lambda_{a1}^s = 0.347$ at the angle of soil friction against the wall $\varphi/2$ and φ , while under water it can not only decrease from $\lambda_{a1}^s = 0.431$ without considering the soil friction against the wall down to $\lambda_{a1}^s = 0.412$ at the angle of soil friction against the wall $\varphi/2$, but also grow up to $\lambda_{a1}^s = 0.434$ at the angle of soil friction against the wall φ .

According to calculations, force E_a^s of lateral active pressure on the retaining wall under seismic impact of 9 points amounts to 341.65, 357.89 and 359.28 kN/m at the angle of soil friction against the wall $\varphi/2$, $\varphi = 0$ and φ . At the seismic intensity of 8 points, lateral active pressure force E_a^s on the retaining

wall reduces to 283.49, 304.53 and 289.05 kN/m while at seismic intensity of 7 point it decreases even further down to 257.47, 280.93 and 259.81 kN/m respectively at the angle of soil friction against the wall $\varphi/2$, $\varphi = 0$ and φ . The proportionate force E_a of lateral active pressure on the retaining wall under operating static load is 172.52, 190.56 and 171.98 kN/m.

The results of the calculations by formula (1) show that the width of the retaining wall bottom under operational load is 7.2 m without considering the friction against the rear surface of the wall. Considering the soil friction against the wall, the width of the retaining wall bottom goes down to 6.8 m for both design cases at the angle of soil friction against the wall $\varphi/2$ and φ .

The calculations by formula (1) for seismic load of 7 and 8 points show that the width of the retaining wall bottom is 8.3 and 8.6 m, respectively without considering the soil friction against the wall. Considering the soil friction against the wall, the width of the retaining wall bottom reduces from 8.3 m down to 7.9 and 8.0 m under seismic load of 7 points and from 8.6 m down to 8.3 m and 8.4 m under seismic load of 8 points, respectively at the angle of soil friction against the wall $\varphi/2$ and φ .

Similar calculations by formula (1) for seismic load of 9 points show that the width of the retaining wall bottom is 9.1 and 9.3 m respectively at the angle of soil friction against the wall $\varphi/2$ and φ , in the latter case being equal to the width of the retaining wall bottom if the calculation does not consider the soil friction against the wall.

In further calculations of the retaining wall for bearing capacity and stability, seismic intensity was assumed to be 9 points.

3.2. Results of the calculations for bearing capacity and stability

The calculations were made given the specified initial parameters for operational static load and compared to the data from previous calculations for a seismic load of 9 points without taking into account the soil friction against the retaining wall ($\varphi = 0$).

Fig. 1 presents a common active pressure diagram drawn for the vertical plane led through the front of the retaining wall, under seismic load of 9 points.

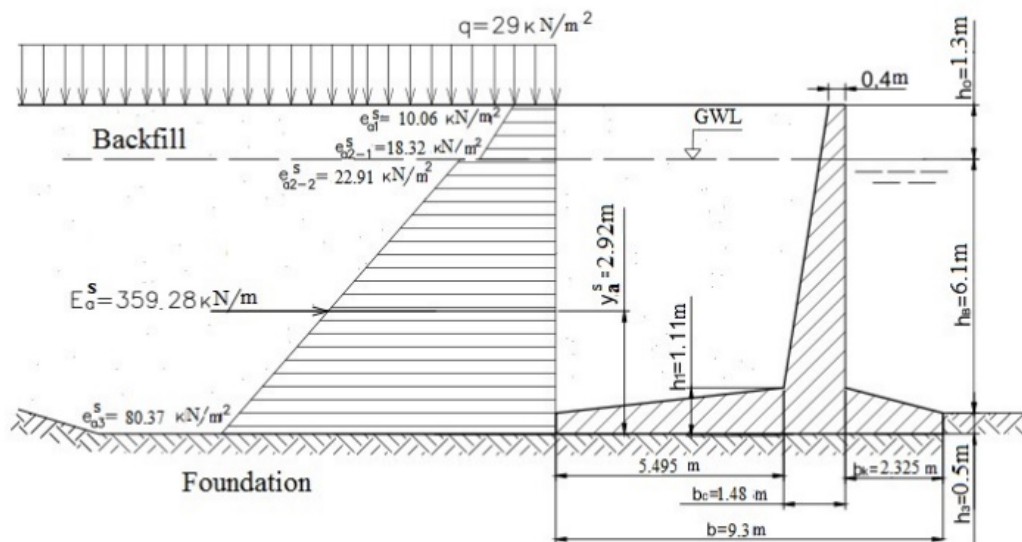


Figure 1. Diagram of active lateral pressure on a reinforced concrete corner retaining wall under seismic load of 9 points at the angle of soil friction against the rear surface $\omega = \varphi$.

The possibility of erecting a reinforced concrete corner retaining wall on natural foundation soils has been checked for construction and operational cases (under static and seismic load) by design pressure on foundation and it has been found out that the values of maximum stresses σ_{max} under the bottom of the retaining wall do not exceed the limit design pressure R^D on foundation soils or the average stress

values $0.5 (\sigma_{\max} + \sigma_{\min})$ of magnitude $1.2 R^p$. Hence the design strength of foundation soils was checked and showed that a retaining wall of this type can be erected directly on natural foundation soils.

At the same time the diagram of φ_c -isolines with highlighted plastic deformation zones at the base of the retaining wall reveals that plastic deformations spread to the depth of 6.63 and 6.66 m respectively at the angle of soil friction against the wall $\varphi/2$ and φ (and $\varphi = 0$).

The width of sand cushion is taken as equal to 4.64 ($4/64/2 = 2.32$) m at the angle of soil friction against the wall $\varphi/2$ and 4.66 ($4/66/2 = 2.33$) m for φ (and $\varphi = 0$).

The stability of the retaining wall for in-plane shear slip under seismic load has been checked and shows that the values of stability coefficient K^{in-psb} for in-plane shear are 1.08, 1.04 and 1.05, respectively for the angle of soil friction against the wall $\varphi/2$, φ and $\varphi = 0$.

The stability of the retaining wall for slip in case of in-plane shear of the bottom due to seismic load has shown that the values of the safety factor K^{in-psb} at in-plane shear do not meet the existing standards.

The calculations show that with the sand cushion layer being 2.32 (2.33) m thick, the stability coefficient rises to 1.23 for all design cases.

Fig. 2 presents a design diagram for checking the stability of a reinforced concrete corner retaining wall for in-depth shear.

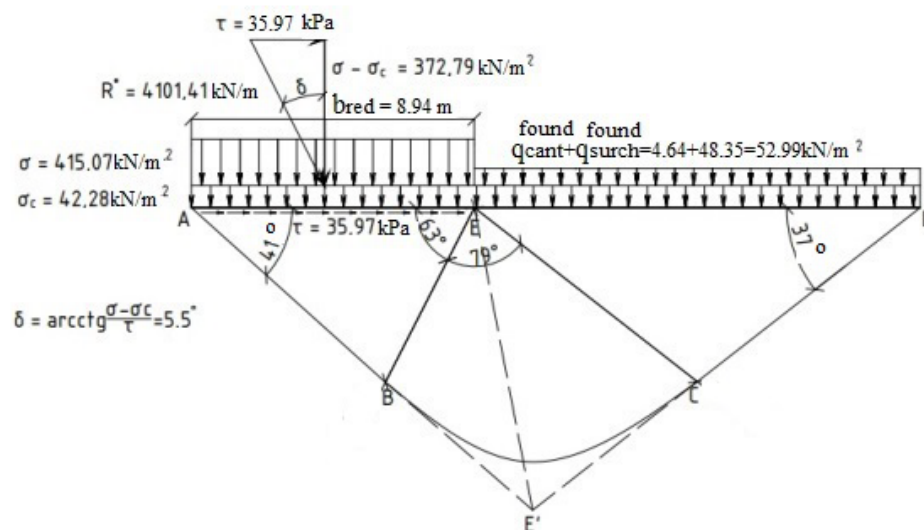


Figure 2. Design diagram for checking the stability of the retaining wall for in-depth shear at an angle of soil friction against the wall $\varphi/2$ with a sand cushion $h/n = 2.32$ m thick

As a result of calculations of the retaining wall for in-depth shear, an even greater decrease in the stability coefficient K^{deep} was revealed with values of 1.02, 0.99 and 0.97 respectively at the angle of soil friction against the wall $\varphi/2$, φ and $\varphi = 0$.

As a result of the calculations of the retaining wall for deep shear, a decrease in the stability margin coefficient K^{deep} is usually less than the value allowable by the existing standards.

At the same time if a sand cushion with the layer of thickness being 2.32 and 2.33 m was built, the stability coefficient could increase from 1.02 to 1.18 and from 0.99(0.97) to 1.15 respectively at the angle of soil friction against the wall $\varphi/2$ and φ (and $\varphi = 0$).

Fig. 3 presents typical diagrams of foundation bearing capacity under the bottom of the retaining wall for the variant of calculation with and without surcharging the areas of soil heave provided a 2.32 m thick sand cushion is built.

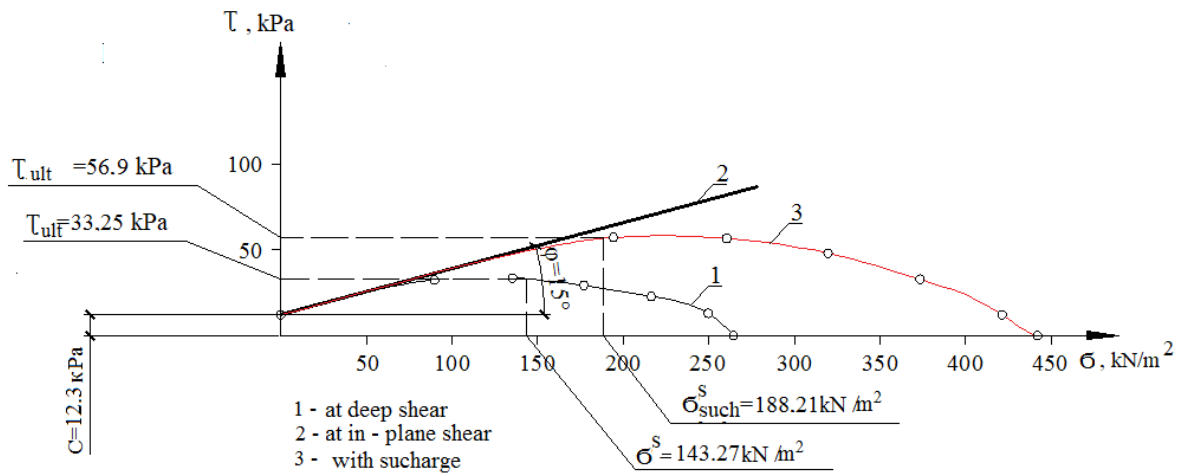


Figure 3. Graphs of the bearing capacity of the foundation of the retaining wall for in-depth shear at the angle of soil friction against the wall $\varphi/2$.

In the base of the reinforced concrete retaining wall, 81, 87 and 83 piles are required per 10 linear meters of the retaining wall, respectively, at the angle of soil friction against the wall $\varphi/2$, φ and $\varphi = 0$.

In general, similar results were obtained with and without considering the soil friction on the rear surface of the retaining wall at seismic intensity of 9 points.

3.3. Analysis of calculation results

Based on studies of soil behavior under dynamic wave loads, carried out under the guidance of Prof. P.L. Ivanova, the author of the article analyzed the results of calculations of the retaining wall, performed on the seismic load.

According to their calculations, force E_a^s of lateral active pressure on the retaining wall under seismic impact of 9 points amounts to 341.65, 357.89 and 359.28 kN/m at the angle of soil friction against the wall $\varphi/2$, $\varphi = 0$ and φ . The proportionate force E_a of lateral active pressure on the retaining wall under operating static load is 172.52, 190.56 and 171.98 kN/m. Hence, the mean value of lateral pressure e_a^{stat} at operational static load on the retaining wall is 21.84, 24.12 and 21.77 kN/m². Then the corresponding mean value of additional lateral pressure e_{as}^{dyn} under seismic impact on the retaining wall is 21.40, 21.18 and 23.71 kN/m².

This verification proves that the values of additional lateral pressure e_{as}^{dyn} under seismic impact on the retaining wall are either slightly less than the values of lateral pressure e_a^{stat} under operational static load or exceed them. This proves the fact that under seismic impact the resistance of soil fractioning against the rear surface of the retaining wall is very insignificant or absent at all.

Fig. 4 presents a typical graph of dynamic wave action on the retaining wall when the active lateral pressure force under seismic load exceeds the pressure under operational static load.

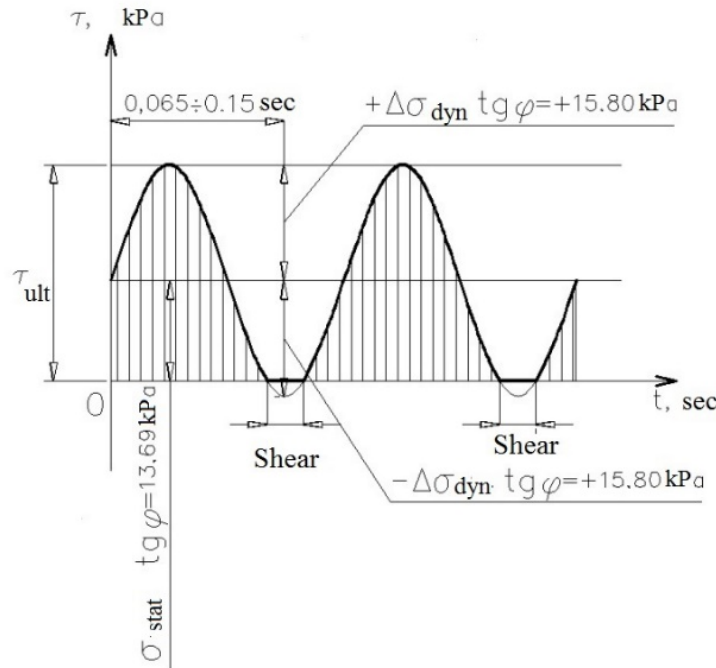


Figure 4. Graph of dynamic wave impact on the retaining wall at seismic intensity of 9 points.

In addition, at the seismic intensity of 8 point, lateral active pressure force E_a^s on the retaining wall reduces to 283.49, 304.53 and 289.05 kN/m while at seismic intensity of 7 point it decreases even further down to 257.47, 280.93 and 259.81 kN/m respectively at the angle of soil friction against the wall $\varphi/2$, $\varphi=0$ and φ . Consequently, the respective mean values of additional lateral pressure e_{as}^{dyn} under seismic impact of 8 points on the retaining wall reduces to 14.05, 14.43 and 14.82 kN/m², while at the seismic impact of 7 point it becomes 10.75, 11.44 and 11.12 kN/m².

It is evident that force of lateral active pressure E_a on the retaining wall under operational static load has to be taken as earlier equal to 172.52, 190.56 and 171.98 kN/m, while the corresponding mean value of lateral pressure e_a^{stat} under operational static load on the retaining wall is 21.84, 24.12 and 21.77 kN/m² at the angle of soil friction against the wall $\varphi/2$, $\varphi=0$ and φ .

Solving the inverse problem using the dependence

$$\omega = \operatorname{arctg} \frac{\tau_{stat} - \Delta\tau_{dyn}}{\sigma_{stat}}, \quad (10)$$

where ω is the design angle of internal soil friction against the wall under dynamic action, degree; τ_{stat} is the resistance to soil friction against the wall under static action, kN/m²; $\Delta\tau_{dyn}$ is the value of reduced resistance to soil friction against the wall under dynamic action, kN/m²; σ_{stat} is normal stresses of lateral pressure of soil on the wall under static load, kN/m². It can be determined that under seismic intensity of 7 and 8 points, the angle ω of soil friction against the rear surface of the retaining wall is 0.569φ and 0.440φ .

Fig. 5 presents a typical graph of dynamic wave action on the retaining wall when the force of active lateral pressure under seismic load does not exceed the force of active lateral pressure under operational static load.

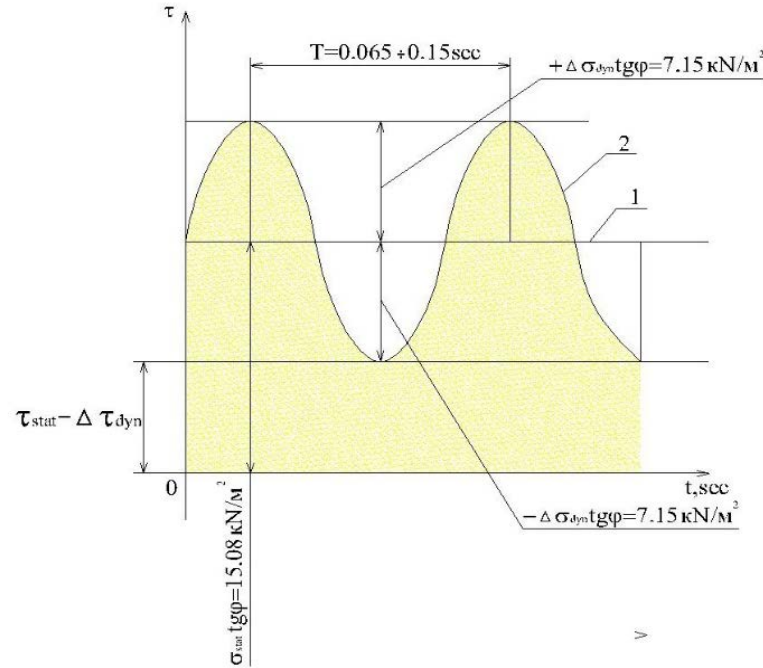


Figure 5. Graph of dynamic wave impact on the retaining wall at seismic intensity of 7 points:
1 – resistance to soil shear against the retaining wall under static load;
2 – change in resistance to soil shear under soil oscillations under seismic load.

Designations in the Figure: $(\tau_{stat} - \Delta\tau_{dyn})$ is the least resistance to soil shear against the rear surface of the wall under dynamic (seismic) action, kN/m^2 ; σ_{stat} is normal stresses of soil on the retaining wall under operational (static) load, kN/m^2 ; $\pm\Delta\sigma_{dyn}$ is the change in normal stresses of soil under dynamic (seismic) action kN/m^2 ; φ is the angle of internal friction of backfill soil, degree; T is the time of soil oscillations under seismic impact, c.

Finally transforming (10), let us write down the dependence for finding the angle ω of soil friction against the rear surface of the retaining wall at different values of the lateral soil pressure force E_a^S on the retaining wall under seismic load in the form of

$$\omega = \arctg \frac{E_a - \Delta E_a^S}{E_a} \text{tg} \varphi = \arctg \left(2 - \frac{E_a^S}{E_a} \right) \text{tg} \varphi, \quad (11)$$

where E_a is the force of lateral pressure of soil on the retaining wall under static load, kN ; ΔE_a^S is the change in force of lateral pressure of soil on the retaining wall under seismic load; E_a^S is the maximum force of lateral pressure of soil on the retaining wall under seismic load; φ is the angle of internal friction of soil backfill.

If the value of the expression in brackets is negative, the angle ω of soil friction against the retaining wall is taken as equal to 0. In this case, under seismic impact, soil slips on the rear surface of the retaining wall.

4. Conclusion

1. At a seismic load of 9 points, the force of active lateral pressure on the retaining wall during seismic action, as a rule, exceeds the force of active lateral pressure during operational static load.

2. In this case, the calculation of the gravitational retaining wall in terms of bearing capacity and stability can be made without taking into account the friction of the soil against the retaining wall.

3. Exception the friction of the soil against the retaining wall is quite consistent with the data of Prof. Ivanova P.L. about the patterns of behavior of sandy soils under dynamic wave loads.

4. With a seismic load of 7 and 8 (or less) points, the angle of friction of the soil against the rear surface of the retaining wall should be determined from the obtained dependence (11) to determine the angle of friction of the soil under a seismic load of various intensity.

References

1. Kulmach, P.P., Filippenok, V.Z., Zaritovsky, N.G. Morskie gidrotehnicheskie sooruzheniya. Chast II_ Prichalnie_ shelfovie i beregoukrepitelnie sooruzheniya [Marine hydraulic structures. Part II: Berthing, shelf and shore protection structures]. Leningrad: LVVVSU, 1991. 391 p.
2. Budin, A.Ya. Gorodskie i portovie naberejnie [City and port embankments]. St. Petersburg: Publishing house Polytechnic, 2014. 424 p.
3. Garibin, P.A., Belyaev, N.D. Vodnie puti i porti. Putevie raboti [Waterways and ports. Travel work]. St. Petersburg: Peter the Great SPbPU, 2014. 120 p.
4. Evtushenko, G.N., Kolosov, M.A., Silin, A.V., Narbut, R.M. Severnie porti Rossii [Northern ports of Russia]. St. Petersburg: Gidrometeoizdat Publishing House, 2006. 340 p.
5. Yakovlev P.I. Ustoichivost transportnih gidrotehnicheskikh sooruzhenii [Stability of transport hydraulic structures]. Moscow: Transport, 1986. 191 p.
6. Bik, Yu.I., Pridanova, O.V. Snizhenie naprjazhjonno-deformirovannogo sostojanija prichal'nyh naberezhnyh s pomoshh'ju armirovanija grunta obratnoj zasypki [Reducing the stress-strain state of quayside embankments with the help of backfill soil reinforcement], River Transport (XXI century). 2009. 42 (6). Pp. 78–79.
7. Semenyuk, S.D., Kotov, Yu.N. Zhelezobetonnye podpornye stenki [Reinforced concrete retaining walls]. Bulletin of the Belarusian - Russian University. 2018. 61 (4). Pp. 86–101.
8. Lisichkin, S.E., Rubin, O.D., Atabiev, I.Zh., Melnikova, N.I. Raschjotnye issledovanija ustojchivosti i prochnosti podpornyh sten pervogo jarusa vodoprijomnika Zagorskoj GAJES [Computational studies of the stability and strength of the retaining walls of the first tier of the water intake of the Zagorskaya PSPP]. Environmental Engineering. 2012. 2. Pp. 44–48.
9. Il'ichev V.A., Mangushev R.A., Nikiforova N.S. Development of underground space in large Russian cities. Soil Mechanics and Foundation Engineering. 2012. 49 (2). Pp. 63–67. DOI: 10.1007/s11204-012-9168-6
10. Abelev, M.Y., Averin, I.V. Determining the Deformability Characteristics of Sandy Soils at a Construction Base Using Field and Laboratory Techniques. Soil Mechanics and Foundation Engineering. 2019. 56 (3). Pp. 164–170. DOI: 10.1007/s11204-019-09585-8
11. Shashkin, A.G., Ulitsky, V.M., Shashkin, K.G. Calculation of soil – Transport structure interaction. Lecture Notes in Civil Engineering. 2020. 50. Pp. 135–146.
12. Kolosov, M.A., Morgunov, K.P. The phenomena of soil liquefaction in the bases of hydraulic structures. IOP Conference Series: Earth and Environmental Science. 2021. 868 (1). 012081. DOI: :10.1088/1755-1315/868/1/012081
13. Khomyakov, V., Yemenov, Y., Zhamek, N. Methods of restoration of deformed retaining walls in seismic conditions. Proceedings of 16th Asian Regional Conference on Soil Mechanics and Geotechnical Engineering, ARC 2019. Taipei, Taiwan, 2020.
14. Idriss, I.M., Boulanger, R.W. Soil liquefaction during earthquakes. EERI. USA, California, 2008. 240 p.
15. Ishihara, K., Ueno, K., Yamada, S., Yasuda, S., Yoneoka, T. Breach of a tailings dam in the 2011 earthquake in Japan. Soil Dynamics and Earthquake Engineering. 2015. 68. Pp. 3–22.
16. Towhata, I. Geotechnical Engineering Accompanied by Risk. Lecture Notes in Civil Engineering. 2021. 140. Pp. 95–109.
17. Kokusho, T. Earthquake-induced flow liquefaction in fines-containing sands under initial shear stress by lab tests and its implication in case histories. Soil Dynamics and Earthquake Engineering. 2020. 130. Pp. 121–134.
18. Zhusupbekov, A.Zh., Khomyakov, V.A., Zhagpar, A.A. Stability of hillsides at construction on sites with high seismicity. Proceedings of 14th Asian Regional Conference on Soil Mechanics and Geotechnical Engineering. Hong-Kong, China, 2011. 3. Pp. 2075–2078.
19. Stavnitser, L.R. Stability of soilbases during earthquakes Proceedings of conference on Soil Mechanics and Foundation Engineering. Florence, Italy, 1991. 2. Pp. 911–912.
20. Minaev, O.P. Features of calculating gravity retaining wall without assumption of base soil liquefaction. Proceedings in Earth and geosciences «Geotechnics Fundamentals and Applications in Construction: New materials, structures, technologies and calculations (GFAC 2019)». Saint Petersburg, Russia, CRC Press: Balkema the Netherlands, Taylor and Francis Group, London, 2019. 2. Pp. 182–186. DOI: 10.1201/9780429058882-35
21. Minaev, O.P. Features of calculating stability of retaining wall with significant horizontal load on base soil. Proceedings in Earth and geosciences «Geotechnics Fundamentals and Applications in Construction: New materials, structures, technologies and calculations (GFAC 2019)». Saint Petersburg, Russia, CRC Press: Balkema the Netherlands, Taylor and Francis Group, London, 2019. 2. Pp. 187–192. DOI: 10.1201/9780429058882-36
22. Stavnitser, L.R. Ceismostoikost osnovanii i fundamentov [Seismic resistance of bases and foundations]. Publishing house of the Association of Civil Engineering Universities. Moscow, 2010. 448 p.
23. Vasil'ev, Yu.S., Minaev, O.P. O vibracionnyh katkah v gidrotehnicheskome stroitel'stve. [About vibratory rollers in hydraulic engineering]. Hydraulic engineering. 2016. 2. Pp. 10–14.
24. Belash, T.A., Gorodnova, E.V., Dergachev, A.M. Ob effektivnosti uplotnenija gruntov osnovanij pri ispol'zovanii tehnologii vzryvov [On the effectiveness of soil compaction of foundations using the technology of explosions]. Natural and man-made risks. Safety of structures. 2019. 6. Pp. 49–56.

Information about author:

Oleg Minaev, PhD in Technical Sciences

ORCID: <https://orcid.org/0000-0003-0920-9081>

E-mail: minaev.op@bk.ru

Received 21.12.2021. Approved after reviewing 27.04.2023. Accepted 28.04.2023.



Research article

UDC 699.844

DOI: 10.34910/MCE.121.3



Calculation method for sound insulation of lightweight enclosures at low frequencies

V.I. Erofeev¹, D.V. Monich² , P.A. Grebnev², I.S. Pavlov¹

¹ Institute of Mechanical Engineering Problems RAS – branch of Federal Research Center Institute of Applied Physics of the Russian Academy of Science, Nizhny Novgorod, Russian Federation

² Nizhny Novgorod State University of Architecture and Civil Engineering, Nizhny Novgorod, Russian Federation

✉ dmitriy.monich@mail.ru

Keywords: sound insulation, enclosing structures of buildings, lightweight enclosures, frame-sheathing partitions, anti-resonance panels, resonant sound transmission, inertial sound transmission, self-consistency of wave fields

Abstract. The objects of the study are lightweight enclosing structures (partitions) located between the premises of buildings. The surface density of lightweight fences lies in the range of $20 < \mu < 100 \text{ kg/m}^2$. The elaboration of methods for calculating the sound insulation of lightweight enclosures, taking into account geometric and physical and mechanical parameters, is an urgent task for building acoustics. The studies are carried out on the basis of the theory of self-consistency of wave fields with account of the resonant and inertial sound transmission through the enclosures. The article presents the results of theoretical studies of sound insulation of lightweight enclosing structures in the frequency range from 50 Hz to 5000 Hz. It was proposed to divide the generalized frequency characteristic of the sound insulation of lightweight enclosing structures into two ranges, the boundary between which is determined by the geometric sizes of the fence. Based on the theory of self-consistency of wave fields, a method was developed for calculating the sound insulation of lightweight enclosing structures in the frequency range above the threshold frequency of sound field diffuseness in the plane of the enclosing structure and below the threshold frequency. The method enables calculating the sound insulation of lightweight enclosures, the threshold frequencies of the areas of resonant sound transmission, as well as the frequency characteristics of the coefficients of resonant and inertial sound transmission. The implementation of this method is considered on the example of a lightweight frame-sheathing partition with anti-resonance panels. The authors obtained theoretical frequency characteristics of the coefficients of sound transmission through a lightweight frame-sheathing partition and the frequency characteristics of the sound insulation of the partition in the calculated frequency range.

Funding: This research is supported by the grant of Russian Science Foundation (RSF) No. 21-19-00813.

Citation: Erofeev, V.I., Monich, D.V., Grebnev, P.A., Pavlov, I.S. Calculation method for sound insulation of lightweight enclosures at low frequencies. Magazine of Civil Engineering. 2023. 121(5). Article no. 12103. DOI: 10.34910/MCE.121.3

1. Introduction

The objects of the study are lightweight enclosing structures (partitions) located between the premises of buildings. The surface density of lightweight fences lies in the range of $20 < \mu < 100 \text{ kg/m}^2$. In the high-level room there is a source of airborne noise, which generates a sound field in the volume of the room. Sound waves fall on a fence at various angles and excite an oscillatory motion in it. Vibrations of the

fence generate the emission of sound waves into an adjacent low-level room, where the sound field is also formed. At present, in the design and construction of residential, public and industrial buildings, lightweight enclosing structures are widely used: walls and partitions between rooms, as well as fences for noisy areas in industrial buildings. The most common design solutions for lightweight enclosures in construction are partitions made of sandwich panels and frame-sheathing partitions. Lightweight enclosures reduce the load on the supporting structures of buildings and decrease the material consumption of construction as a whole. It should be taken into account that the sound insulation of lightweight enclosures in many cases is lower than the sound insulation of massive fences. Therefore, when designing buildings, calculation methods should be used that allow determining the sound insulation of fences in various frequency ranges. Nowadays, there are no reliable theoretical methods for calculating the sound insulation of lightweight enclosing structures in the low-frequency sound range ($f < 100$ Hz). Existing calculation methods fail to take into account the geometric and physical-mechanical characteristics of fences. That is why the creation of methods for calculating the sound insulation of lightweight enclosing structures in the low-frequency sound range is an urgent task for building acoustics.

Numerous studies of the sound insulation of enclosing structures indicate the presence of significant discrepancies between theoretical and experimental values in the low-frequency region. The experimental values of sound insulation exceed the calculated values, as a rule, by 5 to 15 dB. A. London [1] and C.W. Kosten [2] assumed that the explanation of this effect necessitates taking into account the additional resistance of the enclosing structure. V.M.A. Peutz noted that the low-frequency improvement in sound insulation cannot be explained by the influence of the natural frequencies of the reverberation chambers, since the improvement occurs regardless of the size of the chambers [3]. W.A. Utley concluded that the main reason for the discrepancies between the theoretical and experimental results is the different measurement conditions in reverberation chambers [4]. A.C. Nilsson supposed that the main reason for the discrepancies between theoretical and experimental results is the absence of a diffuse sound field in the chambers [5]. M.J. Crocker, M. Battacharya, and A.J. Price applied the method of statistical energy analysis to calculate the sound insulation of enclosing structures [6], which had been previously developed by R.H. Lyon and G. Maidanik [7]. For a single-layer enclosing, the results of the theoretical calculation of sound insulation are in good agreement with the experimental results in the high-frequency range only. The authors explained the discrepancy in the field of low and medium frequencies by the presence of interaction between the natural vibration modes of the room and the partition. The method of statistical energy analysis was used by S.N. Ovsyannikov and O.V. Leliuga to take into account a structural sound transmission between rooms [8, 9].

Theoretical and experimental studies of sound insulation of lightweight enclosures made of sandwich panels are currently carried out by various scientists. The results of theoretical and experimental research of sound insulation of three-layer and five-layer (with additional lining in the middle of the medium layer) sandwich panels are presented by Y. Liu [10]. The conclusion is made about higher sound insulation values for five-layer sandwich panels compared to three-layer enclosures. In papers [11–13], a theoretical model was developed for sound transmission through sandwich panels with air gaps between the facings and the middle layer. In [14], the authors showed that the finite sizes of an enclosure affect its sound insulation, basically, in the low-frequency range. The elastic material of the middle layer makes a strong damping impact in the high-frequency range, improving the soundproofing properties of the sandwich panels. R.R. Wareing with co-authors studied the sound insulation of sandwich panels consisting of various facings [15]. Theoretical and experimental results of investigations are presented in this paper. Conclusions were made about three main factors affecting the soundproofing properties of sandwich panels: the density of the facing material, the thickness of the middle layer, and the method of fastening the facings and the middle layer. Theoretical and experimental studies of sound insulation of sandwich panels with an air gap located between two layers of elastic material of the middle layer were performed by S. Hwang et al. [16].

At present, the sound insulation of lightweight frame-sheathing partitions with various design solutions is also being intensively investigated. J.L. Davy researched the sound insulation of double leaf walls [17]. He revealed that the transmission of sound vibrations through the connecting elements between the fence sheathings must be taken into account only in the region above the resonant frequency "mass-elasticity-mass". In the field of lower frequencies, the transmission of sound vibrations between the fence sheathings occurs only through the air gap. In [18], J.L. Davy, referring to the results obtained by G. Maidanik et al., considered the emission of sound energy by a double enclosure, taking into account the contribution of resonant and non-resonant components. J. Legault and N. Atalla performed a comparative analysis of various theories of sound insulation of frame-sheathing partitions, taking into account the influence of rack profiles of the frame [19]. They confirmed that J.L. Davy's theoretical model, which takes into account the resonant response of the fence in the frequency range above the threshold frequency of wave coincidence, is the most complete. J. Poblet-Puig et al. carried out theoretical investigations of the sound insulation of frame-sheathing partitions with various shapes of rack-mount frame profiles [20]. Paper [21] presents the results of studies on optimizing the design solution of soundproof double enclosing

structures. J. Wang et al. researched the sound transmission through a frame-sheathing partition, taking into account the rack profiles of the frame [22]. The displacements of the skins during their vibrations were determined. In the articles [23] and [24], the influence of boundary conditions on the sound insulation of double enclosing structures were studied. S. Nakanishi investigated the soundproofing properties of various types of frame-sheathing partitions [25]. Partitions with a single and double frame, with single and double skins, with various options for filling the air gap with sound-absorbing material were considered. J.C.E. Wyngaert et al. developed a method for computer simulation of soundproofing frame-sheathing partitions, taking into account the deformation of the rack profiles of the frame [26]. In this case, the sound fields in the sound-transmitting and sound-receiving rooms are modeled as diffuse ones. A.A. Kochkin, N.A. Kochkin and I.L. Shubin developed new design solutions for soundproof lightweight partitions and linings with vibro-damping layers [27, 28]. J.C.E. Wyngaert, M. Schevenels, and E.P.B. Reynders elaborated a method for optimizing the parameters of the rack profiles of light frame-sheathing partitions [29, 30].

It follows from this review that at present there is no method in building acoustics for calculating the sound insulation of enclosing structures in the low-frequency sound range, which enables one taking into account geometric and physical-mechanical parameters.

The aim of this work is elaboration of method for calculating the sound insulation of lightweight enclosing structures in the low-frequency sound range. This method should take into account the geometric and physical-mechanical parameters of the enclosures. For this purpose, the following tasks are planned:

- 1) to investigate the resonant sound transmission in the low-frequency sound range theoretically, taking into account the self-consistency of wave fields;
- 2) to determine the threshold frequency, below which there are significant discrepancies in the results of theoretical and experimental studies of sound insulation of lightweight enclosures;
- 3) to obtain analytical expressions for calculating:
 - threshold frequencies of the areas of resonant sound transmission through the lightweight enclosures;
 - coefficients of both resonant and inertial transmission of sound through the enclosures;
 - sound insulation of lightweight enclosures in the frequency ranges above and below the threshold frequency.

2. Method

Theoretical studies of sound insulation of lightweight building enclosures were carried out based on the theory of self-consistency of wave fields [31–34]. According to this theory, the sound transmission through enclosures has two components: the resonant sound transmission and the inertial sound transmission. The resonant sound transmission occurs during the natural vibrations of enclosing structure and is characterized by the resonant sound transmission coefficient, τ_r . Inertial sound transmission takes place during the inertial (forced) vibrations of the enclosure and is characterized by the inertial sound transmission coefficient, τ_i . The coefficient of sound transmission through a lightweight building enclosure is determined by the formula [31]:

$$\tau = \tau_r + \tau_i. \quad (1)$$

The theory of self-consistency of wave fields enables one calculating the sound insulation of single-layer and multi-layer lightweight building enclosures, taking into account their geometric sizes and physical and mechanical characteristics of materials. The method for calculating of sound insulation of three-layer sandwich panels is presented in [35–36].

3. Results and Discussion

A generalized frequency characteristic of sound insulation of lightweight building enclosures divided into two ranges is shown in Fig. 1:

- 1) the frequency range below the threshold frequency ($f < f_b$). In this range, there are significant discrepancies in the results of theoretical and experimental studies of sound insulation ($\Delta R > 5$ dB);

2) the frequency range above the threshold frequency ($f < f_b$). In this range, there is a good agreement ($\Delta R = \pm 2$ dB) and a satisfactory agreement ($\Delta R = \pm 5$ dB) of the results of theoretical and experimental studies of sound insulation.

It should be noted that numerical values are not indicated on the coordinate axes in Fig. 1, because this graph shows only the qualitative dependence of the sound insulation of enclosure (R , dB) on the sound frequency (f , Hz).

The resonant sound transmission through the enclosure is determined by the degree of self-consistency of wave field of natural vibrations with the sound fields in the air volume of a high-level room and a low-level room.

For the case of incomplete spatial resonance, self-consistency of wave fields occurs along one of the sides of the enclosing structure, and there is no self-consistency of wave fields along the other side of the enclosure [31]:

$$m = m_0; n \neq n_0; m \neq m_0; n = n_0, \quad (2)$$

where m and n are the numbers of projection lengths of free half-waves on sides a and b of the enclosure, respectively. In this case $m = m_0$, $n_0 = 1/2, 3/2, 5/2, \dots$ or $n = n_0$, $m_0 = 1/2, 3/2, 5/2, \dots$

Self-consistency of the wave field of natural oscillations of the enclosing structure with sound fields in the air volume of the high-level room and low-level room is possible in the case when at least one half-wave of the sound field in the high-level room can be located along the smallest side of the enclosure:

$$n_0 > 1, \quad (3)$$

where n_0 is the number of projection lengths of half-waves of the sound field in the high-level room along the smallest side of the enclosure.

Taking into account condition (3), the frequency of self-consistency of wave fields in the high-level room and in the enclosure is determined as follows:

$$f_b > f (n_0 > 1). \quad (4)$$

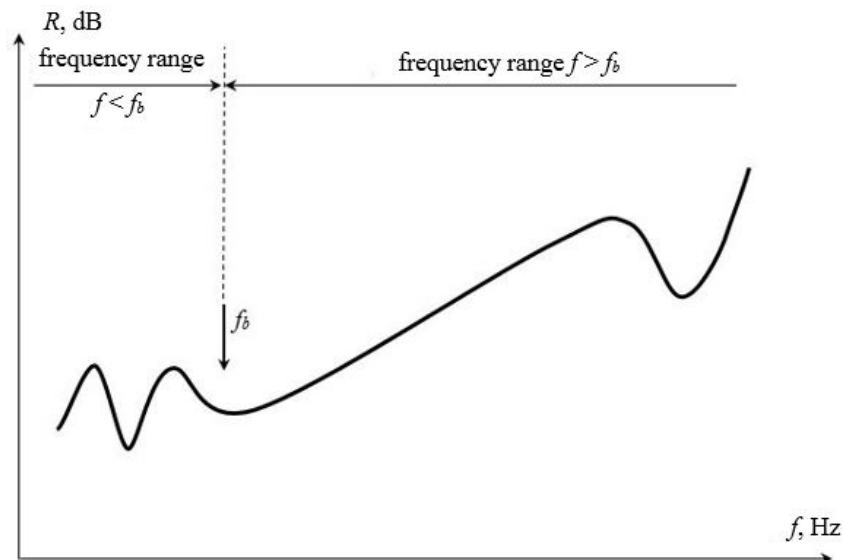


Figure 1. The generalized frequency characteristic of sound insulation of lightweight building enclosures divided into two frequency ranges.

The frequency f_b is the threshold frequency of the diffuseness of the sound field in the plane of the building enclosure. The frequency characteristics of the number of lengths of the sound field half-wave projections in the high-level room along the smallest side of the enclosure, which were calculated for three lightweight frame-sheathing partitions with different geometric sizes (length a and height b), are plotted in Fig. 2.

Analysis of the data presented in Fig. 2 shows that the location of the threshold frequency f_b on the frequency scale is determined by the geometric sizes of the enclosures (length a and height b). In the frequency range $f \geq f_b$, the sound transmission consists of the resonant sound transmission (in the mode of natural oscillations of the enclosure) and the inertial sound transmission (in the mode of forced oscillations of the enclosure). In this frequency range, methods for calculating of sound insulation can be used that assume the diffuse nature of the sound fields in both high-level and low-level rooms. In the frequency range $f < f_b$, the oscillations of the enclosure are close to piston-like movements. Wherein, a sound transmits through the enclosure only in the inertial mode, there is no a resonant sound transmission ($\tau_r = 0$).

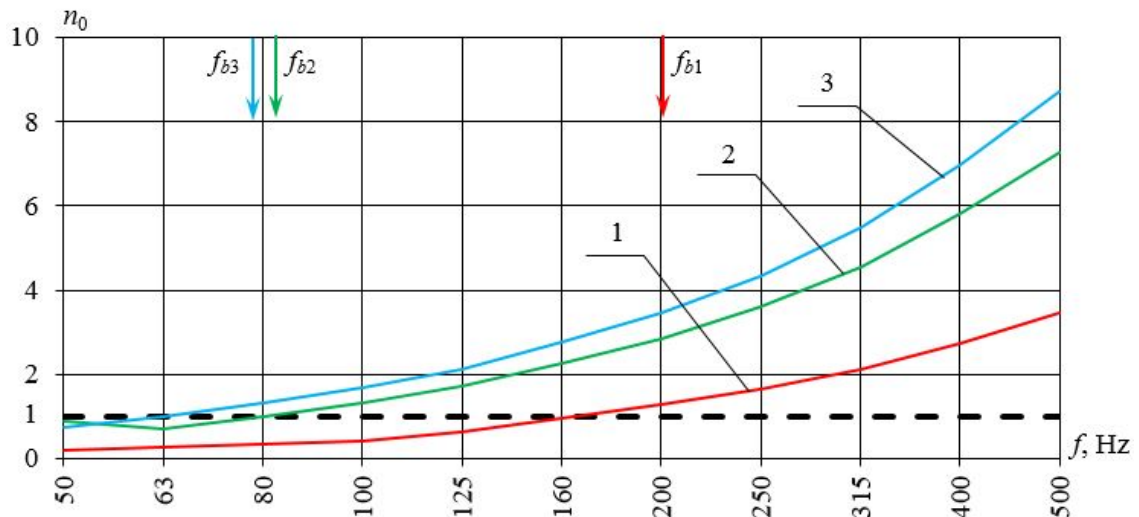


Figure 2. The frequency characteristics of the number of lengths of projections of half-waves of the sound field in the high-level room along the smallest side of the enclosure for three light frame-sheathing partitions: 1 – $a \times b = 2.0 \times 1.2$ m; 2 – $a \times b = 4.2 \times 2.5$ m; 3 – $a \times b = 6.0 \times 3.0$ m; f_b is the threshold frequency of the diffuseness of the sound field in the plane of the building enclosure.

Based on the results of the performed investigations, a method for calculating the sound insulation of lightweight building enclosures in the frequency ranges above the threshold frequency ($f \geq f_b$) and below the threshold frequency ($f < f_b$) was developed. The implementation of the calculation method is considered on the example of a lightweight frame-sheathing partition with anti-resonant panels [37]. This type of soundproofing enclosure was developed at the Department of Architecture of the Nizhny Novgorod State University of Architecture and Civil Engineering. The scheme of the constructive solution of the enclosure is shown in Fig. 3. A new type of lightweight partition has the following advantages over frame-sheathing partitions currently used in constructions: 1) anti-resonant panels are placed in the air gap between the partition sheathings. Thereby, the sound insulation of the enclosure is increased without increasing of its thickness; 2) using of sound-absorbing material (mineral wool) in the air gap between the skins is not required.

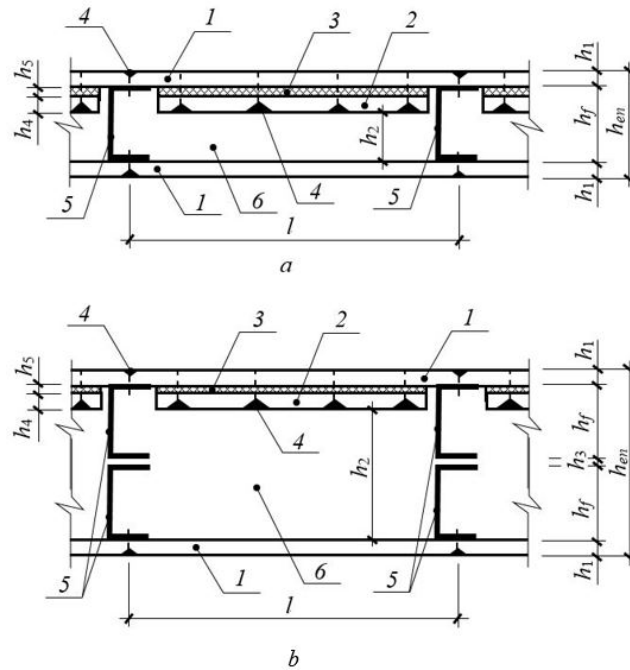


Figure 3. The scheme of a constructive solution for a framed sheathing partition with anti-resonant panels (h_{en} is the total thickness of the enclosure): a is a partition with a single frame; b is a partition with a double frame: 1 is a sheathing with h_1 -thickness; 2 is an anti-resonant panel with thickness $h_4 = h_1$; 3 is a continuous layer of elastic material with h_5 -thickness; 4 are steel self-tapping screws; 5 are rack frame profiles; 6 is an air gap between sheathings with h_2 -thickness.

The calculation is carried out in one-third octave frequency bands in the range from 50 Hz to 5000 Hz. The calculation method consists of six stages.

Stage No. 1. Determination of the threshold frequencies of the ranges of resonant sound transmission through a lightweight enclosure.

The threshold frequency of the range of incomplete spatial resonances (ISR) for a frame-sheathing partition is determined by the formula [31]:

$$f_{bmn_0} = \frac{c_0 \sqrt{a^2 + 4b^2}}{4ab} + \Delta f_{bmn_0}, \quad (5)$$

where c_0 is the velocity of a sound wave in air, m/s; a and b are the length and the height of the enclosure, respectively, m; Δf_{bmn_0} is the positive frequency correction up to the nearest higher frequency of natural oscillations of the leaf sheathing, Hz.

Rack frame profiles form separate rectangular cells along the length of the partition. This leads to the appearance of additional conditions for self-consistency of wave fields within these cells. The length of the frame cell is assumed to be equal to the spacing of the rack profiles of the partition frame ($a_1 = l$). The threshold frequency of the range of incomplete spatial resonances for a frame cell is calculated by the formula:

$$f_{bmn_0}(fc) = \frac{c_0 \sqrt{a_1^2 + 4b_1^2}}{4a_1b_1} + \Delta f_{bmn_0}, \quad (6)$$

where a_1 and b_1 are the length and the height of the frame cell, respectively, m; Δf_{bmn_0} is the positive frequency correction up to the nearest higher frequency of natural oscillations of the leaf sheathing, Hz.

The threshold frequency of the range of total spatial resonances (TSR) for a frame-sheathing partition is determined by the formula [31]:

$$f_{bmn} = \frac{c_0^2}{2\pi} \sqrt{\frac{\mu}{D}}, \quad (7)$$

where μ is the surface density of the sheathing, kg/m²; D is the cylindrical stiffness of the sheathing, Pa·m³.

The resonant frequency of the system "mass-elasticity-mass" ("sheathing – air gap – sheathing") is determined by the well-known formula [31], which can be written for the case of identical sheathings in the following form:

$$f_{msm} = \frac{1}{2\pi} \sqrt{\frac{2E_0}{h_2\mu_1}}, \quad (8)$$

where E_0 is the dynamic modulus of elasticity of the air, Pa; μ_1 is the surface density of the sheathing, kg/m²; h_2 is the thickness of the air gap between the sheathings, m.

For an anti-resonant panel ("leaf sheathing – elastic layer – anti-resonant panel"), in the case of identical materials for leaf sheathings and anti-resonant panels, equation (8) takes on the form:

$$f_{msm(ARP)} = \frac{1}{2\pi} \sqrt{\frac{2E_2}{h_5\mu_1}}, \quad (9)$$

where E_2 is the dynamic modulus of elasticity of the material of the elastic layer located between the leaf sheathing and the anti-resonant panels, Pa; h_5 is the thickness of the elastic layer located between the sheathing and the anti-resonant panels, m.

Stage No. 2. Calculation of the resonant sound transmission coefficient.

The calculation is carried out in the frequency ranges of resonant sound transmission with different conditions of self-consistency of wave fields in the high-level room and low-level room with the wave field of natural oscillations of the partition: in the frequency ranges of simple spatial resonances (SSR), incomplete spatial resonances (ISR), total spatial resonances (TSR). Taking into account the change in the conditions for additional self-consistency of wave fields in the frame cells due to oscillations of the anti-resonant panels (ARP), the formula for calculating the resonant sound transmission coefficient is transformed as follows [31]:

$$\tau_r = \tau_{sr} + \tau_{1r}\tau_{2r}, \quad (10)$$

where τ_{sr} is the coefficient of resonant sound transmission through both sheathings with an elastic connection between them; τ_{1r} is the coefficient of resonant sound transmission through the sheathing located on the side of the high-level room; τ_{2r} is the coefficient of resonant sound transmission through the sheathing located on the side of the low-level room. Equation (10) is valid for the anti-resonant panel in the frequency range above the resonant frequency of the "mass-elasticity-mass" system ($f \geq f_{msm(ARP)}$).

In the range $f < f_{msm(ARP)}$, equation (10) takes on the form:

$$\tau_r = \tau_{sr} + \tau_{1r}\tau_{2r(fc\ ARP)}, \quad (11)$$

where $\tau_{2r(fc\ ARP)}$ is the coefficient of resonant sound transmission through the sheathing located on the side of the low-level room, calculated for the frame cell (with geometric sizes $a_1 \times b_1$) taking into account the anti-resonant panel.

The coefficient of resonant sound transmission through both sheathings with an elastic connection between them is determined by the formula [31]:

$$\tau_{sr} = \frac{1}{\frac{\pi^2}{\rho_0^2 c_0^2} \frac{\mu^2 f^2}{A^2} \left(\frac{f^2}{f_{msm}^2} - 1 \right)^2 + 1}, \quad (12)$$

where $\rho_0 c_0$ is the characteristic air impedance; μ is the surface density of the partition, kg/m²; f is the current sound frequency, Hz; A is the characteristic of self-consistency of the wave field of natural oscillations of the sheathings with the sound fields in the high-level room and low-level room; f_{msm} is the resonant frequency of the "mass-elasticity-mass" system ("sheathing – air gap – sheathing"), Hz.

The coefficients of resonant sound transmission through the sheathings of the partition are calculated by the formulas [31]:

$$- \text{ in the frequency ranges of SSR and ISR } (f_{bm_0 n_0} < f < f_{bmn}):$$

$$\tau_{1r} = \frac{1}{\frac{1.15\pi^3}{8\rho_0^2 c_0^2 A^4} \mu_1^2 f^2 \eta_1 \cos^2 \theta_m + 1}, \quad \tau_{2r} = \frac{1}{\frac{1.15\pi^3}{8\rho_0^2 c_0^2 A^4} \mu_1^2 f^2 \eta_1 \cos^2 \theta_2 + 1}, \quad (13)$$

where $\rho_0 c_0$ is the characteristic air impedance; A is the characteristic of self-consistency of the wave field of natural oscillations of the sheathings with the sound fields in the high-level room and low-level room; μ_1 is the surface density of sheathing, kg/m²; f is the current sound frequency, Hz; η_1 is the coefficient of loss of the sheathing material; $\theta_m = 51.76^\circ$ is the average angle of incidence of diffuse sound field waves on the partition from the high-level room; θ_2 is the angle of incidence of sound waves from the air gap onto the sheathing located on the side of the low-level room, degrees;

- in the frequency range of TSR ($f > f_{bmn}$):

$$\tau_{1r} = \frac{1}{\frac{8\pi}{\rho_0^2 c_0^2} \mu_1^2 \frac{f^3}{f_{bmn}} \eta_1 \cos \theta_m \sqrt{1 - \frac{f_{bmn}}{f}} + 1},$$

$$\tau_{2r} = \frac{1}{\frac{8\pi}{\rho_0^2 c_0^2} \mu_1^2 \frac{f^3}{f_{bmn}} \eta_1 \cos \theta_2 \sqrt{1 - \frac{f_{bmn}}{f}} + 1}, \quad (14)$$

where $\rho_0 c_0$; μ_1 , η_1 , θ_m ; f are the same as in formula (13); f_{bmn} is the threshold frequency of the TSR frequency range for sheathing of partition, Hz.

Stage No. 3. Calculation of the inertial sound transmission coefficient.

The calculation is carried out according to the formula [31]

$$\tau_i = \tau_{si} + \tau_{1i} \tau_{2i}, \quad (15)$$

where τ_{si} is the coefficient of inertial sound transmission through both sheathings with an elastic connection between them; τ_{1i} is the coefficient of inertial sound transmission through the sheathing located on the side of the high-level room; τ_{2i} is the coefficient of inertial sound transmission through the sheathing located on the side of the low-level room.

The coefficient of inertial sound transmission through both sheathings with an elastic connection between them is determined by the formula [31]:

$$\tau_{si} = \frac{1}{\frac{\pi^2}{\rho_0^2 c_0^2} \frac{\mu^2 f^2}{F_{li}^2} \left(\frac{f^2}{f_{msm}^2} - 1 \right)^2 + 1}, \quad (16)$$

where $\rho_0 c_0$ is the characteristic air impedance; μ is the surface density of the partition, kg/m²; f is the current sound frequency, Hz; F_{li} is the response function for the sheathing located on the side of the high-level room; f_{msm} is the resonant frequency of the "mass-elasticity-mass" system ("sheathing – air gap – sheathing"), Hz.

The coefficients of inertial transmission of sound through the sheathings of the partition are determined by the formulas [31]:

$$\tau_{1i} = \frac{1}{\frac{\pi^2}{\rho_0^2 c_0^2} \frac{\mu_1^2 f^2 \cos^2 \theta_m}{F_{1i}^2} + 1}, \quad \tau_{2i} = \frac{1}{\frac{\pi^2}{\rho_0^2 c_0^2} \frac{\mu_1^2 f^2 \cos^2 \theta_2}{F_{2i}^2} + 1}, \quad (17)$$

where μ_1 is the surface density of sheathing, kg/m²; F_{1i} is the response function for the sheathing located on the side of the high-level room; F_{2i} is the response function for the sheathing located on the side of the low-level room.

The frequency characteristics of the coefficients of sound transmission through a frame-sheathing partition with anti-resonant panels, which are calculated using the formulas (1), (10) – (17), are plotted in Fig. 4. Analysis of the data presented in Fig. 4 shows that in the field of low sound frequencies ($f \leq 125$ Hz), the values of the coefficients of resonant and inertial sound transmission are comparable. Here, the inertial sound transmission predominates slightly over the resonant sound transmission. In the medium- and high-frequency sound ranges ($f \geq 160$ Hz), the predominant contribution to the sound transmission through the lightweight partition is made by the resonant component. In the frequency ranges located near resonant frequencies (f_{msm} , $f_{bmn0}(fc)$, $f_{msm}(ARP)$, f_{bmn}), there are rises of the frequency characteristics of the resonant sound transmission coefficient (τ_r) and the total sound transmission coefficient through the partition (τ). The most significant increase of resonant sound transmission through a lightweight partition is observed near the resonant frequency of the "mass-elasticity-mass" system (f_{msm}) and near the threshold frequency of the TSR frequency range for sheathing of partition (f_{bmn}).

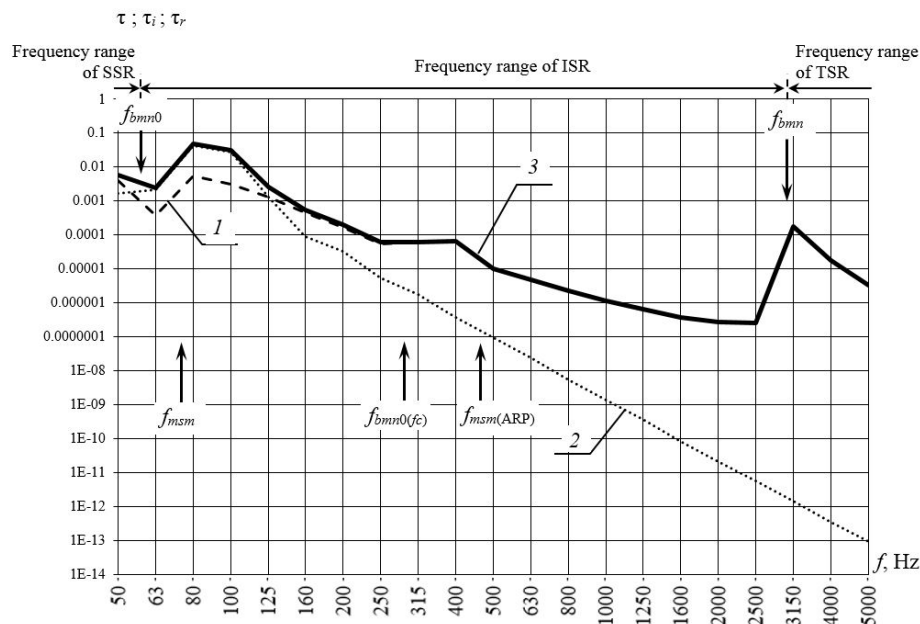


Figure 4. The theoretical frequency characteristics of the coefficients of sound transmission through a lightweight frame-sheathing partition with anti-resonant panels, with a double frame ($a \times b = 4.2 \times 2.5$ m; thickness of the air gap between the sheathings is $h_2 = 89$ mm; sheathings are made by gypsum fiber sheets with thickness $h_1 = 12.5$ mm; spacing of rack profiles of the frame is $a_1 = 0.6$ m; cross-sectional height of rack profiles of the frame is $h_f = 50$ mm; distance between rack profiles of the double frame is $h_3 = 5$ mm; anti-resonant panels are made by gypsum fiber sheets with thickness $h_4 = 12.5$ mm; elastic layer between sheathing and anti-resonant panels is made by mats of polyester fiber with thickness $h_5 = 12.5$ mm; total thickness of the partition is $h_{en} = 130$ mm): 1 – coefficient of resonant sound transmission through the partition (τ_r); 2 corresponds to the coefficient of inertial sound transmission through the partition (τ_i); 3 corresponds to the total coefficient of sound transmission through the partition (τ).

Stage No. 4. Calculation of the threshold frequency of the diffuseness of the sound field in the plane of the enclosure (f_b).

The calculation of the number of lengths of projections of half-waves of the sound field in the high-level room along the smallest side of the partition is performed:

$$n_0 = b \sqrt{\frac{4f^2}{c_0^2} - \frac{1}{a^2}}, \quad (18)$$

where c_0 is the velocity of sound wave in air, m/s; a and b are the length and the height of the enclosure, respectively, m; f is the current sound frequency, Hz.

The nearest one-third octave sound frequency, for which condition (4) is satisfied, is the threshold frequency of the diffuseness of the sound field in the plane of the enclosure (f_b).

Stage No. 5. Calculation of the sound insulation of a lightweight partition in the frequency range above the threshold frequency of the diffuseness of the sound field in the plane of the enclosure ($f \geq f_b$).

The calculation is executed according to the formula given in [31], taking into account the values of the resonant sound transmission coefficient and the inertial sound transmission coefficient found at the previous stages:

$$R = 10 \lg \left(\frac{1}{\tau_r + \tau_i} \right), \quad (19)$$

where τ_r is the resonant sound transmission coefficient and τ_i is the inertial sound transmission coefficient.

Stage No. 6. Calculation of the sound insulation of a lightweight partition in the frequency range below the threshold frequency of the diffuseness of the sound field in the plane of the enclosure ($f < f_b$).

In the frequency range below the threshold frequency of the diffuseness of the sound field in the plane of the enclosure ($f < f_b$), there is no a resonant sound transmission, therefore $\tau_r = 0$. Taking this into account, formula (19) takes on the following form:

$$R = 10 \lg \left(\frac{1}{\tau_i} \right). \quad (20)$$

The inertial sound transmission coefficient, τ_i , is calculated by formula (15), while the response functions of the partition's sheathings are taken to be $F_{1i} = F_{2i} = 1$.

Based on the results of the calculation, the frequency characteristic of the sound insulation of a frame-sheathing partition with anti-resonant panels is constructed. The frequency characteristics of the sound insulation of the lightweight partition under study, which are determined by formulas (19) and (20), are plotted in Fig. 5.

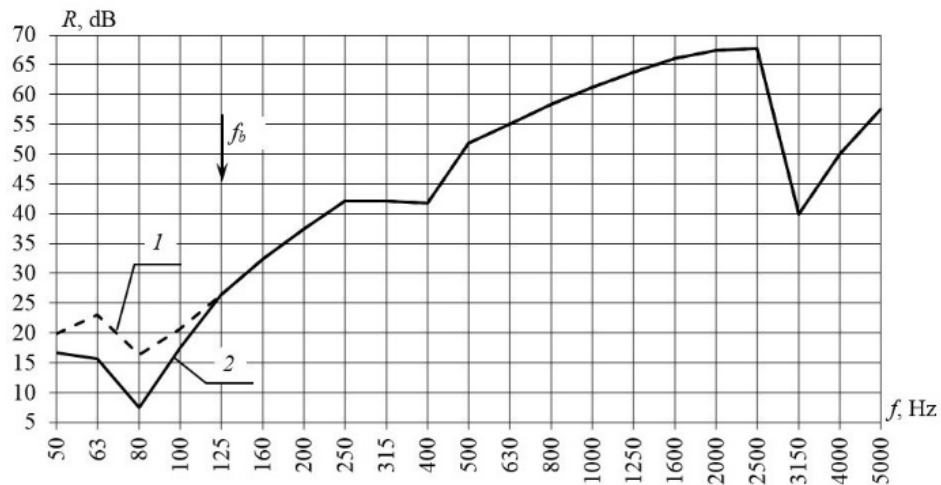


Figure 5. Theoretical frequency characteristics of sound insulation of a light frame-sheathing partition with anti-resonant panels, with a double frame ($a \times b = 2.2 \times 2.65$ m; the remaining parameters of the partition are similar to those given in the caption to Fig. 4): curve 1 corresponds to calculation of sound insulation in the entire frequency range is performed taking into account the resonant and inertial sound transmission (according to formula (19)); curve 2 corresponds to calculation of sound insulation in the frequency range below the threshold frequency ($f < f_b$) is performed taking into account only the inertial sound transmission (according to formula (20)); the calculation of sound insulation in the frequency range above the threshold frequency ($f \geq f_b$) was performed taking into account the resonant and inertial sound transmission (according to (19)).

Analysis of the presented data shows that in the frequency range $f < f_b$, the sound insulation of a light partition, which is calculated according to the proposed method with account only of the inertial sound transmission (graph 2), is 2–8 dB lower than the sound insulation calculated taking into account the resonant and inertial sound transmission (graph 1). In the frequency range above the threshold frequency of the diffuseness of the sound field in the plane of the enclosure ($f \geq f_b$), graphs 1 and 2 coincide.

4. Conclusions

Based on the results of the theoretical studies, the following conclusions can be drawn:

1. We proposed to divide the generalized frequency characteristic of the sound insulation of lightweight enclosing structures into two ranges, the boundary between which is found by the threshold frequency of the diffuseness of the sound field in the plane of the enclosure. The location of the threshold frequency on the frequency scale is determined by the geometric sizes of the fence (the length a and the height b).

2. In the frequency range above the threshold frequency of the diffuseness of the sound field in the plane of the enclosure ($f \geq f_b$), the sound transmission consists of the resonant sound transmission (in the mode of natural oscillations of the enclosure) and the inertial sound transmission (in the mode of forced oscillations of the enclosure). In this frequency range, methods for calculating the sound insulation can be used that assume the diffuse nature of the sound fields in high-level room and low-level room. In the frequency range below the threshold frequency ($f < f_b$), the oscillations of the enclosure are close to piston-like movements, and the sound transmission occurs only in the inertial mode (there is no resonant sound transmission, i.e. $\tau_r = 0$).

3. Based on the theory of self-consistency of wave fields, we developed a method for calculating the sound insulation of lightweight building enclosures in the frequency range above the threshold frequency of the diffuseness of the sound field in the plane of the enclosure ($f \geq f_b$), and below the threshold frequency ($f < f_b$). The method enables one calculating the sound insulation of lightweight enclosures, the threshold frequencies of the ranges of resonant sound transmission, and the frequency characteristics of the resonant and inertial sound transmission coefficients.

4. The implementation of the calculation method is considered on the example of a lightweight frame-sheathing partition with anti-resonant panels. The frequency characteristics of the resonant and inertial sound transmission coefficients, as well as the total coefficient of sound transmission through a light partition are presented. It was established that the most significant increase in the resonant sound transmission occurs near the resonant frequency of the "mass-elasticity-mass" system (f_{msm}) and near the resonant frequency of the TSR range for the partition sheeting (f_{bmn}).

5. The frequency characteristics of sound insulation of a lightweight frame-sheathing partition with anti-resonant panels are presented. It was established that in the range below the threshold frequency of the diffuseness of the sound field in the plane of the enclosure ($f < f_b$) the sound insulation of a lightweight partition, which is calculated according to the proposed method considering only the inertial sound transmission, is 2–8 dB lower than the sound insulation calculated taking into account the resonant and inertial sound transmission.

6. The developed method can be applied to calculate the sound insulation of lightweight building enclosures in the frequency range from 50 Hz to 5000 Hz, including the low sound frequency range ($50 < f < 100$ Hz).

References

1. London, A. Transmission of Reverberant Sound Through Single Walls. *Journal of Research of the National Bureau of Standards*. 1949. 42(6). Pp. 605–615. DOI: 10.6028/jres.042.053
2. Kosten, C.W. General review of section VII. *Proceedings of the 1st ICA-Congress Electroacoustics*. Netherlands, 1953. Pp. 263–270.
3. Peutz, V.M.A. Some fundamental measurements on single and double plate structures. *Proceedings of the 1st ICA-Congress Electroacoustics*. Netherlands, 1953. Pp. 281–284.
4. Utley, W.A. Single leaf transmission loss at low frequencies. *Journal of Sound and Vibration*. 1968. 8(2). Pp. 256–261. DOI: 10.1016/0022-460X(68)90231-9
5. Nilsson, A.C. Reduction Index and Boundary Conditions for a wall Between Two Rectangular Rooms. Part II: Experimental Results. *Acta Acustica*. 1972. Vol. 26, No. 1. Rp. 19–23. ISBN: 1610–1928.
6. Crocker, M.J., Battacharya, M.K., Price, A.J. Sound and vibration transmission through panels and tie beams using statistical energy analysis. *Journal of Engineering for Industry*. 1971. 93 (3). Pp. 775–781. DOI: 10.1115/1.3428011
7. Lyon, R.H., Maidanik, G. Power flow between linearly coupled oscillators. *Journal of the Acoustical Society of America*. 1962. 34(5). Pp. 623–639. DOI: 10.1121/1.1918177
8. Ovsyannikov, S.N., Leliuga, O.V., Gradov, V.A. Calculation model of sound and vibration propagation in a building fragment based on the method of statistical energy analysis. *IOP Conference Series: Materials Science and Engineering*. International Science and Technology Conference "FarEastCon 2019". 2020. 753(4). 042006. DOI: 10.1088/1757-899X/753/4/042006
9. Lelyuga, O., Ovsyannikov, S. Sound insulation of lightweight partition walls with regard to structural sound transmission. *MATEC Web of Conferences*. 2018. 143. 01009. DOI: 10.1051/mateconf/201814301009
10. Liu, Y. Sound transmission through triple-panel structures lined with poroelastic materials. *Journal of Sound and Vibration*. 2015. 339. Pp. 376–395. DOI: 10.1016/j.jsv.2014.11.014
11. Liu, Y., Sebastian, A. Effects of external and gap mean flows on sound transmission through a double-wall sandwich panel. *Journal of Sound and Vibration*. 2015. 344. Pp. 399–415. DOI: 10.1016/j.jsv.2015.01.040
12. Liu, Y., Catalan, J.-C. External mean flow influence on sound transmission through finite clamped double-wall sandwich panels. *Journal of Sound and Vibration*. 2017. 405. Pp. 269–286. DOI: 10.1016/j.jsv.2017.05.049
13. Liu, Y., Catalan, J.-C., Shen, C. Effects of external and air gap flows on sound transmission through finite clamped double-panel sandwich structures. *Composite Structures*. 2018. 203. Pp. 286–299. DOI: 10.1016/j.compstruct.2018.06.104
14. Liu, Y., Daudin, C. Analytical modelling of sound transmission through finite clamped double-wall sandwich panels lined with poroelastic materials. *Composite Structures*. 2017. 172. Pp. 359–373. DOI: 10.1016/j.compstruct.2017.03.024
15. Wareing, R.R., Davy, J.L., Pearse, J.R. Predicting the sound insulation of plywood panels when treated with decoupled mass loaded barriers. *Applied Acoustics*. 2015. 91. Pp. 64–72. DOI: 10.1016/j.apacoust.2014.12.006
16. Hwang, S., Kim, J., Lee, S., Kwun, H. Prediction of sound reduction index of double sandwich panel. *Applied Acoustics*. 2015. 93. Pp. 44–50. DOI: 10.1016/j.apacoust.2015.01.017
17. Davy, J.L. The improvement of a simple theoretical model for the prediction of the sound insulation of double leaf walls. *Journal of Acoustic Society of America*. 2010. 127(2). Pp. 841–849. DOI: 10.1121/1.3273889
18. Davy, J.L. Predicting the Sound Insulation of Walls. *Journal of Building Acoustics*. 2009. 16(1). Pp. 1–20. DOI: 10.1260/135101009788066546
19. Legault, J., Atalla, N. Numerical and experimental investigation of the effect of structural links on the sound transmission of a lightweight double panel structure. *Journal of Sound and Vibration*. 2009. 324. Pp. 712–732. DOI: 10.1016/j.jsv.2009.02.019
20. Pobleu-Puig, J., Rodriguez-Ferran, A., Guigou-Carter, C., Villot, M. The role of studs in the sound transmission of double walls. *Acta Acustica united with Acustica*. 2009. 95(3). Pp. 1–24. DOI: 10.3813/AAA.918176
21. Zhou, J., Bhaskar, A., Zhang, X. Optimization for sound transmission through a double-wall panel. *Applied Acoustics*. 2013. 74. Pp. 1422–1428. DOI: 10.1016/j.apacoust.2013.06.002
22. Wang, J., Lu, T.J., Woodhouse, J., Langley, R.S., Evans, J. Sound transmission through lightweight double-leaf partitions: theoretical modelling. *Journal of Sound and Vibration*. 2005. 286. Pp. 817–847. DOI: 10.1016/j.jsv.2004.10.020

23. Legault, J., Atalla, N. Sound transmission through a double panel structure periodically coupled with vibration insulators. *Journal of Sound and Vibration*. 2010. 329. Pp. 3082–3100. DOI: 10.1016/j.jsv.2010.02.013
24. Shi, S.X., Jin, G.Y., Liu, Z.G. Vibro-acoustic behaviors of an elastically restrained double-panel structure with an acoustic cavity of arbitrary boundary impedance. *Applied Acoustics*. 2014. 76. Pp. 431–444. DOI: 10.1016/j.apacoust.2013.09.008
25. Nakanishi, S., Yairi, M., Minemura, A. Estimation method for parameters of construction on predicting transmission loss of double leaf dry partition. *Applied Acoustics*. 2011. 72. Pp. 364–371. DOI: 10.1016/j.apacoust.2010.12.01
26. Wyngaert, J.C.E., Schevenels, M., Reynders, E.P.B. Predicting the sound insulation of finite double-leaf walls with a flexible frame. *Applied Acoustics*. 2018. 141. Pp. 93–105. DOI: 10.1016/j.apacoust.2018.06.020
27. Kochkin, A.A., Shubin, I.L. Issledovanie sloistykh vibrodempirovannykh elementov i konstruksii iz nikh dlya snizheniya shuma [Investigation of layered vibration-damped elements and structures made of them to reduce noise]. *Izvestiya of higher educational institutions. Technology of the textile industry*. 2018. 375(3). Pp. 184–187.
28. Kochkin, N.A., Shubin, I.L., Kochkin, A.A. Investigation of increasing the sound insulation of existing fences using layered vibration-damped elements [Issledovanie povysheniya zvukoizolyatsii sushchestvuyushchikh ograzhdenii s ispol'zovaniem sloistykh vibrodempirovannykh elementov]. *Izvestiya of higher educational institutions. Technology of the textile industry*. 2019. 381(3). Pp. 215–219.
29. Wyngaert, J.C.E., Schevenels, M., Reynders, E.P.B. Shape optimization of studs in double-leaf plasterboard walls for maximal broadband sound insulation and minimal material use. *Applied Acoustics*. 2021. 183. 108307. DOI: 10.1016/j.apacoust.2021.108307
30. Wyngaert, J.C.E., Schevenels, M., Reynders, E.P.B. Broadband acoustic shape optimization of studs in double-leaf walls. *Journal of Sound and Vibration*. 2020. 485(4). 115562. DOI: 10.1016/j.jsv.2020.115562
31. Sedov, M.S. Sound Insulation. In *Handbook «Noise and Vibration Control in Vehicles»*. Edited by Ivanov N.I. and Crocker M.J. Published in English by INTERPUBLISH. St. Petersburg, 1994. Pp. 68–105. ISBN: 5-7325-0090-1 DOI: 10.1016/0003-682x(95)90015-p
32. Sedov, M.S. Analysis and calculation of noise insulation by light enclosures. *Proceedings of International Noise and Vibration Control Conference "Noise-93"*. Edited by Crocker M.J. and Ivanov N.I. Vol. 3. Saint Petersburg, 1993. Pp. 111–116.
33. Sedov, M.S. Regulation of sound radiation of light insulating structures. *Proceedings of the Second International Symposium "Transport Noise and Vibration-94"*. Edited by Kovinskaya S. Saint Petersburg, 1994. Pp. 393–396.
34. Sedov, M.S. Effect of breaking free waves in thin plates of double construction. *Proceedings of Fourth international congress on sound and vibration*. Edited by Crocker M.J. and Ivanov N.I. Saint Petersburg, 1996. Pp. 1073–1076.
35. Erofeev, V.I., Monich, D.V. Sound insulation properties of sandwich panels. *IOP Conference Series: Materials Science and Engineering*. 2020. 896(1). 012005. DOI: 10.1088/1757-899X/896/1/012005
36. Erofeev, V., Monich, D., Verichev, S. Theoretical Method for Calculating Sound Insulation of Sandwich Panels. *Lecture Notes in Networks and Systems. International Scientific Siberian Transport Forum "TransSiberia-2021"*. 2022. Vol. 403. Springer, Cham. https://doi.org/10.1007/978-3-030-96383-5_138
37. Bobylev, V.N., Erofeev, V.I., Monich, D.V., Grebnev, P.A., Kuzmin, D.S. Zvukoizoliruyushchie ograzhdenie [Sound insulating enclosure]. Patent Russia for utility model no. 209635, 2022.

Information about authors:

Vladimir Erofeev, Doctor of Physics and Mathematics
E-mail: erof.vi@yandex.ru

Dmitriy Monich, Doctor of Technical Sciences
ORCID: <https://orcid.org/0000-0002-5802-8773>
E-mail: dmitriy.monich@mail.ru

Pavel Grebnev, PhD in Technical Sciences
E-mail: p.grebnev@mail.ru

Igor Pavlov, Doctor of Physics and Mathematics
E-mail: ispavlov@mail.ru

Received 29.04.2022. Approved after reviewing 27.04.2023. Accepted 28.04.2023.



Research article

UDC 691.43

DOI: 10.34910/MCE.121.4



High-strength building ceramics based on fly ash – red mud mixtures

T. Vakalova , N. Sergeev , D. Tolegenov , D. Tolegenova

National Research Tomsk Polytechnic University, Tomsk, Russian Federation

✉ tvv@tpu.ru

Keywords: fly ash, red mud, sintering, mechanical strength, anorthite, building ceramics

Abstract. The work is devoted to the actual problem of creating high-strength ceramic materials based on technogenic waste. This problem is solved by using low-calcium (2.26 % CaO) aluminosilicate fly ash from the combustion of solid fuel (coal) as the main raw material component with the additions of high-iron (22–25 % Fe₂O₃ in the calcined state) bauxite sludge. The chemical and mineralogical features of the initial fly ash and bauxite sludge, as well as their structural and phase changes during heating were studied. The predictive analysis of the behavior of ash and bauxite sludge mixtures in the CaO–Al₂O₃–SiO₂, Fe₂O₃–Al₂O₃–SiO₂, and FeO–Al₂O₃–SiO₂ systems made it possible to identify the fluxing effect of bauxite sludge additions to fly ash. The main criteria for designing compositions (Fe₂O₃/Al₂O₃ and CaO/SiO₂ modules) of ceramic masses based on ash and sludge for the production of high-strength ceramics are proposed. The iron-alumina module is responsible for the formation of the melt; the calcium silicate module is responsible for the formation of the crystalline phase (anorthite) during firing. The established sintering-hardening effect of bauxite sludge additives in an amount of 10–25 % in compositions with fly ash provides a 1.7–2-fold increase in the compressive strength of samples of semi-dry pressing (from 95 to 206 MPa) at firing temperatures of 1200 °C. The recommended compositions are promising for obtaining densely sintered calcium aluminosilicate building ceramics (paving stones, porcelain stoneware, clinker bricks) with a predominantly anorthite crystalline phase with a water absorption of 0.5–2 % and a compressive strength of up to 175–200 MPa.

Acknowledgements: The research was carried out using the equipment of the CSU NMNT TPU, supported by the RF MES project No. 075-15-2021-710.

Citation: Vakalova, T., Sergeev N., D. Tolegenov, D. Tolegenova. High-strength building ceramics based on fly ash – red mud mixtures. Magazine of Civil Engineering. 2023. 121(5). Article no. 12104. DOI: 10.34910/MCE.121.4

1. Introduction

The large-scale production of traditional ceramic materials (porcelain, faience, sanitary ceramics, building ceramics, etc.) is accompanied by active consumption of high-quality natural raw materials, leading to a gradual decrease in their reserves. There is a need to expand the scope of the use of non-standard natural raw materials, as well as industrial waste to obtain modern ceramic materials with improved physical and mechanical properties (mechanical strength, frost resistance, chemical resistance, etc.).

Pollution of industrial solid waste has become an increasingly serious problem. Every year, large quantities of metallurgical wastes are generated from the production of various metals. These residues are considered as hazardous wastes due to their soluble metal content, which induces many social problems

such as contaminated water, dust-laden air and alkalized soils, as well as human and animal health and security risks from the disintegration of wastes. For example, worldwide, the alumina industry produces approximately 70 Mt/annum of hazardous bauxite residue (so-called “red mud”) [1, 2]. Typically, red mud is considered as a waste discharged to sea, in ponds or landfills. Moreover, discharge of red mud is environmentally hazardous because of its alkalinity [3]. Many studies have been conducted to develop the uses of red mud. It is widely accepted that using red mud as ceramics and building materials is the most promising approach because of its tremendous consumption [4–12].

Fly ash is generated during the combustion of pulverized coal from thermal power plants. It has been posing a heavy problem to the environment and economic growth throughout the world, since it is utilized much less today than generated [13–15]. Coal fly ash is one of the most complex materials to characterize. Approximately 316 individual minerals and 188 mineral groups have been identified in various fly ash samples [16, 17]. The major components are metallic oxides with varying contents of unburnt carbon as measured by a loss on ignition test. The contents of principal oxides are usually in a descending order: Al_2O_3 . Construction industry is still its chief consumer, but its products including bricks, expanded clay, cement and concrete are generally of low value [18–23]. Recently, increased attention has been focused on how fly ash is utilized in the high-value products, such as high-strength mullite ceramics [24–27], cordierite ceramics and cordierite glass-ceramics [28, 29], anorthite-based ceramics [30, 31], Al_2O_3 -SiC composite materials [32], zirconia–mullite–corundum ceramics [33], zeolite-containing adsorbents for wastewater treatment and radioactive waste immobilization [34].

It is known that the mechanical strength of ceramics primarily depends on its phase composition — the content of the crystalline and glassy phases: the greater the amount of the crystalline phase, the greater the strength [35]. The nature of crystalline phases, the conditions of their formation, the habit of its particles are important for the formation of the mechanical properties of ceramics too. In particular, if the crystals are elongated (for example, particles of acicular mullite or wollastonite), then the strength of ceramics will increase due to the formation of a crystalline framework [36, 37]. If the formation of the crystalline phase occurs with volumetric changes (for example, the transition of quartz to cristobalite), this can lead to an increase in porosity and to a decrease in strength [35]. However, if the content effect of the glass phase and the crystalline phase on the mechanical strength of the ceramic is compared, then an increase in the total content of the crystalline phase and, accordingly, a decrease in the amount of glass phase in the composition of the ceramic material will enhance its strength. On the other hand, the mechanical strength also depends on the degree of sintering behavior (density or porosity) [38]. Therefore, to increase the strength of the ceramic material, it is necessary to reduce its overall porosity and/or to increase the content of the crystalline phase.

The possibility of using fly ash and bauxite sludge as a raw material for obtaining building ceramics with improved functional properties is determined by the proximity of the chemical composition of the waste and traditional ceramic raw materials (clays, kaolins, silica raw materials, etc.).

Thus, the involvement of technogenic waste in the production of ceramic materials will reduce the need for primary mineral resources. There will be no need for specialized quarries to extract natural raw materials, disturb natural landscapes, etc. Utilization of waste from mining and metallurgical, fuel and energy industries in the silicate materials industry will allow solving not only environmental, but also economic problems, since raw materials from waste for the production of ceramics are 2–3 times cheaper than natural ones.

The purpose of this work is to determine the technological parameters for the creation of high-strength building ceramics based on fly ash from the combustion of solid fuels using red mud as a sintering and hardening additive.

To achieve this objective, it is necessary to solve the following tasks:

- to establish the chemical composition, mineralogical (phase) composition, structural features of the initial technogenic raw materials (fly ash and bauxite sludge);
- to study their (fly ash and bauxite sludge) structural and phase changes during heating;
- to carry out theoretical and exploratory research on the development of compositions and technological parameters for the obtaining of high-strength ceramic materials based on man-made waste.

2. Methods

2.1. Characteristics of initial raw materials used

According to the chemical composition, the studied fly ash is a kind of acid ash with a low content of calcium oxide (2.26 % CaO) and a high content of aluminum oxide (29.19 % Al_2O_3) and iron oxide (12.11 % Fe_2O_3) in the calcined state (Table 1).

Table 1. Chemical composition of the investigated raw materials.

Raw materials	Content of oxides, wt. %									
	SiO_2	Al_2O_3	TiO_2	Fe_2O_3	MnO	CaO	MgO	K_2O	Na_2O	LOI
fly ash										
Absolutely dry state	47.37	28.49	0.96	11.82	2.65	2.19	3.35	0.42	0.35	2.39
Calcined state*	48.53	29.19	0.99	12.11	2.71	2.26	3.43	0.43	0.35	-
red mud										
Absolutely dry state	21.03	7.47	2.16	17.27	1.12	23.46	2.33	0.31	0.43	24.37
Calcined state*	27.88	9.88	2.86	22.83	1.48	31.02	3.08	0.41	0.57	-

* – after calcination at 950 °C

Red mud in the initial state is characterized by high values of mass loss upon ignition (up to 24.37 %), which can complicate its use in the technological process of obtaining molded ceramic materials. In the calcined state, the chemical composition of red mud is dominated by the content of calcium oxide (31.02 % CaO), iron oxide (22.83 % Fe_2O_3) and silicon oxide (27.88 % SiO_2), which account for up to 80 % (81.73 %) of the total content all oxides (Table 1).

X-ray analysis of the fly ash indicates that the investigated fly ash in the initial state is a material with a significant content of glass phase, as evidenced by the presence of an intense diffuse background in the X-ray diffraction pattern (Fig. 1).

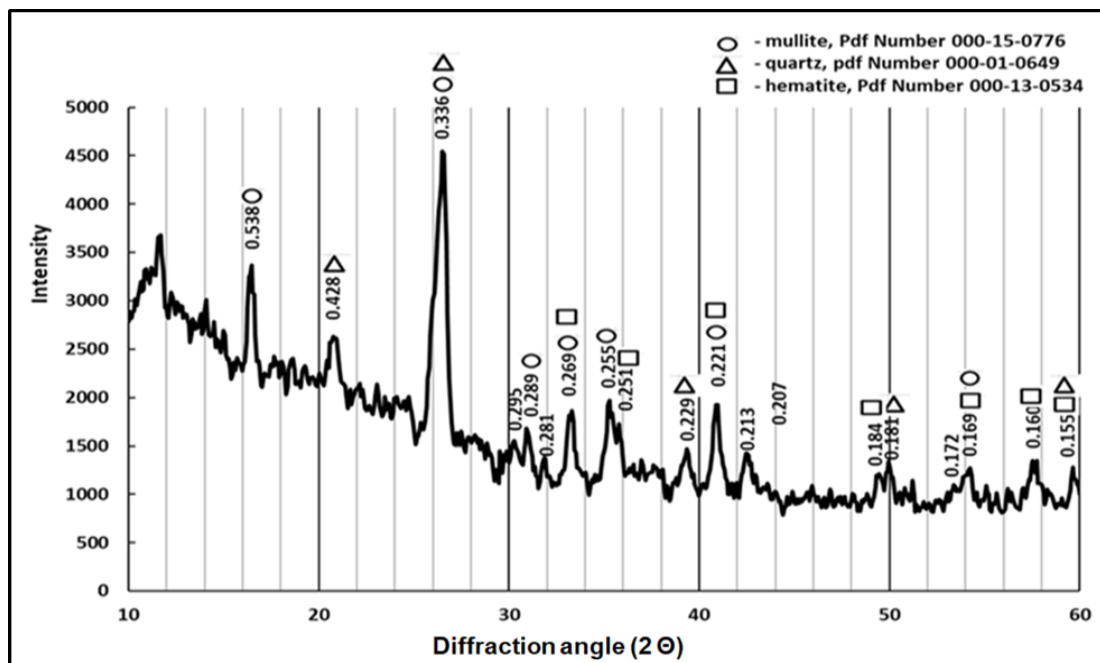


Figure 1. X-ray diffraction pattern of the initial fly ash.

The crystalline part of the fly ash is composed of mullite ($d_a/n - 0.538, 0.336, 0.289, 0.269, 0.255, 0.221$ nm, etc.), quartz ($d_a/n - 0.428, 0.336, 0.229, 0.212, 0.181$ nm, etc.) and iron mineral in the form of hematite ($d_a/n - 0.269, 0.251, 0.219, 0.183$ nm, etc.).

A comparative analysis of the data of chemical analysis (Table 1) and X-ray method (Fig. 2) indicates that the calcium component in the red mud is presented in the form of calcite CaCO_3 , as evidenced by X-ray reflections with $d_a/n - 0.303, 0.250, 0.209, 0.187$ nm, etc., also in the form of hydrated silicates and aluminates calcium: dicalcium hydrosilicate $\gamma - 2\text{CaO} \cdot \text{SiO}_2 \cdot \text{H}_2\text{O}$ ($d_a/n - 0.383, 0.270, 0.189$ nm), as well as hexacalcium tricarbonat hydroaluminat $3\text{CaO} \cdot \text{Al}_2\text{O}_3 \cdot 3\text{CaCO}_3 \cdot 32\text{H}_2\text{O}$ ($d_a/n - 0.383, 0.270, 0.251$ nm, etc.). The iron component is represented by hematite Fe_2O_3 ($d_a/n - 0.270, 0.252, 0.220, 0.184$ nm) and magnetite Fe_3O_4 ($d_a/n - 0.297, 0.252, 0.209, 0.161$ nm).

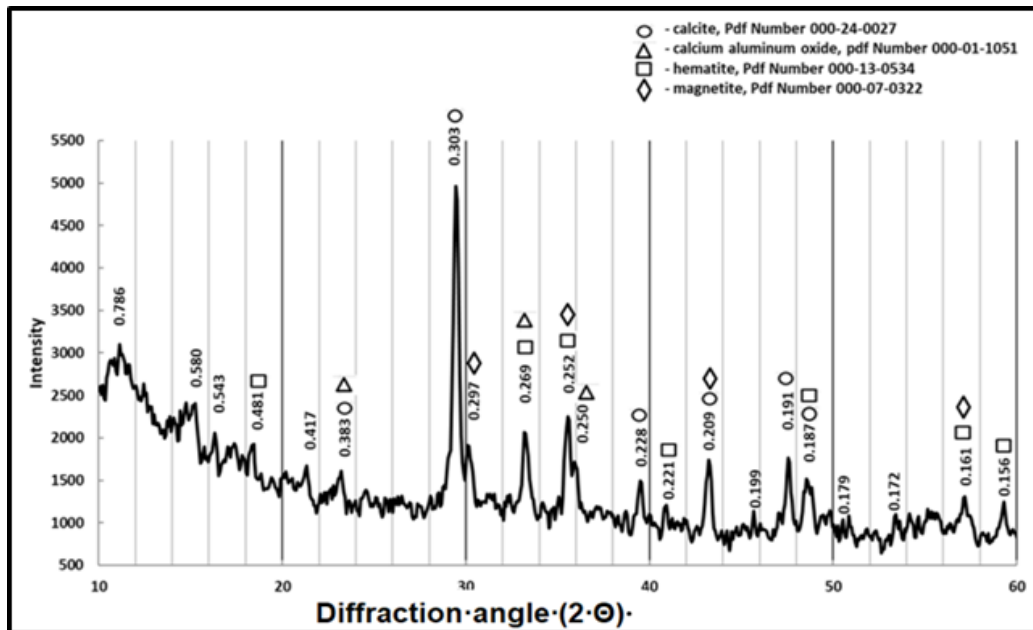
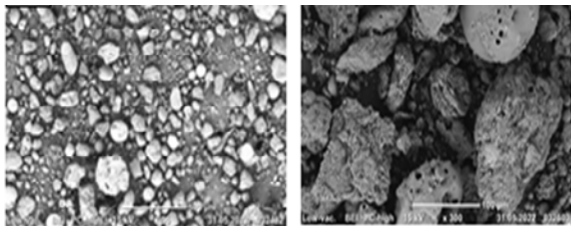
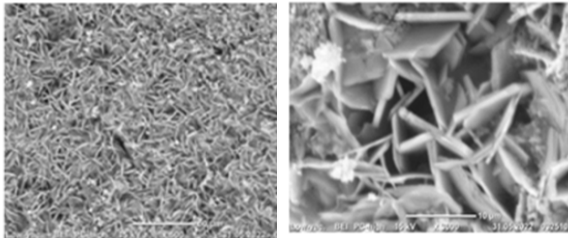


Figure 2. X-ray diffraction pattern of red mud.

According to electron microscopy data, fly ash in the initial state consists of sintered conglomerates of isometric and elongated shapes and rounded particles close to the shape of a sphere (Table 2).

Table 2. Microstructure and dispersion of raw materials.

Raw materials	Microstructure	Particle shape and size
Fly ash		<ol style="list-style-type: none"> 1) round-shaped particles ranging in size from 25 to 95–100 μm, 2) sintered aggregates of isometric shape from 150 to 250 μm, 3) non-metric aggregates 70–100 μm long and 20–30 μm wide.
Red mud		lamellar crystals 11.8 to 15.7 μm long and up to 2 μm thick.

Fly ash microspheres have a hollow structure and a melted surface with numerous sintered particles. The agglomerates have a densely sintered structure with a small number of pores on the surface of the particles. Bauxite sludge is composed of lamellar crystals intertwined with each other.

2.2. Procedures and methods

The study of the behavior of fly ash and red mud upon heating was carried out on specimens in the form of tablets with a diameter of 20 mm (3 samples per temperature) and cylinders 20×20 mm (8 samples per temperature). They were formed from fine powder (less than 0.063 mm) by semi-dry pressing using a 1 % solution of carboxymethylcellulose as a binder. The required degree of compaction of the press powder and the pressure required for this were selected empirically. The specific pressure was varied from 10 to 30 MPa with an interval of 5 MPa, with holding at maximum pressure for 10 sec. The optimum pressing pressure was 20 MPa (based on the maximum bulk density of the compacts). The samples were dried to an air-dry state, after which they were fired in the range of 950–1150 °C with an interval of 50 °C and holding at the final temperature for 2 h. The calcined samples were cooled together with a furnace in a free mode.

The influence of red mud additives in the amount of 10–25 wt.% on mineral formation processes and sintering processes of mixtures with fly ash was assessed on 20×20 mm cylinder samples (5 samples per temperature). The samples were molded by the semi-dry pressing at the pressure of 20 MPa. For this, red mud was pre-calcined at 1100 °C in order to remove chemically bound water and synthesize new crystalline phases in raw materials, and not in molded samples. The fly ash was also pre-calcined at a temperature of 1200 °C to crystallize the glass phase of the fly ash when heated into cristobalite in raw materials, since the formation of cristobalite adversely affects the mechanical properties of the fired samples. Then, mixtures of calcined fly ash and red mud were ground by dry method in a ball mill with a high alumina ceramic lining and grinding balls until the particles completely pass through a 0063 sieve (250 mesh). Sintering of pressed samples was carried out at a temperature of 1200–1300 °C with a heating rate of 1.5 °C/min and an exposure at maximum temperature for 2 hours.

2.3. Experimental method

The physicochemical and processing properties of the initial fly ash and red mud upon heating, the studied mixtures of fly ash with red mud additives and finished products were investigated using physical and chemical methods. These methods include traditional chemical and elemental analyses by an Oxford XSupreme 8000 X-ray fluorescence analyzer. The phase compositions of the specimens were analyzed via an X-ray diffractometer (Shimadzu XRD-7000S) with CuK α radiation ($\lambda K\alpha = 0.154186$ nm) at 40 kV and 25 mA. The specimens were tested in the angle range of 10–60° (2 θ). Moreover, the crystalline phases were identified on the basis of the experimental patterns using the Powder Diffraction File Database of the International Center for Diffraction Data. The microstructures were observed using a scanning electron microscope (Hitachi S-570 and JEOL JSM-840). A thermal analysis was carried out to study the thermal behavior of the rock used up to 1000 °C at a heating rate of 10 °C/min (TG/DSC/DTA thermal analyzer with an SDTQ 60 mass spectrometer).

Air and fire shrinkage was determined on the tablet samples. Sample drying shrinkage were measured by controlling sample length, width and height before and after drying process.

The measurements of water absorption were performed via the Archimedes method. The compressive strength of the fired samples was measured by using cubic samples. The reported compressive strength (MPa) is the average of five measurements.

3. Results and Discussion

3.1. Characteristic of phase changes during heating of the fly ash and red mud used

The use of fly ash and red mud as raw materials for the production of ceramics makes it necessary to study their behavior when heated.

When comparing the X-ray diffraction patterns of the initial ash and the ash fired at 1000 °C, a decrease in the intensity and area of the diffuse background is noted, which indicates a decrease in the content of the glass phase in the fly ash during its heating (Fig. 3). This causes the appearance on the X-ray diffraction pattern of fired fly ash of a low-intensity characteristic reflection of cristobalite SiO₂ with an interplanar distance of $d_a/n - 0.411$ nm, while the intensity of the characteristic reflection of quartz remains unchanged ($d_a/n - 0.427$ nm). The formation of cristobalite nuclei in fly ash at 1000 °C is caused by the crystallization of the glass phase, which leads to a decrease in the area of the diffuse background.

In addition to the appearance of cristobalite at 1000 °C, the formation of another new crystalline phase, anorthite $\text{CaO} \cdot \text{Al}_2\text{O}_3 \cdot 2\text{SiO}_2$ was recorded, as evidenced by the appearance of a low-intensity reflex with $d_a/n = 0.320$ nm.

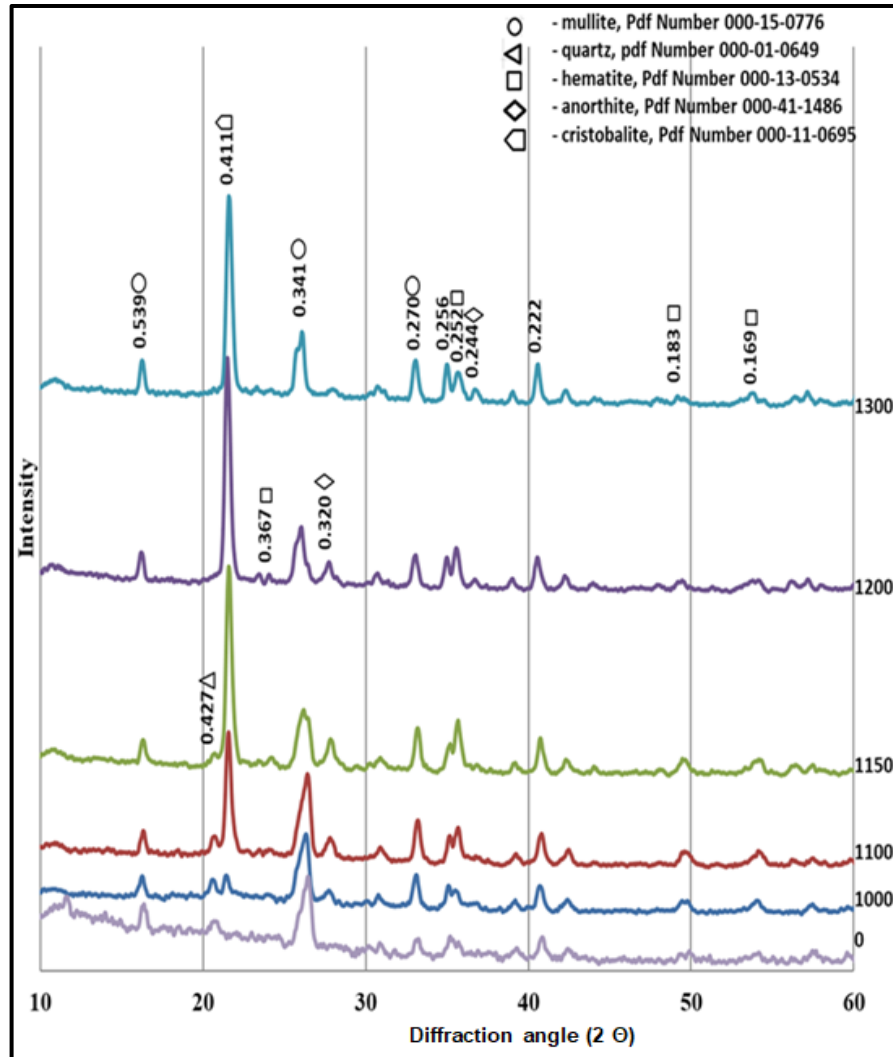


Figure 3. X-ray diffraction patterns of fly ash fired at 1000–1300 °C.

A further increase in the firing temperature from 1000 to 1300 °C has practically no effect on the change in the diffraction pattern of the firing products of the fly ash samples. The difference consists only in the change in the intensity of X-ray reflections. In particular, the height of mullite reflections increases, which may be due to both an increase in the content of mullite and the processes of improving its crystal structure, or both reasons simultaneously. X-ray reflexes of cristobalite grow sharply, which indicates an increase in its content. The intensity of anorthite reflections (0.320, 0.249 nm) increases, although to a lesser extent than for mullite and cristobalite. As for hematite Fe_2O_3 , the mineral component of the initial fly ash, with an increase in temperature up to 1300 °C, its reflections are preserved with a slight decrease in their intensity (0.251, 0.183, 0.169 nm). This may be due to the participation of hematite in the formation of an iron silicate melt during the firing of the initial fly ash at temperatures of 1000–1300 °C.

Thus, the mineralogical composition of the crystalline part of the studied fly ash, fired at 1000–1300 °C, is represented by the initial minerals – mullite $3\text{Al}_2\text{O}_3 \cdot 2\text{SiO}_2$ and hematite Fe_2O_3 , as well as new phases formed during the firing process – cristobalite SiO_2 and anorthite $\text{CaO} \cdot \text{Al}_2\text{O}_3 \cdot 2\text{SiO}_2$ (Table 3).

Table 3. Change in the phase composition of the investigated fly ash after firing at 1000–1300 °C.

Phase	Formula	Presence*		Processes during heating of ash
		in the initial ash	after firing at 1000–1300 °C	
mullite	$3\text{Al}_2\text{O}_3 \cdot 2\text{SiO}_2$	+	++	
quartz	SiO_2	+	--	quartz → cristobalite
hematite	Fe_2O_3	++	+	hematite (partially) → melt
glass phase		+++	+	glass phase (partially) → cristobalite
cristobalite	SiO_2	--	+	
anorthite	$\text{CaO} \cdot \text{Al}_2\text{O}_3 \cdot 2\text{SiO}_2$	--	+	

* + present, -- absent

An assessment of the physical and mechanical properties of samples of semi-dry pressing from finely ground initial fly ash, fired in the temperature range of 1000–1300 °C (Fig. 4), indicates that the highest compressive strength (94 MPa) is achieved at a temperature of 1300 °C (water absorption 10.2 %). Therefore, to exceed the mechanical compressive strength of 95 MPa in the samples of semi-dry pressing, it is necessary to activate the sintering process of the studied fly ash.

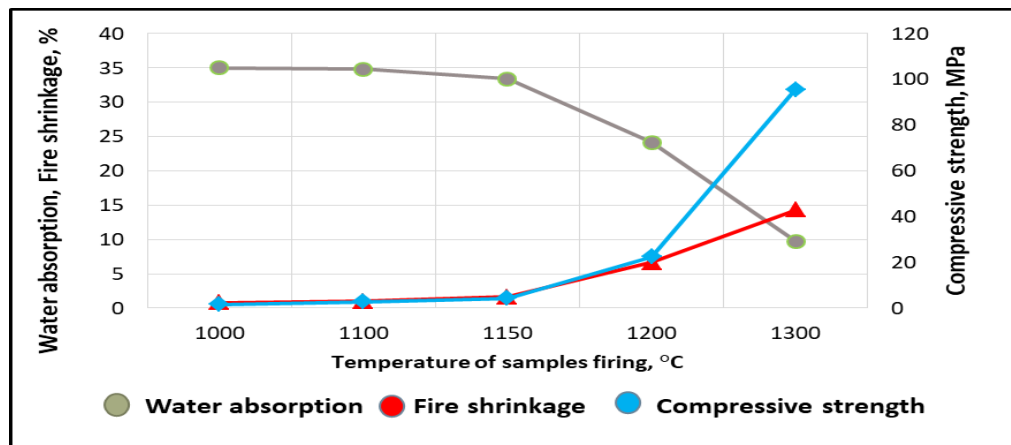


Figure 4. Effect of heating temperature on changes in fire shrinkage, water absorption and compressive strength in the samples made of the studied fly ash.

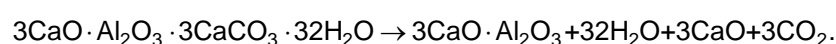
This can be done in different ways: by preliminary heat treatment of aluminosilicate fly ash, by increasing the firing temperature above 1300 °C, by selecting sintering additives. Previously, the authors revealed the effect of various oxide additives on the sintering process of aluminosilicate ceramics, including iron additives [39]. The studied bauxite sludge contains a high content of iron oxide ($22.8 \text{ Fe}_2\text{O}_3$) and may be promising for activating the sintering of aluminosilicate fly ash samples.

According to X-ray studies, the thermal treatment of red mud in the temperature range of 900–1100 °C is accompanied by complex physical and chemical processes, already starting from 900 °C. This leads to a change in the X-ray diffraction patterns of fired red mud samples compared to the initial red mud (Fig. 5):

1. The decrease of the diffuse background in the low-angle region is associated with a decrease in the content of the amorphous phase of red mud due to the crystallization of its components upon heating.

2. Complete decarbonization of calcite CaCO_3 , which manifests itself in the disappearance of the main calcite reflections with interplanar distances of 0.303, 0.250, 0.209, 0.187 nm in the X-ray diffraction patterns.

3. The disappearance of reflections at 0.383, 0.270, 0.250 nm and the appearance of intense reflections at 0.276 and 0.270 nm, as well as less intense reflections at 0.511, 0.424, 0.245, 0.220 nm, are due to the process of dehydration and decarbonization of hexacalcium tricarbonat hydroaluminat $3\text{CaO} \cdot \text{Al}_2\text{O}_3 \cdot 3\text{CaCO}_3 \cdot 32\text{H}_2\text{O}$ to tricalcium aluminate $3\text{CaO} \cdot \text{Al}_2\text{O}_3$:



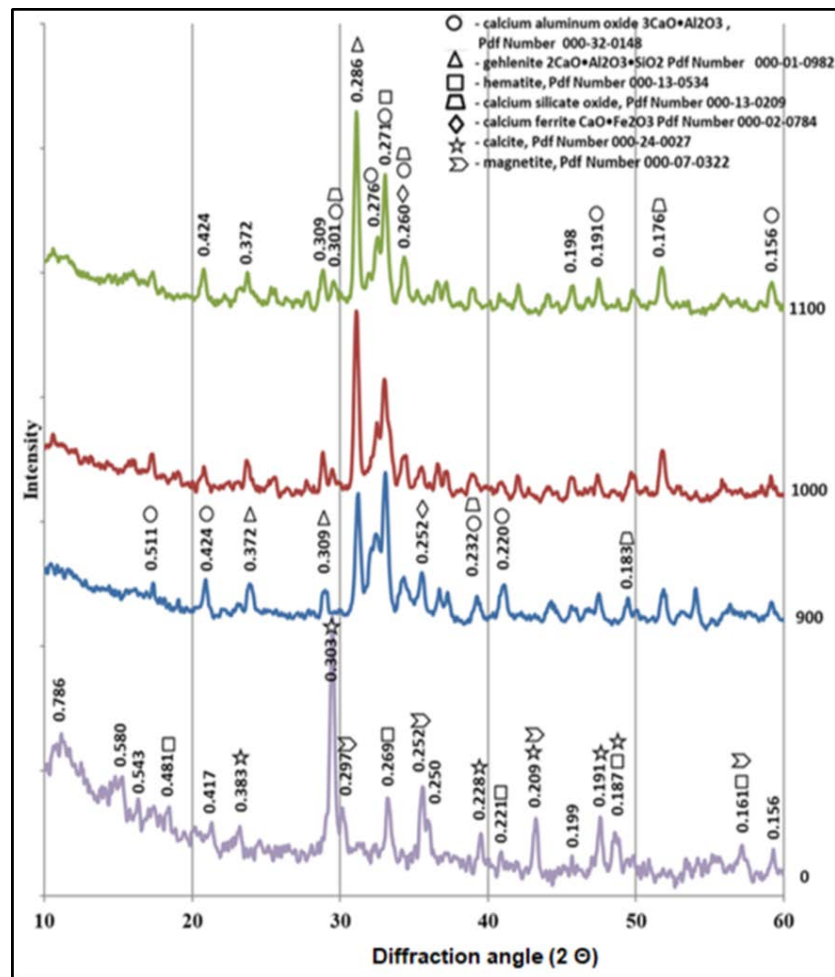


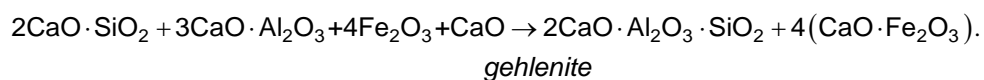
Figure 5. X-ray diffraction patterns of red mud fired at 900–1100 °C.

The presence of calcium aluminum oxide, also found by other authors [11, 40], is consistent with most XRD spectra and is likely in view of the availability of CaO and Al₂O₃ in the chemical composition of red mud.

4. The appearance of an intense reflection at 0.286 nm, as well as reflections at 0.372, 0.307, 0.245, 0.241, 0.204 nm indicate the synthesis of a new crystalline phase in the form of gehlenite 2CaO·Al₂O₃·SiO₂.

An increase in the firing temperature of the red mud from 900 to 1100 °C practically does not change the diffraction pattern of the fired products. The difference consists only in a decrease in the intensity of reflections of tricalcium aluminate 3CaO·Al₂O₃, a decrease in the intensity of reflections of hematite Fe₂O₃, and an increase in the intensity of reflections of gehlenite 2CaO·Al₂O₃·SiO₂.

The recorded changes make it possible to determine the reaction for the synthesis of gehlenite at a temperature within the 900–1100 °C range:



The formation of monocalcium ferrite at temperatures of 900–1100 °C along with gehlenite is indicated by the appearance of its reflexes (d_a/n - 0.261, 0.252, 0.227, 0.215, 0.184 nm) on the X-ray diffraction patterns.

Thus, the mineralogical composition of the crystalline part of red mud fired at 900–1100 °C is represented by tricalcium aluminate 3CaO·Al₂O₃, hematite Fe₂O₃, gehlenite 2CaO·Al₂O₃·SiO₂ and monocalcium ferrite CaO·Fe₂O₃ (Table 4).

Table 4. Change in the phase composition of the investigated red mud firing at 900–1100 °C.

Phase	Formula	Presence*		Processes during heating of red mud
		in the initial red mud	after firing at 900–1100 °C	
calcite	CaCO_3	+	--	$\text{CaCO}_3 \rightarrow \text{CaO}$
dicalcium hydrosilicate	$2\text{CaO} \cdot \text{Al}_2\text{O}_3 \cdot \text{SiO}_2$	+	--	$2\text{CaO} \cdot \text{SiO}_2 \cdot \text{H}_2\text{O} \rightarrow 2\text{CaO} \cdot \text{SiO}$
hexacalcium tricarbonat hydroaluminate	$3\text{CaO} \cdot \text{Al}_2\text{O}_3 \cdot 3\text{CaCO}_3 \cdot 32\text{H}_2$	+	--	$3\text{CaO} \cdot \text{Al}_2\text{O}_3 \cdot 3\text{CaCO}_3 \cdot 32\text{H}_2\text{O} \rightarrow 3\text{CaO} \cdot \text{Al}_2\text{O}_3 \cdot 3\text{CaO}$
magnetite	Fe_3O_4	+	--	$\text{Fe}_3\text{O}_4 \rightarrow \text{Fe}_2\text{O}_3$
hematite	Fe_2O_3	+	++	
tricalcium aluminate	$3\text{CaO} \cdot \text{Al}_2\text{O}_3$	--	+	
gehlenite	$2\text{CaO} \cdot \text{Al}_2\text{O}_3 \cdot \text{SiO}_2$	--	+	
monocalcium ferrite	$\text{CaO} \cdot \text{Fe}_2\text{O}_3$	--	+	

* + present, -- absent

An assessment of the physical and mechanical properties of the samples made of semi-dry pressed finely ground red mud, fired in the temperature range of 900–1100 °C, indicates their complete sintering (to zero water absorption) at a temperature of 1100 °C with the achievement of compressive strength up to 230 MPa (Fig. 6).

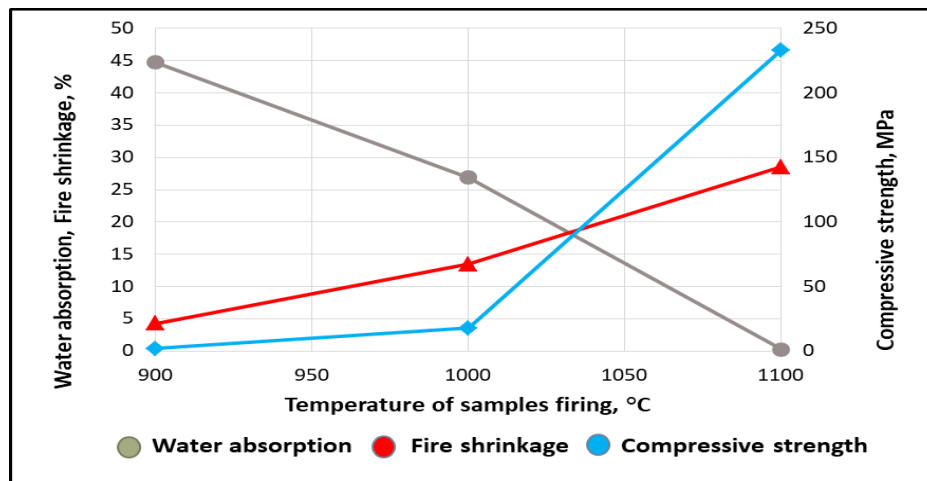


Figure 6. Effect of heating temperature on changes in fire shrinkage, water absorption and compressive strength of the samples made of the studied red mud.

3.2. Theoretical substantiation of the choice of the studied compositions "fly ash – red mud"

To predict the physical and chemical processes during heating of compositions based on the studied fly ash with the addition of red mud in an amount of 10–25 wt. %, i.e. to determine the recommended sintering interval, to establish which firing mode is required, and which phases will crystallize from the melt, a theoretical analysis of the behavior of the studied masses in the $\text{CaO} - \text{Al}_2\text{O}_3 - \text{SiO}_2$ [41, 42], $\text{Fe}_2\text{O}_3 - \text{Al}_2\text{O}_3 - \text{SiO}_2$ [43] and $\text{FeO} - \text{Al}_2\text{O}_3 - \text{SiO}_2$ [41, 43] systems was carried out. These systems were chosen due to the chemical composition of the initial raw materials, namely, the predominance of silica, alumina and iron oxides in the chemical composition of the fly ash, and silica, calcium and iron oxides in the red mud. It should be noted that the studies on compositions with high-iron technogenic components (various fly ash, metallurgical sludge and slag) show that the systems with iron almost always contain both ferric (Fe_2O_3) and ferrous iron (FeO) [44]. This makes it necessary to consider both ternary systems with iron oxides.

For this purpose, initially the chemical compositions of the ceramic masses were calculated (Table 5).

Table 5. Chemical composition of the investigated mixtures of fly ash with red mud in the calcined state.

Mixture code	Content of oxides, %									Modules	
	SiO ₂	Al ₂ O ₃	TiO ₂	CaO	MgO	Fe ₂ O ₃	MnO	K ₂ O	Na ₂ O	ferric iron-alumina Fe ₂ O ₃ /Al ₂ O ₃	calcium silicate CaO/SiO ₂
FA ₁₀₀	48.53	29.19	0.99	2.26	3.43	12.11	2.71	0.43	0.35	0.41	0.05
RM ₁₀₀	27.88	9.88	2.86	31.02	3.08	22.83	1.48	0.41	0.57	2.3	1.11
FA ₉₀ RM ₁₀	46.47	27.26	1.17	5.14	3.39	13.18	2.59	0.43	0.37	0.48	0.12
FA ₈₅ RM ₁₅	45.43	26.29	1.27	6.57	3.38	13.72	2.53	0.43	0.38	0.52	0.15
FA ₈₀ RM ₂₀	44.40	25.33	1.36	8.01	3.36	14.25	2.46	0.42	0.40	0.56	0.18
FA ₇₅ RM ₂₅	43.37	24.36	1.45	9.45	3.34	14.79	2.40	0.42	0.41	0.61	0.22

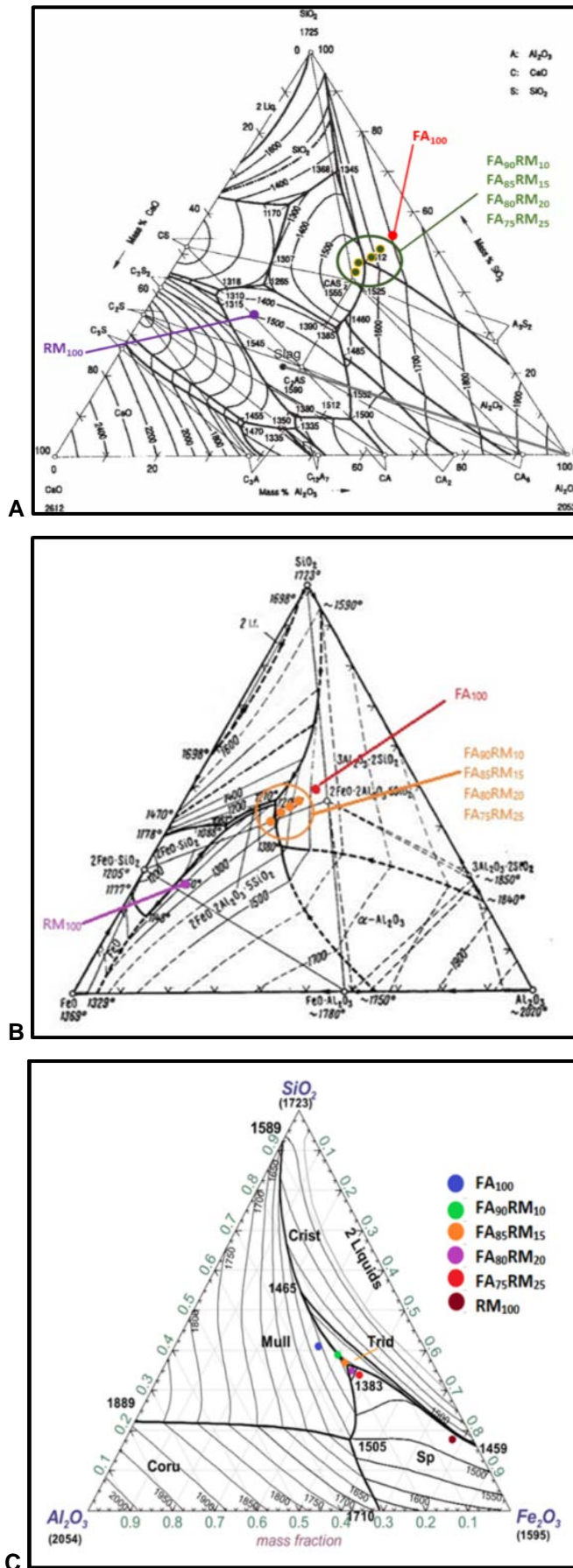
• here and below, the number in the mixture code corresponds to the content of fly ash and red mud, wt. %

The calculated chemical compositions of the studied mixtures indicate that with an increase in the addition of red mud from 10 to 25 %, the content of ferric iron oxide Fe₂O₃ increases from 12.11 to 14.79 % (by 2.6 %) and calcium oxide CaO from 2.26 to 9.45 % (by 7 %) due to a decrease in the content of oxides SiO₂ (from 48.53 to 43.37 %) and Al₂O₃ (from 29.19 to 24.36 %).

Since when red mud is added to the chemical composition of fly ash, two main oxides Fe₂O₃ and CaO are introduced simultaneously, to assess their effect on the firing behavior of mixtures of fly ash with red mud, it was proposed to use the modules – ferric iron-alumina module (Fe₂O₃/Al₂O₃) and calcium-silicate (CaO/SiO₂) module (Table 5).

Then the multicomponent chemical compositions of the studied mixtures (Table 5) were recalculated to the three-component composition CaO – Al₂O₃ – SiO₂, Fe₂O₃ – Al₂O₃ – SiO₂, and FeO – Al₂O₃ – SiO₂ according to the Richter's law of chemical equivalents [45]. For this, the three most important oxides are selected, then all oxides from the chemical composition of the studied raw materials are divided into three groups: first group – oxides of alkali and alkaline-earth metals (CaO, MgO, Na₂O, K₂O, etc.), second group – oxides of amphoteric metals (Al₂O₃, Fe₂O₃, etc.), third group – acid oxides (SiO₂, TiO₂, etc.). Within each group, the content of oxides is recalculated to the content of the most important oxide equivalent to their molecular weights. For recalculation, transition coefficients are used, derived on the basis of the Richter's law, which states that flux oxides affect the temperature according to their equivalent masses, i.e., molecular masses related to the number of cations in the formula [45].

The representative points of the calculated three-component chemical compositions of the studied mixtures were plotted on state diagrams and systems (Fig. 7); melting profiles were determined (Fig. 8).



* The isothermal sections of the liquidus surface are given in Kelvin degrees [43]

Figure 7. Location of studied compositions of the fly ash with red mud additions in the CaO – Al₂O₃ – SiO₂ (A), FeO – Al₂O₃ – SiO₂ (B) and Fe₂O₃ – Al₂O₃ – SiO₂, (C) systems.

To calculate the amount of melt formed in the test mixtures upon heating, it is necessary to determine, firstly, in which triangle the point of the mixture is located, and in the crystallization field of which compound the representative point of the mixture is placed. Secondly, it is necessary to build the crystallization path of the mixture composition with decreasing temperature and to calculate the amount melt according to the lever rule. Thus, if one phase decomposes into two, then the amount of substance of the resulting phases is inversely proportional to the straight line segments from the point of composition of the initial phase to the points of composition of the phases obtained [35].

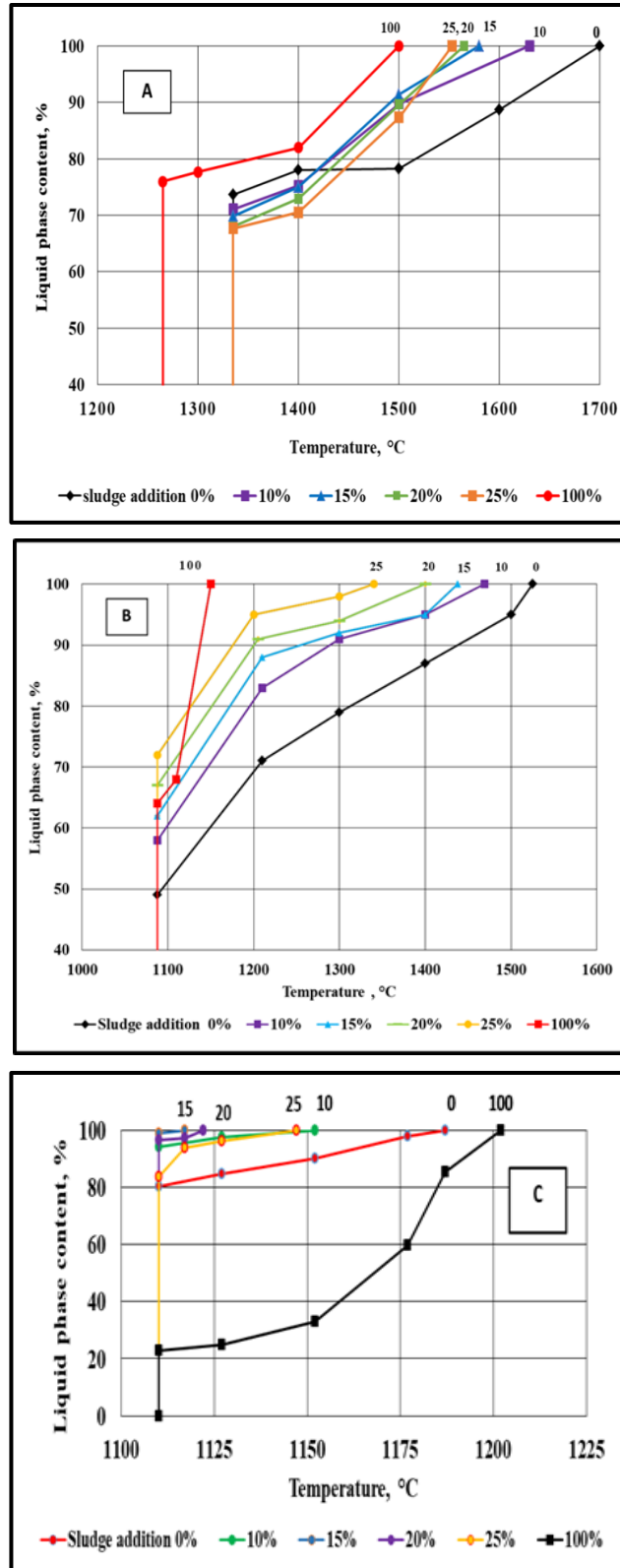


Figure 8. Melting curves of fly ash mixtures with the addition of red mud in the CaO-Al₂O₃-SiO₂ (A), FeO-Al₂O₃-SiO₂ (B) and Fe₂O₃-Al₂O₃-SiO₂, (C) systems.

After plotting the melting profiles along the crystallization path at different temperatures, the main characteristics of the melts formed in the studied compositions upon heating were determined (Table 6–8).

Table 6. Chemical compositions and characteristics of the study mixtures in the CaO – Al₂O₃ – SiO₂ system.

Mixture code	Oxide content, wt.%,			Characteristics of the eutectic phase			Complete melting temperature, °C
	SiO ₂	Al ₂ O ₃	CaO	Temperature, °C	Eutectic melt content, %	Crystalline phase content, %	
FA ₁₀₀	51.35	38.47	10.19	1335	74	26	1700
RM ₁₀₀	32.74	26.64	40.62	1265	76	24	1500
FA ₉₀ RM ₁₀	49.56	37.33	13.11	1335	71	29	1667
FA ₈₅ RM ₁₅	48.66	36.76	14.58	1335	70	30	1580
FA ₈₀ RM ₂₀	47.76	36.19	16.06	1335	68	32	1565
FA ₇₅ RM ₂₅	46.85	35.61	17.54	1335	68	32	1553

Characteristics of the resulting melts in (RM100) is the component of the ternary eutectic with the lowest temperature (1265 °C). Therefore, in the compositions of the studied ceramic masses, it should be the first to melt and to promote sintering of fly ash based samples (FA₁₀₀), which is a component of the ternary eutectic with a temperature of 1335 °C. However, as it was found, the addition of 10 to 25 % of red mud to the fly ash not only does not reduce the temperature of the appearance of eutectic melts, but even increases the total content of the crystalline phase at temperatures up to 1400 °C (Fig. 9).

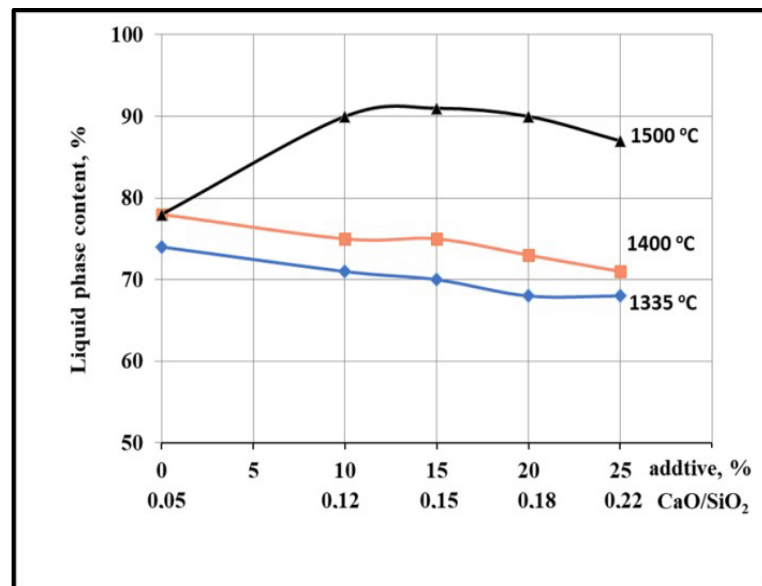


Figure 9. Influence of the composition of fly ash with red mud additives (10–25 %) mixtures on the formation of a melt during heating in the CaO – Al₂O₃ – SiO₂ system.

Thus, the calcium silicate module can be associated with the formation of a crystalline part during firing of the fly ash and red mud mixtures used.

A theoretical consideration of the behavior of the studied compositions upon heating in the ternary systems with iron oxides FeO – Al₂O₃ – SiO₂ and Fe₂O₃ – Al₂O₃ – SiO₂, indicates that the appearance of eutectic melt during heating of all compositions occurs at the same temperature of 1088 °C (in FeO – Al₂O₃ – SiO₂ system) and at 1110 °C (in Fe₂O₃ – Al₂O₃ – SiO₂, system), regardless of the presence of red mud additives in the fly ash (Table 7, 8).

Table 7. Chemical compositions and characteristics of the study mixtures in the FeO – Al₂O₃ – SiO₂ system.

Mixture code	Oxide content, wt. %			Characteristics of the eutectic phase			Complete melting temperature, °C
	SiO ₂	Al ₂ O ₃	FeO	Temperature, °C	Eutectic melt content, %	Crystalline phase content, %	
FA ₁₀₀	48.34	28.64	23.02	1088	49	51	1525
RM ₁₀₀	27.71	9.12	63.17	1088	64	36	1150
FA ₉₀ RM ₁₀	46.16	26.58	27.26	1088	58	42	1469
FA ₈₅ RM ₁₅	45.08	25.56	29.36	1088	62	38	1438
FA ₈₀ RM ₂₀	44.01	24.54	31.45	1088	67	33	1400
FA ₇₅ RM ₂₅	42.94	23.53	33.53	1088	72	28	1340

Table 8. Chemical compositions and characteristics of the study mixtures in the Fe₂O₃ – Al₂O₃ – SiO₂, system.

Mixture code	Oxide content. wt. %			Characteristics of the eutectic phase			Complete melting temperature, °C
	SiO ₂	Al ₂ O ₃	Fe ₂ O ₃	Temperature, °C	Eutectic melt content, %	Crystalline phase content, %	
FA ₁₀₀	41.64	24.67	33.69	1110	80	20	1187
RM ₁₀₀	17.79	5.85	76.35	1110	23	77	1202
FA ₉₀ RM ₁₀	38.38	22.09	39.53	1110	94	6	1152
FA ₈₅ RM ₁₅	36.85	20.89	42.27	1110	95	5	1117
FA ₈₀ RM ₂₀	35.37	19.72	44.90	1110	96	4	1122
FA ₇₅ RM ₂₅	33.96	18.61	47.44	1110	84	16	1147

We compared the data obtained on the effect of iron oxides on the processes during heating in the studied mixtures of fly ash with red mud additives. It indicates the fluxing effect of both types of iron oxides introduced with red mud, regardless of their form – ferric (Fe₂O₃) or ferrous iron (FeO). At the same time, ferric iron has a more active effect in these mixtures than ferrous iron.

It was established that the addition of 10 to 25 % bauxite sludge into the initial aluminosilicate fly ash with its own high content of iron oxide impurities (Table 1) provides an increase in the content of the eutectic melt on average from 9 % to 23 % depending on the composition of the mixture. In addition, a comparative analysis of the melting curves (Fig. 8, B, C) indicates that, in order to ensure liquid-phase sintering of the samples from the compositions under consideration, it is necessary to use a firing temperature below 1100 °C. The continuous increase in the amount of melt in the entire range of temperatures under consideration up to complete melting (Fig. 10) is due to the fluxing effect of iron oxides introduced with high-iron red mud on the formation of a liquid phase when such compositions are heated.

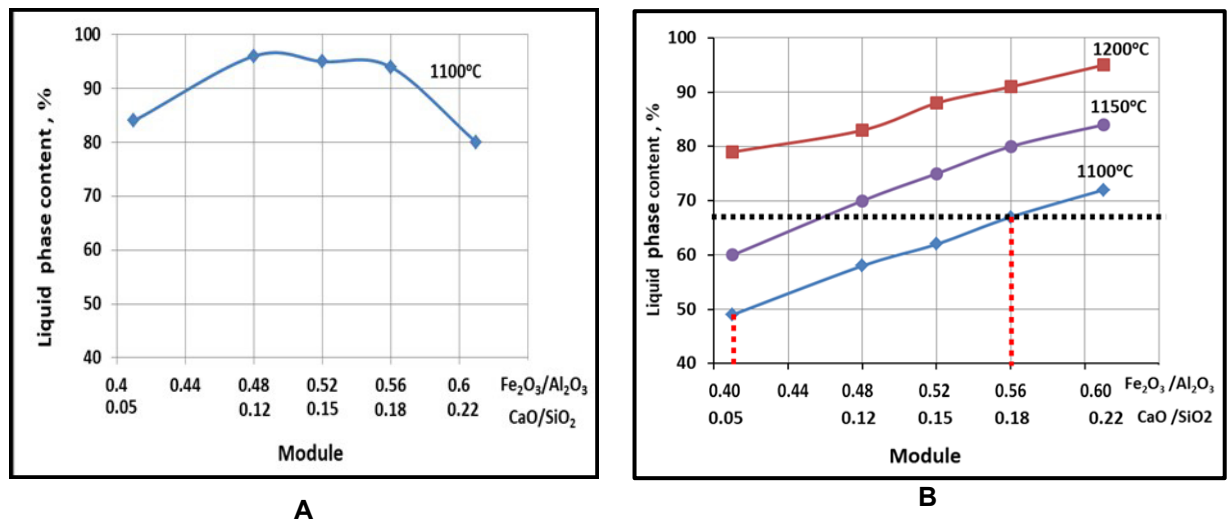


Figure 10. Influence of the composition of fly ash with red mud additives (10–25 %) mixtures on the formation of a melt during heating in Fe₂O₃ – Al₂O₃ – SiO₂, (A) and FeO – Al₂O₃ – SiO₂ (B) systems.

Thus, the predictive analysis of the behavior of fly ash compositions with the addition of bauxite sludge in CaO – Al₂O₃ – SiO₂, FeO – Al₂O₃ – SiO₂ and Fe₂O₃ – Al₂O₃ – SiO₂, systems allowed us to:

- identify the fluxing effect of red mud additives on the fly ash under study;
- determine the optimal firing temperatures for the samples from the analyzed compositions – 1100 °C, at which no more than 65–68 % melt is formed in the samples. An increase of temperature above 1100 °C will theoretically cause the phenomena of melting and deformation of products under the weight of their own mass.
- ensure densely sintered mullite-anorthite ceramics; the raw mixtures of aluminosilicate fly ash with red mud should have a composition with Fe₂O₃/Al₂O₃ module equal to 0.4–0.56 and CaO/SiO₂ module equal to 0.07–0.18.

3.3. The effect of red mud additives on the sample sintering from fly ash by semi-dry pressing

It was established that at firing temperatures of 1100–1200 °C the samples of semi-dry pressing from fly ash without additives (FA₁₀₀) are characterized by high porosity (with water absorption of 19–26 %) and low compressive strength (from 3 to 37.9 MPa) depending on the firing temperature (Fig. 11).

The introduction of the red mud additives activates the sintering of samples at 1150–1200 °C: water absorption decreases from 26 % in the case of fly ash sample without additive (FA₁₀₀) to 22 % in the case of samples from fly ash mixture with 10 % red mud additive (FA₉₀RM₁₀), while the compressive strength increases from 3 to 20 MPa. Higher temperature heating up to 1200 °C ensures the preservation of the general indicated trend.

Further increase in the content of red mud from 10 to 15 % in mixtures (FA₈₅RM₁₅) activates the process of sintering and hardening of samples even more, providing a decrease in the water absorption of samples from 26 to 2 % and an increase in compressive strength from 3 to 170 MPa at a temperature of 1200 °C.

Thus, when designing the compositions of ceramic masses for the production of high-strength ceramics, it is necessary to focus on the established criteria for activating the sintering process of compositions of aluminosilicate fly ash with red mud additives: the composition of the mixture (according to the value of ferric iron-alumina Fe₂O₃/Al₂O₃ and calcium silicate CaO/SiO₂ modules) and the optimal firing temperature of the samples (Fig. 12).

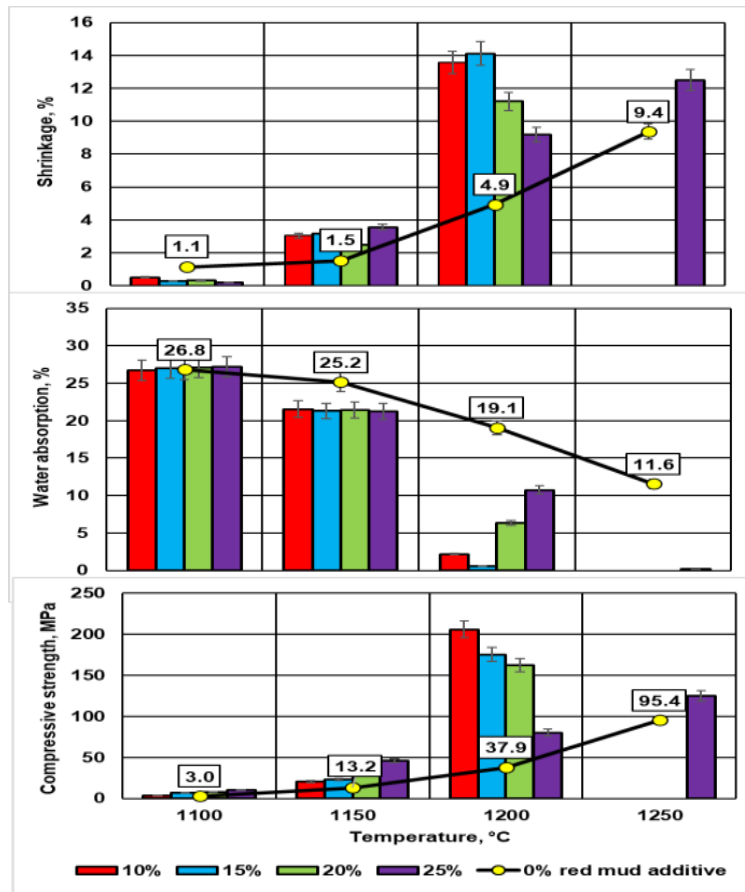


Figure 11. Influence of red mud additive (10–25 % wt.) on the physical and mechanical properties of samples of semi-dry pressing from fly ash, fired at 1100–1250 °C.

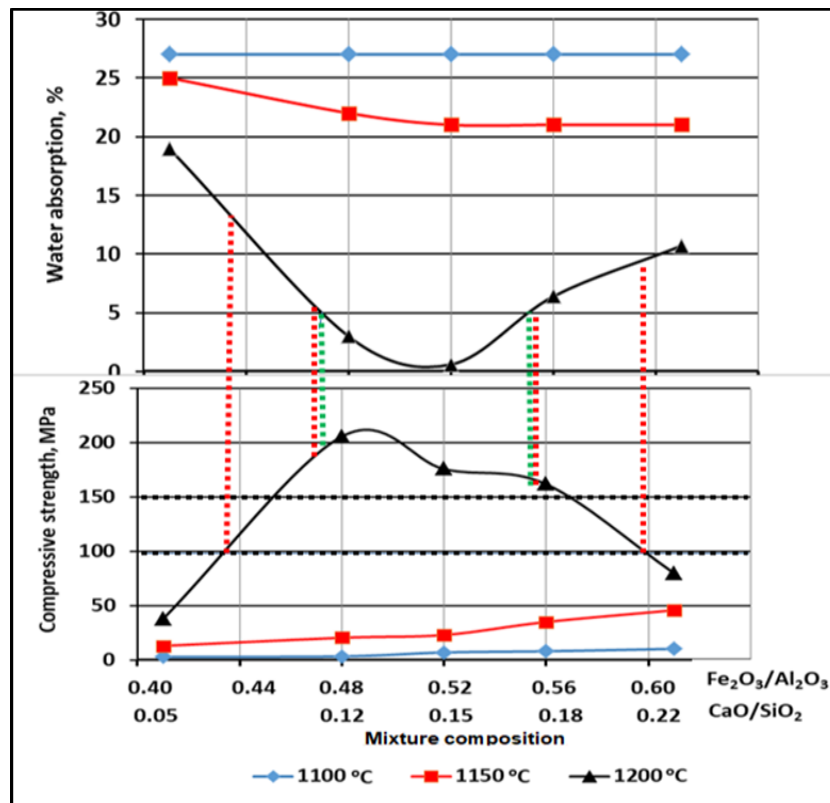


Figure 12. Influence of the composition of fly ash with red mud mixtures on the physical and mechanical properties of samples fired at 1100–1200 °C: (green dotted lines indicate the range of mixture compositions for densely sintered ceramics, red dotted lines – for porous ceramics)

For example, to obtain sintered ceramics (with water absorption less than 5 %) with a compressive strength of at least 150 MPa, it is necessary to use mixtures with $\text{Fe}_2\text{O}_3/\text{Al}_2\text{O}_3$ module equal to 0.47–0.55 and CaO/SiO_2 module equal to 0.11–0.17, and firing of the samples is carried out at a temperature of 1200 °C (green dotted line). To obtain porous ceramics at 1200 °C (with water absorption of more than 5 %) with a compressive strength of more than 100 MPa, it is necessary to use mixtures of two types: 1) with $\text{Fe}_2\text{O}_3/\text{Al}_2\text{O}_3$ module equal to 0.43–0.47, CaO/SiO_2 module equal to 0.08–0.11 and 2) with $\text{Fe}_2\text{O}_3/\text{Al}_2\text{O}_3$ module equal to 0.55–0.60, CaO/SiO_2 module equal to 0.17–0.22 (red dotted line).

The explanation for the processes of formation of these technological properties should be sought in the physical and chemical processes that occur during the firing of these compositions. For this, the phase composition of the investigated mixtures after their heat treatment was studied by the X-ray method.

The obtained X-ray diffraction patterns indicate that, depending on the composition of the fly ash and red mud mixtures and the temperature regime of firing, the main crystalline phases are mullite, anorthite and cristobalite.

It was found that in the absence of red mud additions, the fly ash heating at temperatures of 1100–1200 °C had practically no effect on quantitative changes in the content of the minerals that make up the fly ash. However, in the presence of 10–20 % red mud additives, a decrease in the intensity of mullite and cristobalite X-ray reflections and a significant increase in anorthite reflections are observed, regardless of the firing temperature (Fig. 13).

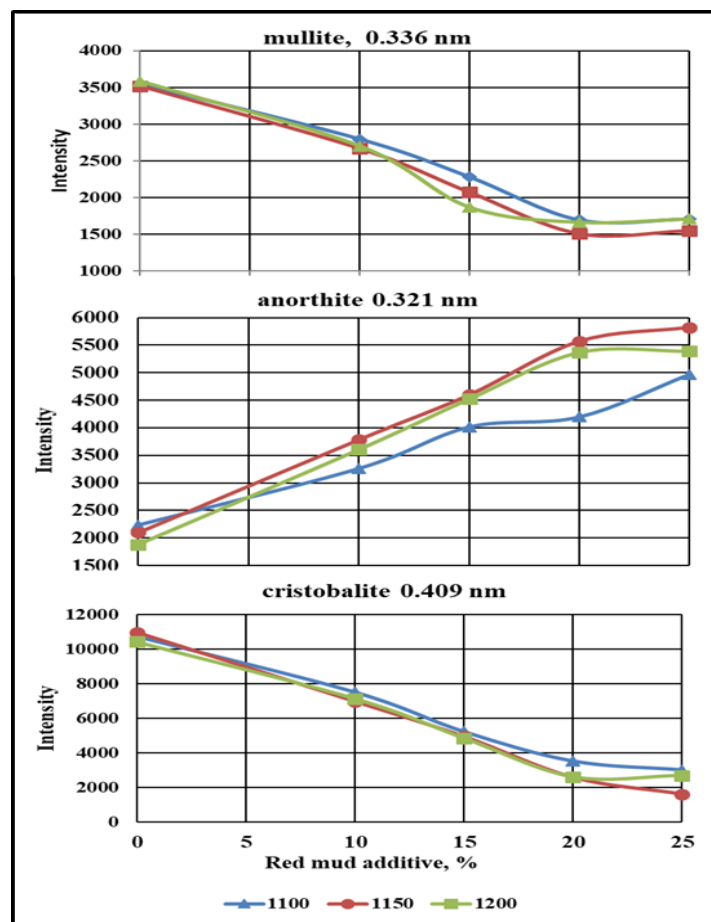


Figure 13. Influence of the red mud additives (10–25 %) on the formation of the phase composition of samples from fly ash fired at 1100–1200 °C.

An increase in the intensity of anorthite X-ray reflections in fired samples from fly ash – red mud mixtures up to 2.5–3 times (depending on the content of the additive and the firing temperature) while reducing the content of mullite up to 2 times and cristobalite – up to 2 times is associated with solid-phase synthesis of anorthite at temperatures 1100–1200 °C according to the reaction:



mullite *cristobalite* *anorthite*

Thus, the resulting product made from researched compositions of fly ash with bauxite sludge are anorthite ceramics. The CaO/SiO_2 module equal to 0.12–0.22 is responsible for the formation of the crystalline phase (anorthite) during the firing of samples from a mixture of fly ash with red mud additives.

The formation of anorthite in samples from mixtures of clay with red mud at a temperature of 1000–1100 °C was recorded in [46].

Recently, a few studies have investigated the effect of the CaO/SiO_2 ratio on the phase crystallization and properties of sintered materials based on anorthite. Overall, these studies have been focusing on the use of industrial wastes combined with natural resources [47, 48]. Tabit et al. [49] found that an increase in the CaO/SiO_2 ratio from 0.12–0.8 in mixtures of coal fly ash and ladle furnace slag promoted crystallization of anorthite as the main phase which is consistent with the results obtained in this study.

The studies carried out make it possible to determine the optimal compositions and technological modes for obtaining ceramics based on the studied raw materials in comparison with the properties of ash samples without the addition of red mud FA₁₀₀ (Table 8).

Table 8. Optimum compositions, technological conditions and properties of ceramics based on fly ash with the studied red mud.

Composition code	Component composition, %		Temperature, °C			Ceramic properties		
	fly ash	red mud	calcination of raw materials		firing of samples	shrinkage %	water absorption, %	compressive strength, MPa
			fly ash	red mud				
FA ₁₀₀	100	0	1200	–	1250	9.4	11.6	95.4
FA ₉₀ RM ₁₀	90	10				13.6	2.2	206.2
FA ₈₅ RM ₁₅	85	15	1200	1000	1200	14.1	0.6	175.5
FA ₈₀ RM ₂₀	80	20				11.2	6.4	162.4

The previously stated hypothesis about the fluxing effect of bauxite sludge additives on the sintering of the fly ash based samples was confirmed by a change in the physical and mechanical properties of samples from these compositions, as well as by electron microscopy (Fig. 14).

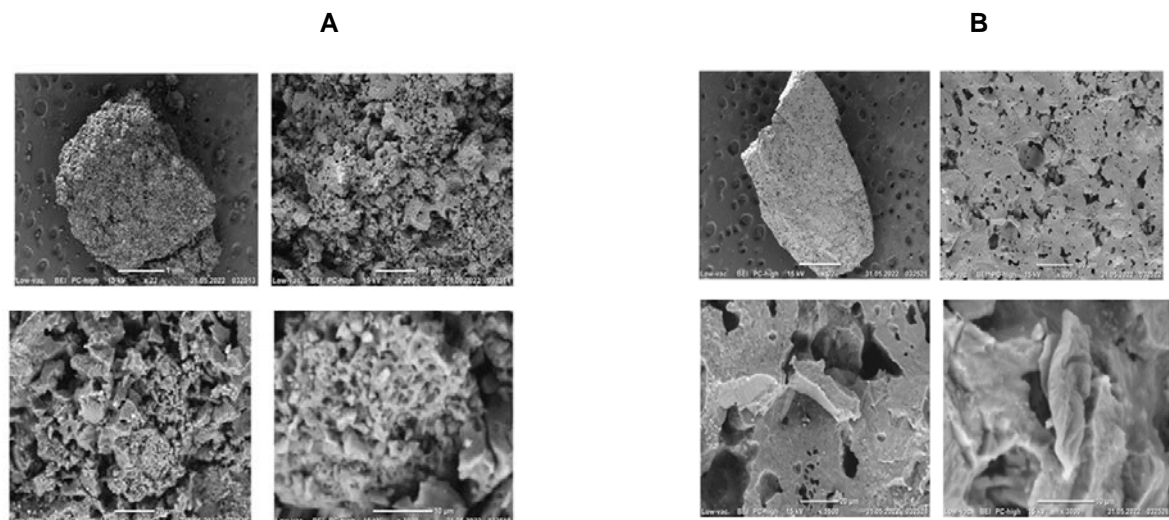


Figure 14. Electron micrographs of semi-dry pressed samples, fired at 1200 °C, from ash without red mud (A) and with addition of 10% red mud (B).

In particular, microscopic images of calcined fly ash without red mud additives show that the sample is a loosely sintered material consisting of individual finely porous aggregates separated from each other by deep winding pores. The introduction of red mud additive in an amount of 10 % sharply activates the process of liquid-phase sintering of samples from fly ash due to red mud melting [50, 51] at 1150 °C, which leads to the formation of a monolithic structure with internal pores approaching a sphere in shape.

4. Conclusion

The following results were obtained upon the completed experimental studies:

1. The chemical composition, mineralogical (phase) composition, structural features of the initial technogenic raw materials and their changes during heating were established. The studied fly ash was a variety of aluminosilicate fly ash with a low content of calcium oxide (2.26 % CaO) and a high content of aluminum oxide (29.19 % Al₂O₃) and iron oxide (12.11 % Fe₂O₃). The content of residual fuel was not more than 2.5 %, the crystalline part of which was composed of mullite, quartz and ferruginous mineral in the form of hematite, with a full sintering temperature (up to water absorption of not more than 5 %) above 1300 °C. Bauxite sludge (red mud) in terms of chemical composition was represented mainly by oxides of silica (21.03 % SiO₂), calcium (23.46 % CaO), iron (17.27 % Fe₂O₃) and aluminum (7.47 % Al₂O₃). In terms of mineralogical composition, it was composed of calcite, hydrated calcium silicates and aluminates, hematite and magnetite, fully sintered at 1100 °C.

2. Theoretical analysis of the behavior of ash compositions with the addition of bauxite sludge (10–25 %) made it possible to reveal the fluxing effect of bauxite sludge additions to the studied fly ash. To determine the optimal firing temperatures for samples from the analyzed compositions (1100–1150 °C), to ensure a densely sintered mullite-anorthite ceramics, the raw mixtures of aluminosilicate fly ash with red mud should have a composition with Fe₂O₃/Al₂O₃ module equal to 0.4–0.54 and CaO/SiO₂ module equal to 0.07–0.17.

3. Theoretical predictions were confirmed by experimental studies. We proved that the resulting ceramics from the investigated compositions of fly ash with bauxite sludge (10–25 %) were mullite-anorthite ceramics. High compressive strength (up to 210 MPa) of the samples from the recommended compositions of fly ash with 10–20 % red mud are promising for further testing in the technology of densely sintered wear-resistant ceramic materials (building clinker ceramics, ceramic proppants and others) with water absorption of 0.5–2 %, and compressive strength up to 175–200 MPa.

References

1. Archambo, M., Kawatra, S.K. Red Mud: Fundamentals and new avenues for utilization. *Mineral Processing and Extractive Metallurgy Review*. 2021. 42(7). Pp. 427–450. DOI: 10.1080/08827508.2020.1781109
2. Li, R., Zhang, T., Liu, Y., Li, G., Xie, L. Calcification–carbonation method for red mud processing. *Journal of Hazardous Materials*. 2016. 316. Pp. 94–101. DOI: 10.1016/j.jhazmat.2016.04.072
3. Liu, S., Guan, X., Zhang, S., Dou, Z., Feng, C., Zhang, H., Luo, S. Sintered bayer red mud based ceramic bricks: Microstructure evolution and alkalis immobilization mechanism. *Ceramics International*. 2017. 43(15). Pp. 13004–13008. DOI: 10.1016/j.ceramint.2017.07.036
4. Hou, L., Liu, T., Lu, A. Red mud and fly ash-based ceramic foams using starch and manganese dioxide as foaming agent. *Transactions of Nonferrous Metals Society of China*. 2017. 27(3). Pp. 591–598. DOI: 10.1016/S1003-6326(17)60066-9
5. Paramguru, R.K., Rath, P.C., Misra, V.N. Trends in red mud utilization – a review. *Mineral Processing and Extractive Metallurgy Review*. 2006. 26(1). Pp. 1–29. DOI: 10.1080/08827500490477603
6. Kavas, T. Use of boron waste as a fluxing agent in production of red mud brick. *Building and Environment*. 2006. 41(12). Pp. 1779–1783. DOI: 10.1016/j.buildenv.2005.07.019
7. Lopesa, D.V., Durana, E., Cesconeto, F.R., Almeida, P.V., Kovalevsky, A.V., Quina, M.J., Frade, J.R. Direct processing of cellular ceramics from a single red mud precursor. *Ceramics International*. 2020. 46(10) Pp. 16700–16707. DOI: 10.1016/j.ceramint.2020.03.244
8. Muraleedharan, M., Nadir, Y. Factors affecting the mechanical properties and microstructure of geopolymers from red mud and granite waste powder: A review. *Ceramics International*. 2021. 47(10). Pp. 13257–13279. DOI: 10.1016/j.ceramint.2021.02.009
9. Xia, F., Cui, S., Pu, X. Performance study of foam ceramics prepared by direct foaming method using red mud and K-feldspar washed waste. *Ceramics International*. 2022. 48(4). Pp. 5197–5203. DOI: 10.1016/j.ceramint.2021.11.059
10. Alekseev, K., Mymrin, V., Avanci, M. A., Klitzke, W., Magalhães, W. L.E., Silva, P.R., Catai, R.E., Silva, D.A., Ferraz, F.A. Environmentally clean construction materials from hazardous bauxite waste red mud and spent foundry sand. *Construction and Building Materials*. 2019. 116860. DOI: 10.1016/j.conbuildmat.2019.116860
11. Sglavo, V.M., Camprostrini, R., Maurina, S., Carturan, G., Monagheddu, M., Budroni, G., Cocco, G. Bauxite 'red mud' in the ceramic industry. Part 1: thermal behavior. *Journal of the European Ceramic Society*. 2000. 20(3). Pp. 235–244. DOI: 10.1016/S0955-2219(99)00088-6
12. Sglavo, V.M., Maurina, S., Conci, A., Salviati, A., Carturan, G., Cocco, G. Bauxite 'red mud' in the ceramic industry. Part 2: production of clay-based ceramics. *Journal of the European Ceramic Society*. 2000. 20(3). Pp. 245–252. DOI: 10.1016/S0955-2219(99)00156-9
13. Yao, Z.T., Ji, X.S., Sarker, P.K., Tang, J.H., Ge, L.Q., Xia, M.S., Xi, Y.Q. A comprehensive review on the applications of coal fly ash. *Earth-Science Reviews*. 2015. 141. Pp. 105–121. DOI: 10.1016/j.earscirev.2014.11.016
14. Blissett, R.S., Rowson, N.A. A review of the multi-component utilization of coal fly ash. *Fuel*. 2012. 97. Pp. 1–23. DOI: 10.1016/j.fuel.2012.03.024
15. Ma, B., Qi, M., Peng, J., Li, Z. The compositions, surface texture, absorption, and binding properties of fly ash in China. *Environment International*. 1999. 25(4). Pp. 423–432 DOI: 10.1016/S0160-4120(99)00010-0
16. Vassilev, S.V., Vassileva, C.G. Geochemistry of coals, coal ashes and combustion wastes from coal-fired power stations. *Fuel Processing Technology*. 1997. 51. Pp. 19–45. DOI: 10.1016/S0378-3820(96)01082-X

17. Vassilev, S.V., Menendez, R., Alvarez, D., Dias-Somoano, M., Martinez-Tarazona, M.R. Phase-mineral and chemical composition of coal fly ashes as a basis for their multicomponent utilization. 1. Characterization of feed coals and fly ashes. *Fuel*. 2003. 82(14). Pp. 1793–1811. DOI: 10.1016/S0016-2361(03)00123-6
18. Leiva, C., Rodriguez-Galán, M., Arenas, C., Alonso-Fariñas, B., Peceño, B. A mechanical, leaching and radiological assessment of fired bricks with a high content of fly ash. *Ceramics International*. 2018. 44(11). Pp. 13313–13319. DOI: 10.1016/j.ceramint.2018.04.162
19. Mi, H., Yi, L., Wu, Q., Xia, J., Zhang, B. Preparation of high-strength ceramsite from red mud, fly ash, and bentonite. *Ceramics International*. 2021. 47(13). Pp. 18218–18229. DOI: 10.1016/j.ceramint.2021.03.141
20. Horiuchi, S., Kawaguchi, M., Yasuhara, K. Effective use of fly ash slurry as fill material. *Journal of Hazardous Materials*. 2000. 76(2–3). Pp. 301–337. DOI: 10.1016/S0304-3894(00)00205-3
21. Vakalova, T.V., Khabas, T.A., Revva, I.B., Pavlova, I.A. Heat-insulating ceramics which have a nanoporous structure and are made with the use of ash-bearing wastes from power plants. *Refractories and Industrial Ceramic*. 2015. 55. Pp. 505–510. DOI: 10.1007/s11148-015-9754-z
22. Vakalova, T.V., Revva, I.B. Highly porous building ceramics based on «clay-ash microspheres» and «zeolite-ash microspheres» mixtures. *Construction and Building Materials*. 2022. 317. 125922. DOI: 10.1016/j.conbuildmat.2021.125922
23. Vereshchagin, V.I., Pogrebenkov, V.M., Vakalova, T.V. Utilization of natural and technogenous raw materials of Siberian region in production of the building ceramics and thermal insulating materials. *Stroitel'nye Materials*. 2004. 2. Pp. 28–32. View Record in Scopus Google Scholar.
24. Park, Y.M., Yang, T.Y., Yoon, S.Y., Stevens, R., Park, H.C. Mullite whiskers derived from coal fly ash. *Materials Science and Engineering: A*. 2007. 454–455. Pp. 518–522. DOI: 10.1016/j.msea.2006.11.114
25. Wu, X., Huo, Z., Ren, Q., Li, H., Lin, F., Wei, T. Preparation and characterization of ceramic proppants with low density and high strength using fly ash. *Journal of Alloys and Compounds*. 2017. 702. Pp. 442–448. DOI: 10.1016/j.jallcom.2017.01.262
26. Ma, B.Y., Su, C., Ren, X., Gao, Z., Qian, F., Yang, W., Liu, G., Li, H., Yu, J., Zhu, Q. Preparation and properties of porous mullite ceramics with high-closed porosity and high strength from fly ash via reaction synthesis process. *Journal of Alloys and Compounds*. 2019. 803. Pp. 981–991. DOI: 10.1016/j.jallcom.2019.06.272
27. Lin, B., Li, S., Hou, X., Li, H. Preparation of high performance mullite ceramics from high-aluminum fly ash by an effective method. *Journal of Alloys and Compounds*. 2015. 623. Pp. 359–361. DOI: 10.1016/j.jallcom.2014.11.023
28. He, Y., Cheng, W., Cai, H. Characterization of α -cordierite glass-ceramics from fly ash. *Journal of Hazardous Materials*. 2005. 120 (1–3). Pp. 265–269. DOI: 10.1016/j.jhazmat.2004.10.028
29. Hui, T., Sun, H.J., Peng T.J. Preparation and characterization of cordierite-based ceramic foams with permeable property from asbestos tailings and coal fly ash. *Journal of Alloys and Compounds*. 2021. 885. 160967. DOI: 10.1016/j.jallcom.2021.160967
30. Zong, Y., Wan, Q., Cang, D. Preparation of anorthite-based porous ceramics using high-alumina fly ash microbeads and steel slag. *Ceramics International*. 2019. 45(17). Pp. 22445–22451. DOI: 10.1016/j.ceramint.2019.08.003
31. Tabit, K., Hajjou, H., Waqif, M., Saâdi, L. Effect of CaO/SiO₂ ratio on phase transformation and properties of anorthite-based ceramics from coal fly ash and steel slag. *Ceramics International*. 2020. 46(6). Pp. 7550–7558. DOI: 10.1016/j.ceramint.2019.11.254
32. Ma, B.Y., Ren, X., Yin, Y., Yuan, L., Zhang, Z., Li, Z., Li, G., Zhu, Q., Yu, J. Effects of processing parameters and rare earths additions on preparation of Al₂O₃-SiC composite powders from coal ash. *Ceramics International*. 2017. 43(15). Pp. 11830–11837. DOI: 10.1016/j.ceramint.2017.05.362
33. Ma, B.Y., Li, Y., Cui, S.G., Zhai, Y.C. Preparation and sintering properties of zirconia–mullite–corundum composites using fly ash and zircon. *Transactions of Nonferrous Metals Society of China*. 2010. 20(12). Pp. 2331–2335. DOI: 10.1016/S1003-6326(10)60650-4
34. Shih, W.H., Chang, H.L. Conversion of fly ash into zeolites for ion-exchange applications. *Materials Letters*. 1996. 28 (4–6). Pp. 263–268. DOI: 10.1016/0167-577X(96)00064-X
35. Kingery, W.D., Bowen, H.K., Uhlmann, D.N. *Introduction to Ceramics*. John Wiley & Sons, Inc. 1976. 1032 p.
36. Kaya, C., Butler, E.G., Selcuk, A., Boccaccini, A.R., Lewis, M.H. Mullite (NextelTM720) fibre-reinforced mullite matrix composites exhibiting favourable thermomechanical properties. *Journal of the European Ceramic Society*. 2002. 22. Pp. 2333–2342. DOI: 10.1016/S0955-2219(01)00531-3
37. Chen, X., Li, T., Ren, Q., Wu, X., Li, H., Dang, A., Zhao, Z., Shang, Y., Zhang, Y. Mullite whisker network reinforced ceramic with high strength and lightweight. *Journal of Alloys and Compounds*. 2017. 700. Pp. 37–42.
38. German, R.M., Suri, P., Park, S.J. Review: liquid phase sintering. *Journal of Materials Science*. 2009. 44. Pp 1–39. DOI: 10.1007/s10853-008-3008-0
39. Vakalova, T.V., Reshetova, A.A., Revva, I.B., Rusinov, P.G., Balamygin, D.I. Effect of thermochemical activation of clay raw materials on phase formation, microstructure and properties of aluminosilicate proppants. *Applied Clay Science*. 2019. 183. 105335. DOI: 10.1016/j.clay.2019.105335
40. Pontikes, Y., Rathossi, C., Nikolopoulos, P., Angelopoulos, G.N., Jayaseelan, D.D., Lee, W.E. Effect of firing temperature and atmosphere on sintering of ceramics made from Bayer process bauxite residue. *Ceramics International*. 2009. 35 (1). Pp. 401–407. DOI: 10.1016/j.ceramint.2007.11.013
41. Toropov, N.A., Barzakovsky, V.P. et al. Diagrams of state of silicate systems (In Russian). 1972. 448 p.
42. Decterov, S.A., Kang, Y.B., Jung, I.H. Thermodynamic Database for the Al-Ca-Co-Cr-Fe-Mg-Mn-Ni-Si-O-P-S System and Applications in Ferrous Process Metallurgy. *Journal of Phase Equilibria and Diffusion*. 2009. 30 (5). Pp. 443–461. DOI: 10.1007/s11669-009-9569-z
43. Prostavka, V., Shishin, D., Shevchenko, M., Jak, E. Thermodynamic optimization of the Al₂O₃-FeO-Fe₂O₃-SiO₂ oxide system. *Calphad*. 2019. 67. DOI: 10.1016/j.calphad.2019.101680
44. Jak, E., Decterov, S., Pelton, A.D., Happ, J., Hayes, P.C.: in: R.P.Gupta, T.F.Wall, L.Baxter (Eds.) Thermodynamic modelling of the system Al₂O₃-SiO₂-CaO-FeO-Fe₂O₃ to characterise coal ash slags, *The Impact of Mineral Impurities in Solid Fuel Combustion*. Kluwer Academic/Plenum Publishers, New York, N.Y., USA, 1999. 723. DOI: 10.1007/0-306-46920-0_55
45. Zemlyanoy, K.G., Pavlova, I.A. Phase equilibria in oxide systems (In Russian). 2021. 228 p.

46. Pérez-Villarejo, L., Corpas-Iglesias, F.A., Martínez-Martínez, S., Artiaga, R., Pascual-Cosp, J. Manufacturing new ceramic materials from clay and red mud derived. *Construction and Building Materials*. 2012. 35. Pp 656–665. DOI: 10.1016/j.conbuildmat.2012.04.133
47. Li, B.W., Chen, H., Zhao, M., Zhang, X.F., Du, Y.S., Deng, L.B. Effect of CaO/SiO₂ ratio and TiO₂ on glass-ceramics made from steel slag and fly ash. *Applied Mechanics and Materials*. 2012. 217–219. Pp. 119–123. DOI:10.4028/www.scientific.net/AM
48. Yang, Z., Lin, Q., Lu, S., He, Y., Liao, G., Ke, Y. Effect of CaO/SiO₂ ratio on the preparation and crystallization of glass-ceramics from copper slag. *Ceramics International*. 2014. 40. Pp. 7297–7305. DOI: 10.1016/j.ceramint.2013.12.071
49. Tabit, K., Hajjou, H., Waqif, M., Saâdi, L. Effect of CaO/SiO₂ ratio on phase transformation and properties of anorthite-based ceramics from coal fly ash and steel slag. *Ceramics International*. 2020. 46(6). Pp. 7550–7558. DOI: 10.1016/j.ceramint.2019.11.254
50. Pei, D., Li, Y., Cang, D. In situ XRD study on sintering mechanism of SiO₂-Al₂O₃-CaO-MgO ceramics from red mud. *Materials Letters*. 2019. 240. Pp. 229–232. DOI: 10.1016/j.matlet.2019.01.019
51. Ren, Y., Ren, Q., Wu, X., Zheng, J., Hai, O. Mechanism of low temperature sintered high-strength ferric-rich ceramics using bauxite tailings. *Materials Chemistry and Physics*. 2019. 238. Pp. 121929. DOI: 10.1016/j.matchemphys.2019.121929

Information about authors:

Tatiana Vakalova, Doctor of Technical Sciences

ORCID: <https://orcid.org/0000-0002-1756-3526>

E-mail: tvv@tpu.ru

Nikolay Sergeev,

ORCID: <https://orcid.org/0000-0002-7656-5628>

E-mail: axioma-13@yandex.ru

Dias Tolegenov,

ORCID: <https://orcid.org/0000-0001-8242-0655>

E-mail: www.dika-92@mail.ru

Diana Tolegenova,

E-mail: diana_donj@mail.ru

Received 01.11.2022. Approved after reviewing 22.05.2023. Accepted 27.05.2023.



Research article

UDC 69.04

DOI: 10.34910/MCE.121.5



Triangular prism finite element based on piecewise constant stress approximations

Yu. Ya. Tyukalov 

Vyatka State University, Kirov, Russian Federation

 yutvgu@mail.ru

Keywords: finite element method, stress approximation, triangular prism, piecewise constant stresses, possible displacements, plates, beams

Abstract. The study object is a three-dimensional triangular prism finite element based on piecewise constant approximations of stresses. The use of such a finite element makes it possible to obtain more accurate stress values, especially at the boundaries of the region and in the stress concentration zones. The solution of the volume theory elasticity problem was obtained on the basis of the additional energy functional and the possible displacements principle. With the help of the possible displacement principle, algebraic equilibrium equations of finite element grid nodes are formed. The resulting equilibrium equations sum up with the additional energy of the system using the Lagrange multiplier method. In this case, the stresses are determined directly at the nodal points, and not at the finite element centers. The stress fields are continuous along finite element boundaries and discontinuous inside them. The paper shows that the displacements obtained by the proposed method, when refining the finite elements mesh, tend to exact values from above. As a test, the article provides calculations for bending plates and beams. As the test problems solutions showed, the proposed finite elements allow obtaining more accurate stress values compared to traditional finite elements based on stress approximation. Comparison of the stresses obtained by the proposed method with analytical solutions shows the high accuracy of the proposed method.

Citation: Tyukalov, Yu.Ya. Triangular prism finite element based on piecewise constant stress approximations. Magazine of Civil Engineering. 2023. 121(5). Article no. 12105. DOI: 10.34910/MCE.121.5

1. Introduction

The finite element method is the most popular method for solving various structural mechanics problems. Most of the developed finite elements are based on the displacements fields approximations. In this case, the stresses are determined through the derivatives of the displacement functions, are discontinuous along the finite element boundaries, and are determined for the finite element centers. Stresses are the most important characteristics, so it is necessary to determine them with greater accuracy. Therefore, development of the finite elements based on the stresses approximations is of relevance, as it will improve their calculation accuracy.

To date, numerous variants of finite elements have been developed for the calculation of rod systems, the elasticity theory plane problems, bending plates [1–3], shells and volume problems [4–7]. The papers [8–10] propose finite elements based on the stresses approximations. The solution is built on the basis of the additional energy functional, which is expanded by including the algebraic equilibrium equations of nodes in it using the Lagrange multipliers method [11, 12]. This approach makes it possible to more accurately determine the stress values, including stresses at nodal points. When solving such problems as the calculation of nodal connections of different sizes elements, the calculation of elements from dissimilar materials, the calculation of structures with a stepwise change in cross sections, a more accurate determination of stresses becomes essential. In this case, as a rule, maximum stresses occur at the subject area boundaries. To model such structures, it is necessary to use volumetric finite elements. In works [13–

17] for the stress-strain state analysis of reinforced concrete beams, columns and their connections, volumetric finite elements are used. In article [18] for the calculation of complex volumetric steel assemblies, variational formulations based on displacements and stresses are considered and the corresponding finite element discretization strategies are selected, giving, respectively, the upper and lower exact solution estimates. The proposed scheme is illustrated on the design of the torque transmission unit. To solve problems of plane elasticity theory, bending of plates and shells, a hybrid finite element formulations based on approximations of both displacements and stresses were used in articles [19–21]. Paper [21] notes that special hybrid elements are used to model the elements connection that do not lie in the same plane. These elements include the so-called plate elements and three-dimensional solid elements designed for the analysis of thin plates and shells. In articles [22, 23] for thermo-mechanical analysis of multilayer plates and shells the authors also used volumetric finite elements. It is noted that the proposed finite volumetric finite elements allow using only a few nodes in the thickness direction to obtain results with satisfactory accuracy. Article [24] investigates the behavior of steel-wood composite joints with bolted connectors embedded in grout pockets using 3D continuum finite element models. Finite element models are used to conduct a parametric study that investigates the effect of compressive strength of cement slurry, yield strength and shear size of bolted connectors, slurry size, pockets and the thickness of the steel profile flange on slippage characteristics under load, operational rigidity, peak load-bearing capacity and joint failure modes. To simulate the stress-strain state of bolted joints, various volumetric finite elements are widely used [25–28]. The volumetric finite elements are successfully used for modeling concrete and fiber-reinforced concrete structures [29–31]. Article [30] is aimed at evaluating the modulus of elasticity and Poisson's ratio of fiber-reinforced concrete using finite element modeling. A theoretical model for predicting the elastic modulus and Poisson's ratio of fiber-reinforced concrete was created using homogenization theory. To study the effect of local corrosion on the bearing capacity of long columns of round reinforced concrete steel pipes under eccentric compression, a numerical model was created using volumetric finite elements [32]. An eight-node 3d solid element of linear reduced integration is adopted for both the outer steel tube and the core concrete. The mesh element size is one tenth of the section diameter. The various volumetric finite elements are also being developed for the composite structures analysis by the finite element method [33, 34]. Various mixed formulations of the finite element method based on the additional energy and Reissner's functionals are developed in articles [35–38] to solve structural mechanics problems.

The review of scientific articles shows that the development and application of volumetric finite elements for the calculation of nodal connections and complex composite structures is relevant. Most of the finite elements currently used for this purpose are based on displacement approximations. This work aims to develop a volumetric triangular prism finite element based on stress approximation. The stresses obtained by the proposed method will be compared with analytical solutions and stresses calculated by the finite element method based on displacement approximation.

2. Methods

The solution to the bulk theory elasticity problem will be built based on the additional energy functional:

$$\Pi = \frac{1}{2} \int_V \left(\frac{1}{E} (\sigma_x^2 + \sigma_y^2 + \sigma_z^2) - \frac{\nu}{E} (\sigma_x \sigma_y + \sigma_x \sigma_z + \sigma_y \sigma_z) + \frac{1}{G} (\tau_{xy}^2 + \tau_{xz}^2 + \tau_{yz}^2) \right) dV. \quad (1)$$

E is the material elastic modulus; ν is Poisson's ratio, $G = 2(1 + \mu)/E$. We write the functional (1) in matrix form:

$$\Pi = \frac{1}{2} \int_V \boldsymbol{\sigma}^T \mathbf{E}^{-1} \boldsymbol{\sigma} dV, \quad (2)$$

$$\boldsymbol{\sigma}^T = (\sigma_x \quad \sigma_y \quad \sigma_z \quad \tau_{xy} \quad \tau_{xz} \quad \tau_{yz}),$$

$$\mathbf{E}^{-1} = \begin{bmatrix} 1/E & -\nu/E & -\nu/E & 0 & 0 & 0 \\ -\nu/E & 1/E & -\nu/E & 0 & 0 & 0 \\ -\nu/E & -\nu/E & 1/E & 0 & 0 & 0 \\ 0 & 0 & 0 & 1/G & 0 & 0 \\ 0 & 0 & 0 & 0 & 1/G & 0 \\ 0 & 0 & 0 & 0 & 0 & 1/G \end{bmatrix}.$$

Fig. 1 shows a triangular prism finite element and six marked regions with constant stresses. In each region, the stresses are constant and equal to the stresses in the corresponding finite element node.

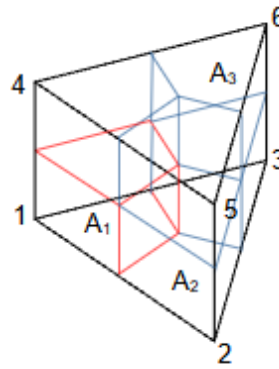


Figure 1. Triangular prism finite element.

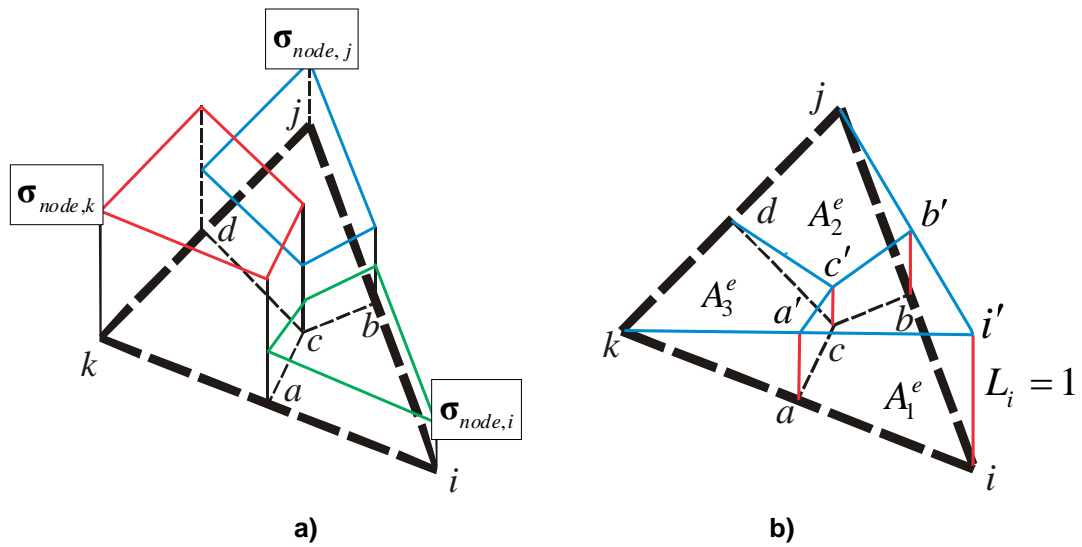


Figure 2. a) stresses distribution; b) triangular coordinate.

The red lines restrict the prism region with stresses, which equal the stresses on node 1. A_1, A_2, A_3 are the squares of prism bottoms and covers. Let us denote the nodal unknown stresses vector, in a global coordinate system, as

$$\sigma_{node,k}^T = (\sigma_{x,k} \quad \sigma_{y,k} \quad \sigma_{z,k} \quad \tau_{xy,k} \quad \tau_{xz,k} \quad \tau_{yz,k}). \quad (3)$$

Vector of finite element unknown stresses is

$$\sigma_{el,k}^T = (\sigma_{node,1}^T \quad \sigma_{node,2}^T \quad \dots \quad \sigma_{node,6}^T). \quad (4)$$

To simplify the notation, let us introduce unit step functions and diagonal matrices

$$h_i(x, y, z) = \begin{cases} 1, & (x, y, z) \in V_i \\ 0, & (x, y, z) \notin V_i \end{cases}, \quad \mathbf{H}_i = \begin{bmatrix} h_i & & \\ & h_i & \\ & & h_i \end{bmatrix}. \quad (5)$$

Then the approximation matrix of stresses in the finite element volume will have the simple form (Fig. 1b):

$$\mathbf{Z}_k = [\mathbf{H}_1 \quad \mathbf{H}_2 \quad \dots \quad \mathbf{H}_6], \quad \sigma = \mathbf{Z}_k \sigma_{el,k}. \quad (6)$$

Using (4)–(6), we express the finite element additional energy in the following form:

$$\Pi_k = \int_{V_k} \sigma_{el,k}^T (\mathbf{Z}_k^T \mathbf{E}_k^{-1} \mathbf{Z}_k) \sigma_{el,k} dV. \quad (7)$$

The pliability matrix of the finite element is

$$\mathbf{D}_k = \int_{V_k} \mathbf{Z}_k^T \mathbf{E}_k^{-1} \mathbf{Z}_k dV. \tag{8}$$

The matrix has a simple block-diagonal form. Global matrix \mathbf{D} of the whole system is formed from local finite elements matrices. Functional (1) of the whole system:

$$\Pi = \frac{1}{2} \boldsymbol{\sigma}_V^T \mathbf{D} \boldsymbol{\sigma}_V. \tag{9}$$

$\boldsymbol{\sigma}_V$ is a global vector of the unknown stresses of the system.

Global matrix \mathbf{D} has a block-diagonal form:

$$\mathbf{D} = \begin{bmatrix} \mathbf{d}_1 & & & & & \\ & \mathbf{d}_2 & & & & \\ & & \ddots & & & \\ & & & \mathbf{d}_i & & \\ & & & & \ddots & \\ & & & & & \mathbf{d}_n \end{bmatrix}. \quad \mathbf{d}_i = \frac{1}{6} \sum_k V_{i,k} \mathbf{E}_k^{-1}. \tag{10}$$

n is number of system nodes; $V_{i,k}$ and k are the volume and index of finite elements adjoining node i .

\mathbf{E}_k^{-1} is material stiffness matrix of finite element k .

Denote the nodal unknown stresses vector, in local coordinate system (Fig. 3), as

$$\bar{\boldsymbol{\sigma}}_{node,k}^T = (\bar{\sigma}_{x,k} \quad \bar{\sigma}_{y,k} \quad \bar{\sigma}_{z,k} \quad \bar{\tau}_{xy,k} \quad \bar{\tau}_{xz,k} \quad \bar{\tau}_{yz,k}). \tag{11}$$

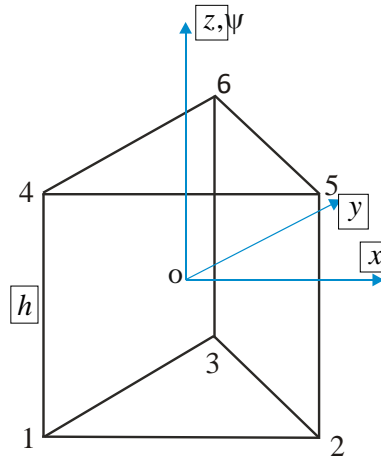
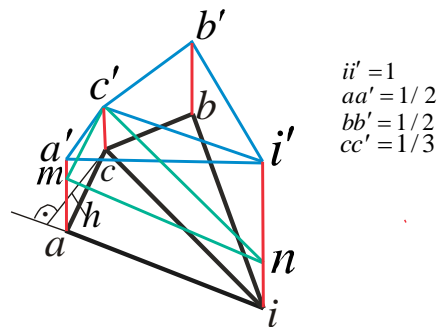


Figure 3. Local coordinate system.



$$\begin{aligned} ii' &= 1 \\ aa' &= 1/2 \\ bb' &= 1/2 \\ cc' &= 1/3 \end{aligned}$$

Figure 4. Integration of a triangular coordinate.

In accordance with the minimum additional energy principle, the stress functions must satisfy the equilibrium equations. Therefore, using the possible displacements principle, we will obtain algebraic equations for the nodes equilibrium along the coordinate axes. As a result, we will have the problem of minimizing the additional energy functional in the presence of constraints in the equations system form. We will solve such problem by the Lagrange multipliers method. It should be noted, that such functional is not a mixed one, in which both stress and displacement approximations are used simultaneously. The proposed solution only uses the approximations of possible displacement when we obtain the equilibrium equations. As known, approximations of possible displacements can be any functions that satisfy the boundary kinematic conditions.

To obtain the equilibrium equations, we give possible node displacements along the local coordinate axes (Fig. 3):

$$\delta\bar{u}_i = u_0 \frac{1}{2} L_i (1 + \psi \psi_i), \quad \delta\bar{v}_i = v_0 \frac{1}{2} L_i (1 + \psi \psi_i), \quad (12)$$

$$\delta\bar{w}_i = w_0 \frac{1}{2} L_i (1 + \psi \psi_i), \quad i = 1, 2, \dots, 6.$$

$$\psi = \frac{2z}{h^e}, \quad L_i = \frac{1}{2A} (a_i + b_i x + c_i y), \quad (13)$$

$$a_i = x_{i+1}y_{i+2} - x_{i+2}y_{i+1}, \quad b_i = y_{i+1} - y_{i+2}, \quad c_i = x_{i+2} - x_{i+1}.$$

Parameters u_0 , v_0 , w_0 are introduced for the convenience of the transition to the global coordinate system and below are taken equal to 1. Possible displacements of node i along the x axis give the following deformations of the finite elements adjacent to this node:

$$\delta\varepsilon_x = \frac{\partial(\delta\bar{u}_i)}{\partial x} = \frac{b_i}{4A^e} (1 + \psi \psi_i), \quad \delta\gamma_{xy} = \frac{\partial(\delta\bar{u}_i)}{\partial y} = \frac{c_i}{4A^e} (1 + \psi \psi_i), \quad (14)$$

$$\delta\gamma_{xz} = \frac{\partial(\delta\bar{u}_i)}{\partial z} = \frac{\psi_i L_i}{h^e}.$$

A^e is bottom area of a triangular prism. The possible finite element strain energy

$$\delta\bar{U}_{i,x}^e = \int_0^{h^e} \int_{A^e} (\bar{\sigma}_x \delta\varepsilon_x + \bar{\tau}_{xy} \delta\gamma_{xy} + \bar{\tau}_{xz} \delta\gamma_{xz}) dAdz. \quad (15)$$

Using (14), let us get

$$\delta\bar{U}_{i,x}^e = \frac{h^e}{2} \sum_{J=1-1}^6 \int_{A_J^e} \left(\frac{b_i (1 + \psi \psi_i)}{4A^e} \bar{\sigma}_{x,j} + \frac{c_i (1 + \psi \psi_i)}{4A^e} \bar{\tau}_{xy,j} + \frac{\psi_i L_i}{d^e} \bar{\tau}_{xz,j} \right) dAd\psi. \quad (16)$$

The first two terms integration in (16) does not cause difficulties. To calculate the third term, it is necessary to integrate the linear function over triangular areas. Fig. 2b shows graphs of stress changes and a linear function over the prism base area. In Fig. 2, points a , b , d bisect the corresponding sides.

Point c has triangular coordinates $L_i = L_j = L_k = 1/3$. Function L_i integral over the area A_1^e is equal to the volume of the figure $acbia'c'b'i'$. This figure can be divided into two equal parts by the plane $cc'ii'$ (Fig. 4). The triangles areas aci and cbi are equal. In Fig. 4, lines $c'n$ and $c'm$ are parallel to the base. The $aciac'i'$ volume can be represented as the sum of a triangular prism $acimc'n$ volume and a pyramid $c'ma'ni'$ volume. Then

$$\int_{A_1^e} L_i dA = 2 \left(\frac{1}{3} \cdot \frac{A^e}{6} + \frac{1}{3} h \cdot mn \cdot \frac{\left(\frac{1}{6} + \frac{2}{3}\right)}{2} \right) = \frac{11}{54} A^e. \quad (17)$$

Product $h \cdot mn = \frac{A^e}{3}$. Function L_i integral over the area A_2^e is equal to the sum of the pyramid's volumes $jdcc'$ and $jcc'bb'$. Let us get

$$\int_{A_2^e} L_i dA = \frac{1}{3} \cdot h_1 \cdot dc \cdot \frac{1}{2} \cdot cc' + \frac{1}{3} \cdot h_2 \cdot cb \cdot \frac{1}{2} (cc' + bb') = \frac{7}{108} A^e. \quad (18)$$

In (18), h_1 , h_2 are the heights lowered from point j to cd and cb , respectively. Considering (17) and (18), we get

$$\delta \bar{U}_{i,x}^e = \sum_{j=1}^6 \left(\frac{h^e b_i (1 + \psi_i \psi_j / 2)}{24} \bar{\sigma}_{x,j} + \frac{h^e c_i (1 + \psi_i \psi_j / 2)}{24} \bar{\tau}_{xy,j} + \frac{k_{ij} \psi_i A^e}{216} \bar{\tau}_{xz,j} \right). \quad (19)$$

If $(i = j) \vee (i = j + 3) \vee (i = j - 3)$ $k_{ij} = 22$, else $k_{ij} = 7$. The strain energy of finite element with a node possible displacement along the Y and Z axes is written by analogy:

$$\delta \bar{U}_{i,y}^e = \sum_{j=1}^6 \left(\frac{h^e c_i (1 + \psi_i \psi_j / 2)}{24} \bar{\sigma}_{y,j} + \frac{h^e b_i (1 + \psi_i \psi_j / 2)}{24} \bar{\tau}_{xy,j} + \frac{k_{ij} \psi_i A^e}{216} \bar{\tau}_{yz,j} \right), \quad (20)$$

$$\delta \bar{U}_{i,z}^e = \sum_{j=1}^6 \left(\frac{h^e b_i (1 + \psi_i \psi_j / 2)}{24} \bar{\tau}_{xz,j} + \frac{h^e c_i (1 + \psi_i \psi_j / 2)}{24} \bar{\tau}_{yz,j} + \frac{k_{ij} \psi_i A^e}{216} \bar{\sigma}_{z,j} \right). \quad (21)$$

Expression (19)–(21) let us write in matrix form:

$$\delta \mathbf{U}_i^e = \begin{cases} \delta \bar{U}_{i,x}^e \\ \delta \bar{U}_{i,y}^e \\ \delta \bar{U}_{i,z}^e \end{cases} = \delta \bar{\mathbf{u}}_i^e \bar{\mathbf{L}}_i^e \bar{\boldsymbol{\sigma}}^e, \quad \delta \bar{\mathbf{u}}_i^e = \begin{bmatrix} u_0 & 0 & 0 \\ 0 & v_0 & 0 \\ 0 & 0 & w_0 \end{bmatrix}. \quad (22)$$

Let us express the stresses and possible displacements $\bar{\boldsymbol{\sigma}}^e$, $\delta \bar{\mathbf{u}}_i^e$ in the local coordinate system in terms of the corresponding parameters $\boldsymbol{\sigma}^e$, $\delta \mathbf{u}_i^e = 1$ in the global system:

$$\bar{\boldsymbol{\sigma}}^e = \mathbf{C}_\sigma \boldsymbol{\sigma}^e, \quad \delta \bar{\mathbf{u}}_i^e = \mathbf{C}_u \delta \mathbf{u}_i^e. \quad (23)$$

The transition matrices \mathbf{C}_σ , \mathbf{C}_u have a standard form. Substituting (23) into (22), we get

$$\delta \mathbf{U}_i^e = \delta \mathbf{u}_i^e \mathbf{L}_i^e \boldsymbol{\sigma}^e, \quad \mathbf{L}_i^e = \mathbf{C}_u^T \bar{\mathbf{L}}_i^e \mathbf{C}_\sigma. \quad (24)$$

The external forces potential with the node possible displacements in the global coordinate system will have the following form:

$$\delta \mathbf{V}_i^e = \delta \mathbf{u}_i^e \mathbf{P}_i^e. \quad (25)$$

From matrices \mathbf{L}_i^e of all finite elements nodes "equilibrium" matrix \mathbf{L} for all system is formed. Matrix \mathbf{L} rows number is equal to the number of system nodes possible displacements, and the columns number

is equal to the the total number of nodal unknown stresses. The matrix has a band structure of non-zero elements. Global load vector \mathbf{P} is formed from vectors \mathbf{P}_i^e of all finite elements nodes.

Let us take the algebraic equations system for the equilibrium of nodes in matrix form:

$$\mathbf{L}\sigma_V + \mathbf{P} = 0. \quad (26)$$

σ_V is the vector of the node's stresses for the whole system. Using the Lagrange multipliers method, we add the equilibrium equations to functional (9):

$$\Pi = \frac{1}{2} \sigma_V^T \mathbf{D} \sigma_V + \mathbf{w}^T (\mathbf{L} \sigma_V + \mathbf{P}) \rightarrow \min. \quad (27)$$

\mathbf{w} is the nodes displacements vector.

Equating the functional derivatives with respect to σ_V and \mathbf{w} to zero, we obtain the system of equations:

$$\mathbf{D} \sigma_V + \mathbf{w}^T \mathbf{L} = 0, \quad \mathbf{L} \sigma_V + \mathbf{P} = 0. \quad (28)$$

We express vector σ_V from the first matrix equation and put it into the second one. Then we get

$$\sigma_V = -\mathbf{L}^T \mathbf{D}^{-1} \mathbf{w}, \quad \mathbf{K} = -\mathbf{L}^T \mathbf{D}^{-1} \mathbf{L}, \quad \mathbf{K} \mathbf{w} = \mathbf{P}. \quad (29)$$

\mathbf{K} is the whole system stiffness matrix. That matrix also has a band structure of the non-zero elements. Matrix \mathbf{D} has a block-diagonal structure and is inversed analytically. When calculating product $\mathbf{L}^T \mathbf{D}^{-1} \mathbf{L}$, the band structure of non-zero elements of matrix \mathbf{L} is taken into account. Solving the equations system, we determine the nodal displacements, and then calculate the nodal stresses (24). Thus, the stress fields are continuous along element boundaries and discontinuous inside ones. On the contrary, when using the finite element method based on the displacement approximations, the stress fields are continuous inside the finite elements and discontinuous along their boundaries.

3. Results and Discussions

To test the method, a pinched beam (Fig. 5) and a hinged plate (Fig. 6) calculations were performed. Such tasks were chosen because there are analytical solutions for them.

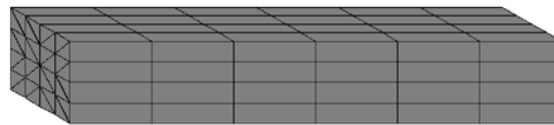


Figure 5. Finite element model of a pinched beam.

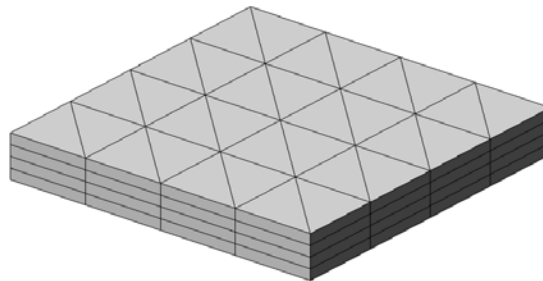


Figure 6. Finite element model of a hinged plate (quarter).

The beam length is 6 meters, the cross-section dimensions are 1 by 1 meter. The material elasticity modulus is 10^6 kN/m². A uniformly distributed vertical load $q = 1$ kN/m² is applied to the cross section at the beam free end. Options for the beam cross section dividing into the finite elements are shown in Fig. 7. The beam length was divided into six (for schemes in Fig. 7a and Fig. 7b) or twelve (for scheme in Fig. 7c) finite elements. The square hinged plate measures 6 by 6 meters and is 0.4 meters thick. The load on the plate is evenly distributed $q = 1$ kN/m². Poisson's ratio is $\mu = 0.3$.

According to the thickness, the plate is divided into 4 finite elements for variants in Fig. 9a, Fig. 9b and into 6 elements for the variant in Fig. 9c. The calculation results in the figures and the table, obtained by the proposed method, are indicated as FEM-S, and the results obtained by LIRA-SAPR program, which use the traditional finite elements, are indicated as FEM-D.

An analytical solution for the hinged plate was obtained in [39]. According to it, the displacement and the bending moment in the plate center are determined by the following expressions:

$$M = 0.0479qa^2, \quad w = \frac{0.00496qa^4}{Eh^3/12(1-\mu^2)}. \quad (30)$$

The analytical values of the plate center displacement and the outer fiber stress are given in Table 1. An analytical solution for the cantilever beam is easily obtained based on Kirchhoff's beam bending theory.

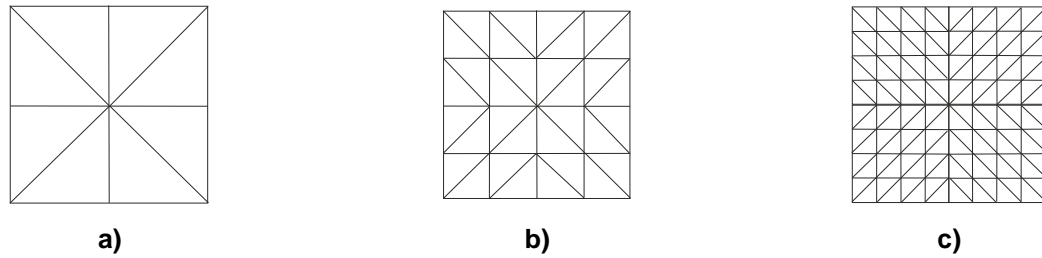


Figure 7. Dividing the beam cross section into finite elements.

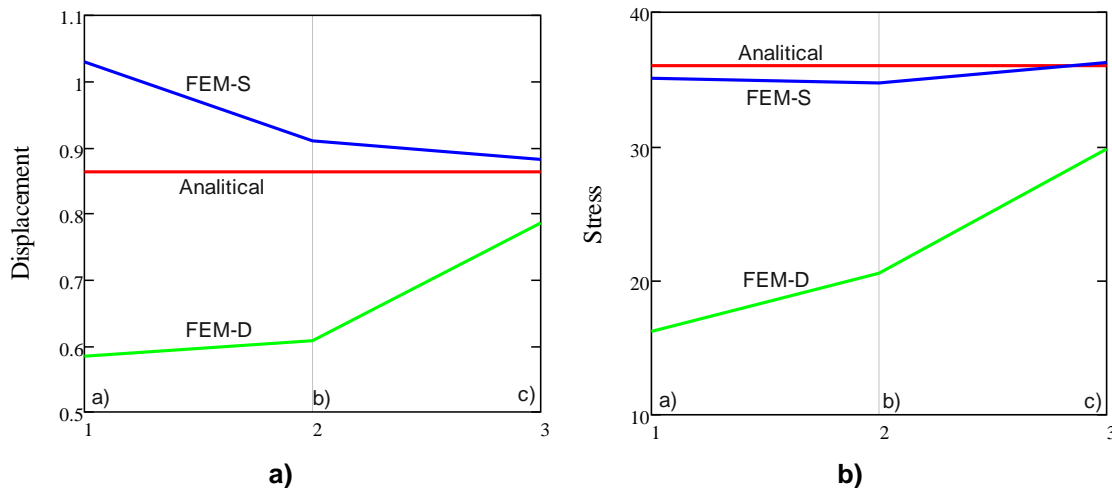


Figure 8. Displacements and stresses of the pinched beam.

Table 1. Displacements and stresses.

Grid	Displacements, mm				Stresses, kN/m ²			
	Free end of the beam		Center of the plate		Pinched end of the beam		Center of the plate	
	FEM-S	FEM-D	FEM-S	FEM-D	FEM-S	FEM-D	FEM-S	FEM-D
a)	1.029	0.585	0.835	0.173	35.08	16.20	42.38	8.275
b)	0.911	0.608	1.030	0.439	34.70	20.50	49.76	25.00
c)	0.883	0.785	1.010	0.729	36.22	29.81	59.24	48.00
Analytical	0.864		0.898		36.0		64.625	

An analysis of the calculation results of the pinched beam shows that when grinding the finite element meshes, with stress piecewise constant approximations, the stresses converge with the exact values from above. In addition, the displacements obtained by the finite element method, based on the displacement approximations, approach the exact values from below. Thus, in terms of displacements, we have two alternative solutions. Similar results were obtained using the finite elements based on piecewise constant stress approximations for the bending plates and the flat theory of elasticity [8, 9].

Moreover, the displacements and stresses values obtained by the proposed method are more accurate than the values calculated by the traditional finite element method based on displacement approximation. For example, the stresses obtained with the finest mesh by the displacement approximation

method are 17% less than the analytical value, and the stresses obtained by the proposed method practically coincide with the exact value. The deviation of the displacement value obtained by the FEM–S method from the analytically obtained one is 2%, and the displacement obtained by the FEM–D method deviates from the exact value by 9%.

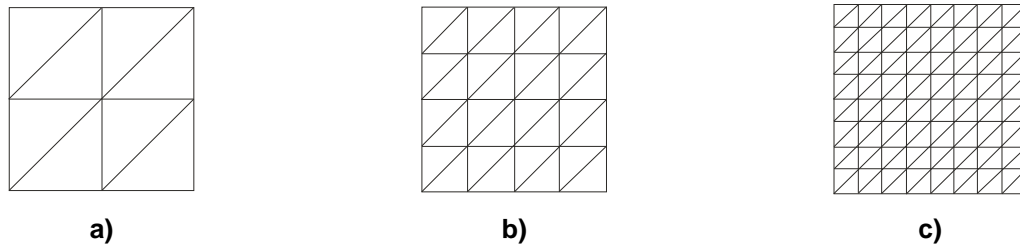


Figure 9. Division of the plate quarter into finite elements.

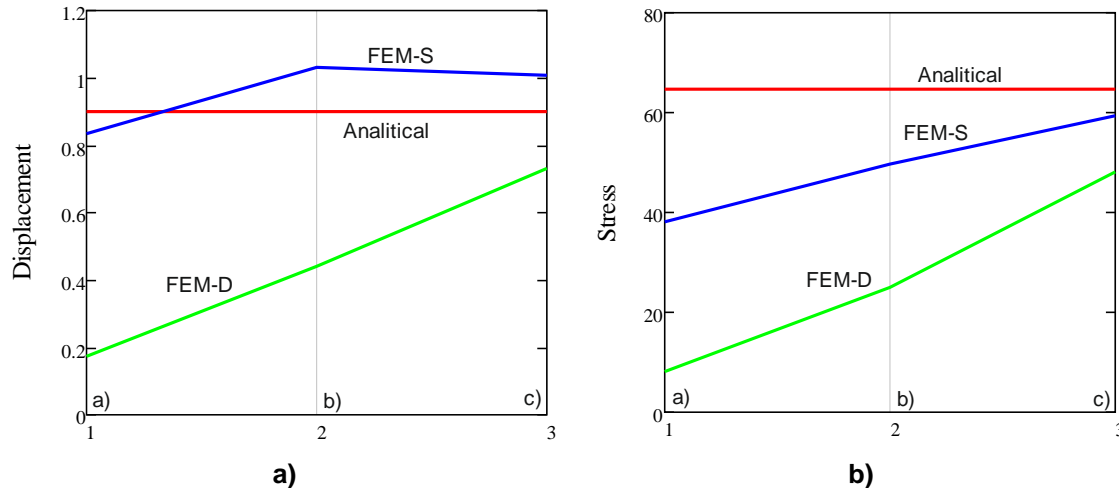


Figure 10. Displacements and stresses of the hinged plate center.

When analyzing the square hinged plate calculating results for a uniformly distributed load, the same trends are observed (Fig. 10). For the finite element mesh shown in Fig. 9c, the displacements obtained by the FEM-S method are 12% more than the analytical value, and the displacements obtained by the FEM-D method are 19% less. In addition, the displacement values obtained by the FEM-S method, when the finite element mesh is refined, approach the exact value from above. The stresses at the plate center, obtained by the FEM-S method, are also more accurate and differ from the analytical value by 8 percent. The stresses obtained by the FEM-D method are less than the analytical value by 26%.

At present, volumetric finite elements are increasingly used to calculate such problems as nodal connections, connections of columns and slabs, and calculation of variable section elements. In such structures, points and areas of increased stresses arise, which, as a rule, are located at the edges and boundaries of the areas. In such cases, the use of the proposed finite elements, based on piecewise constant approximations, will allow more accurate determination of the structure stress-strain state, and, accordingly, increase the design solutions reliability.

4. Conclusion

1. The volumetric triangular prism finite element based on piecewise constant approximations of stresses is presented. The stress fields are continuous along finite element boundaries and discontinuous inside them. The solution of the volume theory elasticity problem was obtained on the basis of the additional energy functional and the possible displacements principle.

2. The displacements obtained by the proposed method, when refining the finite elements mesh, tend to exact values from above; they are more accurate than the values obtained by the finite element method in displacements.

3. As the test problems solutions showed, the proposed finite elements allow obtaining more accurate stress values compared to traditional finite elements based on displacements approximations. In this method, the stresses are determined directly at the nodal points, and not at the finite element centers. For the first example, the stresses obtained with the finest mesh by the displacement approximation method are 17 percent less than the analytical value, and the stresses obtained by the proposed method practically coincide with the exact value. For the second task, the stresses at the plate center, obtained by the

proposed method, are also more accurate and differ from the analytical value by 8% and the stresses obtained by the finite element method in displacement are 26% less than the analytical value.

References

1. Cho, J.R. Natural element approximation of hierarchical models of plate-like elastic structures. *Finite Elements in Analysis and Design*. 2020. 180(September). Pp. 103439. DOI: 10.1016/j.finel.2020.103439
2. Du, L., Qi, J., Cheng, Z., Wang, J. Finite element modeling of UHPC slabs with dovetail joints and steel wire mesh using an innovative interfacial treating method. *Structures*. 2022. 37 (January). Pp. 745–755. DOI: 10.1016/j.istruc.2022.01.057
3. Abdikarimov, R., Amabili, M., Vatin, N.I., Khodzhaev, D. Dynamic stability of orthotropic viscoelastic rectangular plate of an arbitrarily varying thickness. *Applied Sciences (Switzerland)*. 2021. 11 (13). DOI: 10.3390/app11136029
4. Gao, X.-W., Gao, L.-F., Zhang, Y., Cui, M., Lv, J. Free element collocation method: A new method combining advantages of finite element and mesh free methods. *Computers & Structures*. 2019. 215. Pp. 10–26. DOI: 10.1016/j.compstruc.2019.02.002
5. Genikomsou, A.S., Polak, M.A. 3D finite element investigation of the compressive membrane action effect in reinforced concrete flat slabs. *Engineering Structures*. 2017. 136. Pp. 233–244. DOI: 10.1016/j.engstruct.2017.01.024
6. Judge, R., Yang, Z., Jones, S.W., Beattie, G. Full 3D finite element modelling of spiral strand cables. *Construction and Building Materials*. 2012. 35. Pp. 452–459. DOI: 10.1016/j.conbuildmat.2011.12.073.
7. Kebir, H., Zouari, W., Assarar, M., Ayad, R. A specific eight-node hexahedral finite element for the analysis of 3D fibre-reinforced composites. *Composite Structures*. 2023. 303. Pp. 110456. DOI: 10.1016/j.compstruct.2022.116269.
8. Tyukalov, Y.Y. Calculation of bending plates by finite element method in stresses. *IOP Conference Series: Materials Science and Engineering*. 2018. 451 (1). DOI: 10.1088/1757-899X/451/1/012046
9. Tyukalov, Y.Y. Calculation of circular plates with assuming shear deformations. *IOP Conference Series: Materials Science and Engineering*. 2019. 687 (3). DOI: 10.1088/1757-899X/687/3/033004
10. Tyukalov, Y.Y. Method of plates stability analysis based on the moments approximations. *Magazine of Civil Engineering*. 2020. 95 (3). Pp. 90–103. DOI: 10.18720/MCE.95.9
11. Tyukalov, Y.Y. Arbitrary quadrangular finite element for plates with shear deformations. *Magazine of Civil Engineering*. 2021. 107 (7). DOI: 10.34910/MCE.107.7
12. Tyukalov, Y.Y. Equilibrium finite elements for plane problems of the elasticity theory. *Magazine of Civil Engineering*. 2019. 91 (7). Pp. 80–97. DOI: 10.18720/MCE.91.8.
13. Chen, Z., Chen, J., Jiang, X., Mo, L. Experimental research and finite element analysis on seismic behavior of square reinforced concrete columns with four interlocking spirals. *Structures*. 2022. 39 (March). Pp. 1–16. DOI: 10.1016/j.istruc.2022.03.023
14. Izadi, A., Teh, L.H., Polak, M.A., Ahmed, A. Finite element analysis of square FRP-Concrete-Steel columns under concentric compression. *Structures*. 2022. 44 (August). Pp. 1312–1320. DOI: 10.1016/j.istruc.2022.08.051
15. Li, D. bin, Chai, Y. kai, Li, W. long, Xiang, R. Experimental study and finite element analysis of seismic behaviour of novel precast prestressed concrete frames. *Structures*. 2022. 38 (December 2020). Pp. 402–415. DOI: 10.1016/j.istruc.2022.02.019
16. Raza, A., Rehman, A. ur, Masood, B., Hussain, I. Finite element modelling and theoretical predictions of FRP-reinforced concrete columns confined with various FRP-tubes. *Structures*. 2020. 26 (March). Pp. 626–638. DOI: 10.1016/j.istruc.2020.04.033
17. Shoaib Karam, M., Nakamura, H., Yamamoto, Y., Miura, T. Numerical evaluation of the perfbond (PBL) shear connector with transverse rebar using coupled rigid Body spring model (RBSM) and solid finite element method (FEM). *Structures*. 2022. 45 (October). Pp. 1544–1560. DOI: 10.1016/j.istruc.2022.09.117
18. Boustani, C. El, Bleyer, J., Arquier, M., Ferradi, M.K., Sab, K. Elastoplastic and limit analysis of 3D steel assemblies using second-order cone programming and dual finite-elements. *Engineering Structures*. 2020. 221 (May). Pp. 111041. DOI: 10.1016/j.engstruct.2020.111041
19. Zhou, J., Wang, K., Li, P. A hybrid fundamental-solution-based 8-node element for axisymmetric elasticity problems. *Engineering Analysis with Boundary Elements*. 2019. 101. Pp. 297–309. DOI: 10.1016/j.enganabound.2019.01.015
20. Góis, W., Proença, S.P.B. Generalized Finite Element Method on Hybrid Stress Approach: Formulation and Numerical Performance. *Buenos Aires*. 2010. XXIX. Pp. 4687–4705.
21. Pian, T.H.H., Sze, K.-Y. Hybrid Stress Finite Element Methods for Plate and Shell Structures. *Advances in Structural Engineering*. 2003. 4 (1). Pp. 13–18. DOI: 10.1260/1369433011502309
22. Liu, B., Lu, S., Ji, J., Ferreira, A.J.M., Liu, C., Xing, Y. Three-dimensional thermo-mechanical solutions of cross-ply laminated plates and shells by a differential quadrature hierarchical finite element method. *Composite Structures*. 2019. 208 (May 2018). Pp. 711–724. DOI: 10.1016/j.compstruct.2018.10.022
23. Liu, B., Lu, S., Wu, Y., Xing, Y. Three dimensional micro/macro-mechanical analysis of the interfaces of composites by a differential quadrature hierarchical finite element method. *Composite Structures*. 2017. 176. Pp. 654–663. DOI: 10.1016/j.compstruct.2017.05.068
24. Hassanieh, A., Valipour, H.R., Bradford, M.A. Bolt shear connectors in grout pockets: Finite element modelling and parametric study. *Construction and Building Materials*. 2018. 176. Pp. 179–192. DOI: 10.1016/j.conbuildmat.2018.05.029
25. Liu, T., Lu, J., Wang, D., Liu, H., Mo, N., Zhai, L. 3D nonlinear finite element modelling of mechanical behavior of a new wall-beam-strut joint for prefabricated underground construction and validation against experimental testing. *Structures*. 2021. 33 (December 2019). Pp. 3202–3221. DOI: 10.1016/j.istruc.2021.06.059
26. Liu, Z., Yan, X., Zheng, M., Wang, Y., Chen, W., Li, Y. The effect of tightening again on bolt loosening under transverse load: Experimental and finite element analysis. *Structures*. 2022. 44 (August). Pp. 1303–1311. DOI: 10.1016/j.istruc.2022.08.049
27. Najafgholipour, M.A., Sarhadi, F. A finite element study on the ultimate lateral drift capacity of interior reinforced concrete flat slab-column connections. *Structures*. 2022. 46 (November). Pp. 913–926. DOI: 10.1016/j.istruc.2022.10.128
28. Zhao, J., Wang, Z., Qian, F., Peng, Y., Dong, J. Finite element analysis of the shear capacity of stainless-steel screw connections. *Structures*. 2022. 41 (May). Pp. 957–968. DOI: 10.1016/j.istruc.2022.05.048

29. Li, Y., Guan, Z., Wang, Z., Wang, P., Li, Y., Zhang, G., Ding, Q. 3D meso-scale finite element modelling on cement paste corroded in sodium sulfate with X-ray CT technique. *Construction and Building Materials*. 2019. 202. Pp. 727–737. DOI: 10.1016/j.conbuildmat.2019.01.020
30. Li, Y., Li, Y. Evaluation of elastic properties of fiber reinforced concrete with homogenization theory and finite element simulation. *Construction and Building Materials*. 2019. 200. Pp. 301–309. DOI: 10.1016/j.conbuildmat.2018.12.134
31. Xu, R., Bouby, C., Zahrouni, H., Ben Zineb, T., Hu, H., Potier-Ferry, M. 3D modeling of shape memory alloy fiber reinforced composites by multiscale finite element method. *Composite Structures*. 2018. 200 (May). Pp. 408–419. DOI: 10.1016/j.compstruct.2018.05.108
32. Wang, K., Chen, M., Zhang, R., Fang, W. Finite element simulation of load bearing capacity of circular CFST long columns with localized corrosion under eccentric load. *Structures*. 2022. 43 (August). Pp. 1629–1642. DOI: 10.1016/j.istruc.2022.07.029
33. Ye, J., Yan, Y., Li, J., Hong, Y., Tian, Z. 3D explicit finite element analysis of tensile failure behavior in adhesive-bonded composite single-lap joints. *Composite Structures*. 2018. 201 (May). Pp. 261–275. DOI: 10.1016/j.compstruct.2018.05.134
34. Nguyen, M.N., Bui, T.Q., Truong, T.T., Tanaka, S., Hirose, S. Numerical analysis of 3-D solids and composite structures by an enhanced 8-node hexahedral element. *Finite Elements in Analysis and Design*. 2017. 131. Pp. 1–16. DOI: 10.1016/j.finel.2017.04.002
35. Lukashovich, A.A., Lukashovich, N.K. Numerical solution of contact problems with friction under dynamic loads. *IOP Conference Series: Materials Science and Engineering*. 2020. Vol. 753. 022058. DOI: 10.1088/1757-899X/753/2/022058
36. Lukashovich, A.A. Finite element models based on the approximation of discontinuous stress fields. *Magazine of Civil Engineering*. 2022. 110 (2). Article No. 11004. DOI: 10.34910/MCE.110.4
37. Lalin, V.V., Rybakov, V.A., Ivanov, S.S., Azarov, A.A. Mixed finite-element method in Slivker's semi-shear thin-walled bar theory. *Magazine of Civil Engineering*. 2019. 89 (5). Pp. 79–93. DOI: 10.18720/MCE.89.7
38. Ignatyev, A.V., Ignatyev, V.A. On the efficiency of the finite element method in the form of the classical mixed method. *Procedia Engineering*. 2016. Vol. 150. Pp. 1760–1765. DOI: 10.1016/j.proeng.2016.07.167
39. Timoshenko, S.P., Voinovskiy-Kriger, S. *Plastiny i obolochki [Plates and shells]*. Moscow : Nauka, 1966. 636 p.

Information about author:

Yury Tyukalov, Doctor of Technical Sciences

ORCID: <https://orcid.org/0000-0001-6184-2365>

E-mail: yutvgu@mail.ru

Received 31.01.2023. Approved after reviewing 22.05.2023. Accepted 29.05.2023.



Research article

UDC 624.131

DOI: 10.34910/MCE.121.6



Clay soil stiffness under consolidated isotropic drained triaxial tests

R.F. Sharafutdinov 

Gersevanov Research Institute of Bases and Underground Structures (NIIOSP), JSC Research Center of Construction, Moscow, Russian Federation

 linegeo@mail.ru

Keywords: non-linear modelling, numerical modelling, clays, laboratory tests, triaxial test, finite-element method, statistical analysis, stiffness, Hardening Soil model

Abstract. Triaxial tests are common laboratory methods to study the mechanical properties of soils. According to international practice, it allows determining the reliable strength and stiffness properties. This research paper describes the results of statistical analysis of the deformation parameters for clay soils obtained from triaxial tests. The research focused on clay deposits of the Quaternary, Jurassic and Carboniferous periods of diverse genesis. The results of 992 consolidated isotropic drained triaxial tests of clay soils in Russia (Moscow) and Belarus (Minsk) were analysed. More than 50% of the tests were carried out under unloading/reloading conditions. As a result, empirical equations enabling evaluation of the effects of physical properties and stress state on stiffness of clay soils with different age and genesis were proposed. Comparison of accomplished tests of Quaternary and Jurassic soils from Thailand, Europe and the USA showed that stiffness for overconsolidated soils is in the same range as soils from Moscow and Minsk sites. The performed studies revealed the values of the Hardening soil model m-parameter depending on soil forming factors and its preconsolidation degree. In overconsolidated soils, values of the m-parameter are on average twice less than in normally consolidated or lightly overconsolidated soils. Proposed equations can be applied for preliminary estimation of the stiffness parameters for finite element method calculation, as well as used in geotechnical models that allow variability, horizontal and vertical distribution of stiffness to be taken into account. In general, geotechnical engineers may utilize the obtained results by applying them to design of complex soil models.

Acknowledgements: The author extends appreciation to the staff of the Gersevanov Research Institute of Bases and Underground Structures (NIIOSP) for the aid and materials provided.

Citation: Sharafutdinov, R.F. Clay soil stiffness under consolidated isotropic drained triaxial tests. Magazine of Civil Engineering. 2023. 121(5). Article no. 12106. DOI: 10.34910/MCE.121.6

1. Introduction

Triaxial compression is the most common method for characterizing mechanical properties of soil and rock [1, 2]. ASTM D2850, ASTM D4767, ASTM D7181, ISO 17892-9, BS 1377, Russian State Standard GOST 12248.3, regulating the triaxial test, mainly focus on the strength parameters of soil [3]. Practically, undrained triaxial tests are usually carried out, in order to obtain strength parameters with the least time consumption.

The soil stiffness is traditionally obtained from oedometer tests. However, for modern models, which allow predicting highly realistic soil behavior, the results of drained triaxial tests are used [4]. Soil behavior in consolidated isotropic drained triaxial compression (CID test) is well characterized by hyperbolic law [5, 6].

Janbu in [7] suggested a relationship between stiffness and stress state. Dependence of stiffness on stress state and shear deformation was suggested and developed by Duncan and Chang [8]. The tangent stiffness value in isotropic triaxial compression conditions for any stress states can be expressed as:

$$E_t = (1 - R_f S)^2 K p_a \left(\frac{\sigma_3}{p_a} \right)^n, \quad (1)$$

where σ_3 is the minor principal stress; p_a is the atmospheric pressure (100 kPa); K is the modulus number; n is the power for stress-level dependency of stiffness describing the rate of variation E_t and

σ_3 ; $S = \frac{(\sigma_1 - \sigma_3)}{(\sigma_1 - \sigma_3)_f}$; $R_f = \frac{(\sigma_1 - \sigma_3)_f}{(\sigma_1 - \sigma_3)_{ult}}$ is the failure ratio that is always less than one and derived from

test results; $(\sigma_1 - \sigma_3)_f = \frac{2c \cos \varphi + 2\sigma_3 \sin \varphi}{1 - \sin \varphi}$.

Equation (1) characterizes standard consolidated isotropic drained triaxial test performed at a constant minimum stress rate. For evaluating plane and volumetric strains, the specimen destruction and its stress state should be considered with respect to three principal stresses.

The Duncan and Chang variable stiffness model has been widely applied to FEM analyses of soil–structure interaction [9]. For example, the PLAXIS hardening soil model utilizes the dependence that considers cohesion pressure $c \cdot \cot \varphi$ [10]:

$$E_{50} = E_{50}^{ref} \left(\frac{c \cdot \cot \varphi + \sigma_3}{c \cdot \cot \varphi + \sigma_{3ref}} \right)^m, \quad (2)$$

where E_{50}^{ref} is the reference secant modulus at the mobilization of 50 % of the maximum shear strength, corresponding to a reference confining pressure $\sigma_{3ref} = 0.1$ MPa. The E_{50} parameter was considered due to unambiguity of its definition.

Similar general principles using E_{50} stiffness are used in hardening soil models implemented in Midas GTS NX, OPTUM, Z-Soil, etc. software.

At the same time, articles [10–13] proposed more complex variable stiffness models than Duncan and Chang. The most advantageous feature of the variable stiffness models is its simplicity. However, it precludes the coupling between the deviatoric and volumetric components, which is a significant property of dilatant materials such as stiff clay and dense sand. In addition, none of the proposed variable-stiffness models satisfies the continuity condition [14].

The main disadvantage of the described model is the use of isotropic stiffness. Clay soils (especially, dense and stiff) are known to show anisotropy [15–18]: stiffness is different in vertical and horizontal directions. Use of σ_{3ref} equal to effective mean stress is a rough attempt to compensate for this disadvantage. In many researches, triaxial stiffness is obtained from anisotropic triaxial tests [19, 20]. Nonetheless there is the shear creep in a sample which significantly lowers anisotropic stiffness in comparison with values gained during field tests. The shear creep problem is distinguished as independent and in real practice should be solved for particular conditions (slope stability, pile-clay interaction) [21–23]. Most of the models that are currently used do not consider this effect. This is one of the disadvantages of such models, which underestimates settlements in soft clay soils [24].

Another drawback of the currently used models is that the accepted relations do not consider the effect and variation of physical soil properties on stiffness. It is known, that physical (and consequently mechanical) properties could vary in three dimensions. During triaxial compression, the variation of porosity can reach significant values, which noticeably affect the current stiffness [25].

Another essential drawback is that the statistical variability of stiffness is not considered in both horizontal and vertical directions. For most computational problems, the overall results of calculations show good agreement with observational data. In some cases, for sensitive models, stiffness distribution significantly affects the settlement, particularly for those with heterogeneous inclusions [26]. In fact, Paice, Griffiths, and Fenton [27] showed that the average settlement could increase by 12 % with increasing non-uniformity of the soil under foundation. Furthermore, the bearing capacity could change by 20–30 % with the coefficient of variation of the parameters [28]. This significantly affects the design decisions.

Presently, statistical geotechnical models, which take into account the horizontal or vertical distribution of properties, are becoming increasingly widespread [27–29]. Simulations that consider the soil property distribution more accurately reflect soil behavior more realistically [30]. The use of regression relationships and machine learning methods for developing these calculation methods is very promising and it is the most powerful tool for studying the influence of factors on soil properties [31–33].

However, existing correlations seldom incorporate the required input parameters for FEM calculation and they are made for specific regions: a few publications [34–36] present the analysis of a limited number of tests and do not encompass most types of clay soils. In case of variability of physical properties, they do not provide the possibility to evaluate the stiffness with sufficient reliability. The published data do not consider the variability of the soil properties, and therefore, should be used cautiously.

Considering the widespread use of various correlational relationships in engineering practice (at least for preliminary calculations in Russia), a thorough analysis of the experimental data collected for a wide range of clay soils is conducted.

The aim of this study is to obtain empirical equations for stiffness parameters during consolidated isotropic drained triaxial tests depending on age, genesis, stress state and physical properties. The stiffness parameters include E_{50} , E_{ur} , the m -parameter included equation (2), Poisson's ratios in course of primary and unloading/reloading stress path. The data can be applied for estimation of the clay soil stiffness without any further testing. Proposed equations can be used in geotechnical models that allow taking into account variability, horizontal and vertical distribution of stiffness. In general, geotechnical engineers may utilize the obtained results by applying them to design of complex constitutive soil models. The following research is the continuation of the completed work on sands [25].

2. Methods and Materials

2.1. General description of investigated soil

Results of CID triaxial tests were used as the experimental data collected on 15 different construction sites in Moscow (Russia) and Minsk (Belarus) (Fig. 1).

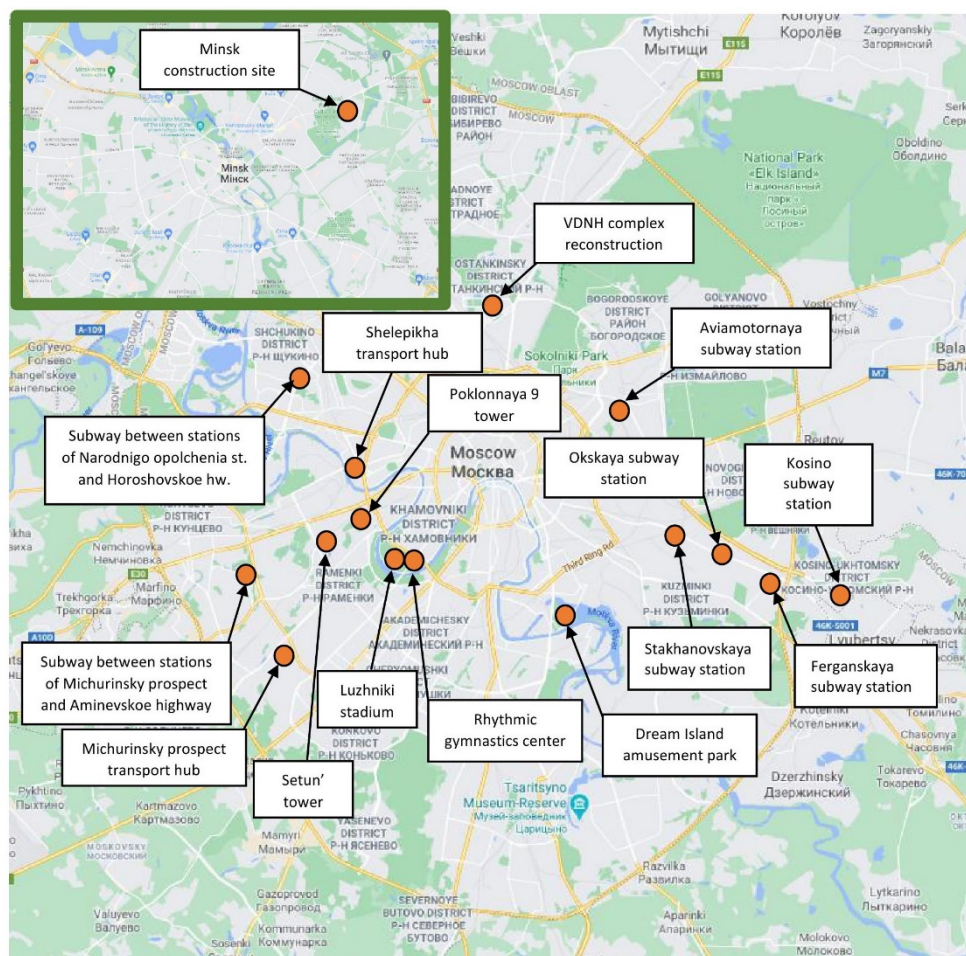


Figure 1. Layout of the construction site locations.

Very stiff and stiff clay soils were collected using single core tube core-barrel and thin wall sampler. Firm-stiff, firm and soft-firm soils were sampled using a thin wall sampler or a single tube core-barrel. The single core tube core-barrel and thin wall sampler equipped with a valve were used for sampling of soft-firm, soft and very soft clays. Sampling of soils was conducted in accordance with the technology described in Interstate Standard GOST 12071-2014 and ISO 22475-1:2006. Diameter of sampled monoliths was in the range of 75...120 mm; height – 100...400 mm.

Clay soils were classified by age and genesis. The physical properties were defined: density and Atterberg limits [37]:

- Plasticity index:

$$I_p = w_L - w_p, \quad (3)$$

where w_L is the liquid limit, defined using Soil Cone Penetrometer according to Interstate Standard GOST 5180; w_p is the plastic limit.

- Liquidity index:

$$I_L = \frac{w - w_p}{w_L - w_p}, \quad (4)$$

where w is the natural moisture.

Clay soils were categorized according to Interstate Standard GOST 25100 depending on plasticity index: at $I_p < 1$ soils are not clayey (and are not subject to study in this research). At $1 \leq I_p \leq 7$ soils are classified as sandy loam; at $7 < I_p \leq 17$ as loam; and $I_p > 17$ as clay.

Liquid limit depends on the testing method. According to International Standard ISO 14688-2:2017 and ASTM D 2487—2017 liquid limit parameter is denoted as LL and calculate using Casagrande method. Transition from LL to w_L is conducted using regional correlations and parallel test data. When there are no such correlations standard GOST 25100 allows the use of the following formula in order to juxtapose parameters of different classifications:

$$w_L = (LL + 8.3)/1.48. \quad (5)$$

Physical and mechanical properties of clay soils are presented in Table 1. The results of 967 consolidated isotropic drained triaxial tests were processed through statistical and regression analysis. Research was carried out for intact structure soils. Before the beginning of the tests, soil samples underwent the B-check procedure in accordance with ISO 17892-9, ASTM D7181 and Interstate Standard GOST 12248.3-2020.

Table 1. Physical and mechanical soil properties of different construction sites.

Construction site	Age and genesis	N	e , e.f.	I_p , e.f.	I_L , e.f.	c , kPa	φ , degree	σ_3 , MPa	E_{50} , MPa	E_{ur} , MPa
Okskaya subway station ^k	fQ	24	0.45–0.76	0.05–0.14	0.05–0.62	27–65	17–31	0.05–0.6	10.8–32.6	–
	gQ	24	0.34–0.49	0.07–0.1	-0.14–0.38	33–98	23–30	0.05–0.25	13.1–39.2	–
	J	51	0.5–1.24	0.08–0.54	-0.29–0.15	40–117	18–26	0.05–0.75	14–52.3	–
Stakhanovskaya subway station ^k	fQ	6	0.55–0.81	0.08–0.14	0.39–0.43	28–45	19–22	0.1–0.55	11.8–22.4	29.4–30.8
	J	18	0.65–1.2	0.21–0.48	-0.22–0.29	43–87	18–23	0.1–0.95	13–36.7	24.6–84.3
	C	12	0.37–0.49	0.12–0.21	-0.4–(-0.3)	110–138	27–30	0.25–1.2	55.9–85.2	133.3–250.0
Luzhniki stadium [41] ^k	J	40	0.77–1.45	0.27–0.66	0.03–0.27	41–111	17–23	0.08–0.35	7.5–20.9	29.1–93.8
Subway between stations Michurinsky prospect and Aminevskoe highway ^k	fQ	13	0.44–0.62	0.08–0.26	0.11–0.64	20–81	16–33	0.03–0.33	5.8–23.2	–
	gQ	14	0.36–0.97	0.12–0.24	0.01–0.40	38–82	16–31	0.02–0.25	6.9–19.8	–
	prQ	5	0.63–0.76	0.18–0.25	0.07–0.34	0.52–63	19–23	0.01–0.035	2.7–13.8	–
	J	49	0.50–1.43	0.08–0.58	-0.26–0.55	25–170	13–31	0.38–1.25	18.4–52.3	167.6–270.4
Subway between stations of Narodnigo opolchenia street and Khoroshovskoe highway ^k	C	4	0.47–0.77	0.08–0.40	0.00–0.73	–	–	1.11–1.24	38.0–82.3	–
	fQ	12	0.45–2.01	0.07–0.44	0.00–0.72	17–28	32–34	0.14–0.18	5.6–18.5	31.7–107.7
	gQ	12	0.35–0.53	0.11–0.15	0.25–0.49	41–48	29	0.07–0.09	7–13.3	44.9–65.1
	K	6	0.66–0.74	0.11–0.17	0.27–0.70	43	27	0.167	13.4–24.5	91.1–128.6
Kosino subway station ^{a,k}	J	66	0.56–1.29	0.09–0.60	0.01–0.48	44–106	17–31	0.12–0.57	11.9–27.9	21.0–198.4
	C	12	0.44–0.86	0.04–0.26	-0.11–0.48	35–84	24–37	0.17–0.68	19.7–29.4	46.8–172.1
	J	17	0.59–1.31	0.17–0.47	-0.35–0.07	179	13	0.36–0.96	9.1–28.1	51.3–184.4
Minsk construction site ^s	fQ	22	0.16–0.69	0.04–0.09	-2.85–0.97	18–28	38–40	0.05–1.3	16.3–20.9	242.1–412.9
	gQ	73	0.14–0.48	0.02–0.08	-2.95–1.56	15–46	37–38	0.05–1.45	8.2–152.5	57.3–443.9
VDNH complex reconstruction ^k	aQ	17	0.33–0.74	0.06–0.11	0.25–0.98	4–32	35–41	0.24–0.37	18.9–38.5	121.2–262.9
Aviamotornaya subway station ^k	fQ	10	0.45–0.70	0.05–0.16	0.27–0.74	8–59	20–32	0.05–0.19	4.3–24.3	59.4–142.9
	gQ	7	0.49–0.51	0.12–0.14	0.51–0.57	24	28	0.03–0.04	2.5–8.5	29.1–45.5
	J	64	0.46–0.98	0.14–0.51	0.03–0.49	47–93	18–31	0.20–0.29	12–27.5	47.1–138
	C	73	0.43–0.39	0.06–0.25	-0.15–0.94	18–163	15–41	0.28–0.74	16.2–45.4	49.7–255.3
Shelepikha transport hub ^k	J	6	1.08–1.52	0.47–0.50	-0.03–0.31	54–96	16–21	0.07–0.1	8.1–10.6	20.1–34.3
	C	23	0.39–1.03	0.07–0.33	-0.22–0.93	20–82	23–36	0.16–0.69	19.7–46.5	59.9–166.3
Setun' tower [35] ^s	aQ	7	0.41–0.53	0.05–0.46	0.59–1.09	31	23–28	0.19–0.24	3.4–39.7	48.7–283.0
Michurinsky prospekt transport hub ^k	J	24	0.48–1.0	0.07–0.35	-0.54–0.78	31–90	20–30	0.5–0.79	6.8–53.6	53.9–296.2
	fQ	6	0.56–0.58	0.11–0.12	0.46–0.47	24–30	18–23	0.16–0.66	4.6–21.5	–
	gQ	27	0.45–0.58	0.11–0.12	0.34–0.50	28–39	20–24	0.18–0.92	8.3–24.7	–
Luzhniki rhythmic gymnastic center ^k	J	36	0.81–1.20	0.22–0.44	0.04–0.19	73–104	18–23	0.19–0.99	10.9–31.3	–
	J	18	0.69–1.4	0.21–0.58	0.02–0.50	44–117	17–22	0.2–0.4	12.6–18.3	–
Dream Island amusement park ^s	aQ	22	0.51–1.87	0.1–0.25	-0.19–1.03	12–57	6–26	0.08–0.85	1.9–31.2	–
	J	5	0.54–1.18	0.1–0.40	-0.34–0.17	37–72	20–28	0.16–0.76	16.8–42.2	–
Poklonnaya 9 tower ^{a, k}	J	4	0.93–1.18	0.24–0.58	-0.08–0.14	153	11	0.4–0.6	11.5–24.6	–
Ferganskaya subway station ^s	J	42	1.0–1.35	0.23–0.45	-0.29–0.05	48–94	18–24	0.2–1.0	16.8–42.1	–

a – tests processed by the author; k – strain-controlled loading mode; s – stress-controlled loading mode; Q – Quaternary age (a for alluvial deposits, f for fluvio-glacial and limnoglacial, g for glacial), J – Jurassic age, C – Carboniferous

The initial diameter of the test specimen varied from 38 to 50 mm and $H/D=2$. Deviator stress was applied under the stress-controlled or strain-controlled loading mode. Though the loading type is pivotal, according to many studies [39, 40], it mainly affects the post-peak parameters which are not considered here.

The test procedure was performed according to Interstate Standard GOST 12248.3-2020 and conformed to ASTM D7181 and ISO 17892-9.

The research was carried out on the soil that comprised Quaternary (alluvial, fluvio-glacial, limnoglacial and glacial), Jurassic (Volgian, Oxfordian and Callovian stages) and Carboniferous (Kasimovsky, Myachkovsky, Neverovsky, Proterozoic, Ratmirovsky, Suvorovsky and Voskresensky stages) deposits. Organic soils were not considered. The depth of sampling varied within 0.6–99.6 m.

The following parameters were determined from CID triaxial test results: secant modulus at 50 % strength E_{50} ; unloading/reloading modulus E_{ur} (Fig. 2); Poisson's ratio ν ; unloading/reloading Poisson's ratio ν_{ur} ; effective angle of friction φ and effective cohesion c .

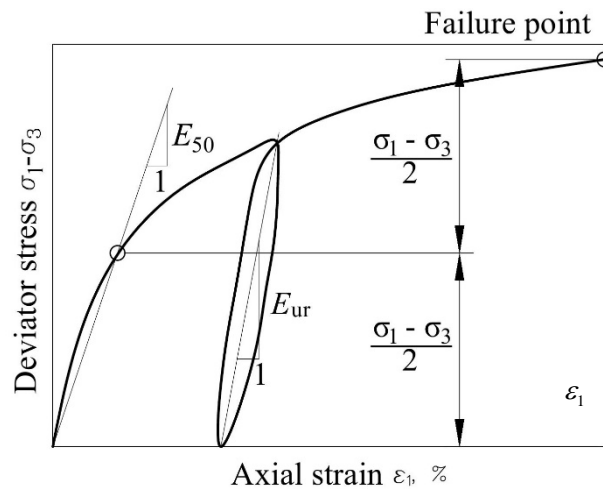


Figure 2. Definition of stiffness parameters.

2.2. Methods

The correlation and regression statistical data analysis technique was employed using MS Excel and IBM SPSS Statistics. The following stiffness parameters were analyzed: stiffness E_{50} and E_{ur} , Poisson's ratios ν and ν_{ur} , and the ratio of unloading/reloading modulus and secant modulus at 50 % strength:

$$k_E = \frac{E_{ur}}{E_{50}}. \quad (6)$$

At present, these parameters are used as input data for FEM computation for the hardening soil models and are of greatest interest for geotechnical engineers.

It should be noted that the ratio between E_{50} , E_{oed} and E_{ur} is not constant and depends on the soil type [10]. The k_E parameter was introduced for statistical analysis similarly to sand stiffness [25].

The experimental approach is as follows.

In the first stage, the experimental data were incorporated in a total sample. The strength of relationships was estimated via correlation analysis without considering the age and genesis. The Pearson's correlation coefficient ρ , significance level (using p-value), and sample correlation ratio η [42] were calculated via statistical analysis.

The Pearson's correlation coefficient ρ is widely used in statistical analysis. It evaluates the correlation relationship among the parameters and lies in the ranges from -1 to $+1$. The closer its value to $+1$ (or -1), the stronger the degree of linear relationship between the parameters is. If the ρ value is close to zero, it indicates a weak linear strength of relationship

The correlation parameter η is the ratio of a between-group dispersion to the total dispersion. It estimates the strength of the non-linear correlation relationship between the parameters and ranges from zero to one. If η is close to zero, the strength of the relationship is weak or does not exist; if it is close to one, the relationship is strong. The correlation ratio and the Pearson's correlation coefficient satisfy the condition $\eta \geq \rho$.

The correlation analysis revealed the most significant factors and nature of the relationship (linear or non-linear). Relationship in correlation interaction was analyzed at the significance level $\alpha = 0.05$. This corresponds to the Interstate Standard GOST 20522-2012 requirements for calculating soil safety factor.

It is well known that stiffness depends on the soil density, stress state, and strength [7, 43–44]. Therefore, the following factors that are considered to affect the soil stiffness were analyzed:

- physical properties: initial void ratio e , plasticity index I_p and liquidity index I_L ;
- stress state considered as radial stress σ_3 and relative radial stress [45] that is expressed as:

$$RRS = \frac{c \cdot \cot \varphi + \sigma_3}{c \cdot \cot \varphi + \sigma_{3ref}}; \quad (7)$$

- strength properties: the friction angle φ , cohesion c , and cohesion pressure $H = c \cdot \cot \varphi$;
- stiffness parameters: E_{50} , E_{ur} , and the Poisson's ratios ν and ν_{ur} .

Relative radial stress RRS reflects stress state in stiffness calculation in the Hardening soil model proposed by Schanz et al [45]. The advantage of the RRS parameter in comparison with σ_3 is in taking into account the cohesion pressure $H = c \cdot \cot \varphi$, which may lead to significant adjustments to stiffness in overconsolidated clay soils with high cohesion. The RRS parameter includes the reference radial stress and treats the dependency of stiffness properties on the soil stress state. Here, the reference pressure σ_{3ref} is considered as 0.1 MPa.

These stiffness parameters were chosen because they were used to characterize sand during engineering surveys at different construction sites (at least in Russia) and in FEM calculations.

In the second stage, the influence of stress state, density and Atterberg limits was studied in detail, based on the age and genesis. Clay deposits were divided into three groups according to age: Quaternary (Q), Jurassic (J) and Carboniferous (C). The Quaternary deposits were then divided into two subgroups depending on the deposition mode: alluvial, fluvio-glacial and limnoglacial (further denoted as aQ), glacial (further denoted as gQ). It is worth mentioning that genesis alluvial, glaci-fluvial, limnoglacial deposits is different, however it was found out during the analysis that genesis had no statistically significant effect on the clay stiffness. Therefore, the mentioned soils were united into one subgroup. The Jurassic and Carboniferous clays were not divided by genesis.

3. Results and Discussion

3.1. Analysis of the total sample

The relationships between all parameters are highly non-linear (Table 2). The radial stress σ_3 and RRS considerably affect the clay soil stiffness parameters E_{50} , E_{ur} . The stiffness/ RRS relationship is 25 % stronger than the stiffness/ σ_3 relationship associated with the strength parameters considered in RRS , which is 2.5 times higher than in a similar research for sands [25]. At the same time, η between RRS and E_{50} or E_{ur} exceeds ρ by 1.5–2.3 times and η is close to one. This indicates a non-linear relationship. Therefore, it is preferable to use RRS for a more effective description of the relation between stiffness and stress state.

However, pressure factor exerts a lower degree of influence in clayey soils than in sands as shown in a similar research [25]. Clay particle content, density and moisture have additional influence, which is confirmed by the high values of correlation parameters η and ρ between stiffness and e_i , I_p and I_L .

Non-linear behavior prevails here, and η exceeds ρ by 1.3–3.5 times. Similar non-linear influence was reported for sands in [4, 7, 25]. Moreover, the same relationship can be observed during triaxial or oedometer tests. When analyzing the stiffness according to triaxial test results, the essential non-linear influence of the void ratio and I_L (due to moisture change during squeezing water out of sample during the test) should be taken into account.

The overconsolidation ratio (OCR) is another significant factor influencing the stiffness. Due to lack of the data, the OCR was not considered within this work. Though, the OCR can be interpreted indirectly through I_L : the more overconsolidated the soil, the lower I_L . High strength of the relationship between I_L and E_{50} indicates the vital influence of overconsolidation on stiffness during the primary loading. At the same time, the relationship between I_L and E_{ur} is not statistically considerable, which means that unloading of the sample in drained triaxial test is located in elastic region. Unloading of the sample takes place under average pressure lower than preconsolidation pressure for each sample.

Table 2. Estimation outcome for the correlated parameters for the total sample.

Stiffness parameter		Factor											
		e_i	I_p	I_L	σ_3	RRS	ϕ	c	H	E_{50}	E_{ur}	ν	ν_{ur}
E_{50}	ρ	-	-	-	0.518	0.649	0.393	-0.03	-0.09	-	-	-	-
	η	0.239	0.162	0.441	0.797	0.980	0.733	0.722	0.778	-	-	-	-
	N	955	950	950	967	963	963	963	963	-	-	-	-
E_{ur}	ρ	-	-	-	0.336	0.398	0.310	-	-	0.676	-	-	-
	η	0.361	0.326	0.053	0.769	0.930	0.720	0.846	0.931	0.954	-	-	-
	N	371	371	371	375	371	371	371	371	362	-	-	-
ν	ρ	-	-	-	0.071	-	0.009	-	-	-	0.015	-	-
	η	0.242	0.274	0.326	0.707	0.686	0.707	0.352	0.930	0.707	0.719	-	-
	N	656	649	649	658	654	654	654	654	649	335	-	-
ν_{ur}	ρ	0.053	0.086	-	0.03	0.005	-	0.035	0.037	0.157	-	-	-
	η	0.681	0.496	0.648	0.699	0.742	0.450	0.607	0.686	0.853	0.877	1	-
	N	265	265	265	267	267	267	267	267	267	266	267	-
k_E	ρ	-	-	-	0.006	0.073	-	-	-	-	0.475	0.006	0.103
	η	0.245	0.275	0.232	0.721	0.781	0.661	0.705	0.811	0.910	0.996	0.704	0.839
	N	349	349	349	353	353	353	353	353	353	353	334	265

- correlation relationship at significance level $\alpha = 0.05$

Similar to sands [25], the direct relationship between stiffness and strength is statistically significant, but it is weak. Poisson's ratio ν exhibits a weak relationship with physical properties. Meanwhile, the ν_{ur} does not statistically relate to the analyzed factors. Boguz and Witowski had similar outcomes for glacial sediments in Poland [46].

The k_E ratio has a weak relationship with the parameters investigated. At the same time, the relationship between k_E ratio and physical parameters is relatively significant. However, the relationship between E_{ur} and E_{50} is non-linear. With an increase in E_{50} due to an increase in confining pressure and change of physical parameters e , I_p and I_L . The stiffness E_{ur} increases less intensively (Fig. 3).

Nevertheless, for the sake of convenience, a linear relationship is appropriate because $\rho = 0.676$ is close to $\eta = 0.954$. It is worth mentioning that the determined strength of the relationship is significantly higher than that described previously [35]. This depends on the volume of the data sample and on the wide range of measurements.

In general, the following conclusions can be drawn based on the performed analysis of the total data sample:

- stiffness of clay soil essentially depends on the radial stress, clay particle content, density and moisture and to a lesser extent, on the strength parameters;
- stiffness E_{ur} does not depend on the degree of overconsolidation;
- stiffness parameters E_{50} and E_{ur} are strongly related to each other;
- the Poisson's ratio ν slightly depends on the physical properties of clayey soil; ν_{ur} coefficient does not depend on physical and mechanical properties of soil.

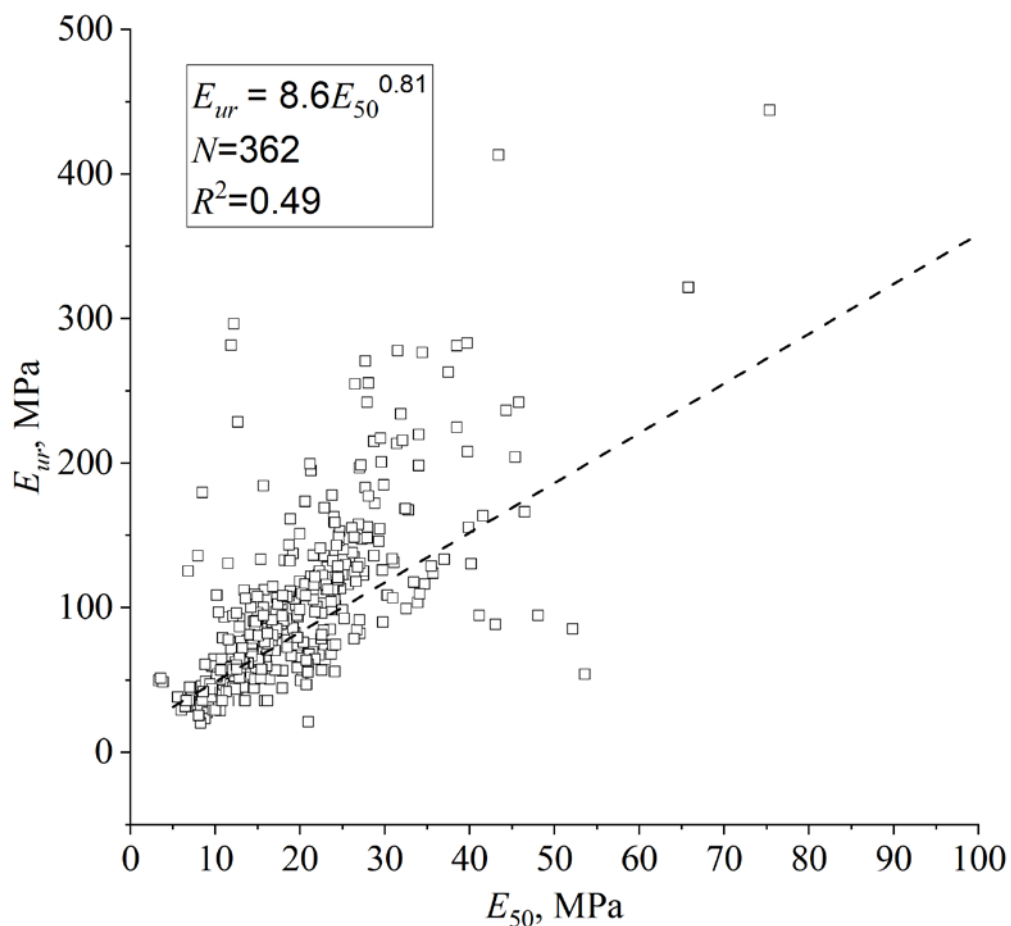
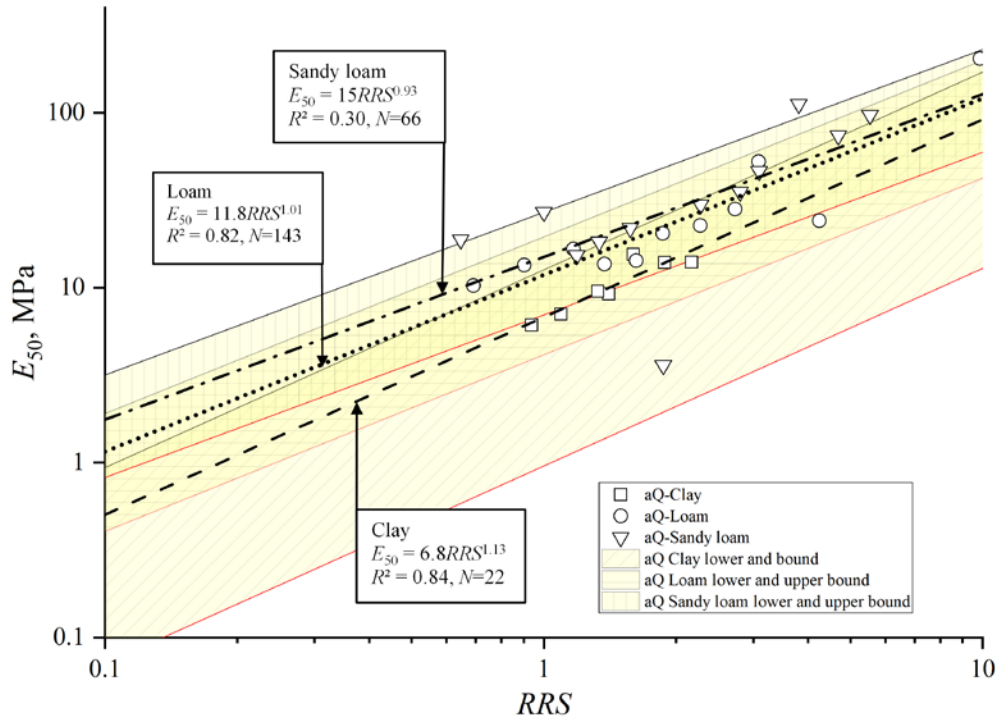
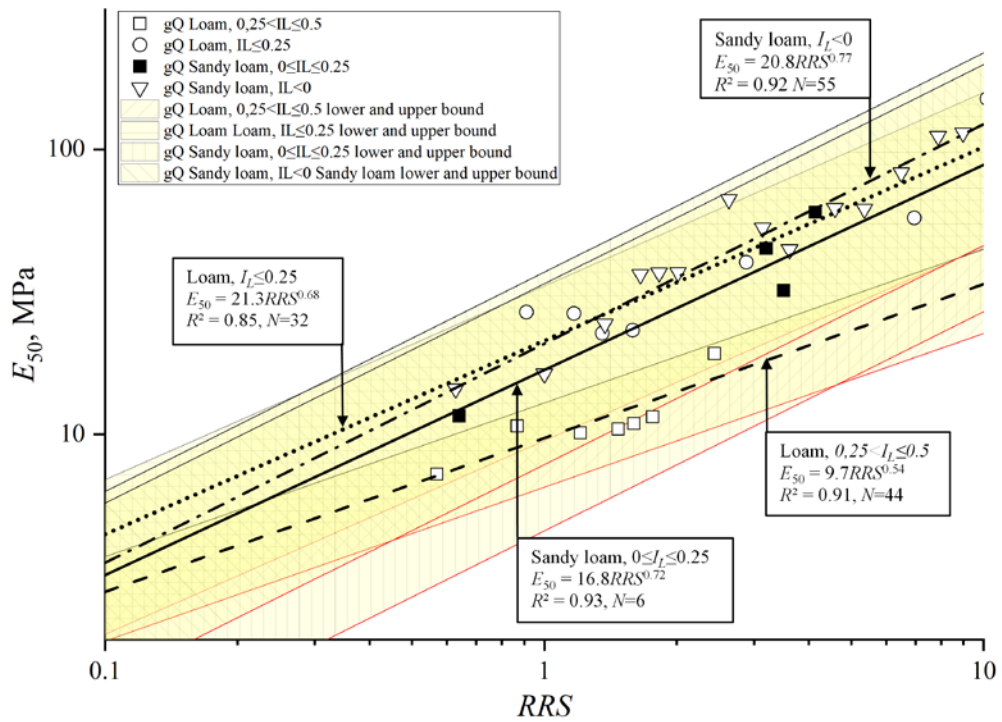


Figure 3. Relationship between stiffness moduli of the total sample $E_{50} - E_{ur}$.

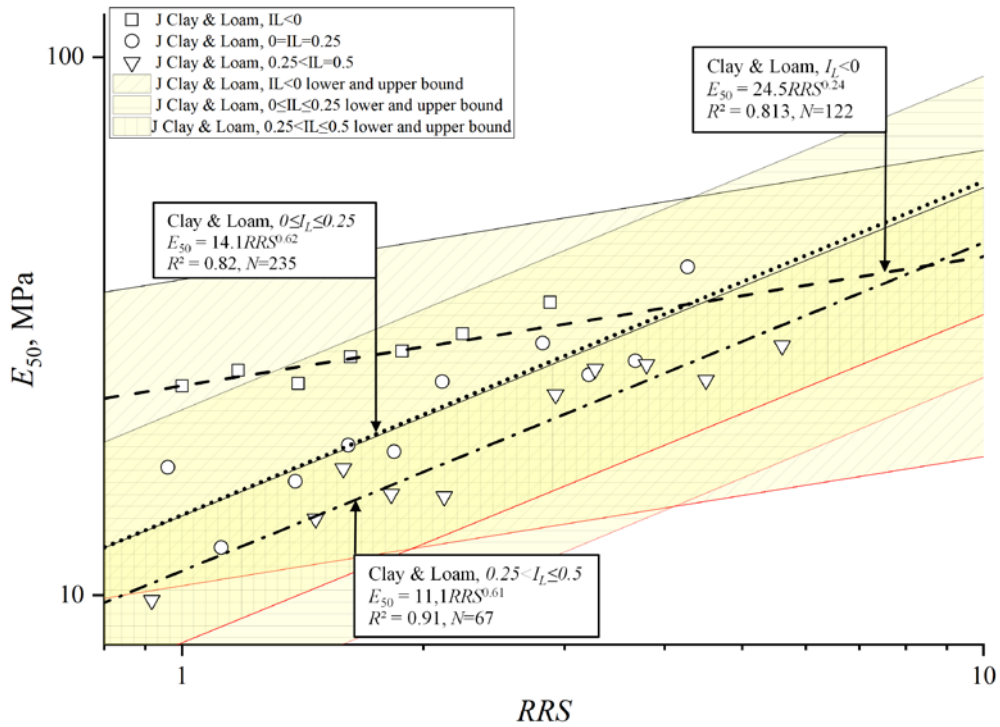
3.2. Influence of the physical parameters and radial pressure on E_{50}



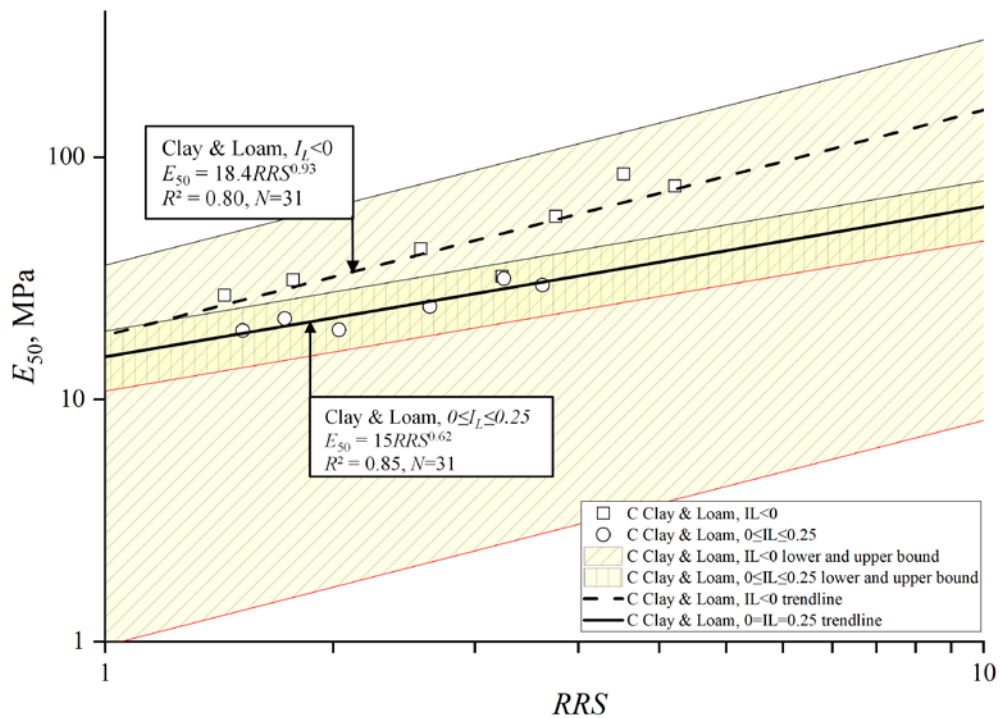
a)



b)



c)



d)

Figure 4. Influence of the relative radial stress on stiffness E_{50} for: alluvial, fluvio-glacial and limnoglacial (a); glacial (b); Jurassic (c); Carboniferous (d) deposits.

Based on the empirical data, the diagram showing the dependency of RRS on stiffness E_{50} was drawn (Fig. 4). Lower and upper bounds correspond to the significance level $\alpha = 0.05$. It is important to highlight relatively low values of E_{50} for Carboniferous clays. In natural stratification in Moscow region

Carboniferous clays alternate with limestones and their stiffness in-situ is near 70–200 MPa [47]. Therefore, the data for Carboniferous formations should be calibrated using results of in-situ plate-load and pressuremeter test.

Fig. 4 provides quantitative and qualitative assessment of the effect of RRS on the measured parameters, depending on clay particle content and moisture. In alluvial, glaci-fluvial and limnoglacial quaternary clay deposits, with increasing of the plasticity index I_p , the intensity of the RRS influence reduces. At the same time, there is no such phenomenon in overconsolidated glacial deposits. It is connected with historic hardening (overconsolidation) and structural strength. This can be observed in Jurassic clays (Fig. 4c) where for the most overconsolidated soils with $I_L < 0$ the intensity of E_{50} growth decreases by 2.6 times with the growth of RRS .

In case of sands, stiffness has strong correlation with stress state and density [25, 48], whereas in clay soils clay particle content and degree of overconsolidation (which is expressed through I_p and I_L) are more significant. In addition to mentioned parameters, density has essential impact on clay soil stiffness E_{50} (Fig. 5). The greatest influence was seen in quaternary deposits, where with growing void ratio stiffness parameter E_{50} decreases according to the power law ($R^2 = 0.658–0.955$) and shows weak dependency on soil consistency. For overconsolidated Jurassic and Carboniferous soils the relation between E_{50} and e is mainly characterized as weak and notable, respectively, and can be described with a linear relationship.

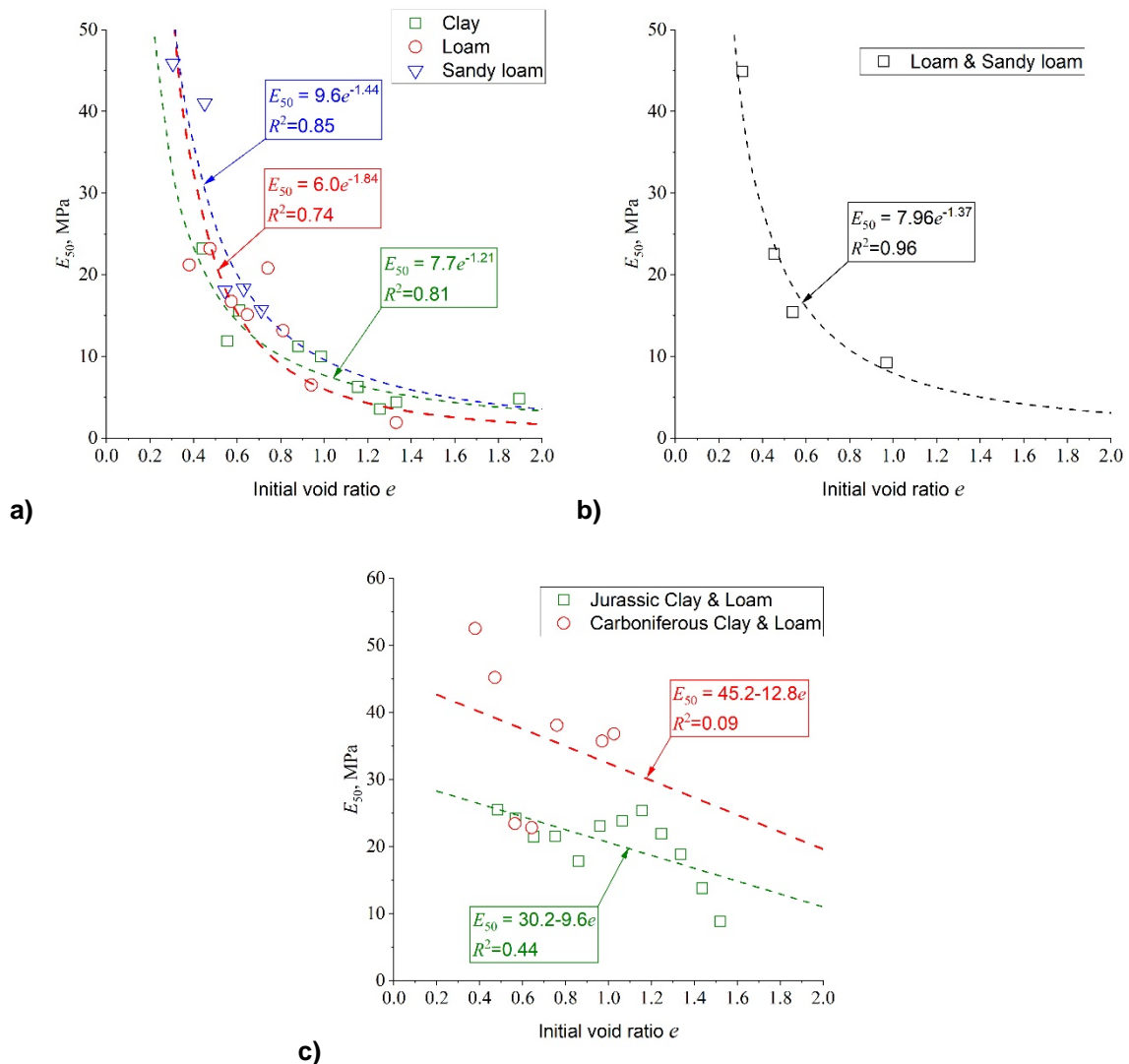


Figure 5. Influence of the void ratio on sand stiffness E_{50} for: alluvial, fluviglacial, limnoglacial (a); glacial (b); Jurassic and Carboniferous (c) deposits.

The relationship incorporating the combined effect of the confining pressure and physical characteristics on the clay soils stiffness is shown above. Considering the processed data of a large number of triaxial tests performed on various types of clay soils, the following empirical dependence was proposed:

$$E_{50} = a_1 RRS + a_2 e + a_3 I_p + a_4 I_L + a_5. \quad (8)$$

The empirical coefficients a_1 , a_2 , a_3 , a_4 and a_5 can be defined for all types of clay soils. Accordingly, Table 3 presents a_1 , a_2 , a_3 , a_4 and a_5 values in dependence of soil age and genesis in the Moscow and Minsk regions. Fig. 6 shows the results of comparing the calculated and actual values of E_{50} . The use of the polynomial function is due to the large number of initial parameters. Other multifactor models (linear and non-linear) [49] produced similar or less significant results. The values observed and calculated, when compared using Fisher's test, do not reveal any statistically significant difference at the bilateral significance level $\alpha = 0.05$.

Table 3. Empirical coefficients of regression equation for E_{50} in relation to age and genesis of the deposits.

Coefficients of regression equation for E_{50}	Quaternary			
	Alluvial, fluvioglacial and limnoglacial	Glacial	Jurassic	Carboniferous*
a_1	14.2	8.6	4.3	9.2
a_2	-6.2	-38.6	-3.5	44.8
a_3	-23.9	-144.6	-6.5	-162.2
a_4	-11	-3.5	-25.7	-76.1
a_5	7.8	38.7	20.7	19.4
Multiple ρ	0.851	0.858	0.687	0.874
Multiple R^2	0.724	0.736	0.472	0.764
	<i>Ranges of parameters</i>			
RRS	0.57–9.85	0.33–12.27	0.76–7.68	1.3–4.08
e	0.18–2.01	0.14–0.58	0.45–1.52	0.37–1.03
I_p	0.04–0.46	0.03–0.16	0.07–0.66	0.12–0.33
I_L	-0.62–1.09	-2.95–1.56	-0.56–0.78	-0.43–0.23

* This estimation needs to be accounted for, since these clays have inclusions of semi-rocky carbonaceous soils and, in fact, the actual deformation modulus value for such soils is much higher than the one stated [47].

The existing scatter can be attributed to the large sample size, in-between laboratory error in stiffness measurement and influence of other factors [50]. Empirical correlation is limited by the range of physical properties of soils, as shown in Table 3.

In addition, E_{50} , defined according to Equation (8), was compared with other published test results (Table 4). Offshore, organic, artificially compacted deposits were not considered, due to the special features, which were not considered in these researches. The stiffness obtained during the undrained and anisotropic triaxial tests was not considered due to different stress-strain state.

The analysis of the open-source data showed that the volume of CID triaxial test results is quite insignificant. Nevertheless, the available volume of data allows us to assess the proposed equation.

Test results obtained by the other researchers are plotted in Fig. 6. The values of E_{50} in Table 4 fall within the same range as those corresponding to the Moscow and Minsk regions mentioned in Table 1. Results obtained using Equation (8) agree well with experimental data.

The best agreement of the suggested equation with the actual data was revealed for the overconsolidated glacial soils. Moreover, soils in Eastern Europe and the USA also agreed well. This confirms the dependence of soil genesis on its stiffness.

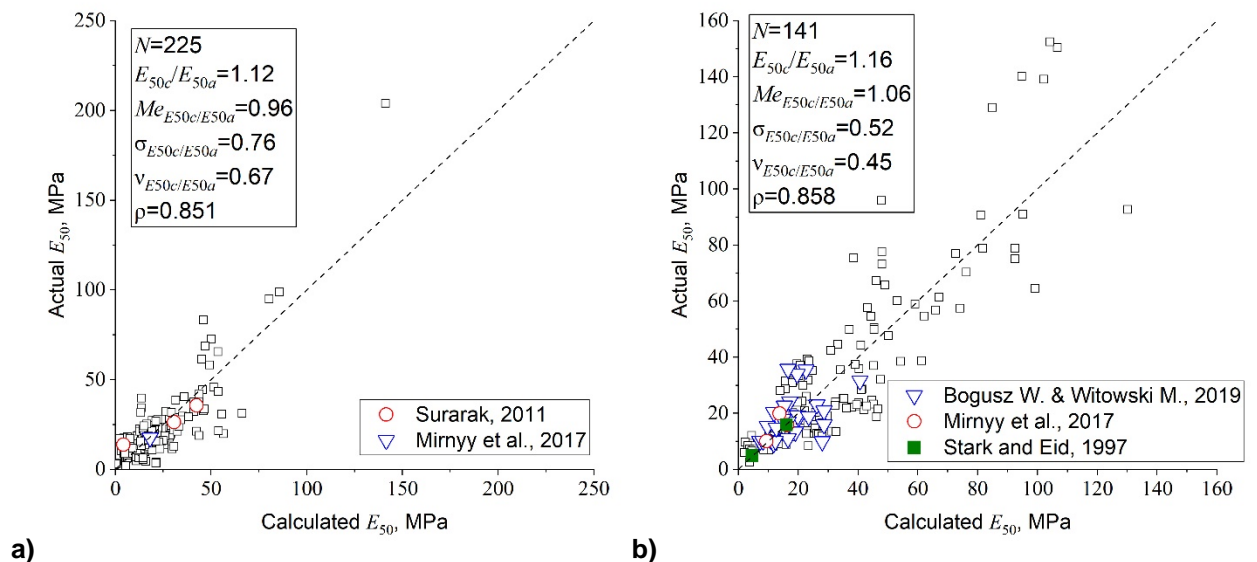
On the other hand, comparison of stiffness modulus of Jurassic Oxford clay at a site near Bedford [51] with the one calculated using Equation (8) showed that values are in the same range as Moscow ones; the difference between calculated and actual values of E_{50} is 1.9...2.6 times with similar physical properties. Both clays are highly overconsolidated as a result of great depths of overlying sediments in the past. At the same time, Jurassic Oxford clays of Moscow have greater stiffness. This might be the reason of different sliding surfaces development: specifically, during landslides in Bedford, the sliding surface was formed in Jurassic clay, near the ground surface; in Moscow, the sliding surface was formed on the border of Jurassic clay with quaternary deposits [52].

Equation (8) can be used for a generalized evaluation of soil stiffness with sufficient engineering accuracy. The comparison analysis of the foreign data confirms the conclusion that the stiffness of the Moscow and Minsk Quaternary glacial till insignificantly differs from the glacial till of the other regions.

Table 4 Summary data used for comparison with the results obtained using Equation (8).

Reference	Soil region	Age and genesis	N	e , e.f.	I_p , e.f.	I_L , e.f.	σ_3 , MPa	E_{50} , MPa	E_{ur} , MPa	m
Surarak et al [34]	Bangkok (Thailand)	aQ	3	1.2	0.41	0.07	0.1–0.55	13.8–35.7	–	0.48
Mirnyy et al [35]	Moscow (Russia)	aQ	18	0.85	0.12	0.625	0.223	17.6	135	0.35
		gQ	54	0.55	0.12	0.375	0.14–0.285	10.1–19.9	59.2–86.8	0.53–0.62
		J	18	0.77–1.2	0.15–0.42	0–0.375	0.565–0.633	22.8–36.9	73.9–132.0	0.30–0.31
	C	24	0.6	0.17	0.25	0.675	23.2	109.0	0.35	
W. Bogusz and M. Witowski [36, 53]	Poland	gQ	27	0.37	0.151	0.19	0.045–0.800	9.3–35.7	–	0.54
T. Stark and H. Eid [54]	Urbana, Illinois (USA)	Glacial till gQ	2	0.85	0.08	-0.95	0.07–0.275	5–16*	–	–
R. Parry [51]	Bedford (UK)	Oxford clay J	3	0.68–1.07	0.45	0.11	0.07–0.21	5.6–9.7*	–	0.7*

* – stiffness calculated by the author



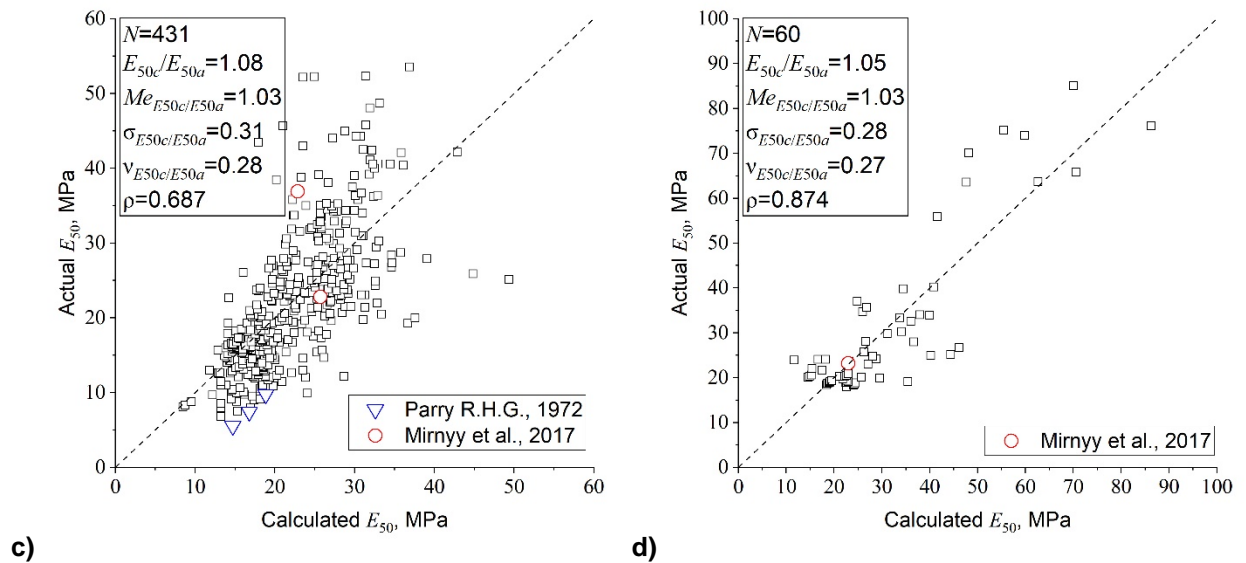


Figure 6. Comparison results for the calculated and actual E_{50} as regards: alluvial, fluvio-glacial and limnoglacial (a); glacial (b); Jurassic (c) and Carboniferous (d) deposits.

3.3. Analysis of the power-law coefficient m

The state-of-art non-linear models with isotropic hardening treat the relation between the stiffness and stress state based on Equation (2). Parameter m is used in the models that consider the dependence between stiffness and stress state [7, 8, 45]. The m can be obtained both on the basis of oedometer tests (to identify the compression law) and on the basis of triaxial compression (to identify the dependence of stress state on the shear stiffness) [25].

Table 5 shows the values of m calculated using Equation (2) for the Quaternary and pre-Quaternary clay deposits. For the Quaternary deposits the value of m tends to increase with the increasing I_p and decreasing I_L . For lightly overconsolidated soils (aQ4), the m -values tend to 1. Similar values are obtained for Thailand soils [34].

For the glacial soils the m parameter varies slightly and lies in the range 0.54...0.77. These values are also close to the glacial soils, which were analyzed for Poland [36], where m values are equal to 0.49...0.516. Parameter m in overconsolidated glacial soils is approximately twice lower than in normally consolidated ones. In other words, the influence of stress state on stiffness in overconsolidated soils (2) is less than in lightly or normally consolidated clays. For example, for overconsolidated Jurassic clays m is equal to 0.24–0.62, for Carboniferous clays its range is 0.62–0.93. Similar findings were obtained for sands, when in loose soils m values were higher [25]. The processed CID triaxial test results [51] showed that for Jurassic clays m value is equal to 0.7.

Parameter m depends on formation conditions and degree of consolidation of clay soils. For overconsolidated soils, it is difficult to find any reliable correlations between m and moisture and density.

Nowadays, m parameter might be obtained based on both triaxial and oedometer tests. In case of sand, there are acknowledged data about decreasing of m with increasing void ratio [4]. If m values obtained by Mirnyy [35] using an oedometer test are compared with triaxial test results, the latter are twice greater.

Table 5. Values of the power-law coefficient m .

Age	Soil type	N	m	
Quaternary	Clay	22	1.13	
Alluvial, fluvioglacial and limnoglacial	Loam	143	1.00	
	Sandy loam	66	0.94	
	Loam	$I_L \leq 0.25$	32	0.68
Glacial	Loam	$0.25 < I_L \leq 0.50$	44	0.54
	Sandy loam	$I_L < 0$	55	0.77
		$0 \leq I_L \leq 0.25$	7	0.72
		$I_L < 0$	122	0.24
Jurassic	Clay and loam	$0 \leq I_L \leq 0.25$	235	0.61
		$0.25 < I_L \leq 0.50$	67	0.62
		$I_L < 0$	31	0.93
Carboniferous	Clay and loam	$0 \leq I_L \leq 0.25$	31	0.62

3.4. Analysis of k_E ratio

Fig. 7 illustrates the correlation between k_E obtained using equation (6) and void ratio for different ages and I_p and I_L for clay soils. It can be observed that with the growth of void ratio k_E noticeably tends to decrease. The correlation has mainly linear character. The mentioned fact, on the one hand, contradicts the research results of Z.G. Ter-Martirosyan et al. [55], where the relation between unloading/reloading stiffness and primarily loading stiffness grows with the increase of void ratio. On the other hand, in [55] the research was carried out based on in-situ plate load test, during which compaction with minor lateral extension takes place. Moreover, there is a lack of data about the deformation interval during which the unloading was carried out, which might affect the results.

The k_E parameter takes into account the development of shear deformation with a slight change in volume (for clay soils the dilatancy can be disregarded). A decrease in k_E with an increase in the void ratio is associated with a difference in the intensity of changes in E_{ur} and E_{50} with a change in e .

For practical application k_E is useful for the E_{ur} stiffness estimation. Coefficient k_E might be determined based on the below given equation of regression, and depends on the physical parameters of e , I_p and I_L :

$$k_E = b_1 e + b_2 I_p + b_3 I_L + b_4 \quad (9)$$

The results of the empirical coefficients are shown in Table 6. It should be considered that E_{ur} is stress-dependent and should be evaluated based on RRS .

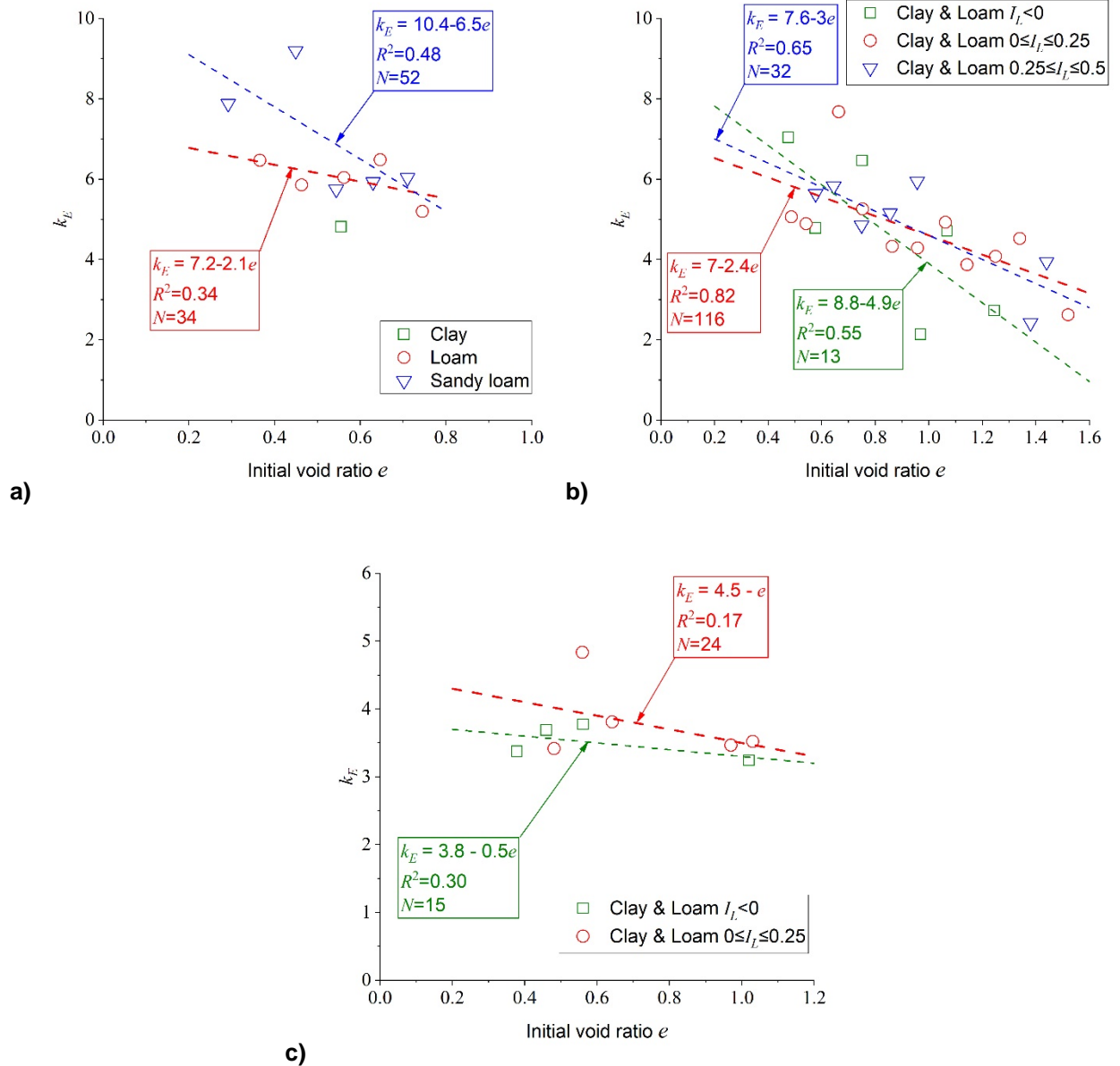


Figure 7. Diagrams of k_E dependency on void ratio e for Quaternary (a), Jurassic (b), and Carboniferous (c) soils.

Table 6. Empirically determined coefficients in the equation of regression for k_E in relation to the deposits age and genesis.

Coefficients of regression equation for k_E	Quaternary			Jurassic	Carboniferous
	Alluvial, fluvio-glacial and limnoglacial	Glacial			
b_1	-2.5	-4.8	-4.5	1.9	
b_2	-2.2	-52.4	2.5	-17.3	
b_3	1.3	2.1	7.2	2.7	
b_4	7.8	13.1	7	6.5	
Multiple ρ	0.346	0.422	0.516	0.530	
N	64	36	176	30	

3.5. Analysis of Poisson's ratio

The outcome of the statistical analysis of Poisson's ratios ν and ν_{ur} is given in Table 7. The Poisson's ratio ν ranges from 0.09 to 0.45, and the average values are in the range of 0.29...0.36 and weakly depend on the age and type of clay soil. A similar feature is observed for the unloading/reloading Poisson's ratio ν_{ur} , which ranges from 0.11 to 0.41 with averages of 0.17...0.20. Besides, the variation coefficients at most do not exceed 0.3, which demonstrates the weak variability of these parameters. For preliminary calculations, the values of the Poisson's ratios given in Table 7 can be used.

Table 7. Results of the statistical analysis of Poisson's ratios.

Soil type	N	Average	Median	Standard deviation	ν_{σ}	Min.	Max.
Poisson's ratio ν							
Quaternary age							
Clay	30	0.35	0.35	0.04	0.11	0.23	0.40
Loam	132	0.33	0.35	0.05	0.14	0.09	0.45
Sandy loam	34	0.32	0.34	0.06	0.17	0.18	0.38
Jurassic age							
Clay	288	0.29	0.29	0.06	0.21	0.11	0.42
Loam	51	0.32	0.34	0.05	0.14	0.21	0.40
Carboniferous age							
Clay	38	0.33	0.35	0.06	0.17	0.20	0.40
Loam	6	0.36	0.36	0.02	0.05	0.34	0.37
Unloading/reloading Poisson's ratio ν_{ur}							
Quaternary age							
Clay	4	0.27	0.29	0.05	0.20	0.19	0.31
Loam	41	0.17	0.17	0.02	0.13	0.12	0.20
Sandy loam	18	0.19	0.16	0.09	0.45	0.12	0.39
Jurassic age							
Clay	92	0.18	0.16	0.07	0.37	0.10	0.41
Loam	20	0.20	0.19	0.04	0.19	0.14	0.27
Carboniferous age							
Clay	30	0.19	0.18	0.06	0.30	0.11	0.35

4. Practical application of the research results

The conducted analysis represents a degree of influence of age, physical properties (clay particle content, moisture and density) and initial stress rate on stiffness of clay soils. For geotechnical calculation purposes the subjects of greater interest are E_{50} , E_{ur} and m parameters.

In some cases, the cost of soil testing can be optimized for acceptance of stiffness characteristics when performing the preliminary calculations. To obtain the final stiffness characteristics for specific soils, it is necessary to confirm the characteristics by direct tests.

Moreover, obtained equations (8) and (9) might be used in geotechnical models, which consider statistical variation of stiffness in three dimensions due to the differences in physical properties and stress state. For example, soil moisture might vary in depth depending on the ground water level and pore pressure distribution. The closer soil is to gravitational water (for instance, in contact with saturated sand), the greater the moisture is. Therefore, I_L in this zone will be higher than normal which significantly reduces soil stiffness.

The suggested equations (8) and (9) can become the basis for constitutive models, where dependence of void ratio change, and, consequently, soil moisture during the volume change is realized. Such an approach was put into practice in sandy soils, where stiffness changed depending on density [25].

In general, geotechnical engineers may utilize the obtained results, applying them to the simulation of complex constitutive soil models.

5. Conclusions

1. The results of 967 consolidated isotropic drained triaxial tests performed on clay soil specimens from Moscow (Russia) and Minsk (Belarus) construction sites were processed using statistical and regression analyses. The empirical equations for determining E_{50} (eq. (8)) and E_{ur} (eq. (6) and (9)) which consider the mutual influence of the confining pressure and physical properties on clay soil stiffness were obtained.

Comparison of the completed tests of Quaternary and Jurassic soils from Thailand, Europe and the USA showed that stiffness for overconsolidated glacial soils is in the same range as soils from Moscow and Minsk sites. At the same time, Jurassic soils in Moscow region, which are located at great depth, have greater stiffness than soils in the UK, which are located closer to the surface. This confirms the influence of clay soil genesis on its stiffness. The degree of influence of genesis, conditions of sedimentation and stress state is higher than physical properties. Therefore, Equation (8) is applicable to samples obtained from places outside the Moscow and Minsk regions, with sufficient engineering accuracy.

The proposed Equations (8) and (9) can be used in geotechnical models that allow variability, horizontal and vertical distribution of stiffness to be taken into account. This facilitates more accurate modelling of the mechanical behavior in the computational model.

2. The m parameter describes the stress-state dependence on the stiffness in non-linear Hardening soil model [45]. The performed studies revealed the values of the m parameter depending on sedimentation conditions and degree of overconsolidation. In overconsolidated soils, values of the m parameter are on average twice less than in normally consolidated or lightly overconsolidated soils. The recommended values of the m parameter for preliminary calculations depending on age, I_p and I_L are presented in table 4. However, this parameter depends on the test method. For compression-type problems, it should be determined using oedometer tests, for shear-type problems, triaxial test data are more appropriate.

3. Numerical values of the ratio of the unloading/reloading stiffness to the secant stiffness at 50 % strength k_E were obtained. The tendency to the decrease of k_E with the increase of void ratio was found out for clay soils. The stated phenomenon differs from field tests obtained by Z.G. Ter-Martirosyan [55]. This phenomenon is explained by the prevalent influence of shear strain during triaxial compression in conditions of minor density change.

4. An obvious direction for further research is the study of the influence of samples quality on stiffness parameters. It is promising to introduce models with the dependence of stiffness on three-dimensional soil physical properties distribution into the FEM software (for example, PLAXIS, etc.). In addition, the influence of statistical variability of physical properties and stiffness on the structures' deformation should be researched.

References

1. Bishop, A.W., Donald, I.B. The experimental study of partly saturated soil in the triaxial apparatus. 5th International Conference on Soil Mechanics and Foundation Engineering. Paris: Dunod, 1961. Pp. 13–21.
2. Mishra, D.A., Janeček, I. Laboratory Triaxial Testing - From Historical Outlooks to Technical Aspects. Procedia Engineering. 2017. 191. Pp. 342–351.
3. Rossato, G., Simonini, P. Stress–strain behavior of sands in triaxial and direct simple shear tests. Canadian Geotechnical Journal. 1991. 28(2). Pp. 276–281.
4. Schanz, T., Vermeer, P.A. On the Stiffness of Sands. Pre-failure deformation behavior of geomaterials. 1998. Pp. 383–387.
5. Botkin, A.I. Issledovanie napryazhyonnogo sostoyaniya v sy'puchikh i svyazny'kh gruntakh [Investigation of the stress state in cohesiveless and cohesive soils]. Izvestiya nauchno-issledovatel'skogo instituta gidrotekhniki [Bulletin of the Research Institute of Hydraulic Engineering]. 1939. 24. Pp. 153–172.
6. Kondner, R.L. Hyperbolic Stress-Strain Response: Cohesive Soils. Journal of the Soil Mechanics and Foundations Division. 1963. 89(1). Pp. 115–143.
7. Janbu, N. Soil compressibility as determined by oedometer and triaxial tests. Proceeding of the European Conference on Soil Mechanics and Foundation Engineering. 1963. 1. Pp. 245–251.
8. Duncan, J.M., Chang, C.-Y. Nonlinear Analysis of Stress and Strain in Soils. Journal of the Soil Mechanics and Foundations Division. 1970. 96(5). Pp. 1629–1653.
9. Wu, J.T.H., Tung, S.C.-Y. Determination of Model Parameters for the Hardening Soil Model. Transportation Infrastructure Geotechnology. 2020. 7(1). Pp. 55–68.
10. Nelson, I., Baron, M.L. Application of variable moduli models to soil behavior. International Journal of Solids and Structures. Pergamon, 1971. 7(4). Pp. 399–417.
11. Breth, H., Schuster, E., Pise, P. Axial Stress-Strain Characteristics of Sand. Journal of the Soil Mechanics and Foundations Division. 1973. 99(8). Pp. 617–632.

12. Nelson, I., Baladi, G.Y. Outrunning Ground Shock Computed with Different Models. *Journal of the Engineering Mechanics Division*. 1977. 103(3). Pp. 377–393.
13. Corotis, R.B., Farzin, M.H., Krizek, R.J. Nonlinear Stress-Strain Formulation for Soils. *Journal of the Geotechnical Engineering Division*. 1974. 100(9). Pp. 993–1008.
14. Mirayama, S. et al. Draft of State-of-the-art report on constitutive laws of soils. ISSMFE Subcommittee on Constitutive laws of soils. 1985. 110 p.
15. Trufanov, A.N., Gabsalyamov, G.U., Klimov, V.Y. et al. Determination of the deformation properties of clayey soils in the vend deposits in Saint Petersburg. *Soil Mechanics and Foundation Engineering*. 2013. 50(2). Pp. 50–55. DOI: 10.1007/s11204-013-9209-9
16. Bishop, A.W., Webb, D.L., Lewin, P.I. Undisturbed Samples of London Clay from the Ashford Common Shaft: Strength–Effective Stress Relationships. *Géotechnique*. 1965. 15(1). Pp. 1–31. DOI: 10.1680/geot.1965.15.1.1
17. Wilfred, A.W.B. The measurement of soil properties in the triaxial test. A. W. Bishop and D. J. Henkel. London: Edward Arnold, 1962. July. Pp. 1–148.
18. González-Hurtado, J.A. The Effect of Stiffness Anisotropy of a Glacial Clay on the Behavior of a Shallow Wind Turbine Foundation Behavior of a Shallow Wind Turbine Foundation. The University of Western Ontario, 2019.
19. Gasparre, A. Nishimura, S., Minh, N.A., Coop, M.R., Jardine, R.J. The stiffness of natural London Clay. 2007. 57(1). Pp. 33–47. DOI: 10.1680/geot.2007.57.1.33
20. Gasparre, A. Nishimura, S., Coop, M. R., Jardine, R. J. The influence of structure on the behavior of London Clay. *Stiff Sedimentary Clays*. 2007. 57(1). Pp. 19–31. DOI: 10.1680/ssc.41080.0007
21. Singh, A., Mitchell, J.K. General Stress-Strain-Time Function for Soils. *Journal of the Soil Mechanics and Foundations Division*. 1968. 94(1). Pp. 21–46. DOI: 10.1061/JSFEAQ.0001084
22. Meschyan, S.R. *Experimental Rheology of Clayey Soils*. CRC Press, 1995.
23. Vyalov, S.S. *Rheological Fundamentals of Soil Mechanics*. Elsevier, 1986.
24. Mangushev, R., Lashkova, E., Smolenkov, V. Experience of construction of deep ditches for underground constructions in weak soils Saint-Petersburg. *Japanese Geotechnical Society Special Publication*. 2016. 2(79). Pp. 2710–2715.
25. Sharafutdinov, R. Statistical and regression analyses of sands stiffness in triaxial tests and application of the results. *Rock and Soil Mechanics*. 2022. 43(10). Pp. 2873–2886. DOI: 10.16285/j.rsm.2022.00006
26. Barvashov, V.A., Boldyrev, G.G. Sensitivity of structures and geological data. *Proceeding of the 6-th ECCOMAS Thematic Conference on Computational Methods in Structural Dynamics and Earthquake Engineering*. Rhodes Island, Greece, 2017.
27. Paice, G.M., Griffiths, D. V., Fenton, G.A. Finite Element Modeling of Settlements on Spatially Random Soil. *Journal of Geotechnical Engineering*. 1996. 122(9). Pp. 777–779. DOI: 10.1061/(ASCE)0733-9410(1996)122:9(777)
28. Nobahar, A., Popescu, R. Spatial variability of soil properties—effects on foundation design. *Proceedings of 53rd Canadian geotechnical conference*. Montreal, 2000. Pp. 1139–1144.
29. Popescu, R., Deodatis, G., Nobahar, A. Effects of random heterogeneity of soil properties on bearing capacity. *Probabilistic Engineering Mechanics*. 2005. 20(4). Pp. 324–341. DOI: 10.1016/j.probengech.2005.06.003
30. Boldyrev, G.G., Barvashov, V.A., Shejnin, V.I., Kashirskij, V.I., Idrisov, I.Kh., Diveev, A.A. Informacionny`e sistemy` v geotekhnike - 3D-geotekhnika [Information systems in geotechnical engineering – 3D geotechnics]. *Geotechnics*. 2019. 11(2). Pp. 6–27.
31. Grønbech, G.L., Nielsen, B.N. Undrained shear strength determination and correlations on Søvind Marl. *Proceedings of the 17th Nordic Geotechnical Meeting*. Reykjavík, 2016. Pp. 431–440.
32. Tho, T.X., Long, V.T., Du, N.L. Establishing the Correlation of Shear Strength Between Consolidated – Undrained and Consolidated – Drained Triaxial Tests of Soft Clay. *Proceeding of the 10th Slovak Conference on Geotechnical Engineering 30-31 may 2011*. Pp. 170–174.
33. Angelim, R.R., Cunha, R.P., Sales, M.M. Determining the Elastic Deformation Modulus From a Compacted Earth Embankment Via Laboratory and Menard Pressuremeter Tests. *Soils and Rocks*. 2016. 39(3). Pp. 285–300. DOI: 10.28927/SR.393285
34. Surarak, C. Likitlersuang, S., Wanatowski, D., Balasubramaniam, A., Oh, E., Guan, H. Stiffness and strength parameters for hardening soil model of soft and stiff Bangkok clays. *Soils and Foundations*. 2012. 52(4). Pp. 682–697. DOI: 10.1016/j.sandf.2012.07.009
35. Mirnyy, A.Iu., Budoshkina, K.A., Shishkina, V.V. Statisticheskij analiz parametrov modeli Hardening soil dlya gruntov moskovskogo regiona [Statistical analysis of Hardening soil model mechanical parameters for Moscow region soils]. *Geotechnics*. 2017. 4. Pp. 58–64.
36. Bogusz, W., Witowski, M. Preliminary assessment of variability of selected hardening soil model parameters for glacial tills and clays from Poland. *E3S Web of Conferences*. EDP Sciences, 2019. 92.
37. Taylor, D.W. *Fundamentals of soil mechanics*. New York: J. Wiley and Sons, 1948.
38. Casagrande, A. Classification and Identification of Soils. *Transactions of the American Society of Civil Engineers*. 1948. 113(1). Pp. 901–930.
39. Chu, J., Leong, W.K. Pre-failure strain softening and pre-failure instability of sand: a comparative study. *Géotechnique*. 2001. 51(4). Pp. 311–321. DOI: 10.1680/geot.2001.51.4.311
40. Chu, J., Wanatowski, D. Effect of Loading Mode on Strain Softening and Instability Behavior of Sand in Plane-Strain Tests. *Journal of Geotechnical and Geoenvironmental Engineering*. 2009. 135(1). Pp. 108–120. DOI: 10.1061/(ASCE)1090-0241(2009)135:1(108)
41. Shulyatiev, O., Isaev, O., Sharafutdinov, R., Gordyshina, G., Sereda, S. Geotechnical aspects of the Moscow Luzhniki Stadium reconstruction. *Proceeding of 19th International Conference on Soil Mechanics and Geotechnical Engineering ICSMGE 2017*. Pp. 2049–2052.
42. Gmurman, V.E. *Rukovodstvo k resheniyu zadach po teorii veroyatnostej i matematicheskoy statistzhe* [Guideline for probability theory and mathematical statistic problems solving]. Moscow: High School, 2004.
43. Wichtmann, T., Kimmig, I., Triantafyllidis, T. On correlations between “dynamic” (small-strain) and “static” (large-strain) stiffness moduli – An experimental investigation on 19 sands and gravels. *Soil Dynamics and Earthquake Engineering*. 2017. 98. Pp. 72–83. DOI: 10.1016/j.soildyn.2017.03.032

44. Mayne, P.W., Kulhawy, F.H. K0-OCR Relationships in Soil. // Journal of the Geotechnical Engineering Division. 1982. 108(6). Pp. 851–872. DOI: 10.1016/0148-9062(83)91623-6
45. Schanz, T., Vermeer, P., Bonnier, P. The hardening soil model: Formulation and verification. In Proceedings of the Plaxis Symposium. Beyond 2000 in Computational Geotechnics. Ed. Brinkgreve R.B.J. Rotterdam: Balkema, 1999. Pp. 281–290.
46. Bogusz, W., Witowski, M. Small-strain stiffness of fine-grained soils from Poland based on a laboratory test database. Proceeding of the 17th European Conference on Soil Mechanics and Geotechnical Engineering, ECSMGE 2019. Pp. 1–6. DOI: 10.32075/17ECSMGE-2019-0129
47. Shulyatiev, O.A. Osnovaniya i fundamenty` vy` sotny` kh zdaniy [Soils and foundations of high-rise buildings]. Moscow: ASV, 2018. 392 p.
48. Shulyatiev, O.A., Isaev O.N., Nayatov D.V., Sharafutdinov R.F. Prognoz razvitiya deformaczij osnovaniya mnogofunkczional`nogo zhilogo doma [Forecast of base strains development for a multifunctional residential complex]. Geotechnics. 2017. 2. Pp. 38–49.
49. Shein E.V. et al. Regressionny`j analiz v gruntovedenii [Regression analysis in soil science]. Vladimir. 2016.
50. Dmitriev V.V. Optimizaczija laboratorny`kh inzhenerno-geologicheskikh issledovanij [Optimization of laboratory geotechnical research]. Moscow: Nedra, 1989.
51. Parry, R.H.G. Some properties of heavily overconsolidated Oxford clay at a site near Bedford. Geotechnique. 1972. 22(3). Pp. 485–507. DOI: 10.1680/geot.1972.22.3.485
52. Kolybin, I.V., Popsuenko, I.K., Kogai, V.K. A Study of a Slump in the Moscow River Slope. Soil Mechanics and Foundation Engineering. 2016. 53(1). Pp. 46–52. DOI: 10.1007/s11204-016-9363-y.
53. Bogusz, W., Witowski, M. Variability of overconsolidated soils from Poland in geotechnical practice. Proceeding of the XVI Danube – European Conference on Geotechnical Engineering. 2018. 2(2–3). Pp. 585–590.
54. Stark, T.D., Eid, H.T. Slope Stability Analyses in Stiff Fissured Clays. Journal of Geotechnical and Geoenvironmental Engineering. 1997. 123(4). Pp. 335–343. DOI: 10.1061/(ASCE)1090-0241(1997)123:4(335)
55. Ter-Martirosyan, Z.G., Akhpatelov, D.M., Sorochan, E.A. Computing the settlement of a foundation constructed in a trench. Soil Mechanics and Foundation Engineering. 1985. 22. Pp. 30–34. DOI: 10.1007/BF01711205

Information about author:

Rafael Sharafutdinov, PhD in Technical Sciences

ORCID: <https://orcid.org/0000-0002-5806-7190>

E-mail: linegeo@mail.ru

Received 11.03.2023. Approved after reviewing 15.05.2023. Accepted 27.06.2023.



Research article

UDC 624.1

DOI: 10.34910/MCE.121.7



Beam on a two-parameter elastic foundation: simplified finite element model

S.B. Akhazhanov¹ , N.I. Vatin² , S. Akhmediyev³, T. Akhazhanov⁴ , O. Khabidolda¹ ,
A. Nurgoziyeva⁵,

¹ Karaganda Buketov University, Karaganda, Republic of Kazakhstan

² Peter the Great St. Petersburg Polytechnic University, St. Petersburg, Russian Federation

³ Abylkas Saginov Karaganda Technical University, Karaganda, Republic of Kazakhstan

⁴ L.N. Gumilyov Eurasian National University (ENU), Astana, Republic of Kazakhstan

⁵ Al-Farabi Kazakh National University, Almaty, Republic of Kazakhstan

✉ oka-kargtu@mail.ru

Keywords: beam, elastic foundation, finite element, stiffness matrix, finite element model, Winkler model, Vlasov model

Abstract. When calculating beams resting on a solid elastic foundation, the simplest foundation models proposed by Winkler-Zimmerman and Vlasov-Leontyev are often used. These hypotheses have been repeatedly subjected to well-founded criticism, because they do not take into account the inclusion in the work of some areas of the base and do not allow determining reactive pressures at the ends of the foundation beam and beyond it. In order to clarify these hypotheses, many authors have proposed some other models that allow smoothing out the shortcomings of these models to varying degrees. This article proposes a new numerical approach to solving the problem of a beam on a two-parameter elastic foundation. To calculate the beam, the finite element method has been used. A separate rod has been proposed as a finite element for solving the bending state of the beam on a two-parameter model of an elastic foundation. There has been presented the construction of the stiffness matrix of this finite element. The elastic foundation is assumed to be linear, homogeneous and isotropic and is taken into account using the parameters r , s . The reactions of the elastic base, deflections and angles of rotation, the formulas for calculating bending moments and transverse forces have been determined. There have been given examples of static calculation of a beam on an elastic two-parameter foundation for the action of various loads. These examples demonstrate the effectiveness of the developed method. Reliability of the method proposed by the authors has been verified on test examples, and good agreement has been obtained with the well-known models of Winkler and Vlasov.

Citation: Akhazhanov, S.B., Vatin, N.I., Akhmediyev, S., Akhazhanov, T., Khabidolda, O., Nurgoziyeva, A. Beam on a two-parameter elastic foundation: Simplified finite element model. Magazine of Civil Engineering. 2023. 121(5). Article no. 12107. DOI: 10.34910/MCE.121.7

1. Introduction

Structures in the form of beams and slabs on the yielding bases are widely used in various branches of technology, in particular in construction. The main problem in such tasks is to take into account the interaction in the "structure-foundation" system. In this case, the difficulty consists in selecting an appropriate mathematical model for the assigned engineering problem.

The study of the stress-strain state of foundation beams is mainly based on the Winkler model [1–3] in the form of two main options: a physical model of a two-parameter support structure [4–6], as well as a foundation beam model in the form of an elastic half-space [7, 8]. The well-known Winkler model does not take into account the bending deformation of the foundation itself, the presence of shear deformation, as well as the structural continuity of the soil; at the same time, the disadvantage is that the subsidence of the base is taken into account only within the area of the foundation structure [9, 10].

When using a foundation model with an elastic half-space, the force interaction between adjacent loads is taken into account, which corresponds to the realities of engineering problems. Based on a similar model, Kontomaris and Malamu [11] determine the contact forces between a rigid stamp in the form of a ball and an elastic body (base). At the same time, Baraldi and Tullini [12] propose a different variant in the form of a numerical model of a two-dimensional contact without taking into account friction between the bodies in the volume of a three-dimensional elastic half-space; meanwhile, bases with isotropic properties were studied to determine deformations (subsidence) and physical relationships between the components of the force vector. The other authors [13–15] introduced original parameters derived from the elastic half-space model to describe various models of elastic anisotropy, taking into account effects, especially of transverse (shear) anisotropy. Still other scientists [16–18] studied the bending of foundation beams by the direct Galerkin method based on power series, the finite element method, etc.

The authors of works [19–22] studied the analysis of beams on elastic foundation of Timoshenko in addition to the classical theory of beams. Theodore [23] developed an original computer code based on the finite element method for beams on an elastic foundation using the Matlab software package. Scientist Dinev [24] proposed an analytical method of calculating a beam of finite length on an elastic foundation based on a variational interpretation of the expression for the total potential energy functional. S. Limkatanyu et al. presented a nonlinear Winkler-based beam element with improved displacement shape functions that was capable of representing the nonlinear interaction mechanics between the beam and the foundation [25]. Sánchez and Roesset proposed a more accurate model of a beam on the elastic foundation for laterally loaded piles and used a consistent boundary matrix to evaluate the computing accuracy [26]. Results of other approaches, such as iterative methods [27], discrete singular convolution method [28], and boundary element method [29], can be found in the literature

The presented models include an elastic foundation of the Winkler, Vlasov, and Pasternak types. An ideal model for calculating the foundation was obtained. Still, with the development of the scale of construction, the interaction of soil and foundation beams, slabs, and other elements requires deeper theoretical studies. The development of more realistic foundation models and simplified methods is very important for the safe and economical design of such type of structure. Therefore, it is important to develop mathematical models and methods for assessing the stress-strain state of beams lying on an elastic base, considering their geometric and physical characteristics.

The present study takes an attractive approach for beams resting on an elastic foundation. The study aims to develop a simplified finite element model for calculating a beam on an elastic foundation is proposed. According to the proposed model, an elastic foundation is considered a single-layer model, the properties of which are described by two elastic characteristics.

The novelty and importance of this article lie in the following:

- a simplified finite element model is proposed, taking into account the elastic foundation, which is fundamentally different from the other models;
- obtaining a simplified model of an elastic foundation adopted for modeling the mechanical behavior of the soil;
- using the finite element method, in which the basic equations are derived, the stiffness matrix is determined, and the boundary conditions for beams of finite length resting on an elastic foundation are taken into account;
- simplifying methods of calculating beams on an elastic foundation for their wider implementation in engineering practice;
- carrying out a comparative analysis based on a simplified model of an elastic foundation and on traditional models of Winkler and Vlasov.

2. *Methods*

The initial differential equation for beam bending on a two-parameter elastic foundation is written in the form

$$\frac{d^4 W_0(x)}{dx^4} - 2r^2 \frac{d^2 W_0(x)}{dx^2} + S^4 \cdot W_0(x) = \frac{q(x)}{EJ}. \quad (1)$$

The $2r^2$ and s^4 dimensionless elastic characteristics are determined in the work [30] as:

$$2r^2 = \frac{6(1-\nu^2)P_1 l^2}{h^2} \cdot \frac{\bar{E}h^2}{Eh_0^2}, \quad s^4 = \frac{6(1-\nu^2)kP_0 l^4}{h^4} \cdot \frac{\bar{E}h^3}{Eh_0^3}.$$

The effect of the elastic foundation on the beam is taken into account by two parameters P_0, P_1 and is determined in [30] by the formula

$$P_0 = \frac{2 \cdot m + \frac{h_0}{h} k (1-\nu)}{2m - (1-\nu)^2}, \quad P_1 = \frac{k \frac{h_0}{h} + (1-\nu)}{2m - (1-\nu)^2}, \quad m = 2 + \frac{(1-\nu^2)}{k} \frac{\bar{E}h}{Eh_0},$$

where ν is the Poisson's ratio, k is the deformed state parameter that depends on the boundary conditions.

The parameter k depends on the boundary conditions and is determined as follows [31]:

- for hinge-supported beam $k = \pi^2 \frac{h^2}{\ell^2}$;
- for fixed-end beam $k = 4\pi^2 \frac{h^2}{\ell^2}$;
- for cantilever beam $k = \frac{\pi^2}{4} \frac{h^2}{\ell^2}$;
- for a statically indeterminate beam $k = \pi^2 \frac{h^2}{\ell^2}$.

Original differential equation (1) differs from the classical equation of beam bending on the elastic foundation of the Winkler model in its structure there is an additional term containing the second derivative, which allows taking into account the effect of shear stresses.

The beam on a two-parameter elastic foundation is calculated by the finite element method. From the mathematical point of view, the finite element method (FEM) is a numerical procedure for finding approximate solutions to boundary value problems for partial differential equations.

When using the FEM, there are the following assumptions underpinning this development:

- the finite element has a unit length and has two nodes at its ends;
- the finite element is connected with other elements only in nodes;
- loading the elements occurs only in nodes.

3. Results and Discussion

3.1. Finite element formulation

A finite element selected from beam structures on an elastic foundation is considered. This element has the length ℓ , the width h_0 and the bending stiffness EJ . Here E is the modulus of elasticity of the material, and J is the axial moment of inertia. The thickness of the elastic base is denoted as h , the modulus of elasticity of the material is \bar{E} (Fig. 1).

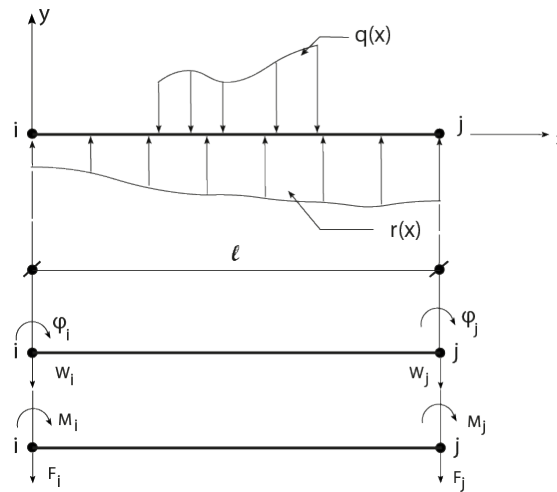


Figure 1. A finite element on an elastic foundation.

The deformed state of this element is determined by the nodal displacements $(W_i, \varphi_i, W_j, \varphi_j)$, and the stressed state is determined by the nodal forces (F_i, M_i, F_j, M_j) .

The deflection function has the following form

$$\begin{aligned}
 W(x) &= q_1(x)W_i + q_2(x)\varphi_i + q_3(x)W_j + q_4(x)\varphi_j \\
 q_1(x) &= \left(1 - 3\frac{x^2}{\ell^2} + 2\frac{x^3}{\ell^3}\right), \quad q_2(x) = \ell \left(\frac{x}{\ell} - 2\frac{x^2}{\ell^2} + \frac{x^3}{\ell^3}\right), \\
 q_3(x) &= \left(3\frac{x^2}{\ell^2} - 2\frac{x^3}{\ell^3}\right), \quad q_4(x) = \ell \left(-\frac{x^2}{\ell^2} + \frac{x^3}{\ell^3}\right),
 \end{aligned} \tag{2}$$

where $q_1(x), q_2(x), q_3(x), q_4(x)$ are the coordinate functions.

The function of deflections (2) can be presented in the vector form

$$W(x) = \vec{q}^T \cdot \vec{V}, \quad \vec{q}^T = [q_1 \ q_2 \ q_3 \ q_4], \quad \vec{V}^T = [W_i \ \varphi_i \ W_j \ \varphi_j], \tag{3}$$

where \vec{q}^T is the transposed vector of the coordinate functions, \vec{V} is the vector of nodal displacements of the finite element.

The potential energy of the finite element on a two-parameter elastic foundation is found as follows

$$U_0 = \frac{1}{2} \int_0^l \frac{M^T M dx}{EJ} + \frac{1}{2} \int_0^l - \left(\frac{dW}{dx}\right)^T 2r^2 \left(\frac{dW}{dx}\right) dx + \frac{1}{2} \int_0^l W^T s^4 W dx, \tag{4}$$

where $M(x)$ is the moment of flexion.

Based on equation (3), the potential energy (4) had written in the following form

$$U_0 = \frac{1}{2} \vec{V}^T \cdot \mathbf{K} \cdot \vec{V} - \frac{1}{2} \cdot 2r^2 \cdot \vec{V}^T \cdot \hat{\mathbf{K}} \cdot \vec{V} + \frac{1}{2} \cdot s^4 \cdot \vec{V}^T \cdot \check{\mathbf{K}} \cdot \vec{V},$$

where

$$\mathbf{K} = \int_0^l \left(\frac{d^2 \vec{q}}{dx^2}\right) \cdot (EJ) \cdot \left(\frac{d^2 \vec{q}}{dx^2}\right)^T dx, \quad \hat{\mathbf{K}} = \int_0^l \left(\frac{d\vec{q}}{dx}\right) \cdot \left(\frac{d\vec{q}}{dx}\right)^T dx, \quad \check{\mathbf{K}} = \int_0^l \vec{q} \cdot \vec{q}^T dx.$$

The finite element stiffness matrix elements $\left(\mathbf{K}, \hat{\mathbf{K}}, \check{\mathbf{K}}\right)$ are determined by the following formulas

$$\begin{aligned}
 K_{ij} &= \int_0^l \left(\frac{d^2 \bar{q}_i}{dx^2} \right) \cdot (EJ) \cdot \left(\frac{d^2 \bar{q}_j}{dx^2} \right) dx, \\
 \hat{K}_{ij} &= \int_0^l \left(\frac{d \bar{q}_i}{dx} \right) \cdot \left(\frac{d \bar{q}_j}{dx} \right) dx, \\
 \check{K}_{ij} &= \int_0^l \bar{q}_i \cdot \bar{q}_j dx.
 \end{aligned} \tag{5}$$

The work of the nodal forces is determined as follows

$$A_0 = \frac{1}{2} \bar{V}^T \cdot \bar{F}_0, \quad \bar{F}_0^T = \begin{bmatrix} F_i & M_i & F_j & M_j \end{bmatrix}. \tag{6}$$

From the condition of the finite element equilibrium ($A_0 = U_0$) there is the basic dependence

$$A_0 = U_0: \quad \bar{F}_0 = K_0 \cdot \bar{V}, \tag{7}$$

where K_0 is the finite element stiffness matrix taking into account the elastic foundation.

Based on equation (2) and formula (5), the stiffness matrix of the finite element on the elastic foundation is determined as follows

$$\begin{aligned}
 K_0 &= K - 2r^2 \cdot \hat{K} + s^4 \cdot \check{K}, \\
 K &= \frac{EJ}{l^3} \begin{vmatrix} 12 & 6l & -12 & 6l \\ 6l & 4l^2 & -6l & 2l^2 \\ -12 & -6l & 12 & -6l \\ 6l & 2l^2 & -6l & 4l^2 \end{vmatrix}, \\
 \hat{K} &= \frac{1}{30l} \begin{vmatrix} 36 & 3l & -36 & 3l \\ 3l & 4l^2 & -3l & -l^2 \\ -36 & -3l & 36 & -3l \\ 3l & -l^2 & -3l & 4l^2 \end{vmatrix}, \\
 \check{K} &= \frac{l}{420} \begin{vmatrix} 156 & 22l & 54 & -13l \\ 22l & 4l^2 & 13l & -3l^2 \\ 54 & 13l & 156 & -22l \\ -13l & -3l^2 & -22l & 4l^2 \end{vmatrix}.
 \end{aligned} \tag{8}$$

The beam internal forces are presented as follows

$$\begin{aligned}
 M(x) &= -EJ \cdot \frac{d^2 W(x)}{dx^2}, \\
 Q(x) &= -EJ \cdot g_0 \cdot \frac{d^3 W(x)}{dx^3}, \\
 g_0 &= 1 + \frac{6(1-\nu^2) P_1 \bar{E} h^2}{k^2 E h_0^2},
 \end{aligned} \tag{9}$$

where M is a bending moment, Q is a shear force, g_0 is the parameter of the beam shear force.

One of the following boundary conditions must be satisfied at the beam edges.

1) If the beam edge has a full contact (touches fully) with the elastic foundation, then the boundary conditions as follows

$$W_* = \frac{Q \cdot L^3}{3EJ_0}, \quad f_* = \frac{M \cdot L}{EJ_0}, \quad J_0 = \frac{h^3}{12},$$

where W_*, φ_* are the beam edge displacements, L is the foundation length beyond the beam, $\bar{E}J_0$ is rigidity with the foundation deflection.

2) If the ends of the beam are hinge-supported, then the boundary conditions as follows

$$W = 0, M = 0.$$

3) If the ends of the beam are fixed, then the boundary conditions as follows

$$W = 0, \theta = 0.$$

4) If the ends of the beam are free, then the boundary conditions as follows

$$M = 0, Q = 0.$$

The stiffness matrix of the internal forces is defined as follows

$$\begin{bmatrix} F_i \\ M_i \\ F_j \\ M_j \end{bmatrix} = \begin{bmatrix} -Q(0) \\ M(0) \\ Q(l) \\ -M(l) \end{bmatrix} = \frac{EJ}{l^3} \begin{bmatrix} 12g_0 & 6lg_0 & -12g_0 & 6lg_0 \\ 6l & 4l^2 & -6l & 2l^2 \\ -12g_0 & -6lg_0 & 12g_0 & -6lg_0 \\ 6l & 2l^2 & -6l & 4l^2 \end{bmatrix} \begin{bmatrix} W_i \\ \phi_i \\ W_j \\ \phi_j \end{bmatrix},$$

$$\bar{K} = \frac{EJ}{l^3} \begin{vmatrix} 12g_0 & 6lg_0 & -12g_0 & 6lg_0 \\ 6l & 4l^2 & -6l & 2l^2 \\ -12g_0 & -6lg_0 & 12g_0 & -6lg_0 \\ 6l & 2l^2 & -6l & 4l^2 \end{vmatrix}. \quad (10)$$

Reactive pressures of the elastic foundation are determined as follows

$$R(x) = EJ \cdot \left(2r^2 \frac{d^2W(x)}{dx^2} - s^4W(x) \right). \quad (11)$$

The reactive pressure stiffness matrix of the elastic foundation is determined as follows

$$\begin{bmatrix} R(0) \\ R(l) \end{bmatrix} = \frac{EJ}{l^3} \begin{bmatrix} -6l \cdot 2r^2 - s^4 \cdot l^3 & -4l^2 \cdot 2r^2 & 6l \cdot 2r^2 & -2l^2 \cdot 2r^2 \\ 6l \cdot 2r^2 & 2l^2 \cdot 2r^2 & -6l \cdot 2r^2 - s^4 l^3 & 4l^2 \cdot 2r^2 \end{bmatrix} \begin{bmatrix} W_i \\ \phi_i \\ W_j \\ \phi_j \end{bmatrix},$$

$${}^0\bar{K} = \frac{EJ}{l^3} \begin{vmatrix} -6l \cdot 2r^2 - s^4 l^3 & -4l^2 \cdot 2r^2 & 6l \cdot 2r^2 & -2l^2 \cdot 2r^2 \\ 6l \cdot 2r^2 & 2l^2 \cdot 2r^2 & -6l \cdot 2r^2 - s^4 l^3 & 4l^2 \cdot 2r^2 \end{vmatrix}. \quad (12)$$

The calculation of a beam on an elastic foundation by the finite element method is performed according to the following algorithm:

- 1 Dividing the beam into finite elements and numbering the nodes and elements from left to right.
- 2 Setting the directions of nodal displacements.
- 3 Forming vectors of nodal displacements and external forces.
- 4 Making the stiffness matrices of the beam elements.
- 5 Forming the general matrix of beam stiffness.
- 6 Determining the vector of nodal displacements of the beam.

- 7 Based on the main dependence, determining the vectors of nodal forces.
- 8 The internal forces of the beam are determined through the vector of nodal displacements and the matrix of internal forces.
- 9 Determining the reactive pressure of the elastic foundation using the reactive pressure matrix.

3.2. Numerical Results and Analysis

To verify the calculation accuracy, in order to compare the solution of the proposed simplified finite element model with other solutions of the Winkler and Vlasov model from the classical theory of beams on an elastic foundation, below there are several examples of solving engineering problems.

In these problems, beams on an elastic foundation with different boundary conditions, external loads, and reaction coefficients of the soil foundation are considered. In this case, the stiffness matrices, internal nodal forces, and reactions of the elastic foundation are obtained using an improved method by applying the corresponding equations (8), (9), and (11).

3.2.1. Example 1

A simply supported beam on an elastic foundation is considered. A beam of length $\ell = 10 \text{ m}$, width $b_0 = 1 \text{ m}$, and height $h_0 = 2 \text{ m}$, with the modulus of elasticity $E = 20 \cdot 10^5 \text{ kPa}$, is considered to be supported by a foundation having depth $h = 5 \text{ m}$, deformation modulus $\bar{E} = 40 \text{ kPa}$ and Poisson's ratio $\nu = 0.25$. The beam carries the external uniform vertical load $q = 200 \frac{\text{kN}}{\text{m}}$.

The calculated values of vertical deformations, internal forces are given in Table 1–3; the largest values are given in Table 4. Analytical and numerical solutions are given for the case of a uniformly distributed load. The results obtained are compared with similar values obtained earlier using the Winkler and Vlasov models (Fig. 2–4).

Table 1. Vertical displacement values (simply supported beam on an elastic foundation).

Case	The length of the beam (ℓ , m)						
	0	2	4	5	6	8	10
Wn	0	11.5997	18.5995	19.5308	18.5995	11.5997	0
Wa	0	11.5918	18.5869	19.5175	18.5869	11.5918	0
Ww	0	11.5623	18.5389	19.4671	18.5389	11.5623	0
Wv	0	11.5901	18.5839	19.5144	18.5839	11.5901	0

Table 2. Bending moment values (simply supported beam on an elastic foundation).

Case	The length of the beam (ℓ , m)						
	0	2	4	5	6	8	10
Mn, 10^6	0	1.59989	2.40124	2.49912	2.40124	1.59989	0
Ma, 10^6	0	1.59887	2.39831	2.49824	2.39831	1.59887	0
Mw, 10^6	0	1.59503	2.39197	2.49156	2.39197	1.59503	0
Mv, 10^6	0	1.59869	2.39789	2.49779	2.39789	1.59869	0

Table 3. Shear force values (simply supported beam on an elastic foundation).

Case	The length of the beam (ℓ , m)						
	0	2	4	5	6	8	10
Qn, 10^5	9.9955	5.9961	1.9993	0	-1.9991	-5.9958	-9.9952
Qa, 10^5	9.9941	5.9965	1.9988	0	-1.9988	-5.9965	-9.9941
Qw, 10^5	9.9734	5.9785	1.9918	0	-1.9918	-5.9785	-9.9734
Qv, 10^5	9.9930	5.9944	1.9979	0	-1.9979	-5.9944	-9.9930

Table 4. Maximum values of vertical displacements, bending moments and transverse forces (simply supported beam on an elastic foundation).

Modular Ratio	Property	Case
---------------	----------	------

$\left(\frac{\bar{E}}{E}\right)$		Winkler Model	Vlasov Model	Analytical Model	Present finite element model
0.2	Max Vertical displacement	2.412	2.465	2.543	2.536
	Max Bending moment, (10^5)	3.047	3.177	3.255	3.202
	Max Shear force, (10^5)	2.346	2.493	2.571	2.506
0.1	Max Vertical displacement	4.247	4.335	4.413	4.402
	Max Bending moment, (10^5)	5.467	5.569	5.649	5.632
	Max Shear force, (10^5)	3.242	3.366	3.448	3.412
0.05	Max Vertical displacement	6.950	7.057	7.137	7.110
	Max Bending moment, (10^5)	8.923	9.053	9.135	9.121
	Max Shear force, (10^5)	4.426	4.573	4.655	4.624

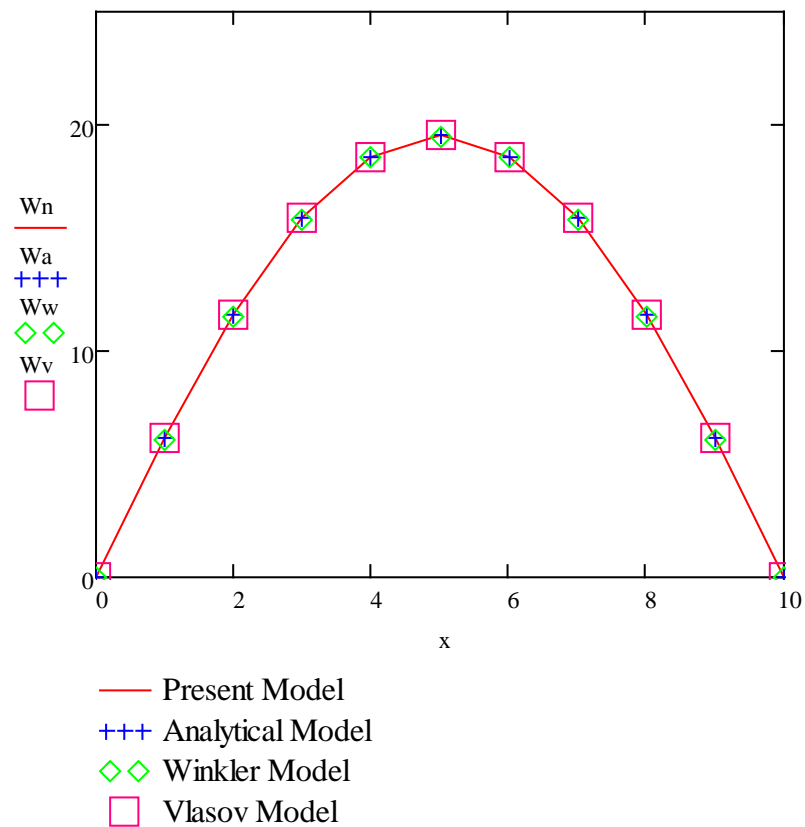


Figure 2. Vertical displacement of the beam on elastic foundation.

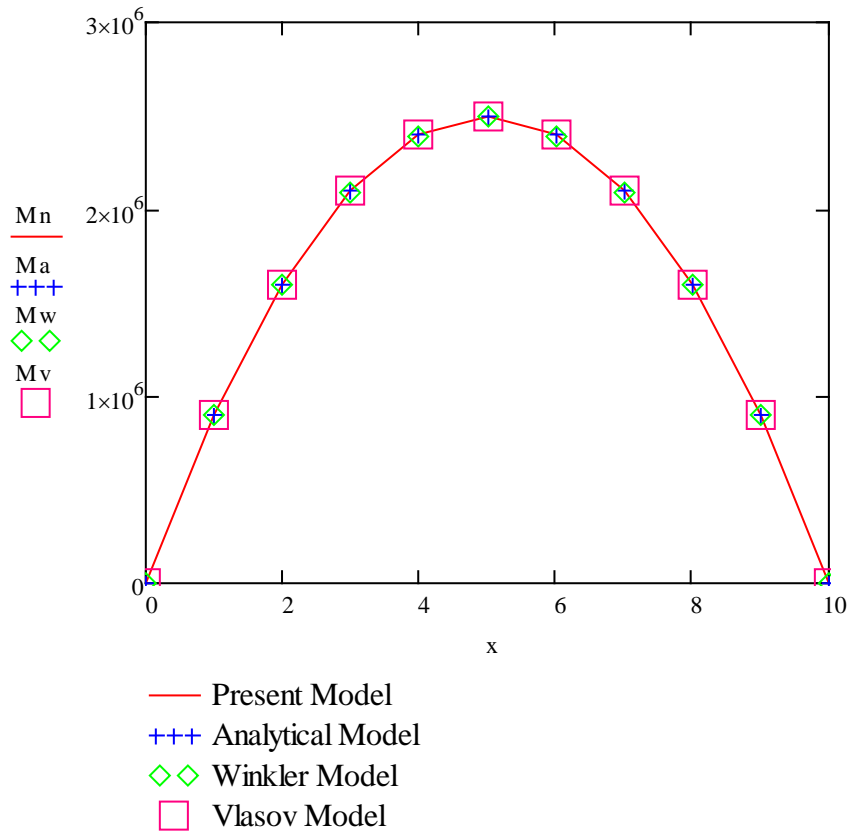


Figure 3. Bending moment of the beam on elastic foundation.

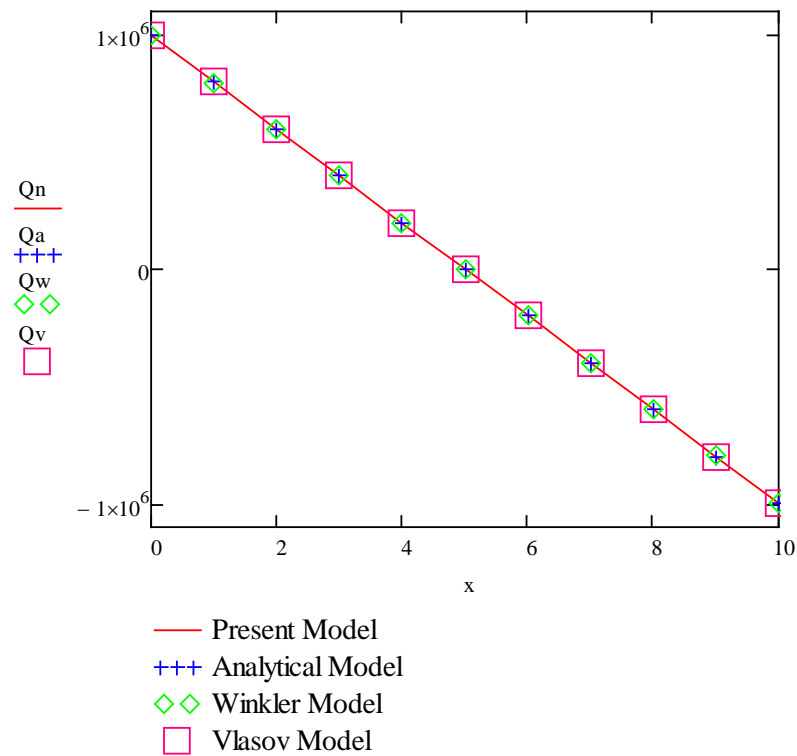


Figure 4. Shear force of the beam on elastic foundation.

The results of the reactive pressure of the elastic foundation are shown in Figure 5.

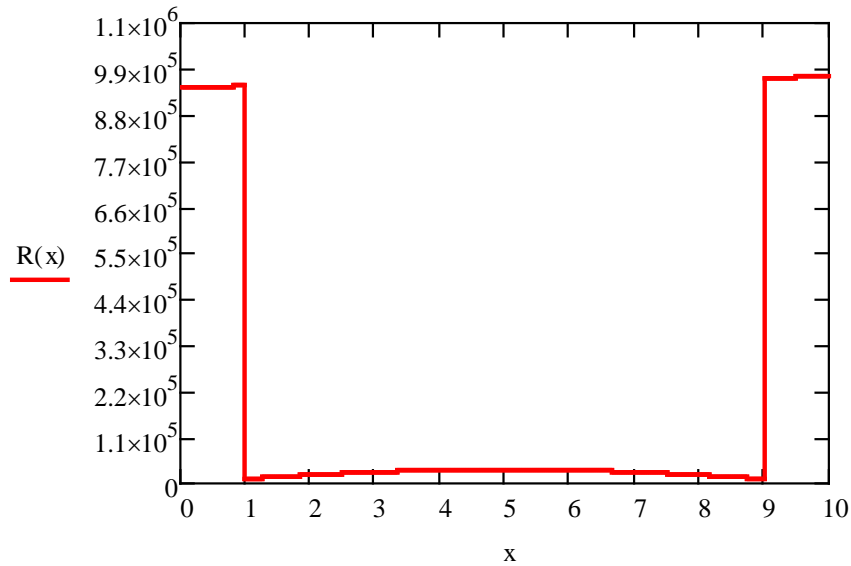


Figure 5. Reactive pressure of the elastic foundation.

3.2.2. Example 2

A fixed-end beam on an elastic foundation is considered. The uniformly distributed load was chosen as $q = 120 \frac{kN}{m}$. A beam of length $\ell = 8 m$, width $b_0 = 1 m$, and height $h_0 = 2 m$. The beam's material has a modulus of elasticity $E = 30 \cdot 10^5 kPa$. The physical and geometry parameters of the elastic foundations were $\bar{E} = 30 kPa$, $\nu = 0.25$ and $h = 4 m$.

The comparison results of the beam displacement, bending moment, and shear force are shown in Tables 5–7 and the maximum value are given in Table 8, which indicate that the values obtained by the present method are in good agreement with the analytical, Winkler, and Vlasov models. Fig. 6–8 show the displacement, bending moment, and shear force diagrams.

Table 5. Vertical displacement values (fixed-end beam on an elastic foundation).

Case	The length of the beam (ℓ , m)						
	0	1	2	4	6	7	8
Wn	0	0.12266	0.35999	0.63998	0.35999	0.12266	0
Wa	0	0.12248	0.35993	0.63987	0.35993	0.12248	0
Ww	0	0.12249	0.35995	0.63992	0.35995	0.12249	0
Wv	0	0.12249	0.35998	0.63997	0.35998	0.12249	0

Table 6. Bending moment values (fixed-end beam on an elastic foundation).

Case	The length of the beam (ℓ , m)						
	0	1	2	4	6	7	8
Mn, 10^5	-6.39905	-2.19986	0.79995	3.19983	0.79995	-2.19986	-6.39905
Ma, 10^5	-6.39875	-2.19957	0.79984	3.19937	0.79984	-2.19957	-6.39875
Mw, 10^5	-6.39925	-2.19968	0.79992	3.19954	0.79992	-2.19968	-6.39925
Mv, 10^5	-6.39976	-2.19989	0.79998	3.19984	0.79998	-2.19989	-6.39976

Table 7. Shear force values (fixed-end beam on an elastic foundation).

Case	The length of the beam (ℓ , m)						
	0	1	2	4	6	7	8
Qn, 10^5	4.79987	3.59982	2.39986	0	-2.39986	-3.59982	-4.79987
Qa, 10^5	4.79926	3.59944	2.39963	0	-2.39963	-3.59944	-4.79926
Qw, 10^5	4.79956	3.59958	2.39965	0	-2.39965	-3.59958	-4.79956
Qv, 10^5	4.79989	3.59986	2.39987	0	-2.39987	-3.59986	-4.79989

Table 8. Maximum values of vertical displacements, bending moments and transverse forces (fixed-end beam on an elastic foundation).

Modular Ratio	Property	Case			
		Winkler Model	Vlasov Model	Analytical Model	Present finite element model
0.2	Max Vertical displacement	0.359	0.361	0.373	0.368
	Max Bending moment, (10^5)	1.809	1.825	1.864	1.847
	Max Shear force, (10^5)	3.446	3.431	3.602	3.586
0.1	Max Vertical displacement	0.449	0.451	0.469	0.458
	Max Bending moment, (10^5)	2.255	2.287	2.344	2.298
	Max Shear force, (10^5)	3.985	3.959	4.039	3.916
0.05	Max Vertical displacement	0.526	0.529	0.530	0.532
	Max Bending moment, (10^5)	2.686	2.689	2.701	2.692
	Max Shear force, (10^5)	4.341	4.352	4.359	4.348

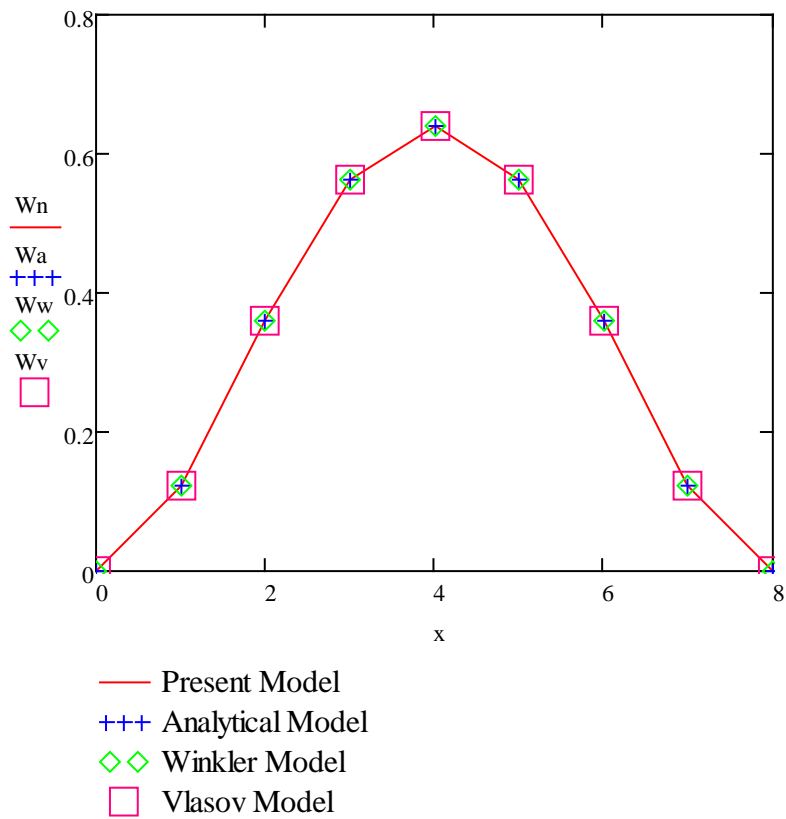


Figure 6. Vertical displacement of the beam on elastic foundation.

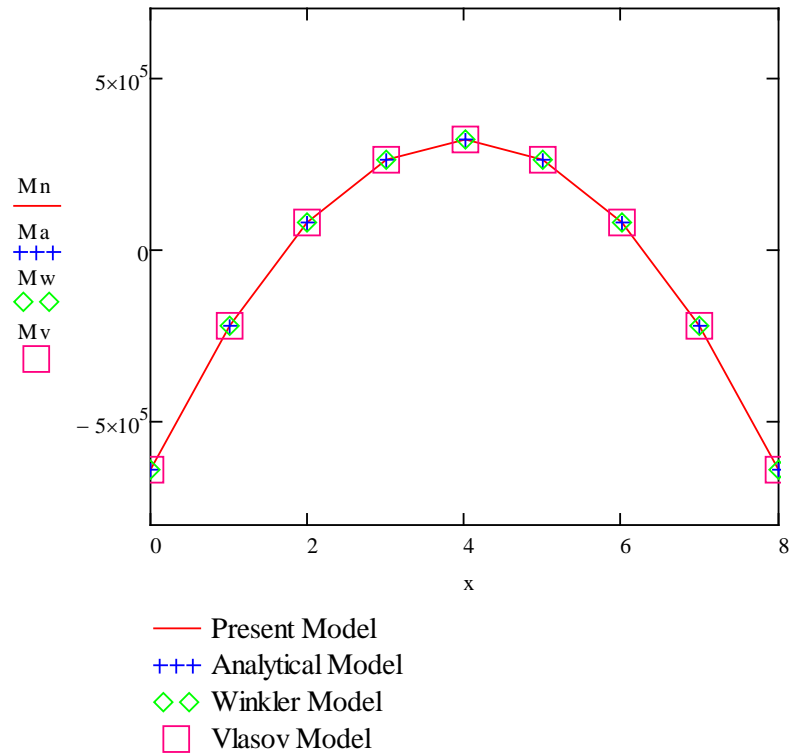


Figure 7. Bending moment of the beam on elastic foundation.

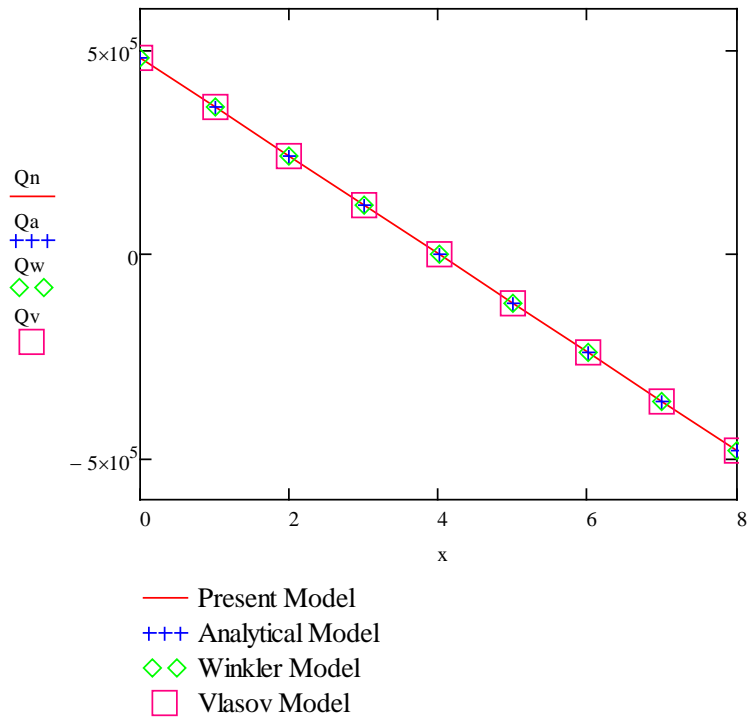


Figure 8. Shear force of the beam on elastic foundation.

3.2.3. Example 3.

A beam fixed at one end and supported at the other on an elastic foundation is considered. The beam on an elastic foundation was assumed to be subjected only to uniform vertical loads. The vertically uniform load was chosen as $q(x) = q_0 \frac{x}{\ell}$, $q_0 = 100 \frac{kN}{m}$. The physical and geometry parameters of the elastic foundations were deformation modulus $\bar{E} = 70 kPa$ and Poissons ratio $\nu = 0.25$, and depth

$h = 6\text{ m}$. A beam of length $\ell = 12\text{ m}$, width $b_0 = 1\text{ m}$, height $h_0 = 2\text{ m}$, and modulus of elasticity $E = 60 \cdot 10^5\text{ kPa}$.

Reliability of the results of the method proposed by the authors was assessed according to the results of Winkler and Vlasov (Tables 9–12). At the same time (Figs. 9–11) it was found that displacements along the normal to the base, the internal forces obtained on the basis of the 4 models described above, are in good agreement.

Table 9. Vertical displacement values (beam fixed at one end and supported at the other on an elastic foundation).

Case	The length of the beam (ℓ , m)						
	0	2	4	6	8	10	12
Wn	0	0.33185	0.97638	1.48647	1.52865	0.98769	0
Wa	0	0.33033	0.97712	1.48400	1.52786	0.98545	0
Ww	0	0.32999	0.97612	1.48254	1.52644	0.98459	0
Wv	0	0.33043	0.97741	1.48444	1.52833	0.98576	0

Table 10. Bending moment values (beam fixed at one end and supported at the other on an elastic foundation).

Case	The length of the beam (ℓ , m)						
	0	2	4	6	8	10	12
Mn, 10^5	-8.39987	-3.10986	1.51123	4.79962	6.08686	4.70752	0
Ma, 10^5	-8.39434	-3.10902	1.51009	4.79677	6.08479	4.70794	0
Mw, 10^5	-8.38555	-3.10597	1.50800	4.79152	6.07935	4.70493	0
Mv, 10^5	-8.39693	-3.10989	1.51048	4.79808	6.08666	4.70964	0

Table 11. Shear force values (beam fixed at one end and supported at the other on an elastic foundation).

Case	The length of the beam (ℓ , m)						
	0	2	4	6	8	10	12
Qn, 10^5	2.69975	2.53647	2.03312	1.19987	0.03341	-1.46785	-3.29982
Qa, 10^5	2.69842	2.53185	2.03214	1.19930	0.03331	-1.46581	-3.29807
Qw, 10^5	2.69530	2.52881	2.02978	1.19832	0.03397	-1.46408	-3.29665
Qv, 10^5	2.69916	2.53236	2.03250	1.19958	0.03345	-1.46606	-3.29919

Table 12. Maximum values of vertical displacements, bending moments and transverse forces (beam fixed at one end and supported at the other on an elastic foundation).

Modular Ratio	Property	Case			
		Winkler Model	Vlasov Model	Analytical Model	Present finite element model
0.2	Max Vertical displacement	0.540	0.545	0.561	0.551
	Max Bending moment, (10^5)	2.082	2.089	2.163	2.095
	Max Shear force, (10^5)	1.384	1.391	1.425	1.396
0.1	Max Vertical displacement	0.792	0.796	0.818	0.806
	Max Bending moment, (10^5)	3.131	3.139	3.157	3.148
	Max Shear force, (10^5)	1.730	1.735	1.757	1.744
0.05	Max Vertical displacement	1.050	1.059	1.074	1.069
	Max Bending moment, (10^5)	4.052	4.059	4.143	4.135
	Max Shear force, (10^5)	1.989	2.001	2.077	2.062

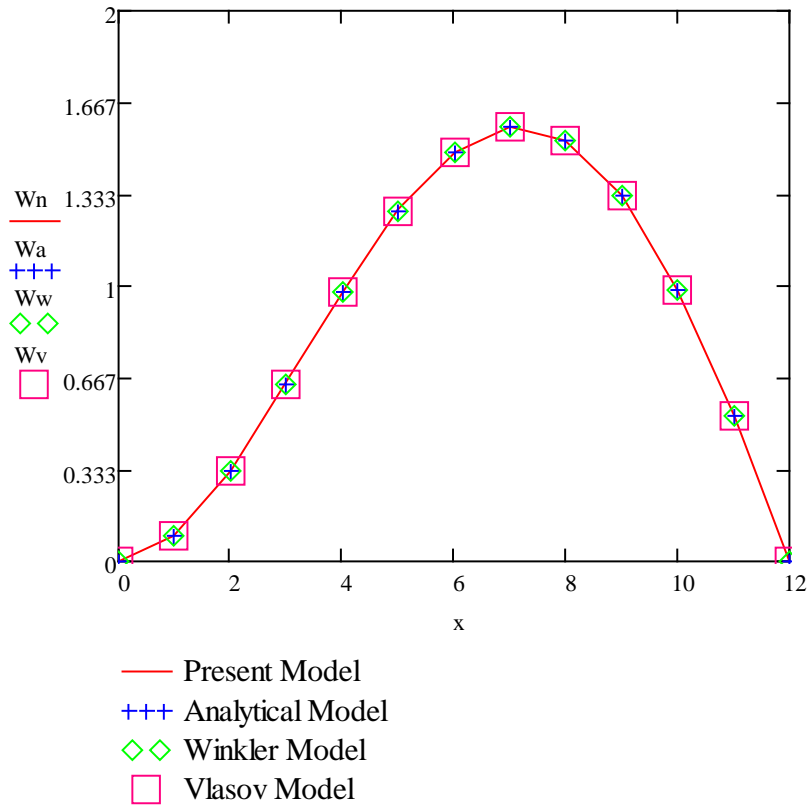


Figure 9. Vertical displacement of the beam on elastic foundation.

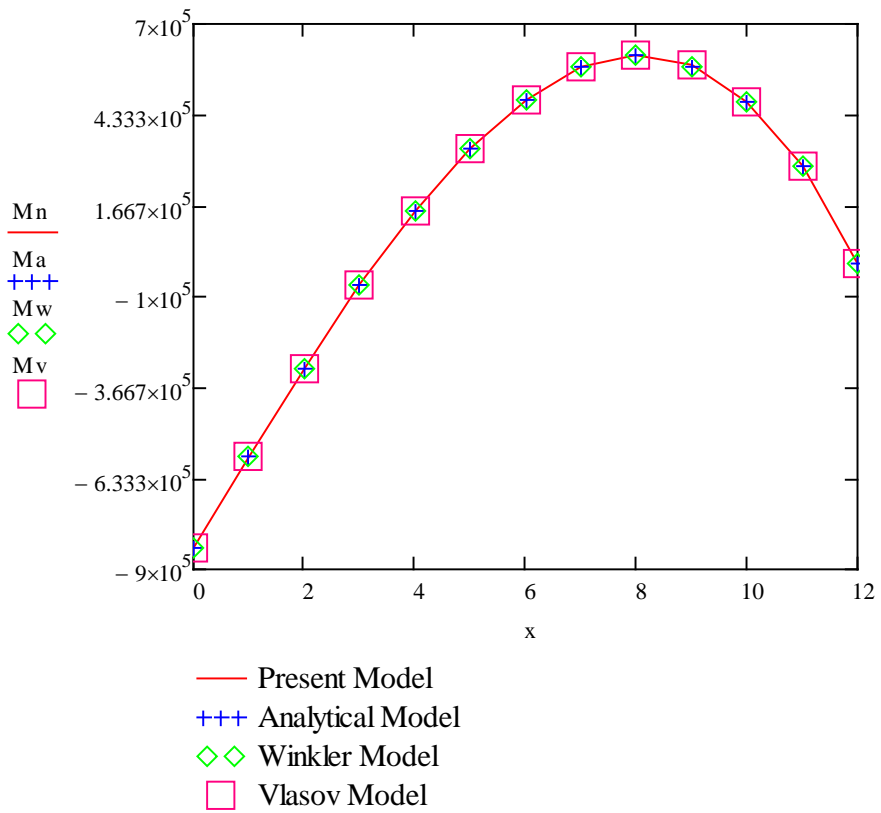


Figure 10. Bending moment of the beam on elastic foundation.

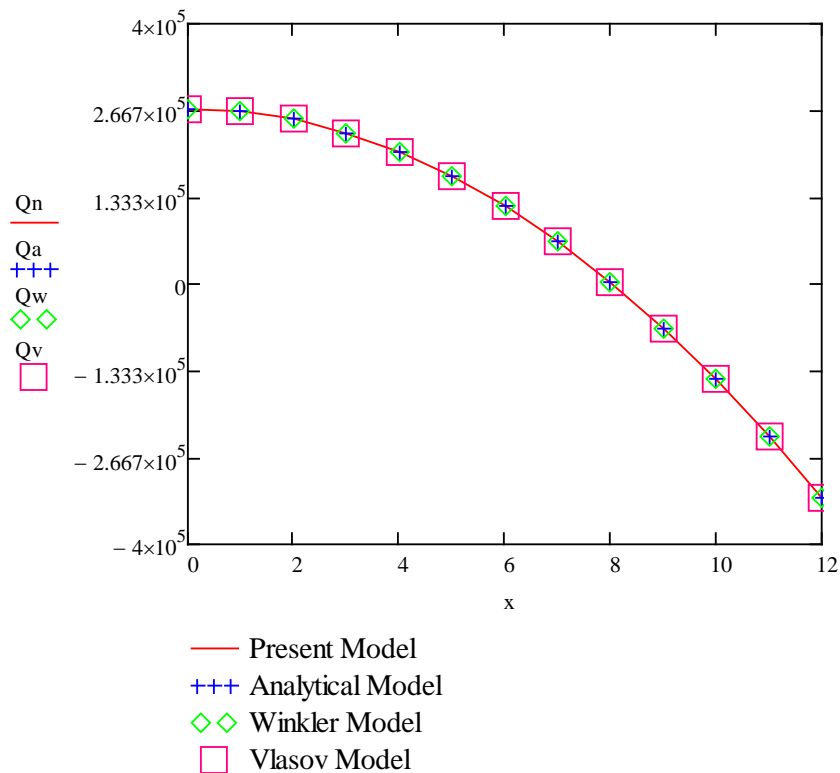


Figure 11. Shear force of the beam on elastic foundation.

In tables and figures W_w , M_w , Q_w means vertical displacement, bending moment, and shear force by Winkler, respectively W_v , M_v , Q_v vertical displacement, bending moment, and shear force by Vlasov. Vertical displacement (W_a), bending moment (M_a), and shear force (Q_a) had determined by the analytical model [32]. The present finite element model found vertical displacement (W_n), bending moment (M_n) and shear force (Q_n).

The presented examples show the advantages of the suggested approach for a numerical beam solution on an elastic foundation. The tables and figures show the excellent agreement of the proposed method with the results obtained by the Winkler and Vlasov models. These results are in good agreement with the results of the author's work, which were obtained using a different approach [32].

4. Conclusions

This article proposes a simplified model of the finite element method of solving the problem of the bending state of finite length beams interacting with a two-parameter base.

Some conclusions can be drawn from the results:

1. The elastic foundation is considered without increasing the degrees of freedom of the finite element.
2. On the basis of the proposed finite element model, which allows determining the deformation (displacement) of the force, an original (the author's) model has been developed.
3. The corresponding formulas for the finite element stiffness matrix, reactive pressure, internal forces, and vertical and nodal displacements are derived.
4. A simplified version of the elastic foundation model is defined. The elastic foundation was taken into account using two parameters.
5. Reliability of the method proposed by the author was evaluated on three test examples; the results obtained are in good agreement with the results obtained on the basis of the Winkler and Vlasov models.

The simplicity of mathematical techniques and the clarity of the scheme make the simplified finite element method under consideration very flexible and allow solving not only the main problems of calculating beams on an elastic foundation but several more complex issues.

Civil engineers use off-the-shelf software for calculations of foundation structures. The proposed finite element model may be of interest to software developers.

References

1. Huang, M.S., Zhou, X.C., Yu, J., Leung, C.F., Jorgin, Q.W.T. Estimating the effects of tunnelling on existing jointed pipelines based on Winkler model. *Tunnelling and Underground Space Technology*. 2019. 86. Pp. 89–99. DOI: 10.1016/j.tust.2019.01.015
2. Balabušić, M., Folić, B., Čorić, S. Bending the Foundation Beam on Elastic Base by Two Reaction Coefficient of Winkler's Subgrade. *Open Journal of Civil Engineering*. 2019. 9. Pp. 123–134. DOI: 10.4236/ojce.2019.92009
3. Avcar, M., Hadji, L., Akan, R. The influence of Winkler-Pasternak elastic foundations on the natural frequencies of imperfect functionally graded sandwich beams. *Geomechanics and Engineering*. 2022. 31(1). Pp. 99–112. DOI: 10.12989/gae.2022.31.1.099
4. Esen, I. Dynamic response of a functionally graded Timoshenko beam on two-parameter elastic foundations due to a variable velocity moving mass. *International Journal of Mechanical Sciences*. 2019. 153. Pp. 21–35. DOI: 10.1016/j.ijmecsci.2019.01.033
5. Kumar, S. Natural Frequencies of Beams with Axial Material Gradation Resting on Two Parameter Elastic Foundation. *Trends in Sciences*. 2022. 19(6). P. 3048. DOI: 10.48048/tis.2022.3048
6. Doeva, O., Masjedi, P.K., Weaver, P.M. Exact analytical solution for static deflection of Timoshenko composite beams on two-parameter elastic foundations. *Thin-Walled Structures*. 2022. 172. 108812. DOI: 10.1016/j.tws.2021.108812
7. Anyaegbunam, A. J. Complete stresses and displacements in a cross-anisotropic half-space caused by a surface vertical point load. *International Journal of Geomechanics*. 2014. 14(2). Pp.171–181. DOI: 10.1061/(ASCE)GM.1943-5622.0000260
8. Mi, C. W. Surface mechanics induced stress disturbances in an elastic half-space subjected to tangential surface loads. *European Journal of Mechanics*. 2017. 50(11). Pp. 59–69. DOI: 10.1016/j.euromechsol.2017.03.006
9. Gholami, M., Alizadeh, M. A quasi-3D modified strain gradient formulation for static bending of functionally graded micro beams resting on Winkler-Pasternak elastic foundation. *Scientia Iranica*. 2022. 29(1B). Pp. 26–40. DOI: 10.24200/SCI.2021.55000.4019
10. Mirsaidov, M., Mamasoliev, Q. Contact problems of multilayer slabs interaction on an elastic foundation. *IOP Conference Series: Earth and Environmental Science*. 2020. 614(1). 012089. DOI: 10.1088/1755-1315/614/1/012089
11. Kontomaris, S. V., Malamou, A. A novel approximate method to calculate the force applied on an elastic half-space by a rigid sphere. *European Journal of Mechanics Physics*. 2021. 42(2). P. 025010. DOI: 10.1088/1361-6404/abccfb
12. Baraldi, D., Tullini, N. Static stiffness of rigid foundation resting on elastic half-space using a Galerkin boundary element method. *Engineering Structures*. 2020. 225. P. 111061. DOI: 10.1016/j.engstruct.2020.111061
13. Tang, C. X., Lu, Z., Yao, H. L., Guo, S., Huang, X. Q., Liu, J. Semianalytical solution for dynamic responses of railway track system on unsaturated poroelastic half-space subjected to moving trainload". *International Journal of Geomechanics*. 2021. 21(3). P. 04021016. DOI: 10.1061/(ASCE)GM.1943-5622.0001955
14. Yubo Chen, Chunliu Li, Shuren Wang, Youkai Wang and Dingqi Li. Theoretical Solution of Elastic Foundation Beam based on the Principle of Minimum Complementary Energy. *Journal of Engineering Science and Technology Review*. 2021. 14(3). Pp. 51–58. DOI: 10.25103/jestr.143.06
15. Kargaudas, V., Adamukaitis, N., Zmuida, M. Elastic foundation displacement approximations. *Baltic Journal of road and bridge Engineering*. 2019. 14(2). Pp. 125–135. DOI: 10.7250/bjrbe.2019-14.436
16. Wieckowski, Z., Swiatkiewicz, P. Stress-Based FEM in the Problem of Bending of Euler–Bernoulli and Timoshenko Beams Resting on Elastic Foundation. *Materials*. 2021. 14. P. 460. DOI: 10.3390/ma14020460
17. Worku, A., Habte, B. Analytical formulation and finite-element implementation technique of a rigorous two-parameter foundation model to beams on elastic foundations. *Geomechanics and Geoengineering*. 2022. 17(2). Pp. 547–560. DOI: 10.1080/17486025.2020.1827162
18. Van Dang, N. Finite Element Modeling for Static Bending Behaviors of Rotating FGM Porous Beams with Geometrical Imperfections Resting on Elastic Foundation and Subjected to Axial Compression. *Advances in Materials Science and Engineering*. 2021. 3835440. DOI: 10.1155/2021/3835440
19. Hariz, M., Le Marrec, L., Lerbet, J. Buckling of Timoshenko beam under two-parameter elastic foundations. *International Journal of Solids and Structures*. 202., 244-245(1–2). 111583. DOI: 10.1016/j.ijsolstr.2022.111583
20. Xia, G. Generalized foundation Timoshenko beam and its calculating methods. *Archive of Applied Mechanics*. 2022. 92(3). Pp. 1015–1036. DOI: 10.1007/s00419-021-02090-1
21. Huang, W., Tahounh, V. Frequency study of porous FGPM beam on two-parameter elastic foundations via Timoshenko theory. *Steel and Composite Structures*. 2021. 40(1). Pp. 139–156. DOI: 10.12989/scs.2021.40.1.139
22. Abubakr E.S. Musa. Galerkin method for bending analysis of beams on non-homogeneous foundation. *Journal of Applied Mathematics and Computational Mechanics* 2017. 16(3). Pp. 61–72. DOI: 10.17512/jamcm.2017.3.06
23. Teodoru, I.B. EBBEF2p - A Computer Code for Analyzing Beams on Elastic Foundations. *Intersections*. 2009. 6. Pp. 28–44.
24. Dinev, D. Analytical solution of beam on elastic foundation by singularity functions. *Engineering Mechanics*. 2012. 19. Pp. 381–392.
25. Limkatanyu, S., Kuntiyawichai, K., Spacone, E., Kwon, M. Nonlinear winkler-based beam element with improved displacement shape functions. *Journal of Civil Engineering, KSCE*. 2013. 17. Pp. 192–201. DOI: 10.1007/s12205-013-1606-0
26. Sánchez, M, Roesset, J.M. Evaluation of models for laterally loaded piles. *Computers and Geotechnics*, 2013. 48. Pp. 316–320.
27. Yue, F. A Refined Model for Analysis of Beams on Two-Parameter Foundations by Iterative Method. *Mathematical Problems in Engineering*. 2021. 5562212. DOI: 10.1155/2021/5562212
28. Akgöz, B., Mercan, K., Demir, Ç., Civalek Ö. Static analysis of beams on elastic foundation by the method of discrete singular convolution. *International Journal of Engineering and Applied Sciences*. 2016. 8(3). Pp. 67–73. DOI: 10.24107/ijeas.255040
29. Ai, Z.Y., Li, Z.X., Cheng, Y.C. BEM analysis of elastic foundation beams on multilayered isotropic soils. *Soils and Foundations*. 2014. 54(4). Pp. 667–674. DOI: 10.1016/j.sandf.2014.06.008
30. Akhazhanov, S.B. Calculation method for a beam on an elastic foundation. Karaganda. 2020. ISBN 978-9965-39-868-1 (in Kazakh)
31. Tursunov K.A. Mechanics of rod structures. Karaganda, 2009, Izdatelstvo KarGU (in Russian)
32. Akhazhanov, S., Omarbekova, N., Mergenbekova, A., Zhunussova, G., Abdykeshova, D. Analytical solution of beams on elastic foundation. *International Journal of Geomate*. 2020. 19(73). Pp. 193–200. DOI: 10.21660/2020.73.51487

Information about authors:

Sungat Akhazhanov, PhD

ORCID: <https://orcid.org/0000-0002-0903-3517>

E-mail: stjg@mail.ru

Nikolai Vatin, Doctor of Technical Sciences

ORCID: <https://orcid.org/0000-0002-1196-8004>

E-mail: vatin@mail.ru

Serik Akhmediyev, PhD in Technical Sciences

E-mail: serik.akhmediyev@mail.ru

Talgat Akhazhanov, PhD

ORCID: <https://orcid.org/0000-0003-3346-4947>

E-mail: talgat_a2008@mail.ru

Omirkhan Khabidolda, PhD

ORCID: <https://orcid.org/0000-0001-7909-7201>

E-mail: oka-kargtu@mail.ru

Aizhan Nurgoziyeva

E-mail: aizhanzhanabai@gmail.com

Received 24.03.2023. Approved after reviewing 23.05.2023. Accepted 23.05.2023.



Research article

UDC 691

DOI: 10.34910/MCE.121.8



Shrinkage of ultra-high performance concrete with superabsorbent polymers

V.S. Lesovik ¹ , D.Y. Popov ¹, R.S. Fediuk ¹ , M.M. Sabri ² , S.V. Vavrenyuk ³, Yu.L. Liseitsev ⁴

¹ Belgorod State Technological University named after V.G. Shukhov, Belgorod, Russian Federation

² Peter the Great St. Petersburg Polytechnic University, St. Petersburg, Russian Federation

³ branch FGBU "TSNIIP Russian Ministry of Construction" DalNIIS, Vladivostok, Russian Federation

⁴ Far Eastern Federal University, Vladivostok, Russian Federation

✉ roman44@yandex.ru

Keywords: superabsorbent polymer, ultra-high performance concrete, polymineral binder, utilization of industrial waste, fly ash, structure formation

Abstract. During the period of hydration and hardening in ultra-high performance concrete (UHPC), a number of destructive processes occur that affect the formation of the structure of the material, which ultimately seriously affects its technical properties and performances. In this regard, the article explores the possibility of increasing the effectiveness of UHPC through the use of polymineral binders (PB) and superabsorbent polymers (SAP). For this, such characteristics as the effect of SAP on the plastic shrinkage of cement paste were investigated; hydration and hardening of cement in the presence of SAP; rheological and physical-mechanical properties of the cement system with the addition of SAP; shrinkage deformations of UHPC. It has been proven that SAP is an effective means of reducing shrinkage deformations of the cement system at the initial stage of structure formation, which helps to reduce the number of destructive phenomena of cement paste. The additive with a dispersion of more than 200 μm reduced vertical deformations by approximately 30%, and with a dispersion of less than 200 μm , by 50%. Despite the fact that SAP does not have a chemical effect on the process of cement hydration. However, the introduction of an additive in an amount of more than 0.1% by weight of PB leads to a significant increase in the setting time (period of active hydration) through the absorption and desorption of water. After 17 and 24 hours after watering, the crystals of neoplasms in the control samples without additives developed more rapidly and had a larger size. However, 41 hours after mixing with water, the larger size of hydration products is typical for samples containing SAP. The introduction of SAP into the composition of cement paste leads to the formation of closed pores filled, depending on storage conditions, with water or air, and a decrease in mechanical properties (by 10-20%). A technological line for the production of UHPC based on polymineral binders using SAP has been developed, it consists of three main stages - the preparation of the polymineral binder, UHPC with desired properties and the manufacture of products from it.

Funding: The study was supported by the RSF grant No. 22-19-20115, <https://rscf.ru/project/22-19-20115/> (accessed on 18 November 2022) and the Government of the Belgorod Region, Agreement No. 3 of 24 March 2022.

Acknowledgements: The work was performed using the equipment of the Center for Collective Use of BSTU n.a. V.G. Shukhov.

Citation: Lesovik, V.S., Popov, D.Y., Fediuk, R.S., Sabri, M.M., Vavrenyuk, S.V., Liseitsev, Yu.L. Shrinkage of ultra-high performance concrete with superabsorbent polymers. Magazine of Civil Engineering. 2023. 121(5). Article no. 12108. DOI: 10.34910/MCE.121.8

1. Introduction

Hydration and hardening of the cement system is accompanied by a number of destructive processes that affect the formation of the structure of the material, which ultimately seriously affects its physico-mechanical properties and performances [1]. Processes such as the occurrence of internal stresses, the formation of structural microcracks, changes in geometric dimensions, etc., are mainly due to shrinkage phenomena of cement paste, which in most cases leads to concrete cracking [2]. According to the results of previous works, compensation for these negative phenomena is carried out mainly due to the introduction of modifiers of a different spectrum of action, however, the methods used are not always effective when using traditional types of binders [3].

The increase in the strength of the hardening cement paste is the result of structural transformations, expressed in crystallization, development and intergrowth of crystalline hydrates, in the accumulation and compaction of the resulting gel [4], [5]. There are several theories of hydration and structure formation of Portland cement and materials based on it such a three-stage one, which uses the kinetics of structural strength (Fig. 1a) [6] and a five-stage one that explains the process in terms of heat release dynamics (Fig. 1b) [7], [8].

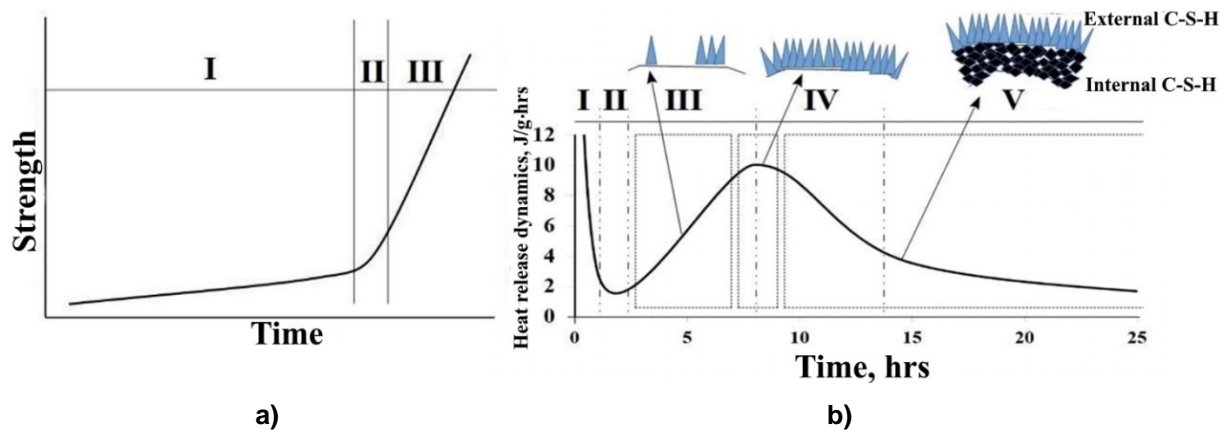


Figure 1. Increase in the structural strength of Portland cement: a) three-stage theory (kinetics of structure formation) [6], b) five-stage theory (heat release dynamics) and the relationship of the main peak of heat release with an increase in C-S-H [8].

The difference lies in the fact that in the first, the chemical process (hydrolysis of calcium silicates with the release of $\text{Ca}(\text{OH})_2$) is carried out immediately after the contact of the reagents, and in the second, after the time (induction) interval I + II, culminating in the main exothermic effect [9]. From the point of view of the dynamics of heat release (Figure 1 b), in the initial period (up to 24 hours), characteristic of heat release during cement hydration, two exothermic effects are separated by an induction period (II) [10], [11]. The first effect (I) is associated with adsorption and chemical interactions [12], [13]. At this stage, there is a rapid increase in the concentration of Ca^{2+} ions in the liquid phase, and after a few minutes from the moment of mixing, supersaturation is reached. After that, the leaching of calcium sharply slows down [14], [15]. This period does not characterize structural transformations [16], [17]. The growth of hydration products nuclei to critical sizes with a gradual increase in calcium supersaturation of the liquid phase can serve as one of the probable reasons for the presence of an induction period [18]. The induction period is the nucleation stage, the duration of which is determined by the nucleation rate, and then hydration passes through the new growth stage, which corresponds to the second exothermic effect [19]. The accelerated period of heat release (III) coincides with the intensive crystallization of hydrolytic lime [20]. Hydration in the accelerated period is a process of accumulation of new growths, going at a constant rate until the deceleration period (IV) [21]. Further monotonic decay of the rate of heat release and hydration (V) is due to the accumulation of reaction products that hinder the access of water to the initial phase and thereby reduce the intensity of their interaction [22]. These periods are characterized by a change in the completeness of hydration and the value of the reaction rate constants [23]. The main structural transformations take place during these periods [24].

In this regard, the working hypothesis of the research is the assumption that it is possible to increase the effectiveness of ultra-high performance concrete (UHPC) through the use of polymineral binders and superabsorbent polymers. The tasks for confirming the proposed hypothesis were: study of the effect of SAP on the plastic shrinkage of cement paste; study of hydration and hardening of cement in the presence of SAP; assessment of rheological and physical-mechanical properties of the cement system with the addition of SAP; study of UHPC shrinkage.

2. Materials and Methods

2.1. Characteristics of the raw materials used

Fig. 2 shows appearance of the materials used. Portland cement CEM I 42.5 N (Verkhnebakansky cement plant, Russia) was used as the base of the polymineral binder. Fly ash from the Novotroitskaya thermal power plant (Russia) and microsilica (StroKorporatsia 74, Russia) were used as supplementary cementitious materials. Glenium 51 (BASF, Germany) was used as a superplasticizer.

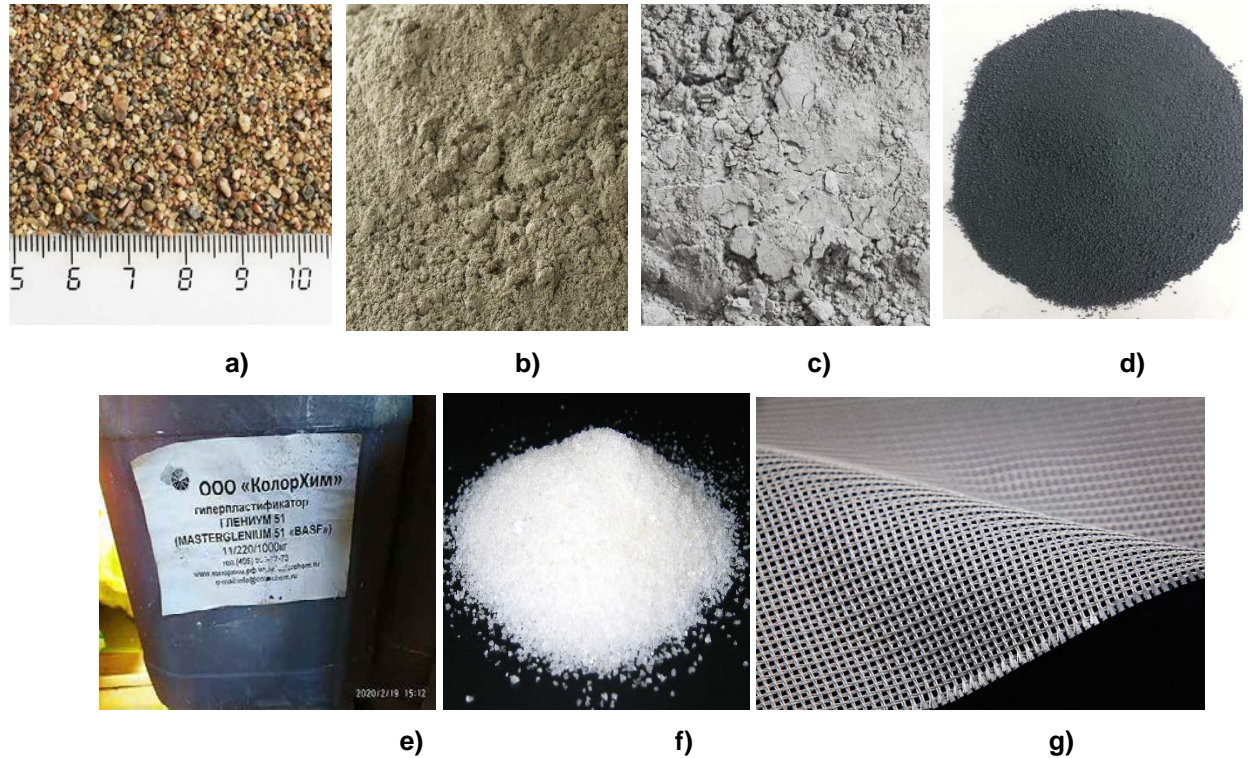


Figure 2. Appearance of the materials used: a) sand, b) fly ash, c) Portland cement, d) microsilica e) superplasticizer, f) SAP, g) glass mesh.

As a filler, fractionated enriched quartz sand of fractions from the Podgorenskoye deposit (Russia) with a fineness modulus of 2.9 was used. The sand characterization is shown in Table 1.

Table 1. The sand characterization.

Type	Fineness modulus	Partial sieve residues, wt. %					Passage through a 0.14 mesh sieve, wt. %
		2.5	1.25	0.63	0.315	0.14	
large	2.9	0	0.1	94.8	4.4	0.7	0

Superabsorbent polymers are a new generation of superabsorbent additives based on high water absorption, retention and release. The additives are cross-linked polyelectrolytes (sodium polyacrylates) that swell upon contact with water or moisture-containing solutions, resulting in the formation of a hydrogel. SAP is used as a dry chemical additive as it absorbs water during the mixing process. The characterization of the superabsorbent polymers used in the paper are presented in Table 2.

Table 2. SAP characterization.

Brand	Modification	Partical size, μm	Designation in the article
Floset	B3	<200	SAP B3 fine
		200-500	SAP B3 coarse
	B4	<200	SAP B4 fine
		200-500	SAP B4 coarse

Article used a textile mesh made of alkali-resistant AR-glass fibers, it is bidirectional (2D), leno weave, has a mesh size of 10×10 mm, and fiber consumption is 520 g/m². Alkali-resistant glasses are produced on the basis of the ZrO₂-SiO₂-Na₂O system. The content of expensive zirconium oxide in them varies from 15 to 23%. Since the melting point of pure zirconium oxide is quite high (2715°), alkali metal

oxides are added to the glass, most often Na₂O (from 12 to 16%). Table 3 shows the chemical composition of the AR glass used for fiberglass production.

Table 3. AR-glass chemical composition, wt. %.

SiO ₂	ZrO ₂	Na ₂ O	TiO ₂	K ₂ O	Al ₂ O ₃
58.3–60.6	18.1–21.2	13.0–14.1	0–2.8	0–2.8	0.2

2.2. Mix design

Table 4 lists investigated mixes of UHPC. The amount of binder for all mixtures was 855 kg per 1 m³. SAP additives were introduced in a dry state in an amount of 0.1% by weight of the binder. Compositions were prepared at water-to-binder ratios of 0.3 (without SAP) and 0.35 (with SAP) according to the regime that provides the best mixing of the components (Table 5).

Table 4. Investigated mixes of UHPC, kg per 1 m³.

Feedstock	Mix ID					
	C1	CS1	CSM1	C2	CS2	CSM2
Portland cement	700	700	700	600	600	600
Fly ash	120	120	120	180	180	180
Microsilica	35	35	35	75	75	75
Sand	1190	1190	1190	1400	1400	1400
Superplasticizer	6	6	6	6	6	6
SAP B3 (<200 μm)	-	-	1.8	-	-	-
SAP B3 (200-500 μm)	-	0.9	-	-	-	-
SAP B4 (<200 μm)	-	-	-	-	0.9	-
SAP B4 (200-500 μm)	-	-	-	-	-	1.8
Water	262	262	306	262	262	306
Mash layers	-	-	2	-	-	2

Table 5. Mode of preparation of concrete mixture using a mixer.

Total time, min.	Stage	Stage duration, min.
00.00–02.00	Mixing of dry components	2
02.00–03.00	Addition of 80% water	1
03.00–04.00	Mixing in normal mode	1
04.00–05.00	Mixing in fast mode	1
05.00–06.00	Scraping off the walls by hand	1
06.00–06.30	Adding the remaining 20% water	0.5
06.30–08.30	Mixing in normal mode	2

2.3. Laboratory equipment and research methods

Granulometry of binder systems and used raw materials was carried out using an ANALYSETTE 22 NanoTec plus laser particle size analyzer. The rheological properties of the test cement paste were determined by measuring the diameter of a slump flow from a mold in the form of a truncated cone ($h = 60$ mm, $D = 100$ mm, $d = 70$ mm) on a smooth surface immediately after preparation.

Shrinkage tests were carried out in a climate chamber under two operating modes simulating normal hardening conditions (moisture evaporation rate 0.25 kg/m²·h) and hot climate (0.75 kg/m²·h) (Fig. 3). The experimental setup consists of four plastic molds with internal dimensions of 300×300×20 mm and is equipped with special sensors necessary to identify the physical quantities that affect the cement system during the test period (Fig. 4). Due to the prefabricated design of the formwork, it is possible to change the thickness of the test samples. The setup allows to carry out researches in the specified operating modes of the climatic chamber, due to changes in environmental factors (temperature and humidity, wind speed) and to record the parameters of vertical and horizontal deformations.

Mode	Air temperature, °C	Air humidity, %	Air speed, m/s	Moisture evaporation rate, kg/m ² ·h
Normal	20	65	4	0.25
Hot	35	40	5.5	0.75

Figure 3. Climate chamber operating modes.

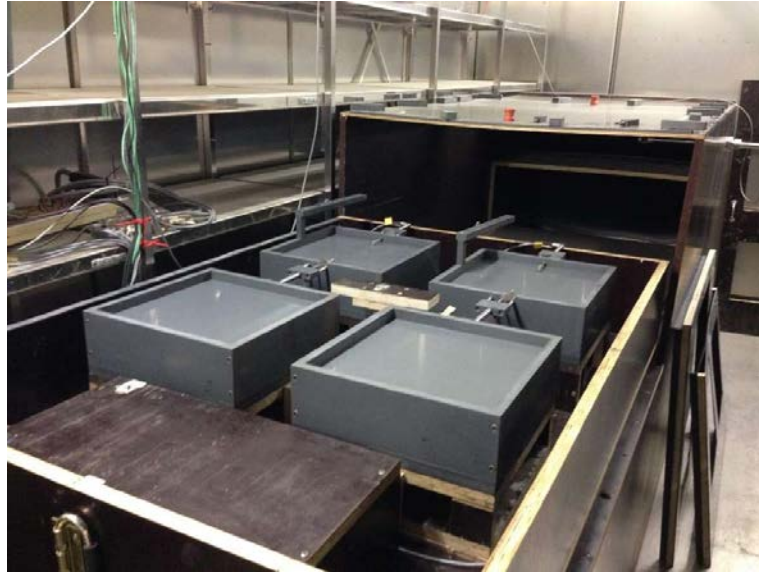


Figure 4. Appearance of the setup for determining the plastic shrinkage of cement systems inside the climatic chamber.

The nature of the effect of superabsorbent polymers on cement hydration was established by determining the dynamics of heat release, expressed by the dependence $dQ / dt = f(t)$, during 24 hours of testing, and the total amount of heat released, described by the function $Q = f(t)$, for 70 hours, using a differential calorimeter. A comparison was made of the results of a control sample of cement without additives, and samples containing SAP in an amount of 0.3% by weight of cement with sizes less than 200 μm and more than 200 μm , and also, in an amount of 0.6%, particle sizes less than 200 μm . Cement samples weighing 10 g were prepared, the amount of water introduced was 5 g. It is also found that within 48 hours after mixing the cement with water, using a TESCAN MIRA 3LMU scanning electron microscope, the morphology of hydration products was studied and a comparative analysis was made.

3. Results and Discussion

3.1. Effect of SAP on the cement paste plastic shrinkage

The effect of SAP additives on vertical deformations is ambiguous (Fig. 5). It is found that when tested in normal climatic conditions (Fig. 5a), all the studied types of additives contributed to an increase in vertical deformations. This effect can be explained by the reduction in the volume of SAP particles, due to water desorption, and filling the free space with cement paste, resulting in a decrease in the volume of the test samples. The best effect was achieved by adding SAP B4 with a dispersion of less than 200 μm . However, when tested in a hot climate mode (Fig. 5b), the introduction of SAP led to a significant reduction in vertical deformations. The greatest effect was achieved by the introduction of SAP B4, while the addition of a dispersion of more than 200 μm reduced vertical deformations by about 30%, and a dispersion of less than 200 μm by 50%, in turn, SAP B3 with a dispersion of less than 200 μm reduced deformations by 28%. Thus, as a result of studying the nature of the influence of the type and dispersion of superabsorbent polymers on plastic shrinkage in cement paste, it was found that SAP is an effective means of reducing shrinkage deformations of the cement system at the initial stage of structure formation, which helps to reduce the number of destructive phenomena of cement paste.

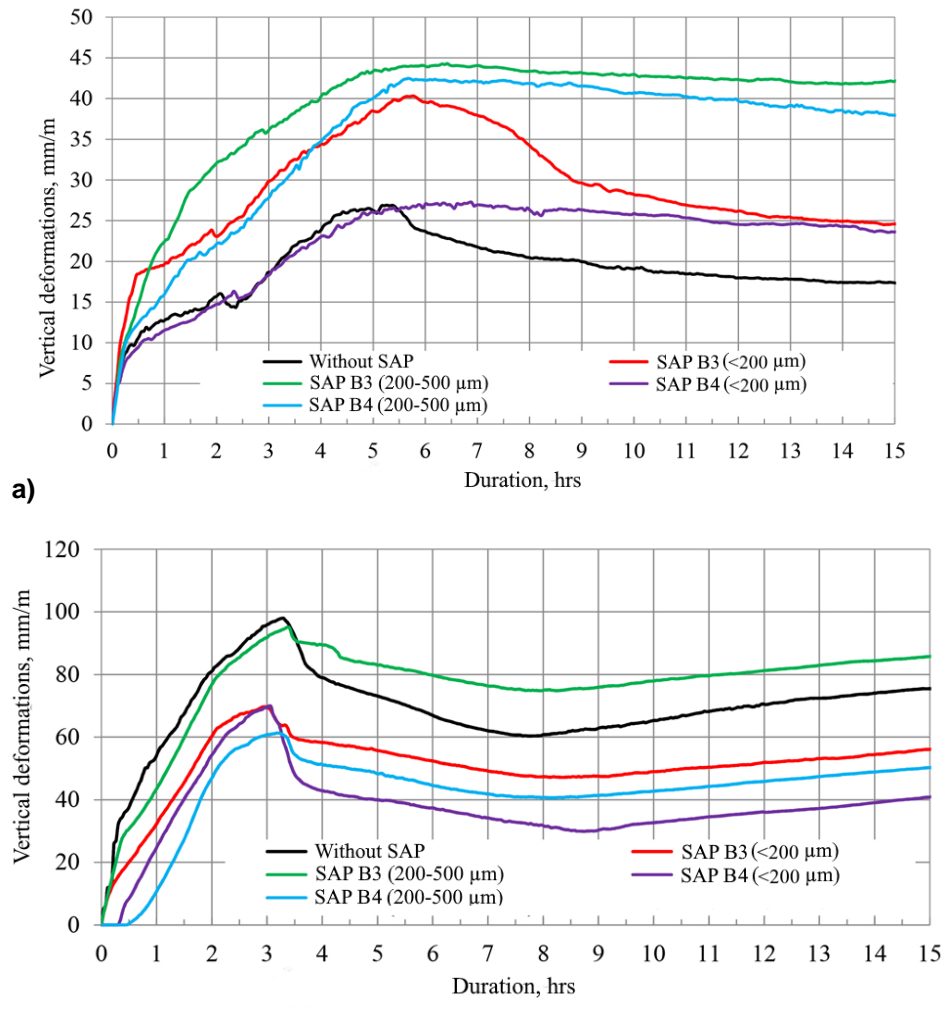


Figure 5. Curves of changes in vertical deformations: a) normal climatic mode, b) hot climatic mode.

The obtained results regarding effect of SAP on the cement paste plastic shrinkage correlate with the works of other authors [25], [26], confirming the potential of using superabsorbent polymers for self-healing building cement materials.

3.2. Hydration and hardening of cement in the presence of SAP

It was established that SAP does not have a chemical effect on the process of cement hydration. However, the introduction of an additive in an amount of more than 0.1% by weight of the binder leads to a significant increase in the setting time (period of active hydration) through the absorption and desorption of water (Fig. 6)

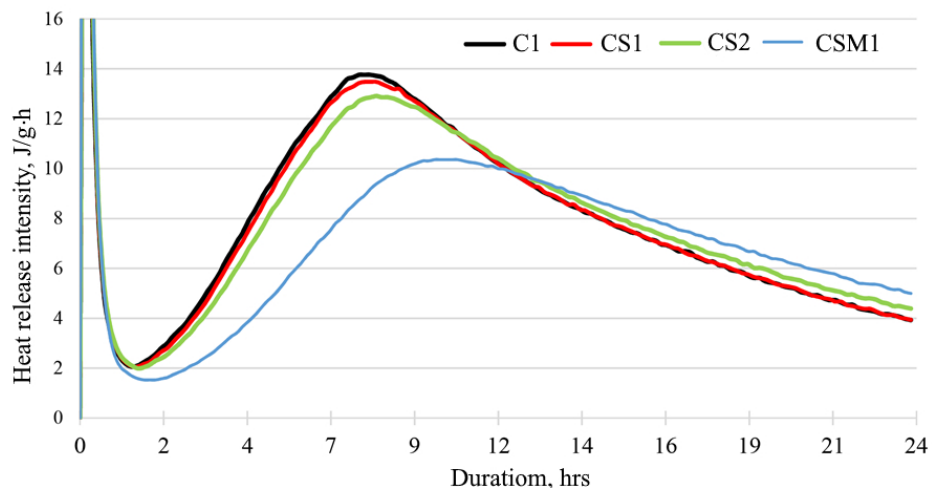


Figure 6. Curves of dynamics of heat release during cement hydration in the presence of SAP.

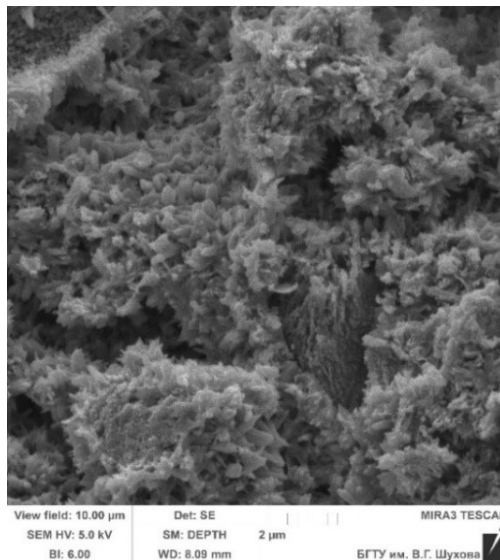
Moisture retention in the first hours after mixing leads to incomplete hydration of the binder, since not all cement particles can be fully provided with the necessary water. However, the subsequent water loss leads to an additional reaction, which is confirmed by the elongated curves of the heat release dynamics of the samples, which contain additives. Based on the total amount of heat released during 70 hours of testing samples containing SAP compared to the control composition, it can be judged that all the water was involved in the cement hydration process (Table 6).

Table 6. Amount of heat released during testing for 70 h, J/g.

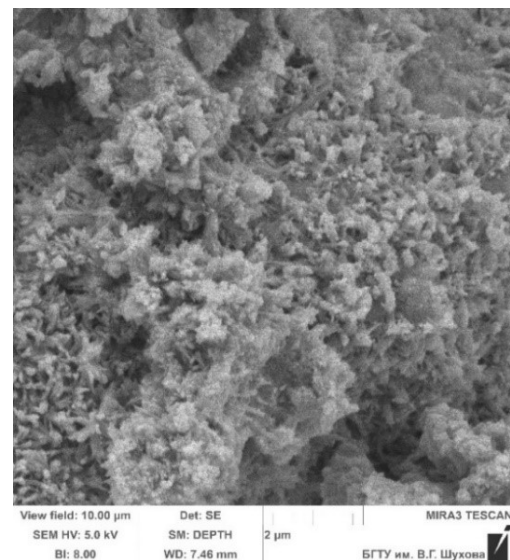
Amount of SAP, wt. % of binder			
0	0.1 (200–500 μm)	0.1 (<200 μm)	0.2 (<200 μm)
280.03	279.80	286.03	281.13

To establish the effect of water loss of additives on the growth of hydration products in the early stages of hardening, samples were prepared at $w/b = 0.3$, with a content of 0.1 wt. % SAP (dispersion less than 200 μm) and control ones without additives. After disassembly, the samples were stored open in laboratory conditions.

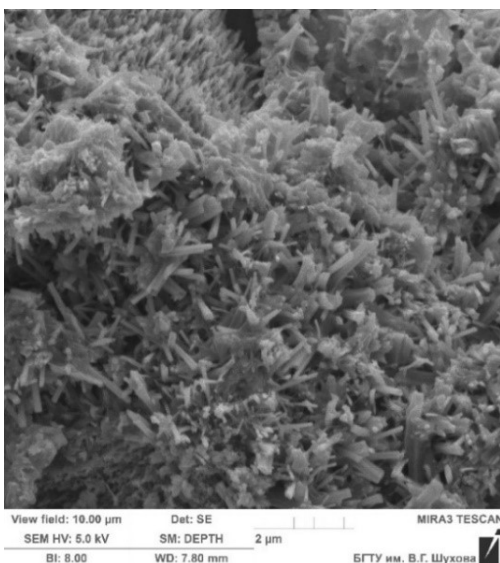
It was established that after 17 and 24 hours after water mixing, the crystals of new growths in the control samples without additives developed more rapidly and had a larger size (Fig. 7a - 7d). However, 41 hours after mixing with water, a larger size of hydration products is characteristic of samples containing SAP (Fig. 7e-7f)



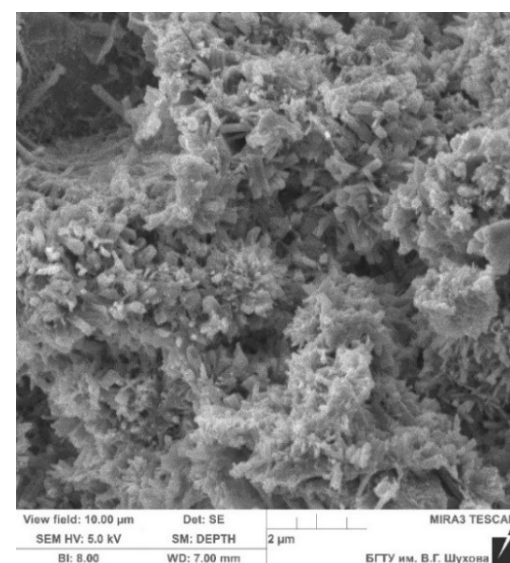
a)



b)



c)



d)

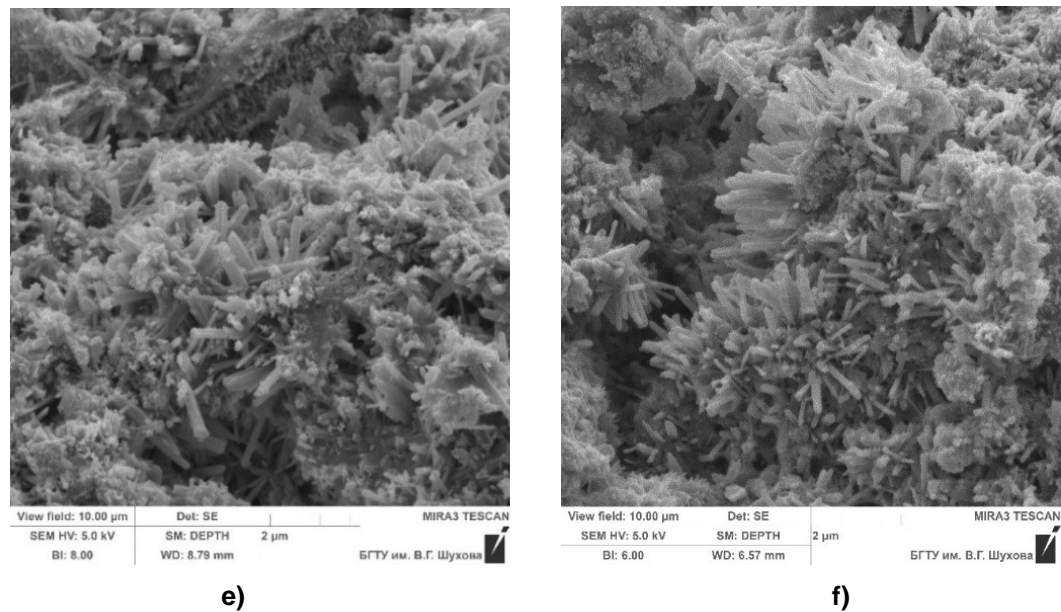


Figure 7. SEM images of hydration products crystals: 17 hours after mixing with water – a) without SAP, b) with SAP; 24 hours after mixing with water – c) without SAP, d) with SAP; 41 hours after mixing with water – e) without SAP, f) with SAP

This effect is achieved as a result of the participation in the hydration process of additional water released from the SAP hydrogel approximately after the maximum exothermic reaction has been reached.

The obtained results regarding hydration and hardening of cement in the presence of SAP correlate with the works of other authors [27], [28], confirming the potential of using superabsorbent polymers for self-healing building cement materials.

3.3. Rheological and physical-mechanical properties of the cement system with the addition of SAP

The test results the *concrete* mix slump flow and the concrete 28-days average density are presented in Table 7. SAP B3 additives, regardless of dispersion, do not have significant moisture saturation in the first 8.5 minutes after contact with water (duration of mixture preparation). However, SAP B4 (<200 µm) reduces the concrete slump flow by 24%, and SAP B4 (200–500 µm) by 14%. The difference in the slump flow of samples containing SAP B4 indicates that with an increase in the dispersion of the additive, the rate of its moisture saturation increases. Further moisture saturation with water will depend on the sorption capacity of the polymer, its size and the amount of free water present. The relative amount of water consumed can be determined from the value of the average density of the concrete.

The effect of superabsorbent polymers on the physical and mechanical properties was established by testing concrete samples prepared in standard forms 40×40×160 mm on days 3, 7 and 28. Tests and processing of results were carried out according to the Russian Standard GOST 30744-2001.

Table 7. The effect of SAP on fresh mix consistency and average concrete density.

Mix ID	Slump flow, mm	Average density, kg/m ³
C1	215	1920
CSM1	206	1880
C1	210	1880
C2	164	1870
CSM2	180	1870

The introduction of additives leads to a decrease in the average density of the concrete. During the period of water mixing and up to solidification, SAP particles absorb water and turn into a hydrogel, thereby reducing the density of the mixture. After the cement stone hardens, SAP particles form a closed pore filled with water, which leads to a decrease in the average density of the samples.

There is a trend between the moisture saturation of SAP additives and the value of the average density of the concrete. The more water a polymer particle is able to absorb, the lower the average density

and the greater the pore volume created in the concrete. The same regularity can be traced when establishing the influence of SAP on the strength properties of the concrete (Fig. 8).

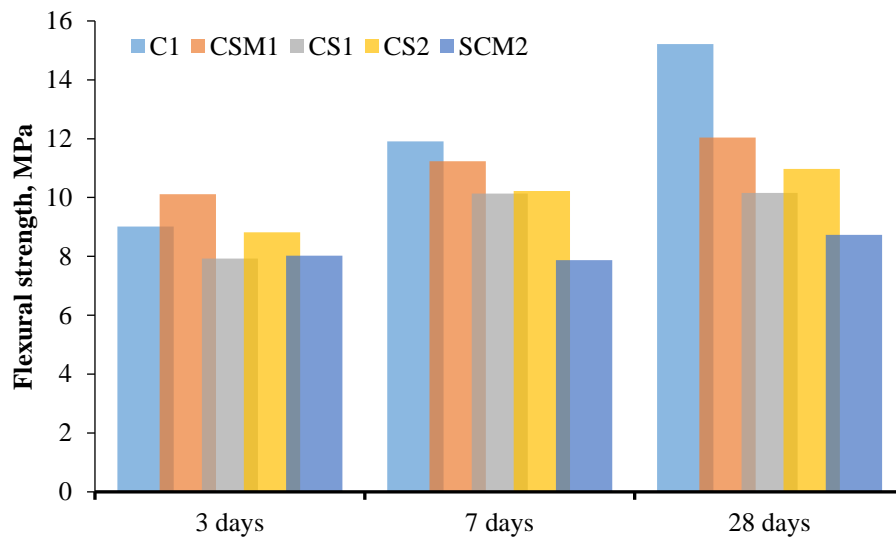


Figure 8. The effect of SAP on the concrete flexural strength.

In the early stages of strength development (day 3), concrete samples containing SAP B3 and SAP B4 of smaller particle size ($<200 \mu\text{m}$) showed an increase in flexural strength by 12.21 and 8.99%, respectively. However, in subsequent periods of testing, the strength decreases. So, on average, on the 7th and 28th day of testing samples containing SAP B3, in comparison with control samples, there is a decrease in flexural strength by 5.71 and 14.19%, respectively, and when testing samples containing SAP B4 by 20.84 and 27.88% respectively.

There is also a decrease in flexural strength depending on the dispersion of additives. For concrete samples with SAP B3, the difference in flexural strength on days 3, 7 and 28 is 21.56, 9.80 and 15.61%, respectively, and for concrete samples containing SAP B4 9.07, 22.99 and 20.42%, respectively. The increase in the pore size due to the introduction of larger SAP leads to a decrease in the resistance of concrete to flexural loads.

A similar trend can be traced when establishing the effect on the compressive strength. So on the 3rd, 7th and 28th day of testing samples containing SAP B3, in comparison with control samples, there is a decrease in compressive strength by an average of 4.73, 13.24 and 16.18%, respectively, and when testing samples containing SAP B4 by 16.74, 17.50 and 16.68%, respectively (Fig. 9).

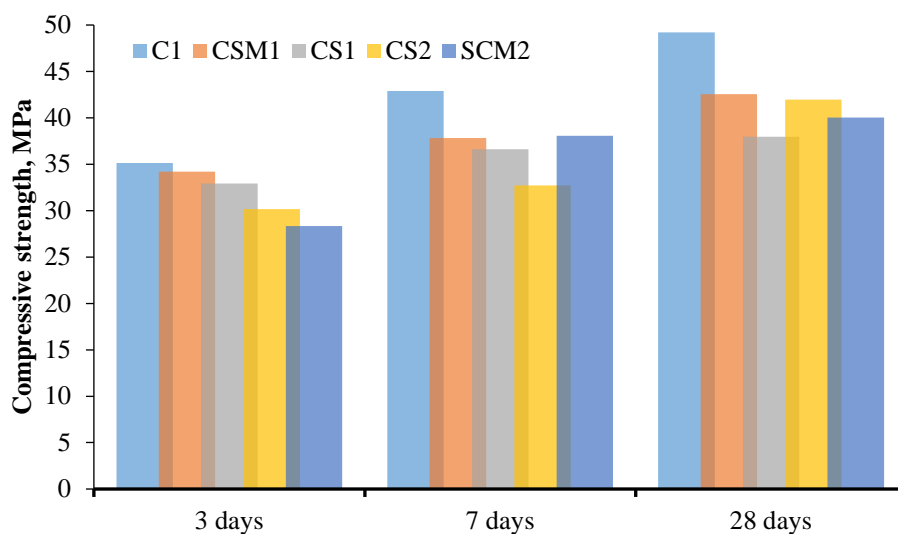


Figure 9. The effect of SAP on the concrete compressive strength.

An increase in SAP particle size results in a decrease in compressive strength. For concrete samples containing SAP B3 on days 3, 7 and 28, the difference in compressive strength is 3.77, 3.17 and 10.77 %, respectively.

respectively, and for samples in the presence of SAP B4 is 6.10, 16.35 and 4.62 % respectively. Thus, the introduction of superabsorbent polymers into the composition of concrete leads to the formation of closed pores filled, depending on storage conditions, with water or air, and a decrease in physical and mechanical properties. At the same time, an increase in the size of SAP particles leads to the greatest decrease in strength indicators.

The obtained results regarding rheological and physical-mechanical properties of the cement system with the addition of SAP correlate with the works of other authors [29], [30], confirming the potential of using superabsorbent polymers for self-healing building cement materials.

3.4. Shrinkage deformations of concrete

The influence of the type of superabsorbent polymers and reinforcing meshes on the shrinkage deformations of the developed UHPC compositions in the early stages of hardening was studied. The most cost-effective type of reinforcing mesh was used, made of alkali-resistant glass of the AR type, with a fiber consumption of 520 g/m² and a mesh size of 10×10 mm. The tests were carried out on a special installation for the study of plastic shrinkage of cement systems in two modes of operation of the climatic chamber.

During the tests, it was found that the introduction of SAP into the composition of UHPC in all cases leads to a reduction in horizontal deformations caused by plastic shrinkage. When tested under normal conditions (moisture evaporation rate 0.25 kg/m².h) in the first 15 hours after water mixing, UHPC compositions with different SAPs have almost equal values of horizontal deformations (Fig. 10a). Due to the peculiarities of hydration and hardening of the polymineral binder, in subsequent periods of testing, a small number of structural defects are observed in concrete.

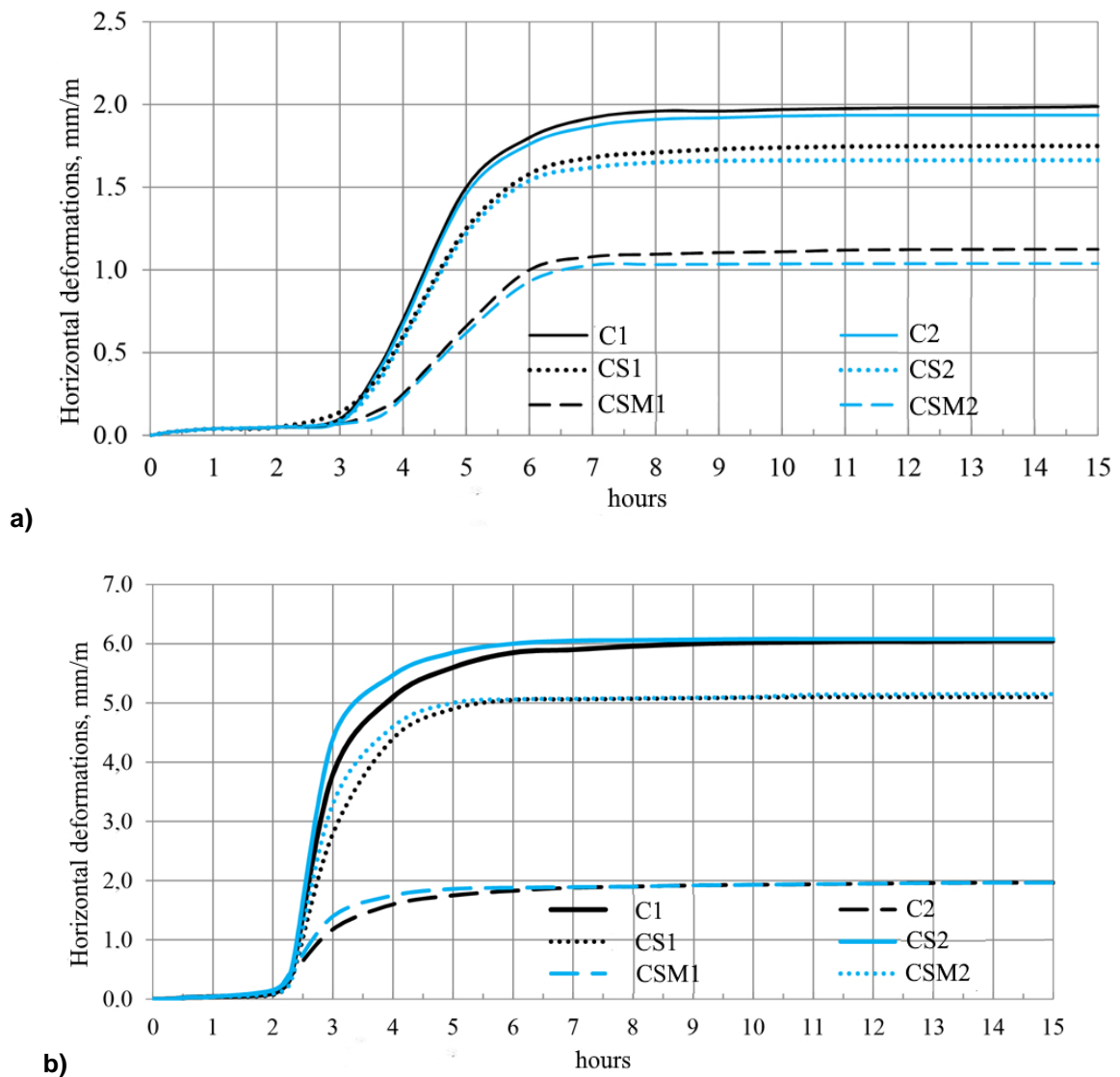


Figure 10. Influence of concrete components on the change in horizontal deformations when tested in normal climatic conditions (a) and hot climatic conditions (b).

When tested in hot climatic conditions (evaporation rate $0.75 \text{ kg/m}^2\cdot\text{h}$), due to more intensive evaporation of moisture from the surface of the concrete mix, volumetric deformations in the first hours, caused by the formation of negative capillary pressure, due to the lack of structural strength of the binder, develop more rapidly (Fig. 10b). Since the setting of Portland cement occurs somewhat earlier than that of supplementary cementitious materials, the deformations of C1, CS1 and CSM1 upon reaching 3 hours are less than C2, CS2 and CSM2. However, in the future, the hydration of the polymineral binder increases, which leads to a reduction in horizontal deformations. When comparing the test results of UHPC and cement stone, a decrease in horizontal deformations by more than a factor of two is observed. This is due to the restraining effect of the filler and fillers during the development of plastic shrinkage of UHPC. A well-chosen ratio of coarse and fine fractions reduces the size of capillary pores, prevents concrete delamination and forms a framework that prevents the development of volumetric deformations. As can be seen from the graphs (Fig. 10), reinforcing mesh is of great importance in curbing shrinkage deformations in the early stages of hardening. When tested under normal conditions, two layers of reinforcing meshes together with SAP in UHPC reduce horizontal deformations by more than 40%, and when tested in hot climates, by more than 60%. As a result of the tests, it was found that the introduction of superabsorbent polymers in an amount of 0.1% by weight of the binder leads to a reduction in shrinkage deformations of the concrete mix, regardless of the type of binder, under normal and hot hardening conditions by 20 and 16 %, respectively, and concrete by 40 and 60% respectively. The effectiveness of the use of polymineral binders will be in the formation of the UHPC structure with increased resistance to destructive processes, manifested in the form of microcracks.

The obtained results regarding shrinkage deformations of concrete correlate with the works of various authors [29–32], confirming the potential of using superabsorbent polymers for self-healing building cement materials.

3.5. Technological line for the production of UHPC

The technological scheme for the production of products from Ultra high performance concrete, based on polymineral binders using superabsorbent polymers, consists of three main stages such the preparation of a binder, the preparation of fine-grained concrete of given properties and the manufacture of products from UHPC, depending on the method adopted (Fig. 11).

Portland cement, fly ash and microsilica in the accepted ratio are subjected to joint grinding in a ball mill for a period of time necessary to achieve a specific surface area of the mixture equal to $550 \text{ m}^2/\text{kg}$. The preparation of the concrete mixture is carried out in accordance with the requirements of the relevant standards and regulations for mixtures of fine-grained concrete. To achieve a uniform consistency, it is recommended to use forced-action concrete mixers (blade). After the ready-mixed concrete is fed into the hopper of the mix distributor, dosing and filling of the molds is carried out with the help of a movable manual distributor, depending on the method of preparation of the UHPC. Molded products are delivered to the storage warehouse. The method of preparing products from UHPC, in each case, is selected depending on the design features. The developed technological line implies three methods of preparing textile-concrete: lamination method (layer-by-layer laying of the concrete mixture), casting method (filling the mold with a rolling stock of the concrete mixture) and shotcrete (layer-by-layer laying of the concrete mixture by spraying using shotcrete equipment).

The developed technological line for the production of self-healing concrete is more efficient than similar ones.

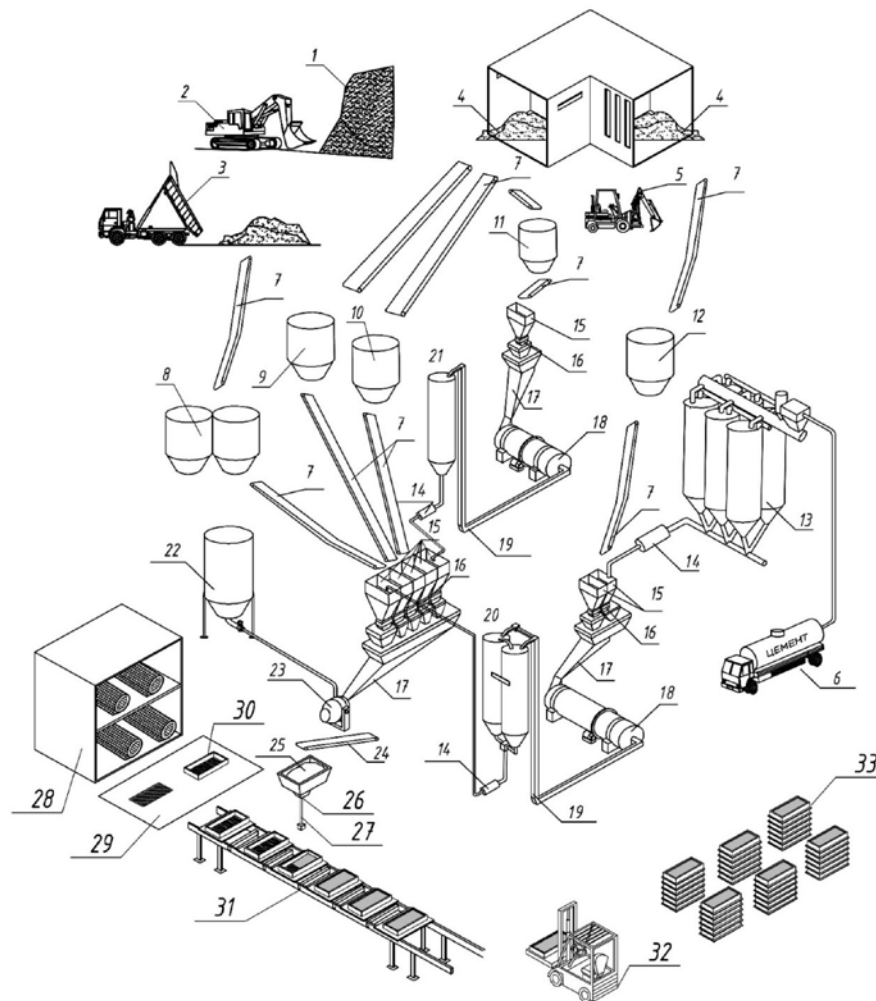


Figure 11. Technological scheme for the production of UHPC products: 1 – sand quarry; 2 – excavator; 3 – vehicles; 4 – warehouse for storage of fly ash and microsilica; 5 – loader of raw materials; 6 – cement carrier; 7 – belt conveyor; 8 – sand storage bunker; 9 and 10 – fly ash storage bunkers; 11 and 12 – microsilica storage bunker; 13 – cement storage bin; 14 – chamber pump; 15 – collection bunker; 16 – weight dispensers; 17 – receiving funnel; 18 – ball mill; 19 – elevator; 20 and 21 – polym mineral binder silos; 22 – water tank; 23 – concrete mixer; 24 – belt feeder; 25 - storage bin; 26 – rotary supercharger; 27 – manual mixture distributor; 28 – storage of glass mesh; 29 – point for cutting and laying glass mesh into the formwork; 30 – formwork; 31 – belt conveyor; 32 – unloader; 33 – storage warehouse for molded products.

4. Conclusions

During the period of hydration and hardening, a number of destructive processes occur in the cement system that affect the formation of the structure of the material, which ultimately seriously affects its technical and operational properties. In this regard, the working hypothesis of the research is the assumption that it is possible to increase the effectiveness of UHPC through the use of polym mineral binders and superabsorbent polymers. The tasks for confirming the proposed hypothesis were: study of the effect of SAP on the plastic shrinkage of cement paste; study of hydration and hardening of cement in the presence of SAP; assessment of rheological and physical-mechanical properties of the cement system with the addition of SAP; shrinkage study of UHPC. As a result of solving these tasks, the following main conclusions were drawn:

- SAP is an effective means of reducing shrinkage deformations of the cement system at the initial stage of structure formation, which helps to reduce the number of destructive phenomena of the cement stone. The greatest effect was achieved by the introduction of SAP B4, while the addition of a dispersion of more than 200 μm reduced vertical deformations by about 30%, and a dispersion of

less than 200 μm by 50%, in turn, SAP B3 with a dispersion of less than 200 μm reduced deformations by 28%.

- SAP does not have a chemical effect on the cement hydration process. However, the introduction of an additive in an amount of more than 0.1 wt. % by weight of the binder leads to a significant increase in the setting time (period of active hydration) through the absorption and desorption of water.
- After 17 and 24 hours after watering, the crystals of new growths in the control samples without additives developed more rapidly and had a larger size. However, 41 hours after mixing with water, the larger size of new growths is typical for samples containing SAP.
- The introduction of superabsorbent polymers into the composition of cement paste leads to the formation of closed pores filled, depending on storage conditions, with water or air, and a decrease in physical and mechanical properties. At the same time, an increase in the size of SAP particles leads to the greatest decrease in strength indicators.
- Ultra high performance concrete, based on polymineral binders using superabsorbent polymers, consists of three main stages - preparation of binder and mineral modifier, preparation of fine-grained concrete of given properties and production of UHPC products, depending on the adopted method

5. Compliance with Ethical Standards

The authors declare no conflict of interest. The research does not involving Human Participants and/or Animals.

References

1. Mosaberpanah, M.A., Eren, O. Statistical models for mechanical properties of UHPC using response surface methodology. *Computers and Concrete*. 2017. 19(6). Pp. 667–675. DOI: 10.12989/cac.2017.19.6.667
2. García Calvo, J.L., Pérez, G., Carballosa, P., Erkizia, E., Gaitero, J.J., Guerrero, A. Development of ultra-high performance concretes with self-healing micro/nano-additions. *Construction and Building Materials*. 2017. 138. Pp. 306–315. DOI: 10.1016/j.conbuildmat.2017.02.015
3. Ganesh, P., Murthy, A.R. Tensile behaviour and durability aspects of sustainable ultra-high performance concrete incorporated with GGBS as cementitious material. *Construction and Building Materials*. 2019. 197. Pp. 667–680. DOI: 10.1016/j.conbuildmat.2018.11.240
4. Azreen, N.M., Rashid, R.S.M., Mugahed Amran, Y.H., Voo, Y.L., Haniza, M., Hairie, M., Alyousef, R., Alabduljabbar, H. Simulation of ultra-high-performance concrete mixed with hematite and barite aggregates using Monte Carlo for dry cask storage. *Construction and Building Materials*. 2020. 263. Pp. 120161. DOI: 10.1016/j.conbuildmat.2020.120161
5. de Oliveira, L.B., de Azevedo, A.R.G., Marvila, M.T., Pereira, E.C., Fediuk, R., Vieira, C.M.F. Durability of geopolymers with industrial waste. *Case Studies in Construction Materials*. 2021. 16. 00839. DOI: 10.1016/j.cscm.2021.e00839
6. Luan, C., Wang, J., Gao, J., Wang, J., Du, P., Zhou, Z., Huang, Y., Du, S. Changes in fractal dimension and durability of ultra-high performance concrete (UHPC) with silica fume content. *Archives of Civil and Mechanical Engineering*. 2022. 22(3). 123. DOI: 10.1007/s43452-022-00443-3
7. Van Tuan, N., Ye, G., Van Breugel, K., Fraaij, A.L.A., Bui, D.D. The study of using rice husk ash to produce ultra high performance concrete. *Construction and Building Materials*. 2011. 25(4). Pp. 2030–2035. DOI: 10.1016/j.conbuildmat.2010.11.046
8. Scrivener, K.L., Juilland, P., Monteiro, P.J.M. Advances in understanding hydration of Portland cement. *Cement and Concrete Research*. 2015. 78. Pp. 38–56. DOI: 10.1016/j.cemconres.2015.05.025
9. He, Z. hai, Du, S. gui, Chen, D. Microstructure of ultra high performance concrete containing lithium slag. *Journal of Hazardous Materials*. 2018. 353. Pp. 35–43. DOI: 10.1016/j.jhazmat.2018.03.063
10. Jung, M., Lee, Y. soon, Hong, S.G., Moon, J. Carbon nanotubes (CNTs) in ultra-high performance concrete (UHPC): Dispersion, mechanical properties, and electromagnetic interference (EMI) shielding effectiveness (SE). *Cement and Concrete Research*. 2020. 131(August 2019). Pp. 106017. DOI: 10.1016/j.cemconres.2020.106017
11. Svintsov, A.P., Shchesnyak, E.L., Galishnikova, V.V. Fediuk, R.S., Stashevskaya, N.A. Effect of nano-modified additives on properties of concrete mixtures during winter season. *Construction and Building Materials*. 2020. 237. 117527. <https://doi.org/10.1016/j.conbuildmat.2019.117527>
12. Xie, T., Fang, C., Mohamad Ali, M.S., Visintin, P. Characterizations of autogenous and drying shrinkage of ultra-high performance concrete (UHPC): An experimental study. *Cement and Concrete Composites*. 2018. 91. Pp. 156–173. DOI: 10.1016/j.cemconcomp.2018.05.009
13. Fediuk, R.S., Lesovik, V.S., Mochalov, A.V., Otsokov, K.A., Lashina, I.V., Timokhin, R.A. Composite binders for concrete of protective structures. *Magazine of Civil Engineering*. 2018. 82(6). Pp. 208–218. DOI: 10.18720/MCE.82.19

14. Provete Vincler, J., Sanchez, T., Turgeon, V., Conciatori, D., Sorelli, L. A modified accelerated chloride migration tests for UHPC and UHPFRC with PVA and steel fibers. *Cement and Concrete Research*. 2019. 117. Pp. 38–44. DOI: 10.1016/j.cemconres.2018.12.006
15. Lesnichenko, E.N., Chernysheva, N.V., Drebezgova, M.Yu., Kovalenko, E.V., Bocharnikov, A.L. Development of a multicomponent gypsum cement binder using the method of mathematical planning of the experiment. *Construction Materials and Products*. 2022. 5(2). Pp. 5–12. DOI: 10.58224/2618-7183-2022-5-2-5-12
16. Park, S. et. al. The Role of Supplementary Cementitious Materials (SCMs) in Ultra High Performance Concrete (UHPC): A Review. *Materials*. 2021. 14. Pp. 1472.
17. Semenov, P., Uzunian, A., Davidenko, A., Al., E. First study of radiation hardness of lead tungstate crystals at low temperatures. *Nuclear instruments & methods in physics research section A: Accelerators spectrometers detectors and associated equipment*. 2007. 582(2). Pp. 575–580. DOI: 10.1016/j.nima.2007.08.178
18. Farzad, M., Shafieifar, M., Azizinamini, A. Experimental and numerical study on bond strength between conventional concrete and Ultra High-Performance Concrete (UHPC). *Engineering Structures*. 2019. 186. Pp. 297–305. DOI: 10.1016/j.engstruct.2019.02.030
19. Juenger, M.C.G., Winnefeld, F., Provis, J.L., Ideker, J.H. Advances in alternative cementitious binders. *Cement and Concrete Research*. 2011. 41(12). Pp. 1232–1243. DOI: 10.1016/j.cemconres.2010.11.012
20. Maddalena, R., Hall, C., Hamilton, A. Effect of silica particle size on the formation of calcium silicate hydrate [C-S-H] using thermal analysis. *Thermochimica Acta*. 2019. 668. Pp. 1–8. DOI: 10.1016/j.tca.2018.09.003
21. Zhang, M.H., Islam, J., Peethamparan, S. Use of nano-silica to increase early strength and reduce setting time of concretes with high volumes of slag. *Cement and Concrete Composites*. 2012. 34(5). Pp. 650–662. DOI: 10.1016/j.cemconcomp.2012.02.005
22. Klyuyev, S.V., Kashapov, N.F., Radaykin, O.V., Sabitov, L.S., Klyuyev, A.V., Shchekina, N.A. Reliability coefficient for fibreconcrete material. *Construction Materials and Products*. 2022. 5(2). Pp. 51–58. DOI: 10.58224/2618-7183-2022-5-2-51-58
23. Farzadnia, N., Noorvand, H., Yasin, A.M., Aziz, F.N.A. The effect of nano silica on short term drying shrinkage of POFA cement mortars. *Construction and Building Materials*. 2015. 95. Pp. 636–646. DOI: 10.1016/j.conbuildmat.2015.07.132
24. Hamada, H.M., Thomas, B.S., Yahaya, F.M., Muthusamy, K., Yang, J., Abdalla, J.A., Hawileh, R.A. Sustainable use of palm oil fuel ash as a supplementary cementitious material: A comprehensive review. *Journal of Building Engineering*. 2021. 40. 102286. DOI: 10.1016/j.jobe.2021.102286
25. Jiang, D., Li, X., Lv, Y., Li, C., Jiang, W., Liu, Z., Xu, J., Zhou, Y., Dan, J. Autogenous shrinkage and hydration property of alkali activated slag pastes containing superabsorbent polymer. *Cement and Concrete Research*. 2021. 149. 106581. DOI: 10.1016/j.cemconres.2021.106581
26. Almeida, F.C.R., Klemm, A.J. Effect of GGBS on water absorption capacity and stability of superabsorbent polymers partially crosslinked with alkalis. *Journal of Materials in Civil Engineering*. 2018. 30(12). 0002511. DOI: 10.1061/(asce)mt.1943-5533.0002511
27. De Belie, N., Gruyaert, E., Al-Tabbaa, A., Antonaci, P., Baera, C., Bajare, D., Darquennes, A., Davies, R., Ferrara, L., Jefferson, T., Litina, C., Miljevic, B., Otlewska, A., Ranogajec, J., Roig-Flores, M., Paine, K., Lukowski, P., Serna, P., Tulliani, J.M., Vucetic, S., Wang, J., Jonkers, H.M. A Review of Self-Healing Concrete for Damage Management of Structures. 2018. 5(17).
28. Sun, B., Wu, H., Song, W., Li, Z., Yu, J. Design methodology and mechanical properties of Superabsorbent Polymer (SAP) cement-based materials. *Construction and Building Materials*. 2019. 204. Pp. 440–449. DOI: 10.1016/j.conbuildmat.2019.01.206
29. Liu, R., Sun, Z., Ding, Q., Chen, P., Chen, K. Mitigation of Early-Age Cracking of Concrete Based on a New Gel-Type Superabsorbent Polymer. *Journal of Materials in Civil Engineering*. 2017. 29(10). DOI: 10.1061/(asce)mt.1943-5533.0001994
30. Yang, J., Liu, L., Liao, Q., Wu, J., Li, J., Zhang, L. Effect of superabsorbent polymers on the drying and autogenous shrinkage properties of self-leveling mortar. *Construction and Building Materials*. 2019. 201. Pp. 401–407. DOI: 10.1016/j.conbuildmat.2018.12.197
31. Kashapov, N.F., Yamaleev, M.M., Lukashkin, L.N., Grebenshikov, E.A., Gilev, I.Yu., Kashapov, R.N., Kashapov, L.N. Structure and analysis of amorphous silicon dioxide nanoparticles. *Construction Materials and Products*. 2022. 5(6). Pp. 85–94. DOI: 10.58224/2618-7183-2022-5-6-85-94.
32. Kashapov, R.N., Kashapov, N.F., Kashapov, L.N., Klyuev, S.V. Plasma electrolyte production of titanium oxide powder. *Construction Materials and Products*. 2022. 5(6). Pp. 75–84. DOI: 10.58224/2618-7183-2022-5-6-75-84
33. Mukhametrakhimov, R.Kh. Investigation of plasticizing additives based on polycarboxylate esters on the properties of concretes formed by 3D printing. *Construction Materials and Products*. 2022. 5(5). Pp. 42–58. DOI: 10.58224/2618-7183-2022-5-5-42-58
34. Makhortov, D.S., Zagorodnyuk, L.H., Sumskey, D.A. Binder compositions based on Portland cement and volcanic ash. *Construction Materials and Products*. 2022. 5(4). Pp. 30–38. DOI: 10.58224/2618-7183-2022-5-4-30-38
35. Jiřičková, M., Pavlík, Z., Fiala, L., Černý, R. Thermal conductivity of mineral wool materials partially saturated by water. *Int. J. Thermophys*. 2006. 27. Pp. 1214–1227. DOI: 10.1007/s10765-006-0076-8
36. Ahmed, A.A.A., Lesovik, R.V. Thermokinetic Processes of Hydration of Binders Based on Scrap Concrete. *Lecture Notes in Civil Engineering*. 2021. 147. Pp. 8–14. DOI: 10.1007/978-3-030-68984-1_2
37. Loganina, V.I., Zhegera, K.V. The effectiveness of use of the composite binder as a dry mix. *Case Studies in Construction Materials*. 2015. Pp. 137–140. DOI: 10.1016/j.cscm.2015.10.004

Information about authors:

Valeriy Lesovik, Doctor of Technical Sciences, associate member of RAACS

ORCID: <https://orcid.org/0000-0002-2378-3947>

E-mail: naukavs@mail.ru

Dmitry Popov

E-mail: popov.dmitry412@yandex.ru

Roman Fediuk, PhD in Technical Sciences
ORCID: <https://orcid.org/0000-0002-2279-1240>
E-mail: roman44@yandex.ru

Mohanad Sabri, PhD
ORCID: <https://orcid.org/0000-0003-3154-8207>
E-mail: mohanad.m.sabri@gmail.com

Svetlana Vavrenyuk, Doctor of Technical Sciences, associate member of RAACS
E-mail: trusanova2014@mail.ru

Yuriy Liseitsev
E-mail: gera210307@ya.ru

Received 04.12.2022. Approved after reviewing 26.05.2023. Accepted 27.05.2023.



Research article

UDC 681.7.035:552.55

DOI: 10.34910/MCE.121.9



Processes of foaming and formation of the structure of porous glass ceramics from siliceous rocks

A.I. Rodin , A.A. Ermakov , V.M. Kyashkin , N.G. Rodina , V.T. Erofeev 

National Research Mordovia State University, Saransk, Russian Federation

✉ al_rodin@mail.ru

Keywords: glass ceramic, construction material, siliceous rocks, processes, foaming, thermal analysis, X-ray phase analysis, physical properties

Abstract. Porous glass-ceramic materials are used in the construction and repair of industrial and civil facilities. They are produced from rocks and industrial waste. The article establishes the influence of the chemical and mineralogical composition of the charge for the production of porous glass ceramics from siliceous (zeolite-containing) rocks and corrective additives ($Mg(OH)_2$, $MgCO_3$, Al_2O_3) on the processes occurring during its heating. The charge was obtained by joint grinding in a planetary ball mill of siliceous rocks, soda ash and corrective additives. The influence of the charge composition on the processes occurring during its heating has been established by methods of thermal analysis (TA), X-ray phase analysis (XRD), etc. Calcite in the composition of siliceous rocks has a significant effect on the foaming process of the charge. The temperature range of foaming is reduced, and the intensity increases. The additives used have a greater influence on the crystallization process of glass ceramics. As a result, anorthoclase, wollastonite, wollastonite-combeite and diopside glass ceramics were developed. Samples of porous glass ceramics have an apparent density from 154.6 kg/m^3 to 298.4 kg/m^3 , compressive strength from 0.84 MPa to 3.31 MPa, bending strength from 0.57 MPa to 1.52 MPa, maximum operating temperature from $840 \text{ }^\circ\text{C}$ to $870 \text{ }^\circ\text{C}$. According to many physico-mechanical and thermophysical properties, the materials obtained are superior to foam glass and other analogues. They can be used as a thermal insulation material in civil and industrial construction.

Funding: The study was funded by a grant Russian Science Foundation No. 21-79-10422. <https://rscf.ru/project/21-79-10422/>

Citation: Rodin, A.I., Ermakov, A.A., Kyashkin, V.M., Rodina, N.G., Erofeev, V.T. Processes of foaming and formation of the structure of porous glass ceramics from siliceous rocks. Magazine of Civil Engineering. 2023. 121(5). Article no. 12109. DOI: 10.34910/MCE.121.9

1. Introduction

Glass-ceramic materials are widely used in many sectors of the national economy. Porous glass-ceramic materials are widely used in the construction industry. They do not burn, have relatively high strength at low density, conduct heat poorly, do not break down when used in chemically aggressive environments and at high temperatures, and also have many other unique properties. Due to their properties, such materials are used for the construction of walls in buildings [1], they insulate facades, ceilings, basements [2, 3], are used as sound insulation materials [4]. Porous glass ceramics are used as thermal insulation of industrial furnaces [5], as well as objects that are operated in chemical aggressive environments [6] and many others.

Construction glass-ceramic materials are obtained both from natural rocks and from industrial waste. Metallurgical slags and ash are mainly used as industrial waste [2, 7, 8], glass production waste is often

used [4, 9]. Siliceous, carbonate, clay and other rocks are used as natural rocks in the production of porous glass-ceramic construction materials [10–13].

According to the literature data, the porous structure of glass-ceramic materials can be obtained in several ways [13–15]. The most widespread method is powder foaming, when the charge is ground together with gas-forming additives. Then it is poured into molds or onto a conveyor belt and fired in an oven. At a certain temperature, the charge begins to soften, and the gas-forming additive releases gas, which foams the charge. Various carbonates [14, 16], manganese oxide together with carbon [4, 17] and many others are used as gas-forming additives. The choice of a gas-forming additive depends on the temperature at which the charge begins to soften. It is very important that the charge is as homogeneous as possible in composition. As a result, preference for obtaining porous glass-ceramic materials is given to raw materials of amorphous composition (slag, ash, glass) [2, 4, 7–9]. As a consequence, it is possible to obtain glass ceramics with a uniform porous structure from natural rocks by powder foaming using a two-stage technology. At the first stage, it is necessary to cook the glass, and then the cooled glass is ground with gas-forming additives and reheated. This technology has found wide application in the production of foam glass. This material, like porous glass ceramics, has a number of unique properties. However, due to the two-stage production process, its cost is significantly higher than glass ceramics [18].

Reducing the cost of production of foam glass, as well as the development of compositions and technologies for obtaining porous glass-ceramic materials from rocks in one heating of raw materials is an important task of modern materials science. One of the solutions to this problem is the production of porous glass ceramics by the method of alkaline activation of components [11–13]. With this method, zeolite-containing rocks are mixed with a high concentration NaOH aqueous solution, granulated and fired. As a result, a porous glass-ceramic material in the form of granules was obtained in one heating of the charge without the use of additional foaming components. The literature describes in detail the mechanism by which the foaming of the material occurs. When heated, zeolite group minerals are dehydrated in the charge and surface hydroxyl groups are clogged in micropores [12, 19]. With a further increase in the heating temperature, the charge softens, and the hydroxyl groups condense with the release of water vapor, which forms a porous structure of the material. However, during the production of porous glass ceramics using this technology, equipment quickly wears out as a result of exposure to alkalis, and harmful substances are released into the atmosphere [20]. Because of this, this technology has not found wide application.

In our early works, a method for obtaining porous glass ceramics in one heating of a charge from siliceous (zeolite-containing) rocks by powder foaming was proposed [21, 22]. Pre-dried siliceous rock with a zeolite content of no more than 25% was ground together with soda ash or thermonatrite in a planetary ball mill. The resulting charge was poured into molds or onto a conveyor belt and fired. As a result, glass-ceramic materials with a uniform fine-porous structure were obtained, which surpass foam glass in many properties. We have described the mechanisms that occur in the charge during grinding, as well as when it is heated [23]. However, the presented mechanisms and dependencies were obtained using a siliceous rock of the same chemical and mineralogical composition. It is known that rocks, including siliceous (zeolite-containing) rocks, have different chemical and mineralogical composition [12, 24]. Samples of porous glass ceramics obtained from different raw materials have different structure, phase composition and properties [22]. For example, with an increase in the composition of glass ceramics Fe_2O_3 and CaO , the limiting temperature of its operation decreases [7, 25], and with an increase in the amount of Al_2O_3 , on the contrary, increases [26]. MgO in the composition of glass ceramics radically changes its phase composition [27, 28]. Impurities (for example, NaCl) that enter the glass ceramics together with the fins can also affect the structure and properties of the material [21]. The influence of the composition of the charge for porous glass ceramics from siliceous rocks on the processes occurring during its heating has not been sufficiently studied in the literature. Therefore, the purpose of the study is to establish the influence of the chemical and mineralogical composition of the charge of siliceous (zeolite-containing) rocks and corrective additives on the processes of foaming and crystallization of porous glass ceramics samples during heating.

Tasks:

- by thermal (TA), X-ray phase (XRD) and other methods of analysis to establish the effect of CaCO_3 , $\text{Mg}(\text{OH})_2$, MgCO_3 , Al_2O_3 in the composition of the charge mixture on the phase transformations in it during heating, as well as the temperature intervals of its foaming;
- to determine the effect of CaO , MgO , Al_2O_3 on the temperature ranges of crystallization and the phase composition of glass ceramic samples by the X-ray method;
- to establish the effect of the charge composition on the properties of porous glass ceramics samples.

2. Methods

2.1. Materials

The following components were used for experimental studies: siliceous rocks (zeolite-containing tripoli from three deposits and diatomite), calcined soda and corrective additives (magnesium hydroxide, magnesium carbonate, aluminum oxide and potassium chloride). The characteristics of the components are presented below. The chemical and mineralogical composition of siliceous rocks is given in Tables 1 and 2.

Table 1. The chemical composition of the rocks.

Composition No.	Chemical composition, % mass									
	SiO ₂	CaO	Al ₂ O ₃	Fe ₂ O ₃	K ₂ O	MgO	TiO ₂	Na ₂ O	SO ₃	Other
R1	70.9	2.4	12.4	3.5	1.7	1.7	0.5	0.1	0.0	6.8
R2	67.9	7.7	7.6	2.0	1.6	1.1	0.3	0.2	0.1	11.5
R3	62.3	11.3	6.7	2.0	1.4	0.9	0.3	0.1	0.0	15.0
R4	81.5	1.5	5.3	2.0	1.0	0.9	0.3	0.2	1.8	5.5

Table 2. The mineralogical composition of the rocks.

Composition No.	Mineralogical composition, % mass						
	Quartz	Calcite	Heulandite	Muscovite	Cristobalite	Tridymite	Amorphous phase
R1	27.8	0.0	18.6	16.1	16.2	1.3	20.0
R2	10.8	12.8	19.2	14.4	21.1	1.7	20.0
R3	8.5	21.3	19.6	9.9	19.2	1.5	20.0
R4	10.9	0.0	0.0	8.1	0.0	0.0	80.0

- Soda ash (Na₂CO₃) with a concentration of the main substance in the composition of more than 99 %.
- Corrective additives: Magnesium hydroxide (Mg(OH)₂), magnesium carbonate (MgCO₃), aluminum oxide (Al₂O₃), potassium chloride (KCl) with a concentration of the main substance in the composition of more than 97 %.

2.2. Compositions and fabrication of samples

In the work, the 6 composition of the charge for the production of porous glass ceramics was studied. The compositions are given in Table 3.

Table 3. Charge compositions.

Composition No.	Composition of the charge, %								
	Rock R1	Rock R2	Rock R3	Rock R4	Na ₂ CO ₃	Mg(OH) ₂	MgCO ₃	Al ₂ O ₃	KCl
C1	81.5	–	–	–	–	–	–	–	–
C2	–	81.5	–	–	–	–	–	–	–
C3	–	–	81.5	–	18.2	–	–	–	0.3
C4	–	–	63.5	15	–	3	–	–	–
C5	–	–	62.1	15	–	–	4.4	–	–
C6	–	–	60.5	15	–	3	–	3	–

The charge was prepared as follows. The components were dried to a moisture content of no more than 1 %, dosed (according to Table 3) and ground together in a Retsch PM 400 planetary ball mill (Germany) for 30 minutes at overloads inside the mill cups equal to 20g.

2.3. Analytical techniques

The phase transformations occurring in the charge during heating were determined by thermal analysis methods: differential thermal analysis (DTA) and differential thermogravimetry (DTG). The studies were performed on the TGA/DSC1 device (Switzerland) according to the following methodology. A charge weighing 20±0.1 mg was poured into an alund crucible with a volume of 150 µl. The crucible together with the charge was placed in the device and heated at a speed of 10 °C/min from 30 to 850 °C, and then cooled at a speed of 10 °C/min to 30 °C. The device recorded changes in the mass and temperature of the sample. The experimental data obtained were processed using the STARE software (Mettler-Toledo, Switzerland).

The temperature intervals of foaming of the charge for porous glass ceramics were determined on samples of cylinders with a diameter of 12 ± 0.1 mm and a height of 12 ± 1 mm according to the following procedure. The samples were made by pressing the charge (weight 5 g) in a mold under a pressure of 1 MPa. The resulting cylinder samples were mounted vertically on a ceramic plate and placed in a muffle furnace. In the furnace, the samples were fired at a speed of $6\text{ }^\circ\text{C}/\text{min}$ to a set temperature and kept at a maximum temperature for 10 minutes. After the samples cooled down together with the furnace to room temperature, their photofixation was carried out and the apparent density of the samples was determined. The arithmetic mean of the test results of three samples of each composition was taken as the final result.

The change in the phase composition of the charge during heating, as well as the beginning and end of crystallization of glass ceramic samples were determined by X-ray phase analysis. The studies were performed on an Empyrean PANalytical device (Netherlands) with a PIXcel^{3D} semiconductor detector. A thin layer of 15 g of charge was poured onto a rectangular ceramic plate with dimensions of $150\times 150\times 5$ mm. The plate with the sample was placed in a muffle furnace and heated at a speed of $6\text{ }^\circ\text{C}/\text{min}$ to a predetermined temperature and kept at a maximum temperature for 10 minutes. In order to fix the phase composition of the charge at a given temperature, it was quickly removed from the furnace, transferred from a ceramic plate to a rectangular steel plate with dimensions of $300\times 300\times 50$ mm and covered with a second steel plate with dimensions of $300\times 300\times 20$ mm. After complete cooling of the charge, it was crushed in an agate mortar with an agate pestle to a fraction <90 microns. The obtained powders were examined on an Empyrean PANalytical device in the mode of linear scanning by a detector in $\text{CuK}\alpha$ radiation in the range of angles $2\theta = 5\text{--}55^\circ$. The sampling rate is $0.0131\text{ }^\circ/\text{minute}$ with an integration time at each point of 150 seconds. The phase composition of the samples was determined by the Hanawalt method using an open database of crystallography.

The method of determining the physical and mechanical properties (apparent density, bending and compressive strength) and thermophysical properties (thermal conductivity coefficient and operating temperature limit) of porous glass ceramics samples is presented in detail in our previous work [22].

3. Results and Discussion

3.1. Phase transformations in the charge during heating and temperature intervals of its foaming

The processes occurring in the charge during heating are determined by the methods of thermal analysis (DTA and DTG) and X-ray phase analysis (XRD). The obtained thermograms of the charge samples are shown in Fig. 1.

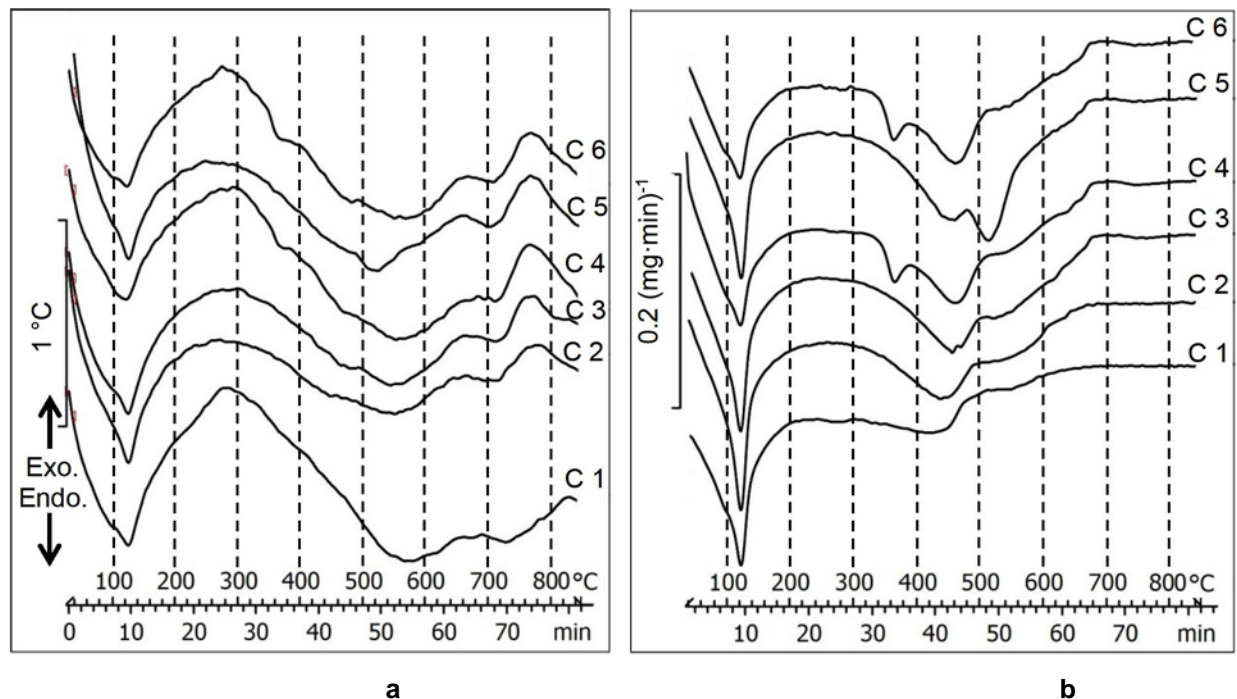


Figure 1. DTA (a) and DTG (b) curves of charge mixture samples.

As a result of the mechanochemical activation of a charge mixture of siliceous rocks, soda ash and additives, a new mineral wegscheiderite ($\text{Na}_5[\text{CO}_3](\text{HCO}_3)_3$) is formed in it. The presence of this mineral in all the studied charge samples is evidenced by the endothermic effect and mass loss of samples with a

maximum at a temperature of ≈ 120 °C (Fig. 1). This conclusion is confirmed by the results of the XRD of the charge before and after its firing at a temperature of 200 °C (Fig. 2). According to Fig. 2, the X-ray image of the charge sample (C3) shows the lines characteristic of the wegscheiderite mineral $[\text{Na}_5[\text{CO}_3](\text{HCO}_3)_3]$, Code: 96-900-7682] before firing, and after firing them at a temperature of 200 °C, the lines disappeared. Similar data were obtained from the results of the X-ray analysis of all the studied samples of the charge mixture (X-ray patterns are not given). According to literature sources, decomposition of sodium hydrosilicates is also possible in the charge mixture for glass ceramics from siliceous rocks in this temperature range [12]. As a result of our research (Fig. 1 and 2), this conclusion was not confirmed.

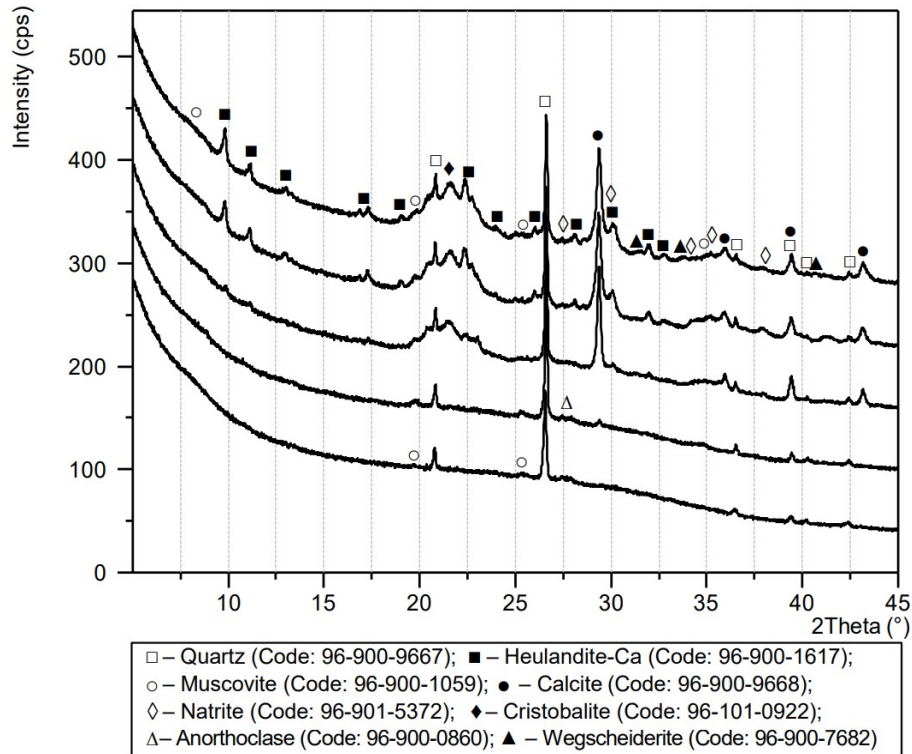


Figure 2. X-ray patterns of a sample of charge C3 after firing at different temperatures.

As a result of the conducted research (Fig. 1 and 2), the temperature ranges of decomposition of the minerals of the charge mixture were established. The endothermic decomposition reaction of sodium began at a temperature of ≈ 300 °C and ended up to 500 °C. Calcite decarbonization, on the contrary, began intensively at a temperature of >500 °C, and ended at 670 °C. This is evidenced by a gradual decrease in the X-ray lines characteristic of natrite $[\text{Na}_2\text{CO}_3]$, Code: 96-901-5372] and calcite $[\text{CaCO}_3]$, Code: 96-900-9668]. The endothermic effect and mass loss in charge samples C4 and C6 in the temperature range from 350 °C to 370 °C is associated with dehydration of $\text{Mg}(\text{OH})_2$. MgCO_3 in the C5 sample was decarbonized in the temperature range from 460 °C to 560 °C. Dehydration of the heulandite mineral (endoeffect) in all samples, the charge was completed at a temperature of ≈ 500 °C (Fig. 1), which is confirmed by the results of the XRD (Fig. 2). On the X-ray of the charge samples after firing at 450 °C, the lines characteristic of the heulandite mineral $[\text{Na}_{1.30}\text{K}_{0.12}\text{Ca}_{3.70}(\text{Si}_{27.11}\text{Al}_{8.89})\text{O}_{72.76} \times 24\text{H}_2\text{O}]$, Code: 96-900-1617] are practically absent. The endothermic decomposition reaction of muscovite in all charge samples began at temperatures up to 450 °C and continued up to >700 °C. The X-ray pattern of the charge mixture samples after firing at a temperature of 700 °C preserved muscovite lines $[\text{KAl}_2(\text{Si}_3\text{Al})\text{O}_{10}(\text{OH})_2]$, Code: 96-900-1059] of weak intensity.

According to literature sources, when firing a charge mixture for glass ceramics from zeolite-containing rocks to a temperature of ≈ 670 °C, it is compacted with blockage in micropores of surface hydroxyl groups (Si–O–H). With a further increase in temperature, the charge mixture begins to soften, and the hydroxyl groups condense into water vapor and foam it [12, 23]. The beginning of softening of all the samples studied by us from the charge with calcite in the composition began at a temperature of ≈ 660 °C (C2–C6), and without calcite ≈ 680 °C (C1). The beginning of the endothermic effect without loss of mass in the samples was recorded on the DTA curves (Fig. 1). This endoeffect is associated with an increase in the heat capacity of an amorphous material as a result of its softening. At the temperature of the beginning of softening of the charge mixture, the process of its foaming begins. The foaming component is most likely water vapor condensed from hydroxyl groups of the mineral muscovite. As noted above, after firing the charge mixture at a temperature of 700 °C, the lines of this mineral were preserved on the X-ray pattern (Fig. 2). As a result of foaming, the charge mixture increases in volume, and the thermal conductivity of the

sample decreases. Consequently, its heat absorption coefficient decreases. On the thermograms (Fig. 1a), the DTA curves are directed upwards. According to the maxima of thermal effects, it is possible to determine the temperature of the completion of the foaming process. A further increase in the firing temperature of the charge samples led to the stabilization of the heat flow. DTA curves are directed downwards.

With an increase in the amount of calcite in the charge mixture, the foaming intensity increases, and the process completion temperature decreases. According to Fig. 1a, the samples of the charge mixture without calcite in the composition (C1) continue to foam slowly to a temperature of ≈ 825 °C. Foaming of charge samples (C3–C6) from the rock with the maximum amount of calcite (R3, calcite 21.3 %) was completed at a temperature of ≈ 750 °C. It was not possible to establish the effect of corrective additives ($\text{Mg}(\text{OH})_2$, MgCO_3 , Al_2O_3) in the composition of the charge mixture on the intensity and temperature intervals of its foaming by thermal and X-ray phase analysis.

Visual confirmation of the influence of the chemical and mineralogical composition of the charge mixture on the sintering processes and the temperature intervals of its foaming are given below. The study was performed on cylindrical samples with a diameter of 12 ± 0.1 mm and a height of 12 ± 1 mm according to the procedure described above. Fig. 3 shows a photo of cylindrical samples before and after firing.

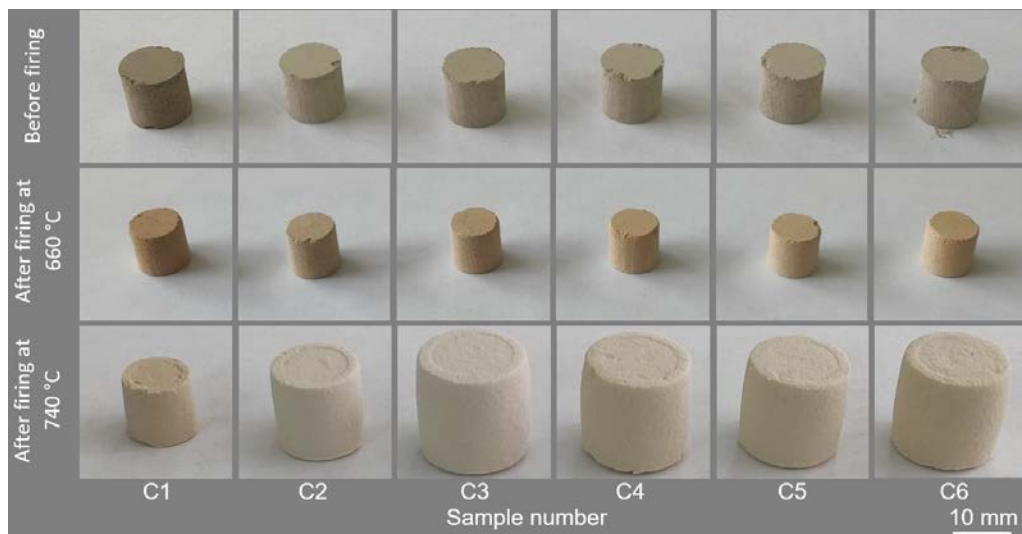


Figure 3. Photos of samples before and after firing.

It can be seen that the charge of siliceous rocks, soda ash and corrective additives after firing at a temperature of 660 °C was sintered (Fig. 3). The volume of cylindrical samples decreased by almost 3 times. The color of the samples changed from light gray to light brown. The photo after firing the charge at a temperature of 740 °C shows already foamed cylindrical samples. The volume of samples increased to varying degrees depending on the composition. The dependences of the change in the apparent density of the charge samples on the firing temperature are shown in Fig. 4. The results of the studies are presented in the temperature range from 620 °C to 840 °C.

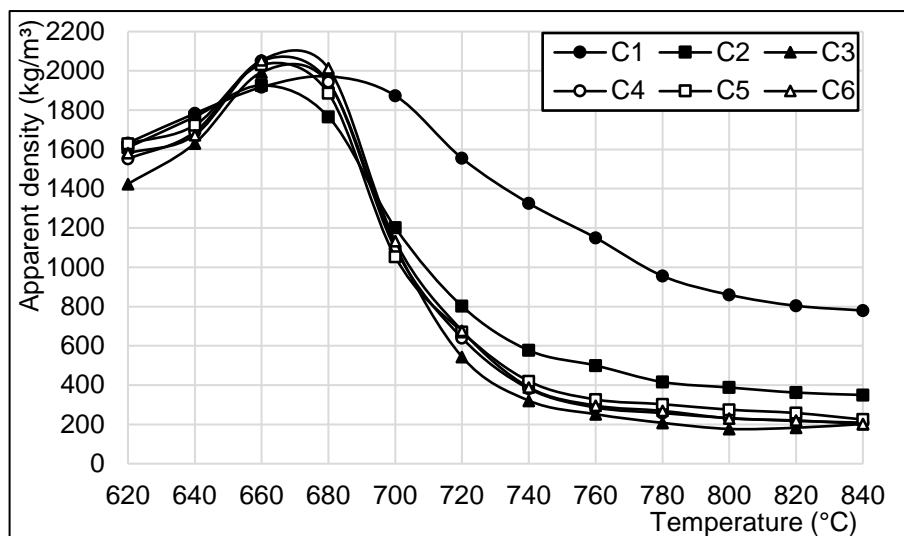


Figure 4. Change in the apparent density of samples from the firing temperature

According to the data (Fig. 4), it was found that with an increase in the firing temperature of cylindrical charge samples with calcite in the composition from 620 °C to 660 °C (C2–C6) and without calcite to 680 °C (C1), their apparent density increased on average from 1570 kg/m³ to 2000 kg/m³. A further increase in the firing temperature to 760 °C led to a sharp decrease in the apparent density of charge samples with an increased calcite content (C3–C6) to ≈300 kg/m³. With an increase in the firing temperature of a sample without calcite in the composition (C1) to 820 °C, its apparent density slowly decreases to ≈800 kg/m³. The obtained results are consistent with the data of thermal and X-ray phase analysis of charge samples. Foaming of charge samples with calcite in the composition begins at a temperature of 660 °C. The process proceeds intensively and ends at a temperature of ≈760 °C. Charge samples without calcite in the composition are foamed slowly in the temperature range of 680–820 °C. Additives used in the work as part of the charge mixture ($\text{Mg}(\text{OH})_2 \leq 3\%$, $\text{MgCO}_3 \leq 4.4\%$, $\text{Al}_2\text{O}_3 \leq 3\%$) do not significantly affect the foaming processes when it is heated.

3.2. Temperature ranges of crystallization and phase composition of glass ceramic samples

The influence of the chemical and mineralogical composition of the charge on the temperature intervals of crystallization of porous glass ceramics samples is shown in Fig. 5.

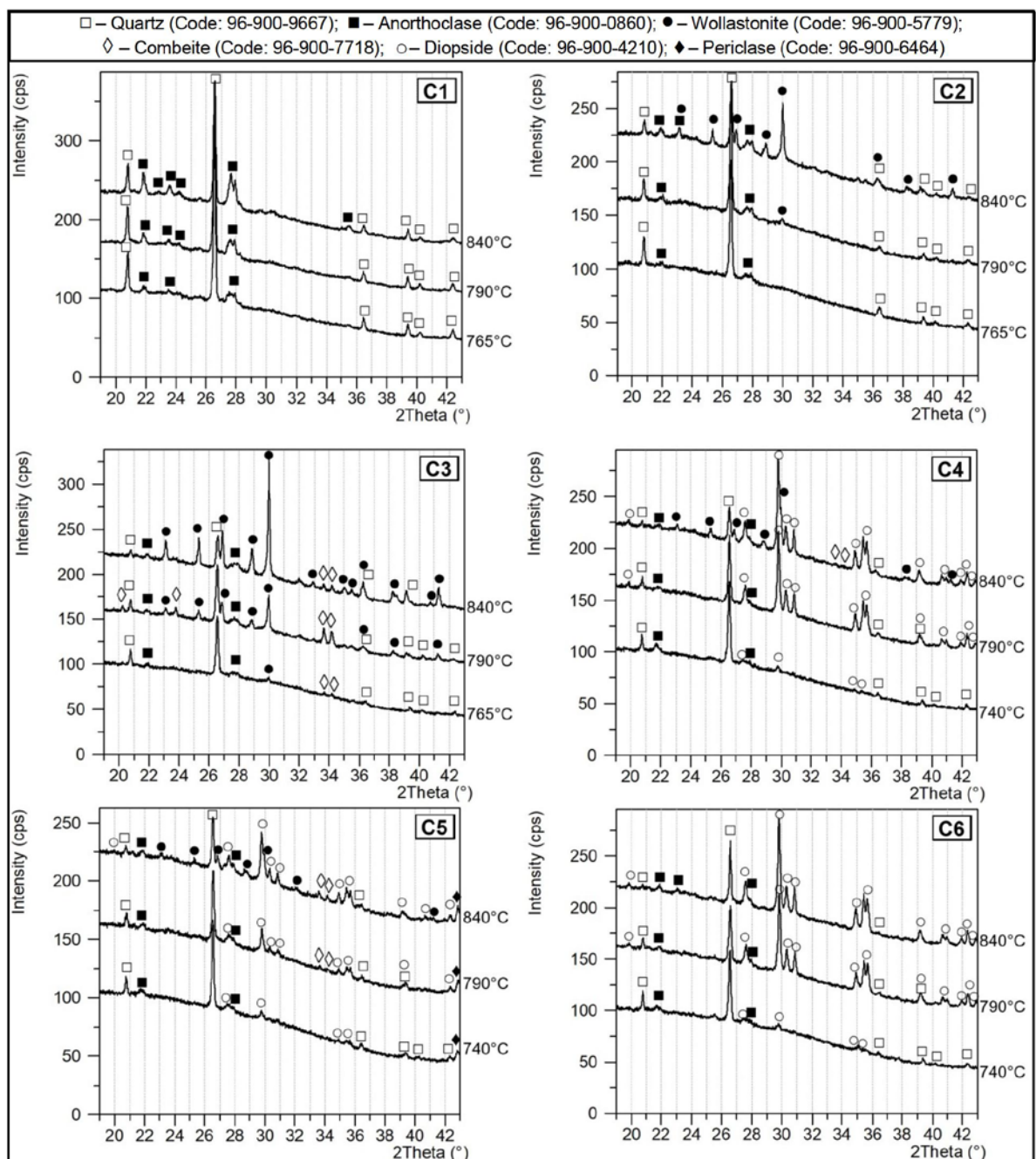


Figure 5. X-ray patterns of glass ceramic samples after firing at different temperatures.

According to the data obtained (Fig. 5), all fired charge samples consist of an amorphous and crystalline phase. The presence of an amorphous phase is characterized by a non-monotonic change in the background on all X-ray patterns in the range of angles up to 37° (2θ). The amount of amorphous phase decreased slightly with an increase in the firing temperature of the charge. The influence of the chemical and mineralogical composition of the charge on the change in the amorphous phase of glass ceramics has not been established.

The crystal phase of glass ceramic samples from siliceous rock R1 (without calcite and corrective additives) consists of quartz [SiO_2 , Code: 96-900-9667] and anorthoclase [$(\text{Na}_{0.85}\text{K}_{0.15})(\text{AlSi}_3\text{O}_8)$, Code: 96-900-0860] (Fig. 5 C1). The presence of quartz in C1 glass ceramics is due to its presence in large quantities in the rock. Anorthoclase, according to Fig. 2, begins to crystallize in glass ceramics at a temperature of $\approx 600^\circ\text{C}$. The amount of this mineral increased almost linearly with an increase in the firing temperature of the samples to 840°C . When firing porous glass ceramics C2 from siliceous rock R2 (12.8 % calcite) at a temperature of $\approx 790^\circ\text{C}$ the wollastonite phase additionally begins to form [CaSiO_3 , Code: 96-900-5779]. The temperature of the beginning of crystallization of wollastonite decreased to 765°C with an increase in the amount of calcite (C3) in the charge mixture. In parallel with wollastonite, combeite also begins to crystallize at a temperature of 765°C [$\text{Na}_2\text{Ca}_2\text{Si}_3\text{O}_9$, Code: 96-900-7718]. On the X-ray of the C3 sample after firing at a temperature of 840°C , the intensity of the combeite lines decreased, and wollastonite sharply increased. This indicates the recrystallization process in the material. This is also confirmed by the exothermic effect on the DTA curve of sample C3 (Fig. 1a) with a maximum at a temperature of $830\text{--}840^\circ\text{C}$. In earlier studies, we found an increase in open porosity to $>70\%$ in glass ceramic samples with an increase in the composition of the calcite charge mixture [21, 22]. Which may also be a consequence of the recrystallization process in the material.

When magnesium-containing additives ($\text{Mg}(\text{OH})_2$) are introduced into the charge mixture and MgCO_3 the crystallization process of glass ceramics differs from additive-free formulations (C4–C6). Instead of wollastonite in the material at a temperature of 740°C diopside begins to form [$\text{Mg}_{0.56}\text{Ca}_{0.44}\text{SiO}_3$, Code: 96-900-4210]. The process of crystallization of this mineral in samples with the addition of $\text{Mg}(\text{OH})_2$ (C4 and C6) was almost completely completed at a temperature of 790°C , and in samples with the addition of MgCO_3 – at 840°C . Periclase crystallizes in parallel with diopside in samples of glass ceramics from the charge with the addition of MgCO_3 [MgO , Code: 96-900-6464]. With an increase in the firing temperature of samples C4 and C5 to 840°C on the X-ray patterns (Fig. 5 C4 and C5), the intensities of the diopside lines did not change and additionally there were lines of wollastonite and combeite of low intensity. This effect was not observed when the charge was simultaneously introduced into the composition with magnesium-containing additives Al_2O_3 (Fig. 5 C6). According to the data obtained, it can be concluded that in diopside glass ceramics from siliceous rocks, the recrystallization of diopside into wollastonite does not occur. Wollastonite and combeite are formed as a result of crystallization of the amorphous phase. This effect can be prevented by introducing Al_2O_3 additives into the charge mixture. The data obtained correlate with the results of studies on the production of glass-ceramic materials from fly ash and industrial waste [27, 28].

3.3. Properties of porous glass ceramics samples

The physico-mechanical and thermophysical properties of porous glass ceramics samples from siliceous rocks of different chemical and mineralogical composition, soda ash and corrective additives ($\text{Mg}(\text{OH})_2$, MgCO_3 , Al_2O_3) are shown in Table 1.

Table 4. Properties of porous glass ceramics samples.

Composition No.	Properties				
	Apparent density, kg/m^3	Compressive strength, MPa	Bending strength, MPa	Coefficient of thermal conductivity, $\text{W/m}\cdot^\circ\text{C}$	Maximum operating temperature, $^\circ\text{C}$
C1	298.4	3.31	1.52	0.080	870
C2	252.6	3.3	1.25	0.067	860
C3	174.2	1.83	1.03	0.057	840
C4	158.7	0.9	0.65	0.055	850
C5	208.6	2.25	0.94	0.063	850
C6	154.6	0.84	0.57	0.054	870

The chemical and mineralogical compositions of siliceous rocks and corrective additives have a significant effect on the apparent density of porous glass ceramic samples. With an increase in the amount of calcite in the composition of siliceous rocks to 21.3 %, the apparent density of glass ceramic samples decreased from 298.4 kg/m^3 to 174.2 kg/m^3 . When 3 % $\text{Mg}(\text{OH})_2$ was introduced into the charge mixture,

as well as 3 % Al_2O_3 together with it, the apparent density of glass ceramic samples decreased further to 158.7 kg/m^3 and 154.6 kg/m^3 , respectively.

The bending and compressive strength, as well as the thermal conductivity coefficient of porous glass ceramic samples are linearly dependent on their apparent density. The effect of magnesium-containing additives and Al_2O_3 on these properties has not been established. The highest bending strength (1.52 MPa) and compression strength (3.31 MPa), as well as the coefficient of thermal conductivity ($0.080 \text{ W/m}\cdot^\circ\text{C}$) samples of composition C1 (apparent density 298.4 kg/m^3). The lowest bending strength (0.57 MPa) and compression strength (0.84 MPa), as well as the coefficient of thermal conductivity ($0.054 \text{ W/m}\cdot^\circ\text{C}$) in C6 samples with the lowest apparent density of 154.6 kg/m^3 .

The dependence of the maximum operating temperature of porous glass ceramics samples on their phase composition is established. Anorthoclase glass ceramics (C1) and diopside glass ceramics (C6) can be operated at a maximum temperature of up to 870°C , and wollastonite glass ceramics (C2) – up to 850°C . With an increase in the amount of the mineral combeite in the glass ceramic samples, the maximum temperature of their operation decreases to 840°C . This is probably due to the recrystallization of combeite into wollastonite, the process of which is described above. According to the physicomechanical and thermophysical properties, the developed porous glass ceramics from siliceous rocks surpasses many analogues [1, 2, 4, 29, 30].

4. Conclusions

Porous glass-ceramic materials were obtained by powder foaming from a charge based on siliceous rocks of different chemical and mineralogical composition, soda ash and corrective additives ($\text{Mg}(\text{OH})_2$, MgCO_3 and Al_2O_3). The components of the charge mixture were ground together in a planetary ball mill and fired. Thermal, X-ray phase and other analysis methods have established the effect of additives, as well as the chemical and mineralogical composition of siliceous rocks on the processes of foaming and crystallization of porous glass ceramics samples during heating:

- Sintering of charge mixture samples without calcite in the composition is completed at a firing temperature up to $\approx 680^\circ\text{C}$, and with calcite and additives up to $\approx 660^\circ\text{C}$. With an increase in the firing temperature of the charge before sintering, the amount of amorphous phase in the sample increases. A further increase in the firing temperature leads to softening of the amorphous phase and foaming of the charge. The foaming component is most likely water vapor condensed from hydroxyl groups of the mineral muscovite. Charge samples without calcite and corrective additives in the composition are foamed slowly in the temperature range of $680\text{--}820^\circ\text{C}$. Foaming of charge samples with calcite begins at a temperature of $\approx 660^\circ\text{C}$. The process proceeds intensively and ends at a temperature of $\approx 760^\circ\text{C}$. Additives used in the work as part of the charge mixture ($\text{Mg}(\text{OH})_2 \leq 3\%$, $\text{MgCO}_3 \leq 4.4\%$, $\text{Al}_2\text{O}_3 \leq 3\%$) do not significantly affect the foaming processes when it is heated.
- The chemical and mineralogical composition of the siliceous rock, as well as additives ($\text{Mg}(\text{OH})_2$, MgCO_3 and Al_2O_3) in the charge mixture have a significant effect on the temperature ranges of crystallization and the phase composition of porous glass ceramic samples. From a charge mixture based on siliceous rocks and soda ash without calcite and additives, anorthoclase porous glass ceramics were obtained, from rocks with calcite – wollastonite and wollastonite-combeite glass ceramics. When magnesium-containing additives are introduced into the charge mixture, diopside glass ceramics crystallizes. The crystallization process of diopside porous glass ceramics is completed at a temperature of $\approx 790^\circ\text{C}$, which is 50°C less than for anorthoclase glass ceramics.
- Porous glass ceramics have been developed with an apparent density from 154.6 kg/m^3 to 298.4 kg/m^3 , compressive strength from 0.84 MPa to 3.31 MPa, bending strength from 0.57 MPa to 1.52 MPa, with a maximum operating temperature from 840°C to 870°C . CaCO_3 , $\text{Mg}(\text{OH})_2$ and Al_2O_3 together with $\text{Mg}(\text{OH})_2$ as part of a charge mixture of siliceous rocks and soda ash contribute to a decrease in the apparent density of glass ceramic samples. An increase in the composition of glass ceramics of the mineral combeite leads to a decrease in the maximum operating temperature of the material to 840°C .
- The developed porous glass-ceramic materials are recommended to be used as a structural thermal insulation material in the construction of residential buildings and industrial facilities, as well as thermal insulation of various industrial equipment (melting boilers, furnaces, etc.) and pipelines.

References

- König, J., Lopez-Gil, A., Cimavilla-Roman, P., Rodriguez-Perez, M.A., Petersen, R.R., Østergaard, M.B., Iversen, N., Yue, Y., Spreitzer, M. Synthesis and properties of open- and closed-porous foamed glass with a low density. *Construction and Building Materials*. 2020. 247. Pp. 118574. DOI: 10.1016/j.conbuildmat.2020.118574
- Zhu, M., Ji, R., Li, Z., Wang, H., Liu, L., Zhang, Z. Preparation of glass ceramic foams for thermal insulation applications from coal fly ash and waste glass. *Construction and Building Materials*. 2016. 112. Pp. 398–405. DOI: 10.1016/j.conbuildmat.2016.02.183
- Vatin, N.I., Nemova, D.V., Kazimirova, A.S., Gureev, K.N. Increase of energy efficiency of the building of kindergarten. *Advanced Materials Research*. 2014. 953–954. Pp. 1537–1544. DOI: 10.4028/www.scientific.net/AMR.953-954.1537
- Kyaw Oo D'Amore, G., Caniato, M., Travan, A., Turco, G., Marsich, L., Ferluga, A., Schmid, C. Innovative thermal and acoustic insulation foam from recycled waste glass powder. *Journal of Cleaner Production*. 2017. 165. Pp. 1306–1315. DOI: 10.1016/j.jclepro.2017.07.214
- Guo, H., Ye, F., Li, W., Song, X., Xie, G. Preparation and characterization of foamed microporous mullite ceramics based on kyanite. *Ceramics International*. 2015. 41. Pp. 14645–14651. DOI: 10.1016/j.ceramint.2015.07.186
- Yatsenko, E.A., Ryabova, A.V., Goltsman, B.M. Development of fiber-glass composite coatings for protection of steel oil pipelines from internal and external corrosion. *Chernye Metally*. 2019. 12. Pp. 46–51.
- Jia, R., Deng, L., Yun, F., Li, H., Zhang, X., Jia, X. Effects of SiO_2/CaO ratio on viscosity, structure, and mechanical properties of blast furnace slag glass ceramics. *Materials Chemistry and Physics*. 2019. 233. Pp. 155–162. DOI: 10.1016/j.matchemphys.2019.05.065
- Cao, J., Lu, J., Jiang, L., Wang, Z. Sinterability, microstructure and compressive strength of porous glass-ceramics from metallurgical silicon slag and waste glass. *Ceramics International*. 2016. 42. Pp. 10079–10084. DOI: 10.1016/j.ceramint.2016.03.113
- Hisham, N.A.N., Zaid, M.H.M., Aziz, S.H.A., Muhammad, F.D. Comparison of foam glass-ceramics with different composition derived from ark clamshell (ACS) and soda lime silica (SLS) glass bottles sintered at various temperatures. *Materials*. 2021. 14. DOI: 10.3390/ma14030570
- Beregovoi, V.A., Sorokin, D.S., Beregovoi A.M. Glass-crystalline materials of a cellular structure, formed by vibration foaming technology. *Defect and Diffusion Forum*. 2021. 410. Pp. 823–828. DOI: 10.4028/www.scientific.net/DDF.410.823
- Ivanov, K.S. Associated Synthesis of Microgranular Foam-Glass-Ceramic from Diatomaceous Shales. *Glass and Ceramics (English translation of Steklo i Keramika)*. 2022. 79. Pp. 234–238. DOI: 10.1007/s10717-022-00491-4
- Kazantseva, L.K., Rashchenko, S.V. Optimization of porous heat-insulating ceramics manufacturing from zeolitic rocks. *Ceramics International*. 2016. 42. Pp. 19250–19256. DOI: 10.1016/j.ceramint.2016.09.091
- Yatsenko, E.A., Goltsman, B.M., Klimova, L.V., Yatsenko, L.A. Peculiarities of foam glass synthesis from natural silica-containing raw materials. *Journal of Thermal Analysis and Calorimetry*. 2020. 142. Pp. 119–127. DOI: 10.1007/s10973-020-10015-3
- Fernandes, H.R., Tulyaganov, D.U., Ferreira, J.M.F. Preparation and characterization of foams from sheet glass and fly ash using carbonates as foaming agents. *Ceramics International*. 2009. 35. Pp. 229–235. DOI: 10.1016/j.ceramint.2007.10.019
- Erofeev, V.T., Korotaev, S.A., Vatin, N.I. Deformation and Heat-Insulating Characteristics of Light Concrete on Porous Burned Binder Under Heating. *Materials Physics and Mechanics*. 2023. 51. Pp. 33–41. DOI: 10.18149/MPM.5112023_4
- Xi, C., Zheng, F., Xu, J., Yang, W., Peng, Y., Li, Y., Li, P., Zhen, Q., Bashir, S., Liu, J.L. Preparation of glass-ceramic foams using extracted titanium tailing and glass waste as raw materials. *Construction and Building Materials*. 2018. 190. Pp. 896–909. DOI: 10.1016/j.conbuildmat.2018.09.170
- König, J., Petersen, R.R., Iversen, N., Yue, Y. Application of foaming agent-oxidizing agent couples to foamed-glass formation. *Journal of Non-Crystalline Solids*. 2021. 553. Pp. 120469. DOI: 10.1016/j.jnoncrysol.2020.120469
- Sopegin, G.V., Rustamova, D.Ch., Fedoseev, S.M. Analysis of existing technological solutions of foam glass production. *Vestnik MGSU [Monthly Journal on Construction and Architecture]*. 2019. 14(12). Pp. 1584–1609. DOI: 10.22227/1997-0935.2019.12.1584-1609 (rus).
- Kazantseva, L.K., Lygina, T.Z., Rashchenko, S.V., Tsyplakov, D.S. Preparation of Sound-Insulating Lightweight Ceramics from Aluminosilicate Rocks with High CaCO_3 Content. *Journal of the American Ceramic Society*. 2015. 98. Pp. 2047–2051. DOI: 10.1111/jace.13581
- Mueller, A., Sokolova, S.N., Vereshagin, V.I. Characteristics of lightweight aggregates from primary and recycled raw materials. *Construction and Building Materials*. 2008. 22. Pp. 703–712. DOI: 10.1016/j.conbuildmat.2007.06.009
- Rodin, A., Ermakov, A., Erofeeva, I., Erofeev, V. Effect of Chlorides Content on the Structure and Properties of Porous Glass Ceramics Obtained from Siliceous Rock. *Materials*. 2022. 15. DOI: 10.3390/ma15093268
- Rodin, A.I., Ermakov, A.A., Kyashkin, V.M., Rodina, N.G., Erofeev, V.T. Porous glass ceramics from siliceous rocks with high operating temperature. *Magazine of Civil Engineering*. 2022. 116. DOI: 10.34910/MCE.116.15
- Erofeev, V.T., Rodin, A.I., Bochkina, V.S., Ermakov, A.A. The formation mechanism of the porous structure of glass ceramics from siliceous rock. *Magazine of Civil Engineering*. 2020. 100(8). Pp. 10006. DOI: 10.18720/MCE.100.6
- Kruszewski, Ł., Palchik, V., Vapnik, Y., Nowak, K., Banasik, K., Galuskina, I. Mineralogical, geochemical, and rock mechanic characteristics of zeolite-bearing rocks of the hatrumim basin, Israel. *Minerals*. 2021. 11. DOI: 10.3390/min11101062
- Li, Y., Zhao, L.-H., Wang, Y.-K., Cang, D.-Q. Effects of Fe_2O_3 on the properties of ceramics from steel slag. *International Journal of Minerals, Metallurgy and Materials*. 2018. 25. Pp. 413–419. DOI: 10.1007/s12613-018-1586-7
- Costa, F.P.D., Morais, C.R.D.S., Pinto, H.C., Rodrigues, A.M. Microstructure and physico-mechanical properties of Al_2O_3 -doped sustainable glass-ceramic foams. *Materials Chemistry and Physics*. 2020. 256. Pp. 123612. DOI: 10.1016/j.matchemphys.2020.123612
- Khater, G.A. Glass-ceramics in the $\text{CaO-MgO-Al}_2\text{O}_3\text{-SiO}_2$ system based on industrial waste materials. *Journal of Non-Crystalline Solids*. 2010. 356(52–54). Pp. 3066–3070. DOI: 10.1016/j.jnoncrysol.2010.02.030
- Abdel-Hameed, S.A.M., El-kheshen, A.A. Thermal and chemical properties of diopside-wollastonite glass-ceramics in the $\text{SiO}_2\text{-CaO-MgO}$ system from raw materials. *Ceramics International*. 2013. 29(3). Pp. 265–269. DOI: 10.1016/S0272-8842(02)00114-1

29. Zeng, L., Sun, H., Peng, T., Zheng, W. Preparation of porous glass-ceramics from coal fly ash and asbestos tailings by high-temperature pore-forming. *Waste Management*. 2020. 106. Pp. 184–192. DOI: 10.1016/j.wasman.2020.03.008
30. Miryuk, O., Fediuk, R., Amran, M. Foam Glass Crystalline Granular Material from a Polymineral Raw Mix. *Crystals*. 2021. 11(12). 1447. DOI: 10.3390/cryst11121447

Information about authors:

Alexander Rodin, *Phd in Technical Sciences*

ORCID: <https://orcid.org/0000-0002-8080-9808>

E-mail: al_rodin@mail.ru

Anatolij Ermakov

ORCID: <https://orcid.org/0000-0002-2560-0948>

E-mail: anatoly.ermakov97@mail.ru

Vladimir Kyashkin, *PhD in Physics and Mathematics*

ORCID: <https://orcid.org/0000-0002-3413-247X>

E-mail: kyashkin@mail.ru

Natalya Rodina

ORCID: <https://orcid.org/0000-0002-4709-4847>

E-mail: rodina.ng@list.ru

Vladimir Erofeev, *Doctor of Technical Sciences, member of the RAACS*

ORCID: <https://orcid.org/0000-0001-8407-8144>

E-mail: yerofeevvt@mail.ru

Received 24.04.2023. Approved after reviewing 15.05.2023. Accepted 15.05.2023.



Research article

UDC 691.42+666.3-1

DOI: 10.34910/MCE.121.10



Structural and phase features of ceramics from loam and incinerated sewage sludge ash

S.A. Shakhov ✉

Siberian Transport University, Novosibirsk, Russian Federation

✉ sashakhov@mail.ru

Keywords: building ceramics, loam, incinerated domestic sewage sludge ash, phase composition, anorthite, structure, frost resistance

Abstract. The relevance of the work is due to the need to expand the raw material base of the construction industry and develop an effective technology for the disposal of waste from water treatment plants. The purpose of the work was to establish the features of the phase composition and structure of loam ceramics and incinerated sewage sludge ash. The work used differential thermal and X-ray phase analysis, electron microscopy. It has been established that the enrichment of loam by the addition of ash from the incineration of domestic sewage sludge (DSS) ensures the connection of aggregates and individual particles into a single system reinforced with anorthite crystals. In this case, an increase in the amount of the anorthite phase and the mechanical strength of ceramics occurs with an increase in the proportion of ash from the incineration of DSS in the charge to more than 20 %. It is shown that the structure of ceramics made from loam with the addition of ash from the combustion of DSS is characterized by a spatial frame, which is a kind of a matrix that combines filler particles according to the "core-shell" type, and an increase in the number of reserve pores, which favorably affects the frost resistance of ceramics.

Citation: Shakhov, S.A. Structural and phase features of ceramics from loam and incinerated sewage sludge ash. Magazine of Civil Engineering. 2023. 121(5). Article no. 12110. DOI: 10.34910/MCE.121.10

1. Introduction

Currently, facade ceramics are widely used both in civil and industrial construction. The demand for such ceramics is due to their high performance properties: strength, durability, fire and environmental safety. However, the limited reserves of high-quality clays hinder the growth in the production of facade ceramics. Therefore, the development of technological processes for obtaining competitive facade ceramics from low-grade clay raw materials and man-made waste is of particular relevance.

In the production of building materials, one of the most popular secondary sources of raw materials is the ashes of thermal power plants [1–7]. The Russian enterprise's experience indicates that the addition of ashes and slags from thermal power plants into the composition of the charge contributes to a decrease in the firing temperature, an increase in the strength and frost resistance of products, and a decrease in fuel consumption [8–10]. The mineral particles contained in their composition and unburned coal form a ready-made additive for emaciated purpose. The use of ash, especially fine-grained ash, as a lean additive helps to reduce the crack resistance of ceramic products during drying [11–14]. The moisture conductivity of ash-clay masses of optimal compositions is 5 times higher than the moisture conductivity of clay raw materials, and shrinkage during drying decreases by 4–5 times [15–18].

Nowadays, recommendations have been developed on the selection of the composition of the raw mixture, taking into account the main patterns of the influence of TPP ash on the properties of clays and loams. The recommended amount of ash added into the charge (vol%) are: 10–20 for clays of low plasticity, 20–30 for moderate plastic, 30–40 for medium plastic [19]. Low-melting ash from coal combustion has an

advantage over ash from brown coal. The brown coal, in the production of wall ceramics, as a rule, adversely affects the properties of the clay mass and finished products.

Among the promising secondary sources of raw materials for the production of building ceramics, along with the ashes from thermal power plants, are ashes from the incineration of domestic sewage sludge (DSS). The properties of such ashes and the possibility of their use in composition with clay raw materials from the construction industry have been studied in a number of works [20–29].

The addition of ash from the incineration of DSS into the composition of the clay charge, which, according to the authors of [22] refers to complex polymineral systems with low-symmetry crystalline modifications, reduces shrinkage during drying of products, promotes the intensive formation of the crystalline structure of ceramics, and also leads to the intensive formation of a melt that binds magnesium and calcium oxides into aluminosilicates. The melt, evenly distributed at the grain boundaries, dissolves silica and prevents the process of its cristobalitization. This leads to the formation of a dense structure of the shard and, as a result, increased strength and frost resistance of products [27].

The water absorption of specimens with an ash content of 50 % DSS, obtained by firing them at a temperature of 1000 °C, was about 20 %, but decreased (down to 12–15 %) with an increase in the firing temperature to 1100 °C [23].

According to the results presented in [24], intensive sintering of ash from the incineration of DSS, accompanied by an increase in the density of the shard, occurs in the temperature range of 1050–1100 °C. After roasting, the samples of the DSS ash reached, on average, a maximum density of 2.25 kg/m³. The discrepancy in the maximum densities achieved is quite low (in the range of 2.09 to 2.36 kg/m³ the coefficient of variation was 4.7 %). Although it is assumed that the compaction initiation temperatures show much higher variability. Density growth seems to start at temperatures between 900 and 1150 °C, and the optimum conditions, i.e. the peak density point, range from 1050 to 1200 °C. The water absorption of specimens with an ash of the DSS content of 50 %, obtained by firing at a temperature of 1000 °C, was about 20 %, but decreased (down to 12–15 %) with an increase in the firing temperature to 1100 °C.

It was noted in [25, 26, 30] that ceramics made with the use of DSS ash do not always have stable strength characteristics, even in the presence of a dense structure. According to the authors of these studies, this is due to the unstable chemical composition of the ashes. In this regard, the study of the physical and chemical patterns of the formation of the phase composition of a ceramic shard during the production of facade ceramics using ash from the incineration of DSS has scientific and practical interest. It can expand the raw material base of enterprises for the production of ceramic materials and ensure the disposal of environmentally hazardous waste, thereby reducing the load on the environment.

The purpose of the work was to identify the relationship and patterns in the "composition – structure – property" system, which allow optimizing the formulations of compositions from loam and incinerated sewage sludge ash to achieve the required levels of technological, physical and mechanical characteristics.

To achieve this goal, the following tasks were solved:

- the dynamics of phase transformations occurring during the firing of ceramics from loam and incinerated domestic sewage sludge ash in the temperature range up to 1100 °C was studied;
- the features of the phase composition and structure of the ceramic shard of samples of different compositions were studied;
- the properties of ceramic products made from a mixture based on loam and incinerated sewage sludge ash were determined.

2. Materials and Methods

To obtain samples of clay-ash ceramics, representative technological samples of loam from the Kamyshensky deposit of the Novosibirsk region were used. The chemical composition of loams is given in Table 1. According to the chemical composition, the raw material is acidic, with a low content of water-soluble salts, coarse and dusty, moderately plastic and sensitive to drying.

Table 1. Composition of the mineral part of loam.

Charge Component	Oxide content, wt%						Total LOI above 100%
	SiO ₂	Al ₂ O ₃	Fe ₂ O ₃	CaO	MgO	K ₂ O	
Loam	68.70	11.78	4.10	4.76	1.68	3.60	5.62

As an additive to the loam, ash obtained from the incineration of domestic sewage sludge was used. Municipal enterprise "Vodokanal" (Novosibirsk) provided a mixture of mineral and organic substances in the form of a colloidal solution (humidity 95–97 %) during settling at a water treatment plant. Before incineration, sewage sludge was preliminarily dried at 120 °C. The sludge was burned for an hour in a laboratory furnace SNOL 6,7/130 at a temperature of 800 °C.

According to the chemical composition, ash is an acidic raw material with a high content of coloring oxides (Table 2).

Table 2. Chemical composition (wt%).

MgO	Al ₂ O ₃	SiO ₂	P	K ₂ O	CaO	TiO ₂	MnO	FeO	Cu	Zn	O
1.9	10.6	53.9	6.1	3.1	6.2	6.3	0.2	7.5	0.12	0.3	47

The effect of domestic sewage sludge incinerated ash on the nature of physical and chemical processes during firing, the phase composition, physical and mechanical properties of clay ash ceramics was studied on samples with a diameter of 20 mm and a height of 20 mm, which were prepared from charges of different composition (Table 3) in the following order.

Table 3. Compositions of charge and structural and mechanical characteristics of samples

Composition No.	Component content, wt%		Structural and mechanical characteristics of samples	
	Loam	Ash of DSS	Average density, g/cm ³	Compressive strength, MPa
1	100	0	2.08	3.3
2	80	20	2.07	10.2
3	50	50	2.08	27.0
4	20	80	2.08	31.6
5	0	100	2.11	30.2

For the preparation of ceramic samples, samples of loam and ash were dried to a constant weight at a temperature of 110 °C in an oven. Prepared raw materials were dosed by weight, thoroughly mixed. The resulting mixture was moistened and aged for a day to evenly distribute moisture throughout the volume of the molding masses. Samples with a diameter of 20 mm and a height of 20 mm were molded on an Across MP15 press at a pressure of 1.5 MPa and dried at a temperature of 110 °C in an oven to constant weight. The samples were fired in a muffle furnace SNOL 6,7/1300. The temperature rise rate was 5–10 °C/min with holding at the maximum firing temperature equal to 1100 °C for two hours. Cooling of the samples to 30 °C was carried out together with the oven for 18 hours.

The dynamics of phase transformations in the studied compositions was evaluated based on the results of X-ray phase and thermal analyses. X-ray phase analysis (XPA) was carried out on a Bruker D8 Advance diffractometer using Cu-K α radiation. The obtained diffraction patterns were identified using the PDF2 database with the Search-Match shell.

Differential thermal analysis was carried out on a Netzsch STA 449C setup. The values of exo- and endoeffects were determined in the temperature range of 20–900 °C at a rate of 10 deg/min in a closed crucible and a helium flow.

The determination of the frost resistance of ceramics was carried out on sample tiles with dimensions of 150×100×8 mm. The samples were saturated with water for 48 hours at a temperature of 20 °C. The samples saturated with water were placed in a freezer maintaining the temperature no less than –18 °C. The test cycle included:

- freezing for 2 hours;
- defrosting for 1 hour under water at a temperature of 20 °C.

Electron micrographs and elemental analysis were obtained on an electron microscope Hitachi TM-1000 equipped with a TM1000 EDS energy dispersive detector.

3. Results and Discussion

The DTA, TG, and DTG curves shown in Fig. 1 indicate that a number of endothermic and exothermic effects are observed when the ceramic mass is heated.

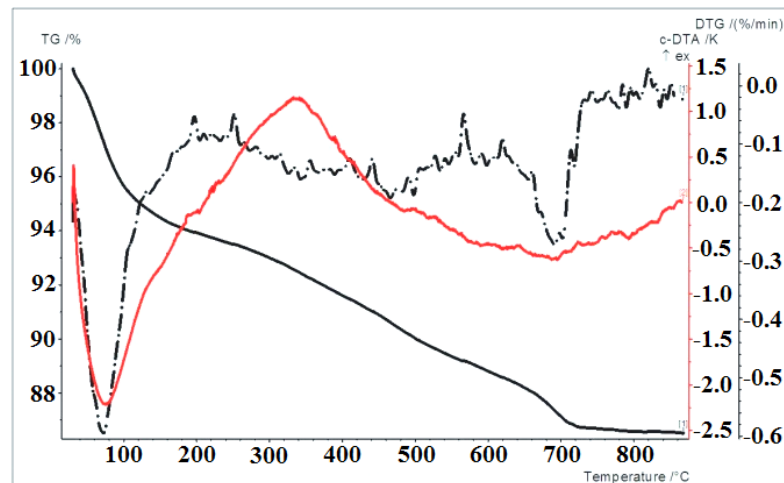


Figure 1. Thermogram of ceramic composition No. 3.

The weight loss of 3.04 % and the endo-effect in the temperature range of 50–220 °C are due to the removal of interpacket and interplanar water from clay minerals. Further reduction in mass when the material is heated to 680 °C occurs at a much lower rate.

In the temperature range of 340–550 °C, the processes of magnetite oxidation and polymorphic transformation of quartz, accompanied by an exothermic effect, occur: the transition of β -quartz to α -quartz.

The endo-effect at 700 °C is associated with the destruction of the kaolinite lattice: kaolinite loses water of crystallization and turns into metakaolinite, which decomposes into oxides at 800–900 °C [31]. A low-intensity exothermic effect at 830 °C can be identified with the oxidation of the remaining magnetite to Fe_2O_3 .

The processes occurring in the temperature range of 770–950 °C are quite diverse. In addition to the oxidation of iron, this is the dissociation of carbonate inclusions in the clay raw material [32], as well as the formation of new crystalline phases: in ceramics after firing at a temperature of 1000 °C according to XRD data (Fig. 2), quartz (3.35 Å) anorthite (3.10; 4.05 Å), and hematite (2.7 Å) are identified.

It should be noted that there is no free calcium oxide (CaO) in the shard, which indicates complete involvement of the dispersed carbonate additive in the physicochemical reactions during the firing process.

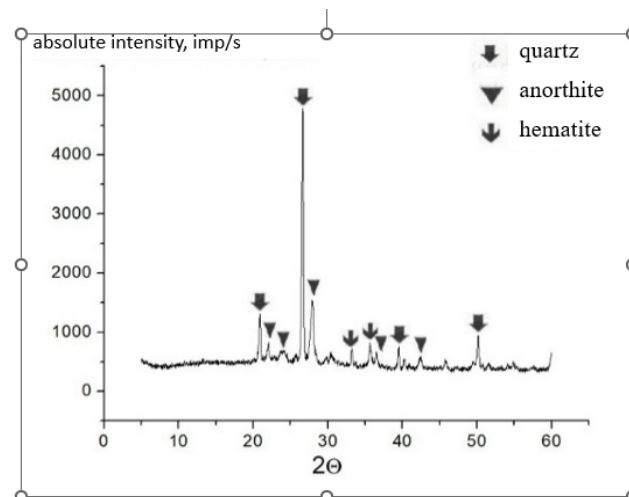


Figure 2. X-ray patterns of ceramic samples from the charge of composition No. 3.

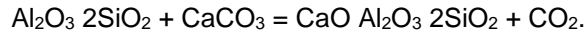
Processing the results of X-ray phase analysis using the corundum number method made it possible to estimate the content of anorthite in the crystalline phase of ceramics from loam with the addition of incinerated DSS ash. The data obtained (Table 4) show that with an increase in the ash content of DSS in the charge above 20 %, the amount of the anorthite phase increases.

Data on the amount of anorthite correlate with data on the strength of ceramic samples (Table 3): a high anorthite content makes it possible to reinforce the ceramic structure more strongly and thereby increase its mechanical strength. This character of the influence of the anorthite phase on the physical and mechanical properties of ceramic materials was previously noted in a number of studies [33–36].

Table 4. Results of quantitative X-ray phase analysis of ceramic samples using the corundum number method.

Composition No. according to Table 3	Phase composition
2	64% anorthite $\text{CaAl}_2\text{Si}_2\text{O}_8$ + 34% quartz SiO_2 + 2% hematite Fe_2O_3
3	68% anorthite $\text{CaAl}_2\text{Si}_2\text{O}_8$ + 29% quartz SiO_2 + 3% hematite Fe_2O_3
4	69% anorthite $\text{CaAl}_2\text{Si}_2\text{O}_8$ + 29% quartz SiO_2 + 2% hematite Fe_2O_3

A possible mechanism for the formation of anorthite may be related to the reaction involving amorphous silica and calcium oxide. According to studies [28, 37–39], the process of crystallization of anorthite in clays with a high content of calcite begins with an exothermic effect at a temperature of 840 °C. The process is activated by the exothermic oxidation of iron $\text{FeO} \Rightarrow \text{Fe}_2\text{O}_3$. Moreover, the released heat contributes to the dissociation of calcium carbonate. The following reaction takes place:



Thus, the amount of anorthite formed during the sintering of the clay ash charge is limited by the amount of newly formed CaO and metakaolinite.

Studies of the surface relief and distribution of the main chemical elements in ceramic samples of different compositions have shown that a feature of ceramics from loam with the addition of ash is the structure characterized by a spatial frame, which is a kind of a matrix that combines filler particles in a "core-shell" type. The organization of the ceramic shard structure according to this principle is confirmed by the electron microscopy data presented in Fig. 4.

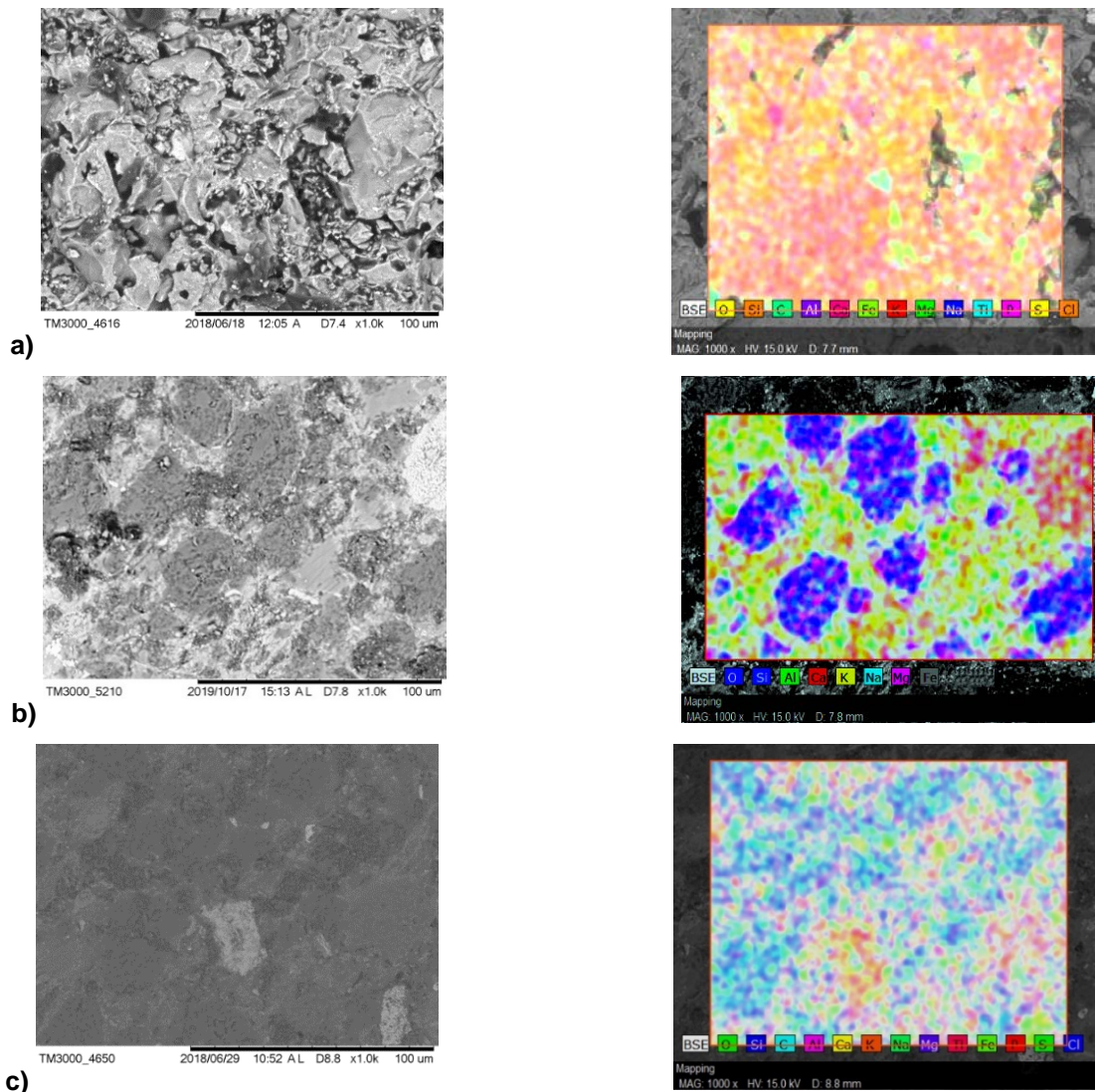


Figure 4. Electron microscopy of ceramic samples: a – composition No. 4; b – composition No. 3; c – composition No. 2.

A feature of the structure of the newly obtained clay-ash ceramics is also the organization of the pore space. The study of the porous-capillary structure of the samples by mercury porosimetry showed a difference in the size distribution of pores in ceramics with and without ash additives.

The integral curves presented in Fig. 5 indicate that the introduction of ash into the mixture leads to an increase in the number of pores with a diameter of 10^{-4} – 10^{-5} m. According to [40], pores of this size are reserve, since they are not filled when water is saturated, and allow water to expand when it freezes, thereby minimizing hydrostatic pressure, which is a favorable factor for increasing the frost resistance of newly developed ceramics.

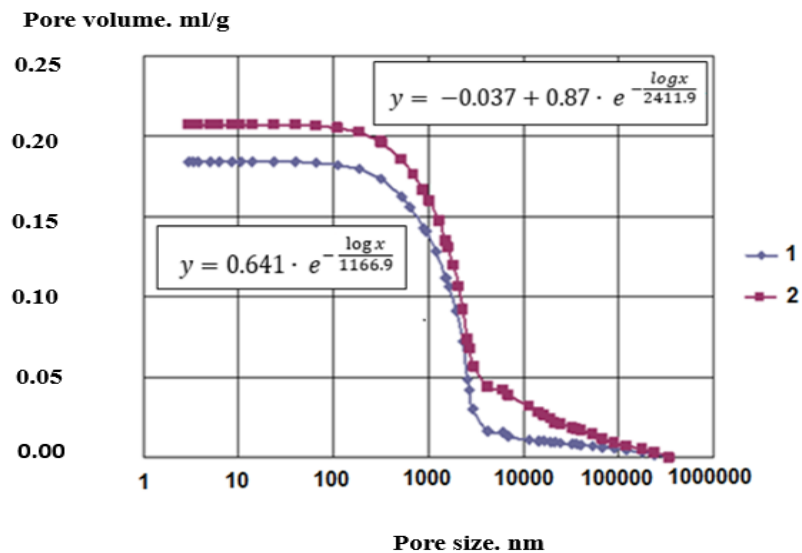
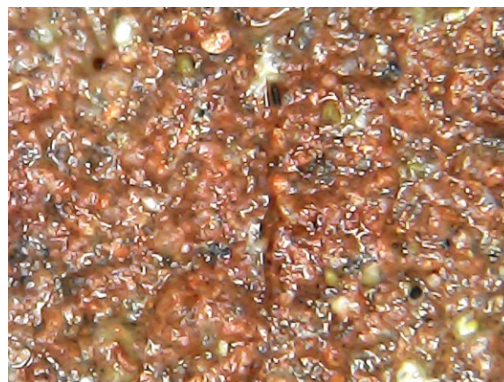


Figure 5. Integral curve of pore size distribution: 1 – composition No. 1; 2 – composition No. 3.

The structure of porosity largely determines the performance properties of wall ceramics. Taking into account the presence of changes in the pore structure of the clay-ash ceramics, the tiles of the experimental batch were additionally tested for frost resistance.

The results of the tests showed the absence of damage and weight loss. During 100 freeze-thaw cycles, no damage, chips, cracks, delaminations were observed both from the front and from the mounting surfaces (Fig. 6), which meets the requirements of Russian State Standard GOST 13996-2019 "Ceramic tiles. General specifications".

Thus, the research results allow us to conclude that the higher strength of the walls of pores and capillaries, due to the composition of the crystalline phases, in particular, the increased content of anorthite, provides resistance to the destructive effect of water freezing in the pores of the material under conditions of changes in the porous-capillary structure of the shard of clay-ash ceramics.



a)

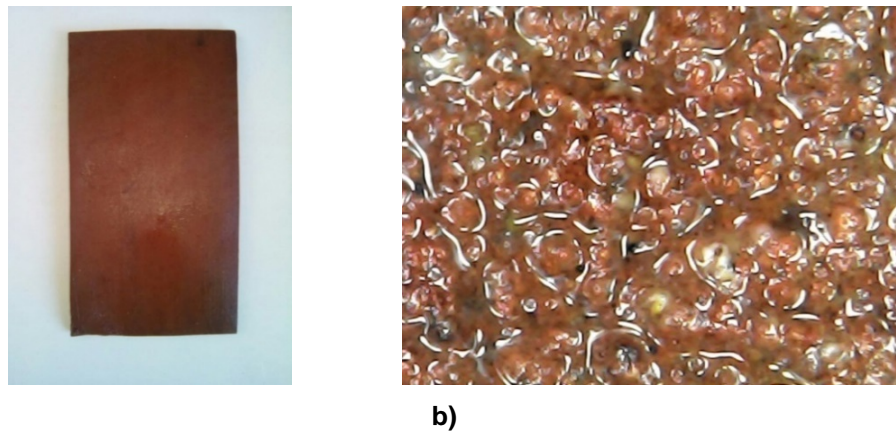


Figure 6. Appearance and macrostructure of ceramic tiles (composition No. 3) before and after frost resistance tests: a – 0 cycles; b – 100 cycles.

To confirm the results of laboratory studies on the development of the charge composition, an experimental batch of facade tiles was made from the newly developed charge composition.

Products were molded on a Ural-M3 vibropress (vibration frequency 65 Hz, pressure 12 MPa). The molded products were kept in the drying chamber for 24 hours. Roasting was carried out at a temperature of 1100 °C. The results of tests of ceramic products are presented in Table 5.

Table 5. Table 5. Properties of facade ceramic tiles from clay-ash mixture.

Charge composition	Sample No.	Flexural Strength (MPa)		Water absorption (%)		Frost resistance (cycles)	
		Requirement of Russian State Standard	Fact	Requirement of Russian State Standard	Fact	Requirement of Russian State Standard	Fact
Ash 50%, loam 50%	1	at least 16	19.5	no more than 9 and no less than 2	4.9	at least 40	112
	2	— —	19.1	— —	5.1	— —	110
	3	— —	18.8	— —	5.6	— —	105
	4	— —	18.7	— —	5.8	— —	104
	5	— —	19.3	— —	5.0	— —	110
	average			19.08		5.28	

4. Conclusions

An analysis of the physicochemical transformations of the phase composition and structure of the ceramic shard, occurring in the studied compositions in the temperature range up to 1100 °C, allows us to conclude that:

- Enrichment of loam with the addition of ash from the incineration of DSS provides:
 - connection of aggregates and individual particles into a single system reinforced with anorthite crystals;
 - an increase in reserve porosity, which favorably affects the frost resistance of the resulting ceramics.
- The special features of ceramics from loam and incinerated domestic sewage sludge ash is:
 - an increase in the amount of anorthite phase with an increase in the ash content in the charge over 20 %. A higher anorthite content makes it possible to reinforce the ceramic structure more strongly and thereby increase its mechanical strength.
 - a structure characterized by a spatial frame, which is a kind of a matrix that combines filler particles according to the "core-shell" type.
- The test results of an experimental batch of facade tiles made from a mixture of a newly developed composition confirm the positive effect of an increase in the content of anorthite and reserve porosity on the performance properties of products, established in the course of laboratory studies.

References

1. Vatin, N.I., Petrosov, D.V., Kalachev, A.I., Lahtinen, P. Use of ashes and ash-and-slag wastes in construction. *Magazine of Civil Engineering*. 2011. 22 (4). Pp. 16–21. (rus). DOI: 10.5862/MCE.22.2
2. Verma, A., Srivastava, D., Sing, N. A review on Partial Replacement of Cement by Fly Ash and Effect of Steel Fibers. *Journal of Mechanical and Civil Engineering*. 2017. 14(3). Pp. 104–107.
3. Coud, V., Soni, N. Partial Replacement of cement with fly ash in concrete and its effect. *JOSP Journal of Engineering*. 2016. 6(10). Pp. 69–75.
4. Kalra, T., Rana, R. A review on Fly Ash Concrete. *International Journal of Latest Research in Engineering and Computing (ULREC)*. 2015. 3(2). Pp. 7–10.
5. Telford, T. *The Properties and Use of Coal Fly Ash*. London. 2001. 261 p.
6. Naik, T., Ramme, B., Kraus, R., Siddique, R. Long-Term Performance of High-Volume Fly Ash Concrete Pavements. *ACI Materials Journal*. 2003. 100(2). Pp. 150–155.
7. Malhotra, V., Mechta, P. *High-Performance, High-Volume Fly Ash Concrete*. Supplementary Cementing Materials for Sustainable Development Inc. Ottawa. 2005. 124 p.
8. Panteleev, V.G., Melentiev, V.A., Dobkin, E.L. *Ash and slag materials and ash dumps [Ash and slag materials and ash dumps]*. Moscow: Energy, 1978. 295 p.
9. Kapustin, A.P., Kalykova, L.F., Stanevich V.T. Production of ceramic bricks from coal mining wastes of the Ekibastuz basin [Production of ceramic bricks from coal mining wastes of the Ekibastuz basin]. *Construction Materials*. 1991. 10. Pp. 13–14.
10. Beck, N.A., Pona, M.G., Shvlyud N.N. The use of fuel slag from the State District Power Plant for the production of ceramic tiles [The use of fuel slag from the State District Power Plant for the production of ceramic tiles]. *Glass and ceramics*. 1981. 7. Pp. 4–5.
11. Khrundzhe, A.V., Babushkin, V.I. Waste from the State District Power Plant for the production of ceramic tiles [Waste from the State District Power Plant for the production of ceramic tiles]. *Glass and ceramics*. 1983. 3. Pp. 5–8.
12. Abbas, S., Saleem, M.A., Kazmi, S.M.S., Munir, M.J. Production of sustainable clay bricks using waste fly ash: mechanical and durability properties. *Journal of Building Engineering*. 2017. 14. Pp. 7–14. DOI: 10.1016/j.jobbe.2017.09.008
13. Pawar, A., Garud, D. Engineering properties of clay bricks with the use of fly ash. *International Journal of Research in Engineering and Technology*. 2014. 3 (9). Pp. 75–80. DOI: 10.15623/ijret.2014.0321016
14. Baykal, G., Doven, A.G. Utilization of fly ash by pelletization process, theory, application areas, and research result. *Resource Conservation Recycling*. 2000. 30 (1). Pp. 59–77. DOI: 10.1016/S0921-3449(00)00042-2
15. Saibulatov, S.Zh. Resource-saving technology of ceramic bricks based on TPP ash [Resource-saving technology of ceramic bricks based on TPP ash]. Moscow: Stroyizdat, 1990. 248 p.
16. Swierczek, L., Cieslik, B.M., Konieczka P. The potential of raw sewage sludge in construction industry: A review. *Journal of Cleaner Production*. 2018. No. 200. Pp. 342–356.
17. Bijen, J.M. Manufacturing processes of artificial lightweight aggregates from fly ash. *The International Journal of Cement Composites and Lightweight Concrete*. 1986. 8 (3). Pp. 191–199.
18. Kayali, O. Fly ash lightweight aggregates in high-performance concrete. *Construction and Building Materials*. 2008. 22 (12). Pp. 2393–2399. DOI: 10.1016/j.conbuildmat.2007.09.001
19. Danilovich, I.Yu. The use of fuel slag and ashes for the production of building materials [The use of fuel slag and ashes for the production of building materials]. Moscow: Higher School, 1988. 330 p.
20. Argunov, N.D., Vatieva, O.B., Veselov, V.M., Salomatina, N.A., Pilgun V.A. Some properties and features of sewage sludge [Some properties and features of sewage sludge]. *Agrochemical Bulletin*. 2013. 4. Pp. 39–43.
21. Shakhov, S.A., Rudaya, T.L. Structural-mechanical properties of loam ceramics with the addition of water treatment sludge [Structural-mechanical properties of loam ceramics with the addition of water treatment sludge]. *Izvestiya TPU*. 2014. 325(3). Pp. 98–105.
22. Polyakov, G.N., Svyatskaya, L.I., Levit, I.M. Introduction of technology for the production of ceramic bricks with the addition of ash from the incineration of sewage sludge [Introduction of technology for the production of ceramic bricks with the addition of ash from the incineration of sewage sludge]. *Construction Materials*. 2002. 10. Pp. 28–30.
23. Korenkova, S.F., Sheina, T.V. Fundamentals and concept of utilization of industrial waste chemical sludge in the construction industry [Fundamentals and concept of utilization of industrial waste chemical sludge in the construction industry]. Samara: SGASU. 2004. 208 p.
24. Lin, K.L. Mineralogy and microstructures of sintered sewage sludge ash as lightweight aggregates. *J. Ind. Eng. Chem*. 2006. 3. Pp. 425–429.
25. Cieslik, B.M., Namiesnik, J., Konieczka P. Review of sewage sludge management: standards, regulations and analytical methods. *Journal of Cleaner Production*. 2015. 90. Pp. 1–15.
26. Cusido, J.A., Cremades L.V. Environmental effects of using clay bricks produced with sewage sludge: Leachability and toxicity studies. *Waste Management*. 2012. 32. Pp. 1202–1208.
27. Tuani, Z., Mariana, B., Naquiele, S., Ana, M.S., Robinson, C.D., Gihad, M., Erich, D.R. Potential re-use of sewage sludge as a raw material in the production of eco-friendly bricks. *Journal of Environment Management*. 2021. 297. Pp. 113–138.
28. Shakhov, S.A., Nikolaev, N.Yu. Peculiarities of the formation of the phase composition and structure of ceramics from an ash-clay charge modified with a silicate sol [Peculiarities of the formation of the phase composition and structure of ceramics from an ash-clay charge modified with a silicate sol]. *News of higher educational institutions. Construction*. 2019. 728(8). Pp. 19–27.
29. Shakhov, S.A., Nikolaev, N.Yu. Mixture for the manufacture of ceramic products [Mixture for the manufacture of ceramic products]. Russian patent No. 2655868, 2018.
30. Shakhov, S.A., Nikolaev, N.Yu. High-temperature phase transformations in ash-clay mixture modified with sludge filtrate [High-temperature phase transformations in ash-clay mixture modified with sludge filtrate]. *Proceedings of the II All-Russian scientific and practical conference with international participation. Novokuznetsk: publishing house of SGIU*. 2019. Pp. 130–134.

31. Klepikov, M.S., Shcherbakov, A.A., Viktorov, V.V. Kaolins of the Southern Trans-Urals are a new source of high-quality raw materials [Kaolins of the Southern Trans-Urals are a new source of high-quality raw materials]. Bashkir chemical journal. 2011. 18(4). Pp. 242–245.
32. Golovanov, S.P., Zubekhin, A.P., Likhota, O.V. Bleaching and intensification of sintering of ceramics using iron-containing clays [Bleaching and intensification of sintering of ceramics using iron-containing clays]. Glass and ceramics. 2004. 12. Pp. 9–11.
33. Vlasov, V.A. Semenov, M.A., Skripnikova, N.K., Shekhovtsov, V.V. Features of the use of substandard types of raw materials for the production of anorthite ceramics [Features of the use of substandard types of raw materials for the production of anorthite ceramics], Vestnik TGASU. 2020. 5. Pp. 122–128.
34. Rozenstrauha, I., Bajare, D., Cimdins, R., Berzina, L., Bossert, J., Boccaccini, A.R. The influence of various additions on a glass-ceramic matrix composition based on industrial waste. Ceramics International. 2006. 32. Pp.115–119.
35. Sergievich, O.A., Alekseenko, I.A., Artemiev, E.A. Ceramic materials with increased wear resistance for machine-building and light industry [Ceramic materials with increased wear resistance for machine-building and light industry]. Proceedings of the Kola Scientific Center of the Russian Academy of Sciences. 2017. 5. Pp.167–172.
36. Tunalia, A., Ozela, E., Turan, S. Production and characterization of granulated frit to achieve anorthite based glass–ceramic glaze. Journal of the European Ceramic Society. 2015. 35. Pp. 1089–1095.
37. Kanygina, O.N., Chetverikova, A.G., Lazarev, D.A., Salnikova E.V. High-temperature phase transformations in iron-bearing clays of the Orenburg region [High-temperature phase transformations in iron-bearing clays of the Orenburg region]. Vestnik OGU. 2010. 112(6). Pp. 113–118.
38. Dhir, K.R., Ghataora, S.G., Lynn, C.J. Sustainable Construction Materials: Sewage Sludge Ash. Woodhead Publishing. 2017. 274 p.
39. Park, Y.J., Moon, S.O., Heo, J. Crystalline phase control of glass ceramics obtained from sewage sludge fly ash. Ceramics International. 2003. 29. Pp. 223–227.
40. Galperina, M.K., Egerev V.M. Interrelation of porous porous-capillary structure and frost resistance of facade ceramic tiles [Interrelation of porous porous-capillary structure and frost resistance of facade ceramic tiles]. Proceedings of the Research Institute of Construction Ceramics. 1985. 55. Pp. 5–15.

Information about author:

Sergey Shakhov, Doctor of Technical Sciences

E-mail: sashakhov@mail.ru

Received 16.01.2023. Approved after reviewing 20.06.2023. Accepted 01.07.2023.

